

**DEVELOPMENT OF YTTERBIUM
SULFIDE/GRAPHENE OXIDE COMPOSITE THIN
FILMS FOR SUPERCAPACITOR APPLICATION**

**A THESIS SUBMITTED TO
D. Y. PATIL EDUCATION SOCIETY (DEEMED TO BE
UNIVERSITY), KOLHAPUR**



**FOR THE DEGREE OF
DOCTOR OF PHILOSOPHY
IN
PHYSICS
UNDER THE FACULTY OF
INTERDISCIPLINARY STUDIES**

**BY
Mr. SHIVAJI BHAURAO UBALE**

M.Sc.

UNDER THE GUIDANCE OF

Prof. C. D. LOKHANDE

M.Sc., Ph.D.

**DEAN AND RESEARCH DIRECTOR,
CENTRE FOR INTERDISCIPLINARY RESEARCH,
D. Y. PATIL EDUCATION SOCIETY (DEEMED TO BE UNIVERSITY),
KOLHAPUR- 416 006, MAHARASHTRA, (INDIA)**

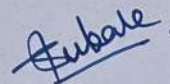
2021

DECLARATION

I hereby declare that the thesis entitled "DEVELOPMENT OF YTTERBIUM SULFIDE/GRAPHENE OXIDE COMPOSITE THIN FILMS FOR SUPERCAPACITOR APPLICATION" submitted for the degree of Doctor of Philosophy (Ph.D.) in the Centre for Interdisciplinary Research faculty of the D. Y. Patil Education Society (Deemed to be University), Kolhapur is completed and written by me, has not before made the basis for the award of any Degree/Diploma/other related heading of this or any other University in India/any other country/examining body to the best of my knowledge. Further, I assert that, I have not dishonored any of the requirements under Copyright and Piracy/Cyber/IPR act amended by UGC from time to time.

Place: Kolhapur

Date: 15/09/2021



Mr. Shivaji B. Ubale

(Research Student)

**D. Y. Patil Education Society (Deemed to be University),
Kolhapur**

Centre for Interdisciplinary Research



CERTIFICATE

This is to certify that the thesis entitled "**DEVELOPMENT OF YTTERBIUM SULFIDE/GRAPHENE OXIDE COMPOSITE THIN FILMS FOR SUPERCAPACITOR APPLICATION**" which is being submitted herewith for the award of the Degree of **Doctor of Philosophy (Ph.D.)** in **Physics** of **D. Y. Patil Education Society (Deemed to be University), Kolhapur**, is the result of the original research work completed by **Mr. Shivaji Bhaurao Ubale** under my supervision and guidance and to the best of my knowledge and belief the work embodied in this thesis has not formed earlier the basis for the award of any Degree or similar title of this or any other University or examining body.

Place: **Kolhapur**

Date: **15/09/2021**

Research Guide

Prof. C. D. Lokhande

Prof. C. D. LOKHANDE
Research Director
D. Y. Patil Education Society
(Institution Deemed to be University)
869, 'E', Kasaba Bawada
KOLHAPUR- 416006

Forwarded through,
Prof. C. D. Lokhande
Head and Research Director,
Centre for Interdisciplinary Research
Prof. C. D. LOKHANDE

Research Director

D. Y. Patil Education Society
(Institution Deemed to be University)
869, 'E', Kasaba Bawada
KOLHAPUR- 416006

ACKNOWLEDGEMENT

A journey is easier when you travel together. Interdependence is certainly more valuable than independence. This thesis is the result of work where I have been accompanied and supported by many peoples.

*At the completion of my Ph.D. thesis, I would like to express my sincere gratitude towards my advisor, **Prof. C. D. Lokhande** [Dean and Research Director, Centre for Interdisciplinary Research (CIR), D. Y. Patil Education Society (Deemed to be University), Kolhapur] for the continuous support during my Ph.D. study and related research, for his motivation, and immense knowledge. I thank him not only for the guidance he rendered in the field of research but also for enlightening the path of my life with a deep love for science. With his support, I could overcome my personal and scientific problems on writing scientific papers including this Ph.D. thesis and this work could not have been completed without his inspiring guidance and constant encouragement during the course of research tenure.*

*I would like to express my sincere thanks to Vice-Chancellor **Prof. R. K. Mudgal**, Pro-Vice Chancellor **Dr. Shimpa Sharma** and Registrar **Dr. V. V. Bhosale** for the inspiration and support. I thank **Dr. J. L. Gunjekar**, **Dr. U. M. Patil** and **Dr. V. M. Khot** who helped me to analyze the results with all their empathy and cooperative mind. I also thank **Dr. A. C. Lokhande**, **Dr. V. C. Lokhande** and **Dr. R. N. Bulakhe** for providing me very important sample characterization data, during entire research work.*

*I would like to express sincere thanks to **Dr. R. B. Pujari**, **Dr. A. M. Patil**, **Dr. A. R. Shelke**, and **Dr. V. S. Kumbhar** for insightful guidelines, scientific discussions and valuable suggestions on the present work. Good scientific research could not blossom in an alienated desert; it is a result of fruitful discussions and co-operative exercises of many analytical minds. I am thankful to **Dr. A. M. More**, Head, Department of Physics, K. N. Bhise College, Kurduwadi (Madha) for his good wishes and support. I am also thankful non-teaching staff of the CIR Department for their kind co-operation during my research work.*

*In addition, I acknowledge the funding support from **Chhatrapati Shahu Maharaj Research Training and Human Development Institute (SARTHI)**, Pune of the **Government of Maharashtra State** for **Chhatrapati Shahu Maharaj National Senior Research Fellowship (CSMNSRF)** sanctioned to me.*

*I wish to express my appreciation towards my seniors **Dr. T. T. Ghogare**, **Dr. S. B. Kale**, **Dr. P. K. Katkar** and **Dr. S. J. Marje** for co-*

operation, scientific discussion and the encouragement provided to me during the course of research work.

I own a word of thanks to all my friends and research colleague from CIR department viz. **Vikas Mane, Dhanaji Malavekar, Priti Bagawade, Navnath Padalkar, Rohini Shinde, Shrikant Sadavar, Sachin Pujari, Suraj Khalate, Satish Jadhav, Vikas Magdum, Yogesh Chitare, Shirin Kulkarni, Sambhaji Kumbhar, Ranjit Nikam, Sambhaji Khot, Vinod Patil, Satish Phalake, Akash Patil, and Shraddha Bhosale.**

I hereby express my deepest appreciation and regards to my beloved parents (**Nana and Tai**), uncle (**Bapu**), brothers (**Yuvraj, Pratap, Prashant and Pradip**) sister (**Renuka**), Daji (**Suhas**), Mama (**Santosh Gandhale and Kantilal Gandhale**), and all of family members who in spite of their hard times and sufferings, continuously supported and encouraged me to complete my research.

I would like to confess that even though I try my best, it is not possible for me to acknowledge and thank all those known and unknown faces individually for their direct and indirect contribution for the successful completion of this work. I am grateful to all of you for your kind cooperation.

Place- Kolhapur

- Shivaji Ubale

Date: 15 / 09 / 2021

SUMMARY OF RESEARCH WORK

A) Published (Indian) Patents: (03)

- 1) C. D. Lokhande, R. B. Pujari, V. V. Bhosale, V. C. Lokhande, **S. B. Ubale**, "Chemically deposited large area and nanostructured samarium oxide thin films for energy storage", (2018), Application No.: **201821022705**.
- 2) C. D. Lokhande, **S. B. Ubale**, V. V. Bhosale, V. C. Lokhande, "Chemically coated ytterbium phosphate film on solid surface and energy storage application thereof", (2019), Application No.: **201921042840**.
- 3) C. D. Lokhande, V. J. Mane, V. C. Lokhande, **S. B. Ubale**, V. V. Bhosale, "Asymmetric solid state supercapacitor for energy storage", Application No.: **202021011232**.

B) Papers Published in International Journals: (11)

- 1) **S. B. Ubale**, S. B. Kale, V. J. Mane, U. M. Patil, C. D. Lokhande, "Supercapacitor devices based as SILAR synthesized ytterbium sulfide @ graphene oxide nanocomposite flexible thin film electrodes" J. Electroanal. Chem., 897, (2021), 115589-115601 **(I.F.- 4.46)**.
- 2) **S. B. Ubale**, S. B. Kale, V. J. Mane, P. P. Bagwade, C. D. Lokhande, "SILAR synthesized nanostructured ytterbium sulfide thin film electrodes for symmetric supercapacitors" J. Solid State Electr., 25, (2021), 1753-1764 **(I.F.- 2.64)**.
- 3) **S. B. Ubale**, R. N. Bulakhe, V. J. Mane, D. B. Malavekar, I. In, C. D. Lokhande, "Chemical synthesis of nano-grained ytterbium sulfide thin films for supercapacitor application" Appl. Nanosci., 10, (2020), 5085-5097 **(I.F.- 3.68)**.
- 4) **S. B. Ubale**, T. T. Ghogare, V. C. Lokhande, T. Ji, C. D. Lokhande, "Electrochemical behavior of hydrothermally synthesized porous groundnuts-like samarium oxide thin films", SN Applied Sciences, 2, (2020), 1-5 **(I.F.- pending)**.
- 5) P. P. Bagwade, D. B. Malavekar, T. T. Ghogare, **S. B. Ubale**, V. J. Mane, R. N. Bulakhe, I. In, C. D. Lokhande, "A high performance flexible solid-state asymmetric supercapacitor based on composite of reduced graphene oxide@ dysprosium sulfide nanosheets and manganese oxide nanospheres", J. Alloys Compd., 859, (2021), 157829- 157847 **(I.F.- 5.31)**.
- 6) V. J. Mane, S. B. Kale, **S. B. Ubale**, V. C. Lokhande, U. M. Patil, C. D. Lokhande, "Lanthanum sulfide-manganese sulfide/graphene oxide (La₂S₃-MnS/GO) composite thin film as an electrocatalyst for oxygen evolution reactions", J. Solid State Electr., 25, (2021), 1775-1788 **(I.F.- 2.64)**.
- 7) V. J. Mane, S. B. Kale, **S. B. Ubale**, V. C. Lokhande, C. D. Lokhande, "Enhanced specific energy of silver doped MnO₂/GO electrodes as facile fabrication symmetric supercapacitor device", Mater. Today Chem., 20, (2021), 100473-100487 **(I.F.- 8.30)**.
- 8) P. P. Bagwade, D. B. Malavekar, **S. B. Ubale**, T. T. Ghogare, R. N. Bulakhe, I. In, U. M. Patil, C. D. Lokhande, "Characterization of Dy₂S₃ thin films deposited by successive ionic layer adsorption and reaction (SILAR) method", Solid State Sci., 119, (2021), 106693-106697 **(I.F.- 3.05)**.
- 9) V. J. Mane, D. B. Malavekar, **S. B. Ubale**, R. N. Bulakhe, I. In, C. D. Lokhande, "Binder free lanthanum doped manganese oxide@ graphene oxide composite as high energy density electrode material for flexible symmetric solid state supercapacitor", Electrochim. Acta., 335, (2020), 135613-135628 **(I.F.- 6.90)**.
- 10) D. B. Malavekar, V. C. Lokhande, V. J. Mane, **S. B. Ubale**, U. M. Patil, C. D. Lokhande, "Enhanced energy density of flexible asymmetric solid state supercapacitor device

fabricated with amorphous thin film electrode materials”, J. Phys. Chem. Solids, 141, (2020), 109425-109435 **(I.F.- 3.99)**.

- 11) V. J. Mane, D. B. Malavekar, **S. B. Ubale**, V. C. Lokhande, C. D. Lokhande, “Manganese dioxide thin films deposited by chemical bath and successive ionic layer adsorption and reaction deposition methods and their supercapacitive performance”, Inorg. Chem. Commun., 115, (2020), 107853-107869 **(I.F.- 2.49)**.

(C) Papers Submitted at International Journals: (03)

- 1) P. P. Bagwade, **S. B. Ubale**, D. B. Malavekar, R. N. Bulakhe, I. In, U. M. Patil, C. D. Lokhande, “Synthesis of nanocauliflower-like cobalt tungsten oxide thin films by successive ionic layer adsorption and reaction (SILAR) Method”, Revision Submitted to Synth. Met., (2021), **(I.F.- 3.26)**.
- 2) V. J. Mane, A. C. Lokhande, **S. B. Ubale**, R. P. Nikam, P. P. Bagwade, N. S. Padalkar, D. S. Dhawale, C. D. Lokhande, “Facile synthesis of MnS-La₂S₃/graphene oxide composite electrodes for high performance flexible symmetric supercapacitor device”, Submitted to Appl. Mater. Today, (2021), **(I.F.- 10.04)**.
- 3) N. S. Shaikh, V. C. Lokhande, T. Ji, P. P. Ngat, **S. B. Ubale**, J. S. Shaikh, S. Prasertthdam, C. D. Lokhande, P. Kanjanaboos, “Sulfur-doped graphene as a rational anode for ionic liquid based hybrid capacitor with 3.5 V working window”, Submitted to Mater. Today Chem., (2021), **(I.F.- 8.30)**.

D) Poster Presented at National/International Conferences: (05)

- 1) **S. B. Ubale**, V. J. Mane, D. B. Malvekar, T. T. Ghogare, S. B. Kale, M. R. Phadatare, C. D. Lokhande, “Hydrothermal synthesis of samarium oxide (Sm₂O₃) thin films for supercapacitor application”, National conf. on Advanced Materials Synthesis, Characterization and Application, (AMSCA-2018), Pune.
- 2) **S. B. Ubale**, V. J. Mane, D. B. Malvekar, S. B. Kale, T. T. Ghogare, M. R. Phadatare, C. D. Lokhande, “Chemical synthesis of ytterbium sulfide (Yb₂S₃) thin film for supercapacitor application, Int. Conf. On Physics of Materials and Materials Based Device Fabrication”, (4th ICPM-MDF-2019), Kolhapur.
- 3) **S. B. Ubale**, V. J. Mane, D. B. Malvekar, S. B. Kale, T. T. Ghogare, P. P. Bagwade, C. D. Lokhande, “SILAR synthesis of ytterbium sulfide thin films by chemical route and their supercapacitor application”, Int. Conf. on Advancements in Renewable Energy (ICARE-2020), Nanded.
- 4) **S. B. Ubale**, V. J. Mane, D. B. Malvekar, T. T. Ghogare, S. B. Kale, C. D. Lokhande, “Chemically synthesis ytterbium sulfide thin films and their supercapacitor study”, Int. Conf. on Smart Materials and Nanotechnology (ICSMN-2020), Pandharpur.
- 5) **S. B. Ubale**, V. J. Mane, D. B. Malvekar, T. T. Ghogare, S. B. Kale, C. D. Lokhande, “Chemical synthesis of ytterbium thin films for supercapacitor application”, National Seminar on Modern Approaches in Sciences (MAS-2019) K. N. Bhise Arts, Commerce and Vinayakrao Patil Science College, Bhosare (Kurduwadi), Solapur.

E) Workshops Attended: (02)

- 1) Participated in “Biodiversity conservation and biodiversity act 2002” held at D. Y. Patil Education Society (Deemed to be University), Kolhapur at **15th February 2019** organized by Department of Stem Cell and Regenerative Medicine, Centre for Interdisciplinary Research.
- 2) Participated in “Entrepreneurship and innovation as carrier opportunity” held at D. Y. Patil Education Society (Deemed to be University), Kolhapur during **19th December 2019** organized by Institution Innovation Council (IIC).

INDEX

Title	Page No.
<i>Candidate's declaration</i>	<i>ii</i>
<i>Certificate of Guide</i>	<i>iii</i>
<i>Acknowledgement</i>	<i>iv-v</i>
<i>Summary of research work</i>	<i>vi-vii</i>
<i>Index</i>	<i>viii</i>
<i>List of Figures</i>	<i>ix-xii</i>
<i>List of Tables</i>	<i>xiii</i>
<i>List of Abbreviations and Acronyms</i>	<i>xiv-xv</i>
Chapter-I: <i>Introduction of supercapacitor and literature survey</i>	<i>1-24</i>
Chapter-II: <i>Theoretical background of thin film, synthesis methods, characterization techniques and supercapacitor</i>	<i>25-52</i>
Chapter-III: <i>Chemically synthesized ytterbium sulfide thin films: characterization and supercapacitive performance</i>	<i>53-74</i>
Chapter-IV: <i>SILAR synthesized ytterbium sulfide, graphene oxide and graphene oxide/ytterbium sulfide composite thin films: characterization and supercapacitive performance</i>	<i>75-92</i>
Chapter-V: <i>Synthesis, characterization and supercapacitive performance of manganese oxide thin films</i>	<i>93-104</i>
Chapter-VI: <i>Fabrication and performance evaluation of flexible solid state symmetric and asymmetric supercapacitor devices based on Yb_2S_3, GO/Yb_2S_3 and MnO_2 electrodes</i>	<i>105-136</i>
Chapter-VII: <i>Summary and conclusions</i>	<i>137-144</i>

LIST OF FIGURES

Chapter-I (Introduction of supercapacitor and literature survey)

- Fig. 1.1 The Ragone plot of energy storage devices.
Fig. 1.2 The schematic representation of conventional electrochemical capacitor.
Fig. 1.3 Classification of supercapacitor with different types and subtypes.
Fig. 1.4 Schematic of charge storage mechanisms for (A) EDLC and (B) pseudocapacitor.

Chapter-II (Theoretical background of thin film, synthesis methods, characterization techniques and supercapacitor)

- Chart 2.1 Brief taxonomy of thin film deposition methods.
Fig. 2.2 The schematic of L-b-L method.
Fig. 2.3 The schematic of CBD method.
Fig. 2.4 The schematic of SILAR deposition method.
Fig. 2.5 (A) Photograph of Rigaku Miniflex-600 XRD unit and (B) the schematic of X-ray diffractometer.
Fig. 2.6 Ejection of photoelectron after bombardment of Al $K\alpha$ ($h\nu = 1486.6$ eV)/Mg $K\alpha$ ($h\nu = 1253.6$ eV) radiations in the XPS measurements.
Fig. 2.7 The block ray diagram of FT-Raman spectrophotometer.
Fig. 2.8 Energy level diagram showing states involved in Raman spectroscopy.
Fig. 2.9 The block diagram of FE-SEM.
Fig. 2.10 General layout of electron beam path in TEM.
Fig. 2.11 Photographs of (A) TEM grid holder and (B) copper grid.
Fig. 2.12 (A) Photograph of Rame-Hart contact angle meter and (B) the contact angle image of a liquid drop on a solid thin film surface.
Fig. 2.13 Types of supercapacitor device.
Fig. 2.14 The typical CV curve.
Fig. 2.15 The typical GCD curve.
Fig. 2.16 A typical Nyquist curve.

Chapter-III (Chemically synthesized ytterbium sulfide thin films: characterization and supercapacitive performance)

- Fig. 3.1 The schematic representation of steps involved the preparation of Yb_2S_3 thin film by CBD method.
Fig. 3.2 The X-ray diffraction pattern of Yb_2S_3 thin film.
Fig. 3.3 (A) The XPS survey spectrum of Yb_2S_3 thin film, (B) XPS spectrum of Yb4d region and (C) XPS spectrum of S2p region, and (D) FT-Raman spectrum for Yb_2S_3 thin film.
Fig. 3.4 (A) Contact angle and SEM images of Yb_2S_3 thin films at (B) 50 kX and (C) 150 kX magnifications.
Fig. 3.5 (A-B) HR-TEM images and (C) selected area electron diffraction (SAED) pattern of Yb_2S_3 sample.
Fig. 3.6 (A) The CV curves at scan rates from 5-200 mV s^{-1} , (B) plot of specific capacitance versus scan rates, (C) galvanostatic charge-discharge curves of Yb_2S_3 film at 0.2-0.5 A g^{-1} current densities, and (D) plot of specific capacitance versus current density.
Fig. 3.7 (A) The cyclic stability of Yb_2S_3 film electrode at scan rate of 50 mV s^{-1} in 1 M KOH electrolyte, (B) the plot of capacity retention versus cyclic number and (C) Nyquist plot of Yb_2S_3 film [Inset shows the equivalent circuit].

- Fig. 3.8 Experimental setup of SILAR method for preparation of Yb_2S_3 thin film [Inset shows the photograph of Yb_2S_3 thin film]
- Fig. 3.9 The X-ray diffraction pattern of Yb_2S_3 thin film.
- Fig. 3.10 (A) The XPS survey spectrum of Yb_2S_3 thin film, (B) XPS spectrum of Yb4d region and (C) XPS spectrum of S2p region.
- Fig. 3.11 (A) Contact angle and FE-SEM images of Yb_2S_3 thin films at magnifications of (B) 5 kX and (C) 10 kX.
- Fig. 3.12 (A) The CV curves of Yb_2S_3 at different scan rates of 5-200 mV s^{-1} , (B) plot of Cs versus scan rate, (C) GCD curves at current densities of 1-5 A g^{-1} , and (D) plot of Cs versus current density.
- Fig. 3.13 (A) Electrochemical cyclic stability of Yb_2S_3 sample at scan rate of 100 mV s^{-1} (B) plot of capacity retention versus cycle number and (C) Nyquist plot of Yb_2S_3 sample (Inset illustrates the best fitted equivalent circuit).

Chapter-IV (SILAR synthesized ytterbium sulfide, graphene oxide and graphene oxide/ytterbium sulfide composite thin films: characterization and supercapacitive performance)

- Fig. 4.1 Flow chart for synthesis of GO.
- Fig. 4.2 The schematic of L-b-L method for deposition of GO thin film [Inset shows the photograph of GO thin film].
- Fig. 4.3 The schematic of SILAR method for the synthesis of $\text{GO}/\text{Yb}_2\text{S}_3$ composite thin film [Inset shows the photograph of $\text{GO}/\text{Yb}_2\text{S}_3$ thin film].
- Fig. 4.4 The X-ray diffraction patterns of (A) GO, (B) Yb_2S_3 and (C) $\text{GO}/\text{Yb}_2\text{S}_3$ composite thin films.
- Fig. 4.5 (A) The XPS survey spectrum of $\text{GO}/\text{Yb}_2\text{S}_3$ composite thin film and XPS spectra of (B) Yb4d region, (C) S2p region, (D) C1s region and (E) O1s region of $\text{GO}/\text{Yb}_2\text{S}_3$ thin film.
- Fig. 4.6 Contact angle images of (A) Yb_2S_3 , (B) GO and (C) $\text{GO}/\text{Yb}_2\text{S}_3$ composite thin films.
- Fig. 4.7 FE-SEM images of (A) Yb_2S_3 , (B) GO and (C) $\text{GO}/\text{Yb}_2\text{S}_3$ composite thin films at magnification of 10 kX.
- Fig. 4.8 (A, B) HR-TEM images and (C) selected area electron diffraction (SAED) pattern of $\text{GO}/\text{Yb}_2\text{S}_3$ composite material.
- Fig. 4.9 The CV curves of (A) Yb_2S_3 , (B) GO and (C) $\text{GO}/\text{Yb}_2\text{S}_3$ composite thin films at varied scan rates of 5-200 mV s^{-1} , and (D) plots of specific capacitance versus scan rates for Yb_2S_3 , GO and $\text{GO}/\text{Yb}_2\text{S}_3$ composite thin films.
- Fig. 4.10 The GCD curves of (A) Yb_2S_3 , (B) GO and (C) $\text{GO}/\text{Yb}_2\text{S}_3$ composite thin films at various current densities 1-5 A g^{-1} , and (D) plots of specific capacitance versus current densities for Yb_2S_3 , GO and $\text{GO}/\text{Yb}_2\text{S}_3$ composite thin films at current density of 1-5 A g^{-1} .
- Fig. 4.11 The cyclic stability CV curves of (A) Yb_2S_3 , (B) GO and (C) $\text{GO}/\text{Yb}_2\text{S}_3$ composite thin films at scan rate 100 mV s^{-1} , and (D) capacitance retentions of Yb_2S_3 , GO and $\text{GO}/\text{Yb}_2\text{S}_3$ composite thin films.
- Fig. 4.12 Nyquist plots of (A) Yb_2S_3 , (B) GO and (C) $\text{GO}/\text{Yb}_2\text{S}_3$ composite thin films [Inset shows the equivalent fitted circuit].

Chapter-V (Synthesis, characterization and supercapacitive performance of manganese oxide thin films)

- Fig. 5.1 The schematic preparation for deposition of MnO_2 thin film electrode by SILAR method [Inset shows the photograph of MnO_2 thin film electrode].
- Fig. 5.2 The XRD pattern of MnO_2 thin film.

- Fig. 5.3 (A) XPS survey spectrum of MnO₂ thin film. The XPS spectra of MnO₂ thin film for (B) Mn2p region and (C) O1s region and (D) FT-IR spectrum of MnO₂ thin film.
- Fig. 5.4 (A) The contact angle image of MnO₂ thin film. The FE-SEM images of MnO₂ thin film at magnifications of (B) 20 kX and (C) 50 kX.
- Fig. 5.5 (A) The CV curves of MnO₂ thin film at varied scan rates from 5 to 200 mV s⁻¹, (B) plot of Cs versus different scan rates at 5-200 mV s⁻¹, (C) the GCD curves of MnO₂ thin film at various current densities of 1-5 A g⁻¹ and (D) plot of Cs versus current densities at 1-5 A g⁻¹.
- Fig. 5.6 (A) The stability curves of MnO₂ thin film, (B) plot of capacity retention versus cycle number of MnO₂ thin film and (C) Nyquist plot of MnO₂ thin film.

Chapter-VI (Fabrication and performance evaluation of flexible solid state symmetric and asymmetric supercapacitor devices based on Yb₂S₃, GO/Yb₂S₃ and MnO₂ electrodes)

- Fig. 6.1 Photographs of (A) Yb₂S₃ electrode with sealed edges by tape, (B) application of thin layer of gel electrolyte on both Yb₂S₃ electrodes and (C) assembly of device (5 x 5 cm²).
- Fig. 6.2 (A) The CV curves for selection of potential window at different voltages, (B) the CV curves for Yb₂S₃/PVA-KOH/Yb₂S₃ FSS-SSc device at scan rates of 5-200 mV s⁻¹, (C) plot of specific capacitance versus scan rate, (D) the GCD curves for Yb₂S₃/PVA-KOH/Yb₂S₃ FSS-SSc device at 0.2-0.5 A g⁻¹ current densities, and (E) plot of specific capacitance versus current density.
- Fig. 6.3 (A) The Ragone plot for Yb₂S₃/PVA-KOH/Yb₂S₃ FSS-SSc device, (B) the CV curves of FSS-SSc device at various bending angles, (C) plot of capacitive retention versus bending angle [Insets show photograph of different bending angles], (D) stability of Yb₂S₃/PVA-KOH/Yb₂S₃ FSS-SSc device at scan rate of 100 mV s⁻¹ with PVA-KOH gel electrolyte, (E) capacitive retentions up to 3000 cycles at a scan rate of 100 mV s⁻¹ and (F) Nyquist plot for Yb₂S₃/PVA-KOH/Yb₂S₃ FSS-SSc device [Inset shows the equivalent circuit].
- Fig. 6.4 Images two red LEDs glowing at (A) 1 and (B) 55 s.
- Fig. 6.5 (A) The I-V characteristic of two red LEDs and (B) the current, voltage and power versus time graphs of FSS-SSc device during discharging.
- Fig. 6.6 Photographs of (A) Yb₂S₃ deposited on the SS substrate electrodes with (5x5 cm²) area, (B) PVA-Na₂SO₄ gel electrolyte painted on Yb₂S₃ electrodes, (C) both the electrode edges sealed with insulator tape and (D) assembled FSS-SSc device.
- Fig. 6.7 (A) Potential window selection in the voltage ranging from 1.0 to 1.8 V at 100 mV s⁻¹ scan rate, (B) the CV curves of FSS-SSc device at different scan rates of 5-200 mV s⁻¹, (C) plot of Cs versus scan rate, (D) GCD curves at current densities from 0.5-1.0 A g⁻¹ and (E) plot of Cs versus current density.
- Fig. 6.8 (A) The Ragone plot of FSS-SSc device, (B) the CV curves of FSS-SSc device at different bending angles, (C) plot of capacitive retention versus bending angle [Insets show photograph of different bending angles], (D) cyclic stability curves of FSS-SSc device at scan rate of 100 mV s⁻¹ for 3000 CV cycles, (E) plot of capacity retention versus cycle number and (F) Nyquist plot of FSS-SSc device (Inset demonstrates the equivalent circuit).
- Fig. 6.9 Photographs of two red LEDs glowing at (A) 1 and (B) 60 s.
- Fig. 6.10 The current, voltage and power versus time graphs of FSS-SSc

- device during discharging.
- Fig. 6.11** The schematic representation of FSS-SSc device formation of GO/Yb₂S₃//GO/Yb₂S₃ composite electrodes.
- Fig. 6.12** (A) Potential window selection in the voltage range from 1.0 to 1.8 V, (B) the CV curves of FSS-SSc device at varied scan rate from 5-200 mV s⁻¹, (C) plot of specific capacitance versus scan rate, (D) the GCD curves at charging current densities from 1-5 A g⁻¹ and (E) plot of specific capacitance versus current density.
- Fig. 6.13** (A) The Ragone plot of FSS-SSc device, (B) the CV curves of FSS-SSc device at various bending angles, (C) plot of capacitive retention versus bending angle [Insets show the different bending angles photograph], (D) stability curves of FSS-SSc device at 100 mV s⁻¹ over 10000 CV cycles, (E) plot of capacitance retention versus cycle number and (F) Nyquist plots of before and after stability of FSS-SSc device and (inset shows best fitted equivalent circuit).
- Fig. 6.14** (A, B) Practical demonstration of FSS-SSc device glowing (211) red LEDs panel images at 1 (A) and (B) 30 s.
- Fig. 6.15** (A) The I-V characteristic of 211 red LEDs panel and (B) the current, voltage and power versus time plots of FSS-SSc device during discharging.
- Fig. 6.16** The schematic representation of FSS-ASSc device formation using GO/Yb₂S₃//MnO₂.
- Fig. 6.17** The CV curves of GO/Yb₂S₃ composite and MnO₂ electrodes at scan rate of 100 mV s⁻¹.
- Fig. 6.18** (A) Potential window selection in the voltage ranging from 1.2 to 2.0 V at scan rate of 100 mV s⁻¹, (B) the CV curves of asymmetric device at different scan rate of 5-200 mV s⁻¹, (C) plot of specific capacitance versus scan rates, (D) the GCD curves at current densities from 1-5 A g⁻¹ and (E) plot of specific capacitance versus current density.
- Fig. 6.19** (A) The Ragone plot of FSS-ASSc device, (B) the CV curves of FSS-ASSc device at various bending angles, (C) cyclic stability curves of asymmetric device at 100 mV s⁻¹ over 10000 CV cycles, (D) plot of capacity retention versus bending angle [Insets show photograph of different bending angles], (E) plot of capacitance retention versus cycle number and (F) Nyquist plots of asymmetric device before and after stability (inset shows best fitted equivalent circuit).
- Fig. 6.20** (A, B) Practical demonstration of FSS-ASSc device glowing red (211) LEDs panel images at 1 (A) and (B) 90 s.
- Fig. 6.21** (A) The I-V characteristic of 211 red LEDs panel and (B) the current, voltage and power versus time graphs of FSS-ASSc device during discharging.

LIST OF TABLES

Chapter-I (Introduction of supercapacitor and literature survey)

Table 1.1 Literature survey on rare earth chalcogenide thin films and their physical properties.

Table 1.2 Literature survey on rare earth chalcogenide thin films for supercapacitor performance.

Table 1.3 Literature survey on GO based composite thin films for supercapacitor performance.

Chapter-III (Chemically synthesized ytterbium sulfide thin films: characterization and supercapacitive performance)

Table 3.1 The optimized preparative parameters for deposition of Yb₂S₃ film.

Table 3.2 The electrochemical impedance parameters of Yb₂S₃ thin film.

Table 3.3 Preparative parameters for synthesis of Yb₂S₃ thin film by SILAR method

Table 3.4 The EIS parameters of Yb₂S₃ thin film in 1M Na₂SO₄ electrolyte.

Table 3.5 The supercapacitive performance of CBD and SILAR deposited Yb₂S₃ thin films.

Chapter-IV (SILAR synthesized ytterbium sulfide, graphene oxide and graphene oxide/ytterbium sulfide composite thin films: characterization and supercapacitive performance)

Table 4.1 Optimized preparative parameters for room temperature deposition of GO thin films.

Table 4.2 The optimized preparative parameters at the room temperature for deposition of GO/Yb₂S₃ composite thin films (SILAR method).

Table 4.3 Electrochemical impedance parameters of Yb₂S₃, GO and GO/Yb₂S₃ thin films.

Table 4.4 Supercapacitive performance of Yb₂S₃, GO and GO/Yb₂S₃ thin films.

Chapter-V (Synthesis, characterization and supercapacitive performance of manganese oxide thin films)

Table 5.1 Preparative parameters for deposition of MnO₂ thin film by SILAR method.

Table 5.2 The EIS parameters of MnO₂ thin film in 1M Na₂SO₄ electrolyte.

Chapter-VI (Fabrication and performance evaluation of flexible solid state symmetric and asymmetric supercapacitor devices based on Yb₂S₃, GO/Yb₂S₃ and MnO₂ electrodes)

Table 6.1 Capacitive retention values at different bending angles of FSS-SSc device.

Table 6.2 The electrochemical impedance parameters for FSS-SSc device.

Table 6.3 Capacitive retention values at different bending angles of FSS-SSc device.

Table 6.4 Impedance parameters for FSS-SSc device.

Table 6.5 Capacitive retention values at different bending angles for FSS-SSc device.

Table 6.6 Impedance parameters of FSS-SSc device.

Table 6.7 Capacitive retention values at different bending angles for FSS-ASSc device.

Table 6.8 Impedance parameters for FSS-ASSc device before and after stability.

Table 6.9 Supercapacitive performance of symmetric and asymmetric devices.

Chapter-VII (Summary and conclusions)

Table 7.1 Supercapacitive performance evaluation for various thin film material electrodes.

Table 7.2 Supercapacitive performance evaluation of symmetric and asymmetric devices.

LIST OF ABBREVIATIONS AND ACRONYMS

AC	Activated carbon
AHC	Asymmetric hybrid capacitor
ALD	Atomic layer deposition
ASc	Asymmetric supercapacitor
C	Capacitance
CA	Citric acid
CBD	Chemical bath deposition
CE	Counter electrode
CNTs	Carbon nanotubes
CRT	Cathode ray tube
Cs	Specific capacitance
CV	Cyclic voltammetry
CVD	Chemical vapour deposition
DDW	Double distilled water
ED	Energy density
EDLC	Electric double layer capacitor
EDTA	Ethylenediamine tetraacetic acid
EIS	Electrochemical impedance spectroscopy
ESR	Equivalent series resistance
FE-SEM	Field emission scanning electron microscopy
FSS-ASC	Flexible solid state asymmetric supercapacitor
FSS-SSC	Flexible solid state symmetric supercapacitor
FT-Raman	Fourier transform-Raman spectroscopy
FWHM	Full width at half maxima
GCD	Galvanostatic charge discharge
GO	Graphene oxide
GO/Yb₂S₃	Graphene oxide composite with ytterbium sulfide
Hg/HgO	Mercury/mercury oxide
HR-TEM	High resolution-transmission electron microscopy
HSc	Hybrid supercapacitor
IP	Ionic product
IBS	Ion beam sputtering
JCPDS	Joint committee on powder diffraction standards
KOH	Potassium hydroxide
L-b-L	Layer-by-layer
L-CVD	Laser-chemical vapour deposition
LEDs	Light emitting diodes
M-CBD	Modified-chemical bath deposition

MnO₂	Manganese oxide
MOVCD	Metal-organic chemical vapour deposition method
Na₂SO₄	Sodium sulphate
OA	Oxalic acid
PD	Power density
PE-CVD	Plasma enhanced-chemical vapour deposition
PP-CVD	Plasma photochemical vapour deposition
PVA	Polyvinyl alcohol
PVA-KOH	Polyvinyl alcohol-potassium hydroxide
PVA-Na₂SO₄	Polyvinyl alcohol-sodium sulphate
R_{ct}	Charge transfer resistance
RE	Reference electrode
REM	Rare earth metal
RS	Reacting sputtering
R_s	Solution resistance
SP	Solubility product
SAED	Selected area electron diffraction
Sc	Supercapacitor
SEM	Scanning electron microscopy
SILAR	Successive ionic layer adsorption and reaction
SS	Stainless steel
SS_c	Symmetric supercapacitor
TA	Tartaric acid
TE	Thermal evaporation
TEA	Triethanolamine
TEM	Transmission electron microscopy
W	Warburg resistance
WE	Working electrode
XPS	X-ray photoelectron spectroscopy
XRD	X-ray diffraction
Yb₂S₃	Ytterbium sulfide

Chapter-I

*Introduction of supercapacitor and
literature survey*

Chapter-I

Introduction of supercapacitor and literature survey

Sr. no.	Title		Page no.
1.1	General introduction		1
	1.1.1	<i>Necessity of supercapacitor</i>	1
	1.1.2	<i>Principle of supercapacitor</i>	2
	1.1.3	<i>Taxonomy of supercapacitor</i>	4
		1.1.3.1 <i>Electrochemical Double Layer Capacitor</i>	5
		1.1.3.2 <i>Pseudocapacitor</i>	6
		1.1.3.3 <i>Hybrid supercapacitor</i>	6
	1.1.4	<i>New trends in supercapacitor</i>	7
1.2	Literature survey on rare earth chalcogenides and graphene oxide (GO) based composite thin films		8
	1.2.1	<i>Literature survey on rare earth chalcogenide thin films and their physical properties</i>	8
	1.2.2	<i>Literature survey on rare earth chalcogenides thin films for supercapacitor performance</i>	13
	1.2.3	<i>Literature survey on graphene oxide based composite thin films for supercapacitor performance</i>	14
1.3	Orientation and purpose of dissertation		17
1.4	References		20

1.1 General introduction:

1.1.1 Necessity of supercapacitor:

In the last decade, developing industrialization, environmental pollution and the human population along with the diminishing fossil fuels have become most critical problems for the present and future generations [1]. Furthermore, natural resources are limited in a global ecosystem. To overcome these issues, there is an urgent requirement for the development of eco-friendly and safe renewable energy resources [2, 3]. In recent years, renewable energy resources, such as hydropower, wind and solar are more useful for energy conversion systems. Exploiting these renewable energy resources for the replacement of fossil fuels to employ continuous energy production is more essential. However, the discontinuity of these resources is the main disadvantage. Energy storage is one of the crucial parts which can resolve the problems. The systems of electrical energy storage play a vital role in various practical applications [4, 5]. The role of energy storage technologies in the field of renewable energy generation and hybrid/electric vehicles has become essential. Moreover, to meet the next generation energy demands, low-cost, lightweight, flexible and high-performance energy storage gadgets are necessary requirements. The supercapacitor (electrochemical capacitors or ultracapacitors) is the device for energy storage device which holds great promise in many applications [6-8]. Supercapacitors are employed in several applications which incorporate hybrid vehicles, memory backup systems and portable electronic devices, due to their promising features like superior cycling stability, fast charge-discharge process and high power density [9, 10]. It can store electrical energy and deliver it like batteries, but they utilize various electrochemical mechanisms. The battery stores electricity through chemically, while the ultracapacitors store physically by sorting out negative and positive charges. The performance of energy storage devices can be explained in terms of their capacity to deliver energy and power density.

The Ragone plot of energy storage devices is illustrated in **Fig 1.1**, which shows a comparison with ordinary devices in terms of energy density and power density. The conventional capacitor has less energy density and high power density, whereas the battery has higher energy density and lower power density. As a result, if we extract energy quickly from a lithium-ion battery, its ability is decreased, by means if we need higher powers from the battery it is enforced to extract the lower amount of energy. In the Ragone plot, supercapacitors occupy a significant position as they fill the gap between conventional capacitors and fuel cells/batteries. They have more power ability

and comparatively huge energy density than the conventional capacitors. They can deliver extensive energy at a higher power density. In addition, they have long stability than the batteries, low equivalent series resistance (ESR) and high capacitance as compared to conventional capacitors. For the more functional devices, supercapacitors propose a promising approach to overcome the growing power demands [12-14].

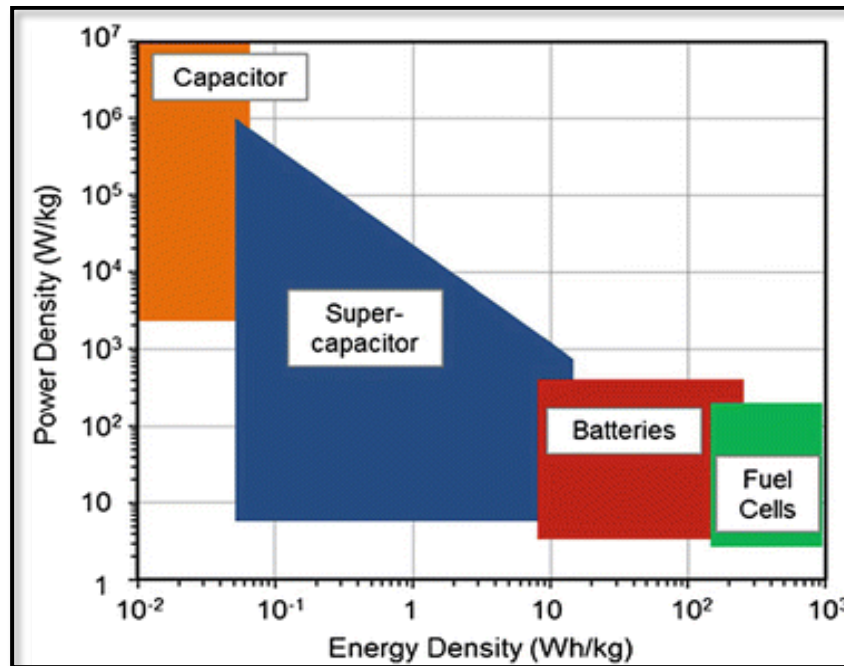


Fig. 1.1: The Ragone plot of energy storage devices [11].

1.1.2 Principle of supercapacitor:

The conventional capacitor stores energy over electrode surface separated by a dielectric material, whereas a supercapacitor stores energy through the formation of an electric double-layer at the interface of electrode and electrolyte. In the conventional capacitor, charges are accumulated at electrode/electrolyte interface, which creates an electric double layer separated in a few Angstrom. Fig. 1.2 shows the charge storage mechanism of the conventional capacitor. It consists of two conducting plates, which are separated through the dielectric material. When a voltage is applied across the conductor plates, the ions are adsorbed over the electrode with opposite polarity and form an electric double layer at the electrode interface and applied electrolyte. Capacitance is a number of charges stored with respect to potential. The ratio of the charge stored in the applied voltage is called capacitance (C).

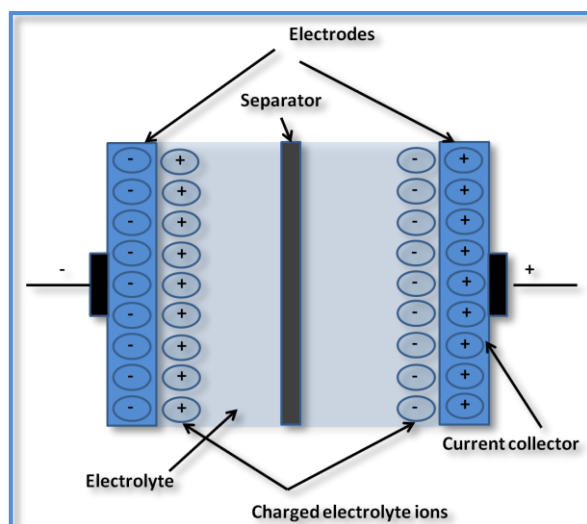


Fig. 1.2: The schematic representation of conventional electrochemical capacitor [15].

$$C = Q/V \quad (1.1)$$

Here, Q and V are the charges stored with respect to mass over the electrode and potential window. In conventional capacitor, C is inversely proportional to the distance between both electrodes and directly proportional to the electrode surface area.

$$C = \epsilon_r \epsilon_o A/d \quad (1.2)$$

Here, ϵ_r , ϵ_o , A and d are the permittivity of vacuum, the relative permittivity of the medium in electric double layer, electrode specific surface area and electric double layer effective thickness, respectively. As the lower distance of separated charges with high surface area to storing charges, the higher is C . In addition, the measurement of energy storage ability of capacitor is calculated by the following equation;

$$E = 0.5CV^2 \quad (1.3)$$

Here, E and V are the energy density and electrochemical capacitor voltage window, respectively. Power density is energy released with respect to time. Generally, the resistance across the supercapacitor components (e.g. substrate, electrode material, separator and electrolyte) are required for evaluating power density, which known as the ESR. It is calculated from voltage drop of during the discharge, which gives the maximum voltage. The maximum power density is calculated by following relation;

$$P_{\max} = V^2/ESR \quad (1.4)$$

Here, P and V are the power density and cell voltage.

As compared to battery, conventional capacitor has high power density but low energy density. The battery can store the more energy than the capacitor but it cannot deliver power density as quick as supercapacitor. Generally, the power density of a

capacitor is high due to the less energy storage with respect to mass or volume but discharges very rapidly to store more power. Supercapacitor has same principle as conventional capacitor, however it incorporates electrode with maximum surface area (A) and less distance (d) between two electrodes. As a result, from equations 1.2 and 1.3, supercapacitor leads to enhanced capacitance as well as energy.

1.1.3 Taxonomy of supercapacitor:

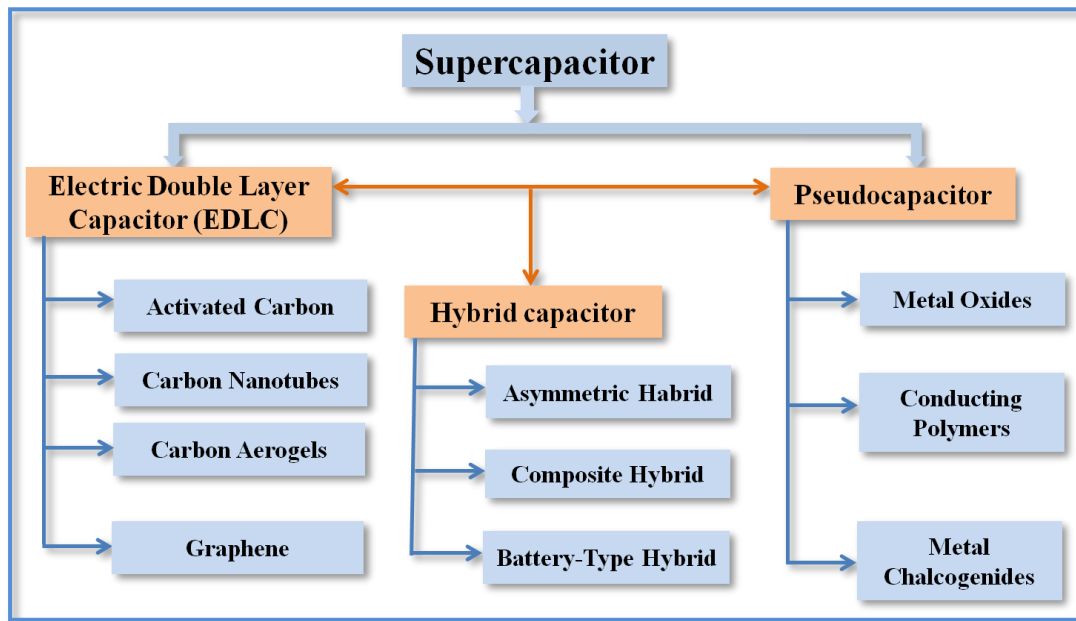


Fig 1.3: Classification of supercapacitors with different types and subtypes.

The taxonomy of supercapacitor is basically depends on charge storage mechanism and material used, it divided into three main categories namely, electrochemical double layer capacitor (EDLC), faradic capacitor (Pseudocapacitor) and hybrid capacitor. For charge storage, the type of supercapacitor is characterized by its unique charge storage mechanism. It includes the redox, electrostatic and combination of both processes, respectively. In redox process, charge transfer takes place through the oxidation and reduction reactions between electrode surface and applied electrolyte. In electrostatic process, chemical reaction does not involve, charges are stored over electrode surface through physical process. EDLC stores charges via electrostatic mechanism and fabricated from carbon based material [16-18]. Faradic capacitor stores charges through redox reaction occurring near surface or in bulk material [19]. Generally, faradic capacitors are constituted using the metal sulfides, conducting polymer and metal oxides [20-22]. The combinations of carbon-based material with conducting polymers, metal oxides/hydroxide/sulfides are used to form

hybrid capacitors [23-25]. This part gives an overview of each type of supercapacitor in details. **Fig. 1.3** shows the classification of supercapacitor with different types and subtypes.

1.1.3.1 Electric double layer capacitor (EDLC):

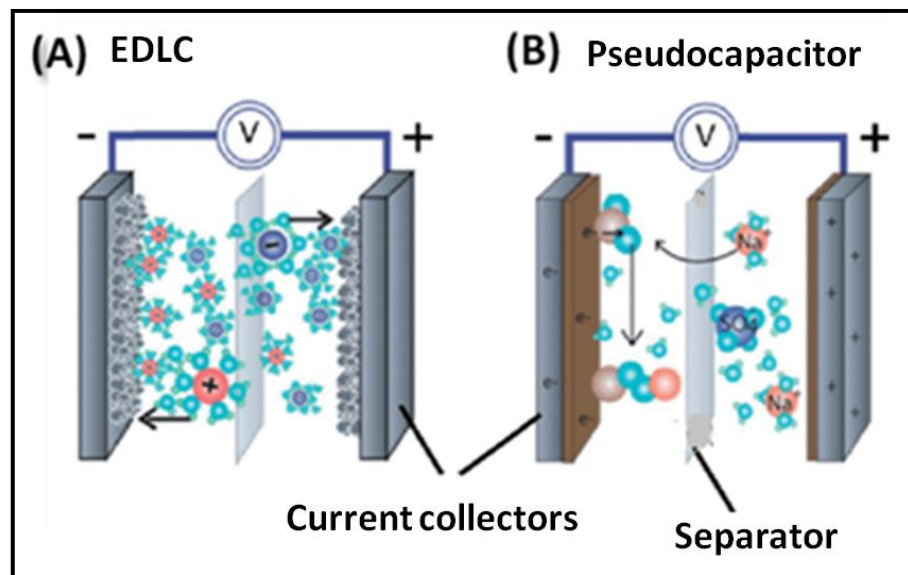


Fig. 1.4: Schematic of charge storage mechanisms for (A) EDLC and (B) pseudocapacitor [27].

EDLC is an electrochemical capacitor which store charges non-Faradically because of the accumulation of charges at interface of electrode or electrolyte. It is composed of two carbon-based electrodes, separator and electrolyte which prevent direct contact between both electrodes. In EDLCs, charges store electrostatically, there is no transfer of charges between electrolyte and surface electrode. At charging time, electrons travel from negative to positive electrode through the external loop. In electrolyte, anions travel in the direction of positive electrode whereas cations travel in the direction of negative electrode. During the process of discharging ions and electrons travel in reversed direction [26]. The charge storage mechanism of EDLC is demonstrated in **Fig. 1.4(A)**. The oppositely charged ions form double layer and separated in the atomic scale distance which is extremely reversible process. The EDLCs have achieved high capacitance because of the large surface area of carbon-based electrodes and tiny separation between the charged ions. The EDLCs can provide extreme power density and excellent stability because of the absence of charge transfer reactions. The EDLCs include the carbon-based materials like an activated carbon, carbon aerogels, carbon nanotubes, graphene, mesoporous carbon, etc. [6].

1.1.3.2 Pseudocapacitor:

Pseudocapacitor is another class of supercapacitor. The charge storage mechanism of pseudocapacitor basically depends upon the transfer charge through redox reactions between electrolyte and electrode surface. The schematic of pseudocapacitor with redox reaction is illustrated in **Fig. 1.4(B)**. If a voltage is applied to pseudocapacitive electrodes, oxidation-reduction reactions occur over the electrode surfaces. The conducting polymers, transition metal oxides or hydroxides, sulfides, such as polyaniline, polypyrrole, Co_3O_4 and NiS are mostly used in pseudocapacitors as an electrode material [23, 28-32]. The pseudocapacitor stores energy through redox reaction, therefore it produces high capacitance than the EDLCs. Also, charge storage capability of pseudocapacitor is higher as compared to EDLCs, which means that it provides maximum energy density in comparison with EDLCs. Moreover, pseudocapacitor offers less stability as compared to EDLCs owing to the degradation of electrode material for the period of electrochemical faradic reactions.

1.1.3.3 Hybrid supercapacitor:

The carbon based electrode materials are used in EDLCs, which offer higher surface area than the pseudocapacitive electrode materials. The EDLCs achieve relatively less specific capacitance (C_s) with lower energy density. However, the pseudocapacitor has high energy density as compared to EDLCs, but they have some limitations such as electrical conductivity, power densities and less stability due to their redox reactions. To overcome these limitations of pseudocapacitor and EDLCs, another class of supercapacitor was developed which is called as hybrid capacitors. The hybrid capacitor is formed by combination of pseudocapacitor and EDLC materials, utilizing both redox and electrostatic processes to store charges [33-37]. In hybrid capacitor system, pseudocapacitive or faradic electrode with high capacitance provides high energy density, while the electrostatic in EDLCs electrode enables higher power density. The hybrid capacitors can exhibit high capacitance, chemical stability, energy density and power density compared to both mechanisms like as pseudocapacitor and EDLCs. Researchers are interested in to develop a new type of electrode such as hybrid electrode material for supercapacitors which has high C_s , cyclic stability, energy density and power density etc. A combination of different materials and some advantages of forming composite is an effective approach with optimizing each component and raising their performance for supercapacitors. Carbon based materials with large surface area raise the contact between electrode of pseudocapacitive

materials and electrolyte, whereas redox reactions boost the charge storing ability of composite electrodes. It possesses higher capacitance with superior energy density compared to EDLCs and excellent stability than pseudocapacitors [38].

1.1.4 New trends in supercapacitor:

Supercapacitor is an up coming energy storage device technology which will take a role of solution in worldwide future energy systems. The main characteristic of supercapacitor is a high energy storage ability which makes them a required decision among different manufacturers [39]. With steady development in technology and research, supercapacitor is attaining much more interest in all over the global markets. For the occasion, rail and automotive sections are opening innovative possibilities in emerging regions as like grid energy storage. Boost in the demand of electric/hybrid vehicles due to the severe administration rules about emissions is proposed to encourage and implementation in the supercapacitor markets [40]. Indeed, up to date the novel consumer electronic devices such as sensors and cell phones require various power demands due to their number of functionalities. At room temperature battery gives slowly response owing to its chemical reactions. Therefore, in the next generation energy storage systems in multiple cases, it will not provide required power of all these electronic/hybrid appliances. The demand of supercapacitors from industries is increasing because of its advantages verses lithium-ion batteries such as stability and power density. It can convey large amount of energy at a higher power and fast charge/discharge rates, which results are appropriate for supplying high power in multifunctional electronic devices. Even these superior characters of supercapacitors, the commercial applicability of supercapacitors are restricted owing to its low energy density. Currently, the researchers are trying to improve the energy density of supercapacitors by applying different approaches without hindering their other characteristics.

Carbon-based materials have been widely utilized in commercial supercapacitors, in the last few decades [41]. Nevertheless, the carbon-based materials exhibit low specific capacitance and restrict their commercial use. Current research suggests that pseudocapacitive transition metal oxides, hydroxides and sulfides are promising electrode materials for supercapacitor applications because of their some useful features like lower resistance value, cost effectiveness and environmental compatibility [42]. Also, the fast and faradic surface oxidation and reduction reactions of pseudocapacitive materials boost in the energy storage ability and specific

capacitance of the supercapacitor. The electrochemical stability of pseudocapacitive materials is inadequate owing to the degradation of electrode material in liquid electrolyte during the cycling. Therefore, investigations of solid-state supercapacitor devices have received great interest in which solid polymer gel electrolyte is used as a substitute to liquid electrolyte.

The solid-state supercapacitor devices have advantages versus aqueous capacitors as it overcomes the problem of flexibility, ease of handling and electrolyte leakage [43]. Also, the current research is mainly focused on the improvement of supercapacitor performances using various ionic liquid electrolytes. These electrolytes have many advantageous, as they are nontoxic, thermally stable at temperature over 290 °C and non-flammable. Further, in ionic liquid electrolyte the operational window of supercapacitor is amplified up to 4-6 V [44]. The electrochemical behaviour of supercapacitor not only depends on the used electrode material but also on the applied electrolyte, supporting substrate and separator which affects on the practical electrochemical supercapacitive performance. The selection of superior electrode material along with suitable electrolyte effectively enhances the Cs and energy density of supercapacitor. The operation of better performance, cost-effective and nontoxic electrode materials and appropriate electrolyte useful to achieve energy density and peak values of Cs of supercapacitor [45].

1.2. Literature survey on rare earth chalcogenide and graphene oxide (GO) based composite thin films:

1.2.1 Literature survey on rare earth chalcogenide thin films and their physical properties:

Table 1.1 illustrates the crystal structure, band gap values exhibited via various rare earth metal (REM) chalcogenide materials using different physical and chemical methods. According to literature survey, the REM chalcogenide thin films have been deposited by different methods and studied its various properties like electrochemical properties, gas sensing, optical and superconducting. Yadav et al [46] investigated structural and morphological properties for rod-like lanthanum oxide (La_2O_3) thin film deposited by chemical bath deposition (CBD) method. Atta et al [47] synthesized samarium oxide (Sm_2O_3) thin film by using RF sputtering method and studied optical properties with band gap of 4.5 eV. Yadav et al [48] reported band gap of 4.2 eV for spray pyrolysis synthesized hexagonal La_2O_3 thin film. Kariper et al [49] prepared nanosheets cerium sulfide (CeS_2) thin film by CBD method and showed band gap of

3.4 eV. Yadav et al [50] studied gas sensing properties for CBD deposited rod-like La_2O_3 thin film. Al-kuhaili et al [51] showed optical band gap of 5.8 eV for cubic dysprosium oxide (Dy_2O_3) thin film deposited by thermal evaporation (TE) route. Balkrushnan et al [52] synthesized cubic cerium oxide (CeO_2) thin films by using pulse laser deposition method. Channei et al [53] found that the bandgap of 3.4 eV for spin coating deposited CeO_2 thin films. Cwik et al [54] obtained amorphous neodymium sulfide (Nd_2S_3) thin films via metal-organic chemical vapour deposition (MOCVD) method and showed optical bandgap of 2.3 eV and studied photoluminescent behaviour. Kaya et al [55] deposited monoclinic Sm_2O_3 thin film by reacting sputtering (RS) method. Wang et al [56] prepared hexagonal La_2O_3 thin film via atomic layer deposition (ALD) route and investigated the structural and thickness characteristics. Baskys et al [57] obtained La_2O_3 thin film by sol-gel route and discussed X-ray photoelectron spectroscopy (XPS) study. Paumier et al [58] synthesized yttrium oxide (Y_2O_3) thin film on different substrates (Si, MgO and SrTiO_3) by the ion beam sputtering (IBS) method and studied internal strain relaxation. Also, Ramana et al [59] reported optical properties of nanostructured Y_2O_3 thin film deposited by sputtering method. Boehme et al [60] deposited nanocubes Sm_2O_3 thin film by simple and cost-affective electroless deposition method. Kumbhar and Lokhande [61] synthesized dysprosium (Dy) thin film by electrodeposition route. Ramay et al [62] prepared cubic Dy_2O_3 thin film via magnetron sputtering (MS) over various substrates method. Jundhale and Lokhande [63] fabricated samarium (Sm) thin films by electrodeposition method. Jundhale and Lokhande [64] obtained orthorhombic samarium telluride (SmTe) thin films via simple electrodeposition route. Jundhale and Lokhande [65] reported optical band gap of 2.08 eV for cubic samarium sulfide (Sm_2S_3) thin film by electrodeposition method. Jundhale and Lokhande [66] showed band gap of 2.52 eV for electrodeposition method deposited SmTe thin film. Jeong and Bae [67] obtained Y_2O_3 nanopowder by solvothermal method. Mohite et al [68, 69] synthesized yttrium selenide (YSe) and yttrium sulfide (YS) thin films by electrodeposition method and reported band gaps of 1.6 and 1.85 eV, respectively. Mohite and Lokhande [70] prepared YSe thin film by electrodeposition method and reported band gap of 1.84 eV.

Table 1.1: Literature survey on rare earth chalcogenide thin films and their physical properties

Sr. No.	Material	Deposition method	Crystal structure	Band gap (eV)	Ref. No.
1	La ₂ O ₃	CBD	Hexagonal	4.1	[46]
2	Sm ₂ O ₃	RF sputtering	-	4.5	[47]
3	La ₂ O ₃	Spray pyrolysis	Hexagonal	4.2	[48]
4	CeS ₂	CBD	Nanosheets	3.4	[49]
5	La ₂ O ₃	CBD	Hexagonal	-	[50]
6	Dy ₂ O ₃	Thermal evaporation	Cubic	5.8	[51]
7	CeO ₂	Pulsed laser deposition	Cubic	-	[52]
8	CeO ₂	Spin Coating	Cubic	3.4	[53]
9	Nd ₂ S ₃	MOCVD	Amorphous	2.3	[54]
10	Sm ₂ O ₃	Reactive sputtering	Monoclinic	-	[55]
11	La ₂ O ₃	Atomic layer deposition	Hexagonal	-	[56]
12	La ₂ O ₃	Sol-gel	-	-	[57]
13	Y ₂ O ₃	Ion beam sputtering	Cubic	-	[58]
14	Y ₂ O ₃	sputtering	Cubic	-	[59]
15	Sm ₂ O ₃	Electroless	-	-	[60]
16	Dy	Electrodeposition	-	-	[61]
17	Dy ₂ O ₃	Magnetron sputtering	Cubic	-	[62]
18	Sm	Electrodeposition	-	-	[63]
19	SmTe	Electrodeposition	Orthorhombic	-	[64]

20	Sm ₂ S ₃	Electrodeposition	Cubic	2.08	[65]
21	SmTe	Electrodeposition	-	2.52	[66]
22	Y ₂ O ₃	Solvothermal	Cubic	-	[67]
23	YSe	Electrodeposition	-	1.6	[68]
24	YS	Electrodeposition	-	1.85	[69]
25	YSe	Electrodeposition	-	1.84	[70]

Table 1.2: Literature survey on rare earth chalcogenide thin films for supercapacitor performance

Sr. No.	Material	Deposition method	Surface morphology	Electrolyte Used	Specific capacitance (F g ⁻¹)	Energy density (Wh kg ⁻¹)	Power Density (kW kg ⁻¹)	Stability	Ref. No.
1	La ₂ O ₃	CBD	Rod-shaped	1 M KOH	147	-	-	2000 (96%)	[78]
2	La ₂ O ₃	Hydrothermal	Rod-like	1 M KOH	248	80	1.5	1000 (81%)	[79]
3	La ₂ O ₃	CBD	Rod-like	1 M KOH	288	42.9	0.10	2000 (92%)	[80]
4	α-La ₂ S ₃	SILAR	Nano-grains	1 M LiClO ₄	256	-	-	1000 (85%)	[75]
5	La ₂ S ₃	CBD	Grains	1 M LiClO ₄	294	-	-	1000 (89%)	[81]
6	La ₂ S	Hydrothermal	Nano-petals-like	1 M Na ₂ SO ₄	121	-	-	-	[82]
7	La ₂ S ₃	SILAR	Wave - like	1 M Na ₂ SO ₄	358	1.26	-	1000 (78%)	[83]
8	La ₂ Se ₃	CBD	Nano-rods	2 M KOH	331	-	-	1000(81%)	[84]
9	La ₂ Se ₃	SILAR	Nan- flakes	1M LiClO ₄	363	80	2.5	1000 (83%)	[85]

10	La_2Te_3	CBD	Cinnamon-like	1 M KOH	469	126	1.5	1000 (71%)	[76]
11	La_2Te	SILAR	Pine leaf-like	1 M $\text{LiClO}_4\text{-PC}$	194	60	4.22	1000 (82%)	[86]
12	Sm_2O_3	Hydrothermal	Ground-nuts	1 M KOH	155	-	-	-	[87]
13	Sm_2S_3	SILAR	Honycomb	1 M LiClO_4	294	48.9	-	-	[74]
14	Sm_2Te_3	CBD	Barley-like	1 M $\text{LiClO}_4\text{-PC}$	207	25.60	14.18	-	[88]
15	Sm_2Te_3	SILAR	Cloud like	1 M $\text{LiClO}_4\text{-PC}$	144	10	-	-	[89]
16	Sm_2Se_3	CBD	Nano-rods	1 M $\text{LiClO}_4\text{-PC}$	316	-	-	1000 (87%)	[90]
17	Yb_2S_3	Hydrothermal	Nanoparticles and Nanorods	1 M Na_2SO_4	270	-	-	1000 (78%)	[91]
18	Se	CBD	Nanocubes	1 M Na_2SO_4	22	2.04	-	1000 (91%)	[92]
19	CeO_2	Hydrothermal	Nanoparticles	1 M NaCl	523	-	-	2000 (82%)	[93]

1.2.2 Literature survey on rare earth chalcogenide thin films for supercapacitor performance:

Table 1.2 demonstrates the surface morphology, Cs, stability, energy density and power density values exhibited by various rare earth metal chalcogenide materials using various chemical methods with different electrolyte solutions. The REM chalcogenide thin films received great attention because of their good chemical, electrical and physical characteristics that are helpful in various applications such as optical, electronic and optoelectronic devices [71, 72]. It is a new class of energy storage material. Recently, the nano and microstructured REM chalcogenides thin films have been studied for energy storage application because of the wider potential window, better charge-discharge performance and energy density. For the higher technological supercapacitive devices, they possess unique and superior property, suitable for wide potential applications [73]. The REM chalcogenide thin films showed excellent contribution in supercapacitive properties [74-76]. The REM chalcogenides show high Cs due to two or more oxidation states [77].

Recently, Yadav et al [78] synthesized rod shape La_2O_3 thin film by CBD method and found Cs of 147 F g^{-1} at scan rate 5 mV s^{-1} in 1 M KOH electrolyte with 96 % cyclic retention. Yadav et al [79] has deposited rod-like La_2O_3 electrode by hydrothermal method and reported Cs, energy density and power density of 248 F g^{-1} , 80 Wh kg^{-1} and 1.5 kW kg^{-1} with good cyclic stability. Yadav et al [80] prepared rare earth oxide (REO) such as La_2O_3 thin film material by CBD method for electrochemical behavior and reported Cs of 288 F g^{-1} with 92 % electrochemical stability in 1 M KOH aqueous electrolyte. Patil et al [75] prepared nano-grains of lanthanum sulfide ($\alpha\text{-La}_2\text{S}_3$) thin films via successive ionic layer adsorption and reaction (SILAR) method and reported. Ghogare et al [81] deposited nano petals-like lanthanum sulfide (La_2S) electrode by hydrothermal method and obtained 121 F g^{-1} Cs at a scan rate of 5 mV s^{-1} in $1 \text{ M Na}_2\text{SO}_4$ electrolyte. Patil and Lokhande [82] obtained Cs of 294 F g^{-1} at a scan rate of 5 mV s^{-1} in 1 M LiClO_4 electrolyte for SILAR synthesized grains-like La_2S_3 thin films.

Patil et al [83] reported Cs of 358 F g^{-1} at a scan rate of 5 mV s^{-1} for SILAR deposited wave-like La_2S_3 thin films. Patil et al [84] has reported Cs of 321 F g^{-1} for nano-rods La_2S_3 thin films prepared by CBD method. Patil et al [85] showed maximum Cs of 363 F g^{-1} for SILAR synthesized nanoflakes lanthanum selenide (La_2Se_3) thin films. Patil et al [76] obtained Cs of 469 F g^{-1} at a scan rate of 2 mV s^{-1} in 1 M KOH

electrolyte for CBD deposited cinnamon-like lanthanum telluride (La_2Te_3) thin films. Patil et al [86] synthesized pine leaf-like La_2Te_3 thin films and obtained Cs of 194 F g^{-1} at 5 mV s^{-1} scan rate in $1 \text{ M LiClO}_4\text{-PC}$ electrolyte. Ubale et al [87] deposited groundnuts-like nanostructured Sm_2O_3 thin films through a facile and one-step hydrothermal method and delivered Cs of 155 F g^{-1} .

Kumbhar et al [74] prepared honeycomb-like samarium sulfide (Sm_2S_3) thin films and showed 294 F g^{-1} Cs at scan rate 5 mV s^{-1} in LiClO_4 electrolyte. Kumbhar et al [88] reported Cs of 207 F g^{-1} for barley-like Sm_2Te_3 films prepared via simple SILAR method. Kumbhar et al [89] obtained cloud-like Sm_2Te_3 thin films which showed Cs of 144 F g^{-1} at a scan rate of 5 mV s^{-1} . Kumbhar et al [90] reported Cs of 316 F g^{-1} at a constant scan rate of 5 mV s^{-1} for CBD synthesized cross-linked nanorods Sm_2Te_3 thin films. The Cs values are mainly depending on the surface texture, which has been investigated extensively. Pujari et al [91] showed Cs of 270 F g^{-1} for hydrothermally prepared monoclinic or nanoparticles and distributed nanorods-like ytterbium sulfide (Yb_2S_3) thin films. Patil et al [92] deposited cube-like selenium thin films by CBD method and reported 22 F g^{-1} in $1 \text{ M Na}_2\text{SO}_4$ electrolyte. Pandit et al [93] obtained the Cs of 523 F g^{-1} in 1 M NaCl solution for one-pot hydrothermally synthesized nanoparticles cerium oxide (CeO_2) thin films.

Conclusions:

The REM chalcogenides thin films have been synthesized by different chemical methods such as SILAR, CBD, spray pyrolysis, electrodeposition and hydrothermal. Moreover, the electrochemical behavior of REM chalcogenides thin films has been studied mostly in the aqueous and non-aqueous electrolytes such as KOH, NaOH, Na_2SO_4 and PC- LiClO_4 . In REM chalcogenides, particularly metal telluride showed excellent electrochemical properties in KOH electrolyte, which was prepared by CBD method.

1.2.3 Literature survey on graphene oxide (GO) based composite thin films for supercapacitor performance:

Table 1.3 displays the surface morphology, stability, specific capacitance, energy and power density values exhibited by various GO based composite materials using various chemicals methods with different electrolyte solutions. Gund et al [94] synthesized porous nanograins GO/ Mn_3O_4 composite thin film via SILAR method for electrochemical study and exhibited maximum Cs of 344 F g^{-1} at a scan rate of 5 mV s^{-1} in $1 \text{ M Na}_2\text{SO}_4$ electrolyte and excellent stability over 3000 cycles. Zang et al [95]

reported 500 F g⁻¹ Cs in 1 M KOH electrolyte for sandwich-like GO/conducting polymer composite electrode by the exfoliation method. Nwankwo et al [96] prepared slab-like GO/Mn₃O₄ composite electrode by using SILAR method and obtained Cs of 532 F g⁻¹ in 1 M KOH electrolyte with better cyclic stability of 97 % for 2000 cycles. It delivered energy density and power density of 61 Wh kg⁻¹ and 0.6 kW kg⁻¹. Patil et al [97] showed highest Cs of 623 F g⁻¹ and 98 % stability in 1 M Na₂SO₄ electrolyte for deposited nanosheets GO/MoS₂ composite electrode via electrophoretic method. Khalid et al [98] deposited GO/PANI nanoplates-like composite electrode by electrodeposition method and exhibited maximum Cs of 623 F g⁻¹ and achieved energy density of 64.5 Wh kg⁻¹ at power density of 1.15 kW kg⁻¹ in 1 M H₂SO₄ electrolyte. Ghogare et al [99] studied electrochemical performance of nano-strips-like GO/Sm₂S₃ composite electrode deposited by SILAR route. It showed maximum Cs of 360 F g⁻¹ with electrochemical stability of 88 % for 2000 cycles. Ghogare et al [100] exhibited 312 F g⁻¹ Cs and cyclic stability of 94 % for SILAR deposited grass-like GO/Sm₂S₃ composite electrode. Konwer et al [101] obtained GO/PANI composite electrode by using polymerisation method and showed 543 F g⁻¹ Cs in 1 M KCl solution. Huang et al [102] prepared hollow sphere-like GO/CNT electrode using the solvothermal route and reported Cs of 2317 F g⁻¹ and cyclic stability of 96 % over the 2000 cycles in 6 M KOH electrolyte. Aboutalebi et al [103] investigated supercapacitor behaviour of nanosheets-like GO/MWCNT thin film prepared by the exfoliated route and showed Cs of 251 F g⁻¹. Singhal et al [104] showed 597 F g⁻¹ Cs and 80 % stability over 5000 cycles for hydrothermally synthesized nanocrystals GO/CuS composite electrode in 1M KOH. Wan et al [105] deposited porous nanodiscs-like GO/ZnS composite thin film via one-pot hydrothermal route and reported Cs of 327 F g⁻¹ with the stability of 95 % over long cycles (10000) in 3 M KOH.

Conclusions:

The literature survey shows that, GO-based composite thin films have been prepared for physical and chemical methods. However, chemical methods showed better supercapacitive performance, particularly SILAR. The GO-based thin films showed enhancement in the specific capacitance, energy density and electrochemical stability.

Table 1.3: Literature survey on GO based composite thin films for supercapacitor performance

Sr. No.	Material	Deposition method	Surface morphology	Electrolyte used	Specific capacitance (F g ⁻¹)	Energy density (Wh kg ⁻¹)	Power Density (kW kg ⁻¹)	Stability	Ref. No.
1	GO/Mn ₃ O ₄	SILAR	Porous Nanograins	1 M Na ₂ SO ₄	344	100	1.03	3000 (87%)	[94]
2	GO/conducting polymer	Exfoliated method	Sandwich -like	1 M KOH	500	-	-	1000 (70%)	[95]
3	GO/Mn ₃ O ₄	SILAR	Slab-like	1 M Na ₂ SO ₄	532	61	0.6	2000 (97%)	[96]
4	GO/MoS ₂	Electrophoretic method	Nanosheets	1 M Na ₂ SO ₄	623	23	17	1000 (98%)	[97]
5	GO/PANI	Electrodeposition	Nanoplates	1 M H ₂ SO ₄	662	64.5	1.15	-	[98]
6	GO/Sm ₂ S ₃	SILAR	Nano-strips-like	1 M Na ₂ SO ₄	360	-	-	2000 (88%)	[99]
7	GO/La ₂ S ₃	SILAR	Grass - like	1 M Na ₂ SO ₄	312	-	-	1000 (94%)	[100]
8	GO/PANI	Polymerization	Pore galleries-like	1 M KCl	543	-	-	-	[101]
9	GO/CNT	Solvothermal	Hollow spheres	6 M KOH	2317	-	-	1200 (96%)	[102]
10	GO/MWCNs	Exfoliated method	Nanosheets	1 M H ₂ SO ₄	251	-	-	1000 (105%)	[103]
11	GO/CuS	Hydrothermal	Nanocrystals	1 M KOH	597	12	5.5	5000 (80%)	[104]
12	GO/ZnO	Hydrothermal	Porous Nanodiscs-like	3 M KOH	327	11.8	-	10000 (95%)	[105]

1.3 Orientation and purpose of dissertation:

Energy crisis in the 21st century, since the rapid growth of global economy, depletion in fossil fuels and boosting pollution needed for the development of clean, renewable and efficient energy sources. Among the many energy storage devices, supercapacitors have been regarded as an extensive replacement for the batteries. The purpose of supercapacitor has many potential features in their performance, including superior stability, high power density, and fast charging-discharging times. For the supercapacitor practical applications, it is essential to enhance the energy and power density of supercapacitor without compromising its other properties. The overall performance of efficient supercapacitor generally arises from its high surface area as well as fast and reversible redox reactions of active materials. Therefore, the design and development of proper electrode material created an opportunity in the field of supercapacitors.

The literature study shows that, many materials including REM metal oxides/sulfides, carbon materials, conducting polymers and or their composites have been studied as an electrode material for the fabrication of supercapacitors. The recent trends of research are focused towards the deposition of mixed metal oxides/sulfides or carbon-based composite materials to better supercapacitive performance with energy density and power density. The rise in both the operating potential window with an energy density of metal sulfide based electrodes result in the enhancement in the overall supercapacitor performance. GO composite with REM sulfides are the scanty studied materials which have potential in the field of the supercapacitor. To develop the high-performance efficient supercapacitors, it is essential to fabricate advanced electrode material, which is capable of high C_s with enhanced energy density without compromising its power density. The main purpose behind making GO/Yb₂S₃ composite thin film is to accomplish improvement in supercapacitive performance and energy density.

The current study is concerned with the preparation, characterization and electrochemical performance analysis for chemically synthesized Yb₂S₃, GO and GO composite with Yb₂S₃ thin films. The high reduction potential of ytterbium with the number of oxidation states (Yb²⁺ and Yb³⁺) and GO may be useful to enhance the operating potential window with energy as well as power densities for supercapacitor device. The low temperature chemical methods are used to deposit thin films. These

chemical methods are binder-free, cost-effective simple, and convenient for large scale area deposition than the physical methods. Also, the synthesis of thin films, there is no need for high-temperature furnaces and high vacuum. The preparative parameters such as dipping time, rinsing time, the concentration of precursors, complexing agent, pH of the solution, deposition time and bath temperatures are used in chemical methods. All the preparative parameters are simply controllable. At low temperature depositions are carried out which helps to avoid oxidation or corrosion of metal electrodes. In chemical methods, the nucleation and growth process plays a vital role to deposit nanocrystalline materials. The different chemical methods include sol-gel synthesis, hydrothermal, electrodeposition, SILAR, spin coating, CBD, spray pyrolysis etc.

The chemical electrodeposition method requires current and/or potential controlled driving force for a particular species to be synthesized by means of reduction over the substrate and deposition is possible only for conducting substrate. The hydrothermal method requires as an extra source of heat in a controlled atmosphere to increase the temperature and thereby pressure at the desired level to carry out chemical reactions. Similarly, the spin coating method needs an additional energy source to control and maintain a rotating speed of motor used in the film deposition. Among these methods, SILAR and CBD are binder-free, cost-effective and simple for deposition of thin films. By these chemical methods, the preparation of thin films is possible for conducting or nonconducting substrates.

In this work, Yb_2S_3 , GO and GO composite with Yb_2S_3 thin films are prepared using SILAR and CBD methods. The CBD method basically depends upon the solubility product of a compound to be formed in the bath. When ionic product exceeds its solubility product, cations and anions of a compound to be formed, combine on the substrate and/or in the solution and depending upon that the deposition is classified as heterogeneous or homogeneous. The SILAR is a modified version of the CBD method, which avoids the wastage of material.

As a first part of the work, Yb_2S_3 , GO and GO composite with Yb_2S_3 thin films are synthesized via SILAR and CBD methods. To deposit good quality films, many preparative parameters like as concentration of the solution, the temperature of the bath, pH, deposition time, rinsing time and dipping time are optimized. Consequently, thin films are characterized by elemental, structural, surface texture and wettability studies. The crystallite size and phase formation are investigated using X-ray diffraction (XRD)

technique. The elemental composition and presence of oxidation states are determined by X-ray photoelectron spectroscopy (XPS) technique. The formations of deposited materials are confirmed using Fourier transform Raman spectroscopy (FT-Raman) and Fourier transform infrared spectroscopy (FT-IR) techniques. The wettability of films with electrolyte is studied using contact angle measurement technique. The surface nature and particle size of the films surface material is investigated via field emission scanning electron microscopy (FE-SEM) and transmission electron microscopy (TEM) techniques.

The electrochemical properties of Yb_2S_3 , GO and GO composite with Yb_2S_3 thin films are studied by various supercapacitive techniques such as cyclic voltammetry (CV) Galvanostatic charge discharge (GCD) and electrochemical impedance spectroscopy (EIS) techniques. These techniques are carried out to identify the current-voltage, time-voltage behavior and resistive parameters of the film in three-electrode system using the aqueous electrolyte. Electrochemical supercapacitive study is carried out in three-electrode system consisting of the prepared electrode (Yb_2S_3 , GO and GO composite with Yb_2S_3) as a working electrode, platinum as a counter electrode and mercury/mercury oxide electrode (Hg/HgO) as a reference electrode.

The main purpose of this work is to increase the C_s , energy density as well as power density for supercapacitor using rare earth sulfide material and its composite with GO. The aim is the preparation of GO, Yb_2S_3 and GO/ Yb_2S_3 composite thin films by facile, simple and binder free chemical methods (SILAR and CBD). In addition, symmetric and asymmetric supercapacitor devices based on best supercapacitive properties of Yb_2S_3 , MnO_2 and GO/ Yb_2S_3 composite thin film electrodes are fabricated. Finally, their supercapacitive performances are evaluated to find out C_s and resistive parameters such as R_s , R_{ct} and W , as well as energy and power densities.

1.4 References:

- 1 K. B. Oldham and J. C. Myland, 'Fundamentals of Electrochemical Science', Academic Press Inc, New York, (1994), pp.1- 496.
- 2 A. Nishino, *J. Power Sources*, 60, (1996), 137-257.
- 3 <http://electronics.wikia.com/wiki/Capacitor>.
- 4 M. S. Halper and J. C. Ellenbogen, *MITRE.*, 74 (2006), 10-19.
- 5 K. Kotz and M. Carlen, *Electrochim. Acta.*, 45, (2000), 2483-2498.
- 6 E. Frackowiak and E. Beguin, *Carbon*, 39, (2001), 937-950.
- 7 M. Jayalakshmi and K. Balasubramanian, *Int. J. Electrochem. Sci.*, 3, (2008), 1196-1217.
- 8 B. Conway, V. Birss, J. Wojtowicz, *J. Power Sources*, 66, (1997), 1-14.
- 9 Q. Chen, Y. Meng, C. Hu, Y. Zhao, H. Shao, N. Chen, L. Qu, *J. Power Sources*, 247, (2014), 32-39.
- 10 Y. Qian, R. Liu, Q. Wang, J. Xu, D. Chen, G. Shen, *J. Mater. Chem. A*, 2, (2014), 10917-10922.
- 11 Source of Figure 2.1 <http://en.wikipedia.org/wiki/File: Supercapacitors-chart.svg>. (accessed 2014).
- 12 G. A. Snook, P. Kao, A. S. Best, *J. Power Sources*, 196, (2011), 1-12.
- 13 A. Balducci, U. Bardi, S. Caporali, M. Mastragostino, F. Soavi, *Electrochem. Commun.*, 6, (2004), 566-570.
- 14 R. B. Rakhi, N. A. Alhebshi, D. H. Anjum, H. N. Alshareef, *J. Mater. Chem. A*, 2, (2014), 16190-16198.
- 15 R. A. Rightmire. Electrical energy storage apparatus. U. S., Patent 3288641, (1966), 1-9.
- 16 T. Chen and L. Dai, *Mater. Today*, 16, (2013), 272-280.
- 17 W. Wang and S. Wu, *Appl. Surf. Sci.*, 396, (2017), 1360-1367.
- 18 X. Li, Y. Zhao, Y. Bai, X. Zhao, R. Wang, Y. Huang, Q. Liang, Z. Huang, *Electrochim. Acta.*, 230, (2017), 445-463.
- 19 Y. Wang, Y. Song, Y. Xia, *Chem. Soc. Rev.*, 45, (2016), 5925-5950.
- 20 B. Zhang, W. Li, J. Sun, G. He, R. Zou, J. Hu, Z. Chen, *Mater. Lett.*, 114, (2014), 40-48.
- 21 W. Li, G. He, J. Shao, Q. Liu, K. Xu, J. Hu, I. P. Parkin, *Electrochim. Acta.*, 186, (2015), 1-6.
- 22 A. Xie, F. Tao, C. Jiang, W. Sun, Y. Li, L. Hu, X. Du, S. Luo, C. Yao, *J. Electroanal. Chem.*, 789, (2017), 29-46.
- 23 A. M. Patil, A. C. Lokhande, N. R. Chodankar, V. S. Kumbhar, C. D. Lokhande, *Mater. Des.*, 97, (2016), 407- 416.
- 24 Y. Li, X. Wang, Q. Yang, M. S. Javed , Q. Liu, W. Xu, C. Hu, D. Wei, *Electrochim. Acta.*, 234, (2017), 63-70.
- 25 M. G. Hosseini and E. Shahryari, *J. Colloid Interface Sci.*, 496, (2017), 371-381.
- 26 G. Ma, G. Sriakesh, A. Mohan, V. Arivazhagan, *Appl. Surf. Sci.*, 403, (2017), 578-583.
- 27 K. Jost, G. Diona, Y. Gogotsi, *J. Mater. Chem. A*, 2, (2014), 10776-10786.
- 28 F. Shi, L. Li, X. L. Wang, C. D. Gu, J. P. Tu, *RSC Adv.*, 4, (2014), 41910-41921.

- 29 R. B. Pujari, A. C. Lokhande, A. A. Yadav, J. H. Kim, C. D. Lokhande, *Mater. Des.*, 108, (2016), 510-517.
- 30 Z. Wen, W. She, Y. Li, R. Che, *J. Mater. Chem. A*, 2, (2014), 20729-20738.
- 31 L. L. Xing, K. J. Huang, L. X. Fang, *Dalton Trans.*, 45, (2016), 17439-17446.
- 32 J. Xu, T. Xiao, X. Tang, P. Xiang, L. Jiang, D. Wu, J. Li, S. Wang, *J. Alloys Compd.*, 706, (2017), 351-357.
- 33 W. Chen, R. B. Rakhi, H. N. Alshareef, *Nanoscale*, 5, (2013), 4134-4138.
- 34 S. Lyu, H. Chang, F. Fu, L. Hu, J. Huang, S. Wang, *J. Power Sources*, 327, (2016), 438-446.
- 35 X. Zhao, L. Zhang, S. Murali, M. D. Stoller, Q. Zhang, Y. Zhu, R. S. Ruoff, *ACS nano*, 6, (2012), 5404-5412.
- 36 C. T. Hsieh, W. Y. Lee, C. E. Lee, H. Teng, *J. Phys. Chem. C*, 118, (2014), 15146-15153.
- 37 T. L. Chen and Y. A. Elabd, *Electrochim. Acta*, 229, (2017), 65-72.
- 38 T. Nguyen, M. Boudard, M. J. Carmezim, M. F. Montemor, *Energy*, 126, (2017), 208-216.
- 39 S. I. Kim, S. W. Kim, K. Jung, J. B. Kim, J. H. Jang, *Nano Energy*, 24, (2016), 17-24.
- 40 A. Castaings, W. Lhomme, R. Trigui, A. Bouscayrol, *Appl. Energy*, 163, (2016), 190-200.
- 41 L. L. Zhang and X. S. Zhao, *Chem. Soc. Rev.*, 38, (2009), 2520-2531.
- 42 C. D. Lokhande, D. P. Dubal, O. S. Joo, *Curr. Appl. Phys.*, 11, (2011), 255-270.
- 43 H. Pang, X. Li, Q. Zhao, H. Xue, W. Lai, Z. Hu, W. Huang, *Nano Energy*, 35, (2017), 138-145.
- 44 L. Miao, H. Duan, M. Liu, W. Lu, D. Zhu, T. Chen, L. Li, L. Gan, *Chem. Eng. J.*, 317 (2017), 651-659.
- 45 C. Guan, X. Qian, X. Wang, Y. Cao, Q. Zhang, A. Li, J. Wang, *Nanotechnol.*, 26, (2015), 094001-0940018.
46. A. A. Yadav, A. C. Lokhande, C. D. Lokhande, *Mater. Lett.*, 160, (2016), 500-502.
47. A. A. Atta, M. M. EL-Nahass, K. M. Elsabawy, M. M. Raheem, A. M. Hassanien, A. alhuthali, A. Badawi, A. Merazga, *Pramana, J. Phys.*, 87, (2016), 72-88.
48. A. A. Yadav, A. C. Lokhande, P. A. Shinde, J. H. Kim, C. D. Lokhande, *J. Mater. Sci.: Mater. Electron.*, 28, (2017), 13112-13119.
49. İ. A. Kariper, *Pro Nat Sci-Mater.*, 24, (2014), 663-670.
50. A. A. Yadav, A. C. Lokhande, J. H. Kim, C. D. Lokhande, *RSC Adv.*, 6, (2016), 106074-106080.
51. M. F. Al-Kuhaili, S. M. A. Durrani, *J. Alloys and Compd.*, 591, (2014), 234-239.
52. G. Balakrishnan, A. K. Panda, C. M. Raghavan, A. Singh, M. N. Prabhakar, E. Mohandas, P. Kuppusami, J. il. Song, *J Mater Sci: Mater Electron.*, 30, (2019), 16548-16553.
53. D. Channei, A. Nakaruk, S. Phanichphant, P. Koshy, C. C. Sorrell, *J. Chem.*, 1, (2013), 1- 4.
54. S. Cwik, M. J. Beer, M. Schmidt, Nils C. Gerhardt, T. de. L. Arcos, D. Rogalla, Jana Webing, I. Giner, M. Hofmann, G. Grundmeier, A. D. Wieck, A. Devi *Dalton Trans.*, 1, (2018), 1-13.

55. S. Kaya, E. Yilmaz, H. Karacali, A.O. Cetinkaya, A. Aktag , *Mat. Sci. Semicon. Proc.*, 33, (2015), 42-48.
56. X. Wang, H. Liu , L. Zhao, C. Fei, X. Feng, S. Chen, Y, Wang *Nanoscale Res. Lett.*,12, (2017), 233-340.
57. E. Baškys , V. Bondarenka , S. Grebinskij , M. Senulis , R. Sereika , *Lith. J. Phys.*, 54, (2014), 120-124.
58. F. Paumier, R. J. Gaboriaud, A. R. Kaul, *Cryst. Eng.*, 5, (2002), 169-175.
59. C. V. Ramana, V. H. Mudavakkat, K. K. Bharathi, V. V. Atuchin, L. D. Pokrovsky, V. N. Kruchinin, *Appl. Phys. Lett.*, 98, (2011), 031905-031908.
60. M. Boehme, E. Ionescu , G. Fu, W. Ensinger, *J. Exp. Nanosci.*, 7, (2012), 344-353.
61. P. P. Kumbhar and C. D. Lokhande, *Indian. Chem.Technol.*, 1, (1994), 194-196.
62. S. M. Ramay, A. Mahmmud, H. M. Ghithan, N. S. Zayed, A. Aslam, A. Murtuza, N. Ahamad, S. A. Saleem, *J. Rare Earths*, 37, (2019), 989-994.
63. S. B. Jundale and C. D. Lokhande, *mater. Chem. Phys.*, 27, (1991), 265-278.
64. S. B. Jundale and C. D. Lokhande, *mater. Chem. Phys.*, 38, (1994), 325-331.
65. S. B. Jundale and C. D. Lokhande, *Indian J. Pure Appl. Phys.*, 30, (1992), 215-220.
66. S. B. Jundale and C. D. Lokhande, *mater. Chem. Phys.*, 37, (1994), 333-338.
67. K. Jeong and D. Bae, *Korean J. Mater. Res.*, 22, (2012), 22-29.
68. U. K. Mohite, S. A. Jodgudri, C. D. Lokhande, *J. Phys.*, 19, (1995), 1152-1157.
69. U. K. Mohite, K. M. Gadave, C. D. Lokhande, *Indian J. Pure Appl. Phys.*, 32, (1994), 772-777.
70. U. K. Mohite and C. D. Lokhande, *Bull. Electrochem.*, 13, (1997), 71-74.
71. S. L Yang, H. B. Yao, M. R. Gao, S. H. Yu, *Cryst. Eng. Comm.*, 11, (2009), 1383-1390
72. C. L. Stender, T. W. Odom, *J. Mater. Chem.*, 17, (2007), 1866-1869.
73. P. N. Kumta, S. H. Risbud, *Prog. Cryst. Growth Charact. Mater.*, 22, (1991), 321-383.
74. V. S. Kumbhar, A. D. Jagadale, C. D. Lokhande, *J. Power Sources*, 234, (2013), 107-110.
75. S. J. Patil, V. S. Kumbhar, B. H. Patil, R. N. Bulakhe, C. D. Lokhande, *J. Alloys Compd.*, 611, (2014), 191-196.
76. S. J. Patil, B. H. Patil, R. N. Bulakhe, C. D. Lokhande, *RSC Adv.*, 4, (2014), 56332-56341.
77. H. Wang, M. Liang, X. Zhang, D. Duan, W. Shi, Y. Song, Z. Sun, *Ionics*, 24, (2018), 2063-2072.
78. A. A. Yadav, V. S. Kumbhar, S. J. Patil, N. R. Chodankar, C. D. Lokhande, *Ceram. Int.*, 42, (2016), 2079-2084.
79. A. A. Yadav, A. C. Lokhande, J. H. Kim, C.D. Lokhande, *Int. J. Hydrog. Energy*, 41, (2016), 18311-18319.
80. A. A. Yadav, A. C. Lokhande, J. H. Kim, C. D. Lokhande, *J. Ind. Eng. Chem.*, 56, (2017), 90-98.
81. T. T. Ghogare, R. B. Pujari, A. C. Lokhande, C. D. Lokhande, *Appl. Phys.*, A, 124, (2018), 248-252.
82. S. J. Patil and C. D. Lokhande, *Mater. Des.*, 87, (2015), 939-948.

- 83 S. J. Patil, A. C. Lokhande, C. D. Lokhande, *Mater. Sci. Semicond. Process.*, 41, (2016), 132-136.
- 84 S. J. Patil, R. N. Bulakhe, C. D. Lokhande, *ChemPlusChem.*, 80 (9), (2015), 1478-1487.
- 85 S. J. Patil, V. C. Lokhande, N. R. Chodankar, C. D. Lokhande, *J. Colloid Interface Sci.*, 469, (2016), 318-324.
- 86 S. J. Patil, A. C. Lokhande, D.W. Lee, J. H. Kim, C. D. Lokhande, *J. Colloid Interface Sci.*, 490, (2017), 147-153.
- 87 S. B. Ubale, T. T. Ghogare, V. C. Lokhande, T. Ji, C. D. Lokhande, *SN Applied Sciences*, 2, (2020), 1-5.
- 88 V. S. Kumbhar, A. C. Lokhande, N. S. Gaikwad, C. D. Lokhande, *J. Phys. Chem. Lett.*, 645, (2016), 112-117.
- 89 V. S. Kumbhar, A. C. Lokhande, N. S. Gaikwad, C. D. Lokhande, *Mat. Sci. Semicon. Proc.*, 46, (2016), 29-34.
- 90 V. S. Kumbhar, A. C. Lokhande, N. R. Chodankar, N. S. Gaikwad, C. D. Lokhande, *Mater. Lett.*, 223, (2018), 45-48.
- 91 R. B. Pujari, A. C. Lokhande, T. T. Ghogare, S. B. Kale, C. D. Lokhande, *J. Mater. Sci.: Mater. Electron*, 29, (2018), 14116-14121.
- 92 A. M. Patil, V. S. Kumbhar, N. R. Chodankar, A.C. Lokhande, C. D. Lokhande *J. Colloid Interface Sci.*, 469, (2016), 257-262.
- 93 B. Pandit, N. Kumara, P. M. Koinkar, B. R. Sankapal, *J. Electroanal. Chem.*, 839, (2019), 96-107.
- 94 G. S. Gund, D. P. Dubal, B. H. Patil, S. S. Shinde, C. D. Lokhande, *Electrochim. Acta.*, 92, (2013), 205-215.
- 95 L. Zang, S. Zhao, X. N. Tian, X. S. Zhao, *Langmuir*, 26, (2010), 17664-17628.
- 96 M. C. Nwankwo, B. Ezealigo, A. C. Nwanya, A. C. Nkele, A. Agbogu, U. Chime, P. U. Asogwa, B. A. Ezekoye, A. B. C. Ekwealor, R. U. Osuji, P. M. Ejikeme, M. Maaza, F. I. Ezema, *Inorg. Chem. Commun.*, 119, (2020), 107983-108011.
- 97 U. M. Patil, M. S. Nam, S. Kang, J. S. Sohn, H. B. Sim, S. Kang, S. C. Jun, *RSC Adv.*, 6, (2016), 43261-43271.
- 98 M. Khalid, M. A. Tumelero, V. C. Zoldan, C. C. Pla Cid, D. F. Franceschini, R. A. Timm, L. T. Kubota, S. A. Moshkalevd, A. A. Pasa, *RSC Adv.*, 4, (2014), 34168-34178.
- 99 T. T. Ghogare, V. C. Lokhande, T. Ji, U. M. Patil, C. D. Lokhande, *Surf. Interfaces*, 19, (2020), 100507-100514.
- 100 T. T. Ghogare, A. C. Lokhande, R. B. Pujari, C. D. Lokhande, *SN Applied Sciences*, 1, (2019), 1-7.
- 101 S. Konwer, *J. Mater. Sci: Mater. Electron*, 27, (2016), 4139-4146.
- 102 Z. D Huang, J. Z. Zhang, S.W. Oh, Q. B. Zheng, X. Y. Lin, N. Yousefi, J. H. Kim, *Chem.*, 22, (2012), 3591-3599.
- 103 S. H. Aboutalebi, A. T. Chidembo, M. Salari, K. Konstantinov, D. Wexler, H. K. Liua, S. X. Doua, *Energy Environ. Sci.*, 4, (2011), 1855-1865.
- 104 R. Singhal, D. Thorne, P. K. LeMaire, X. Martinez, C. Zhao, R. K. Gupta, D. Uhl, E. Scanley, C. C. Broadbridge, R. K. Sharma, *AIP Advances*, 10, (2020), 035307-035315.
- 105 L. Wan, S. Sun, T. Zhai, *J. Mater. Res.*, 26, (2017), 1-12.

Chapter-II

*Theoretical background of thin film,
synthesis methods, characterization
techniques and supercapacitor*

Chapter-II

Theoretical background of thin film, synthesis methods, characterization techniques and supercapacitor

Sr. no.	Title	Page no.
2.1	General introduction	25
2.2	Introduction to thin films	25
2.3	Theoretical background of chemical methods	27
	2.3.1 <i>Layer -by-Layer method</i>	27
	2.3.2 <i>Chemical bath deposition (CBD) method</i>	28
	2.3.3 <i>Successive ionic layer adsorption and reaction (SILAR) method.</i>	31
2.4	Thin film characterization techniques	34
	2.4.1 <i>X-ray diffraction (XRD)</i>	34
	2.4.2 <i>X-ray photoelectron spectroscopy (XPS)</i>	35
	2.4.3 <i>Fourier transform Raman spectroscopy (FT-Raman)</i>	36
	2.4.4 <i>Field emission scanning electron microscopy (FE-SEM)</i>	38
	2.4.5 <i>Transmission electron microscopy (TEM)</i>	40
	2.4.6 <i>Contact angle measurement system</i>	42
2.5	Theoretical background of supercapacitor	43
	2.5.1 <i>Supercapacitor device</i>	43
	2.5.2 <i>Cyclic voltammetry (CV)</i>	45
	2.5.3 <i>Galvanostatic charge discharge (GCD)</i>	46
	2.5.4 <i>Electrochemical impedance spectroscopy (EIS)</i>	47
2.6	References	50

2.1 General introduction:

This chapter elaborates the introduction of thin films with the theoretical background of chemical deposition methods. In this chapter, successive ionic layer adsorption and reaction (SILAR) and chemical bath deposition (CBD) methods are discussed in detail. The thin film characterization techniques for structural, wettability and surface morphological studies are discussed. Moreover, the electrochemical supercapacitor performances and parameters of the supercapacitor are explained at the end of this chapter.

2.2 Introduction to thin films:

The recent vast attention is focused on thin film technology due to their use in various thin film applications because of their particular electrical, optical and magnetic characteristics. This technology is utilized on the basis of specific features of film materials that can be simply controlled using various preparative parameters. The properties of materials in the bulk significantly differ when examined in the case of thin films. A material film is known as thin film when its thickness is in the range of fractions (nanometer to less than one micrometer) or a surface bounded between two parallel planes extending infinitely in two directions restricted in dimension along third direction.

For the preparation of thin films, there are two main synthesis approaches used as physical and chemical methods. **Chart 2.1** demonstrates the brief taxonomy of thin film synthesis methods. In the physical thin film deposition methods, sputtering [1] and vacuum evaporation [2] are main fundamental subtypes, which are further classify into magnetron sputtering [3], Radio frequency (RF) sputtering [4], electron beam evaporation [5] and laser evaporation [6].

The sputtering method relies on plasma to knock out material from a target in a few atoms at a time. At a low temperature evaporation rate is very low/negligible, therefore the target always kept at a lower temperature. Physical methods necessitate high vacuum with high working temperature, high cost, cleaning of deposition chamber after every deposition, small area deposition, etc. The gas phase and liquid phase are the two main categories of chemical technique [7, 8]. The gas phase involves plasma enhanced chemical vapour deposition (PE-CVD), chemical vapour deposition (CVD), laser chemical vapour deposition (L-CVD), metal organic chemical vapour deposition (MO-CVD), plasma photochemical vapour deposition (PC-CVD), etc [9-13].

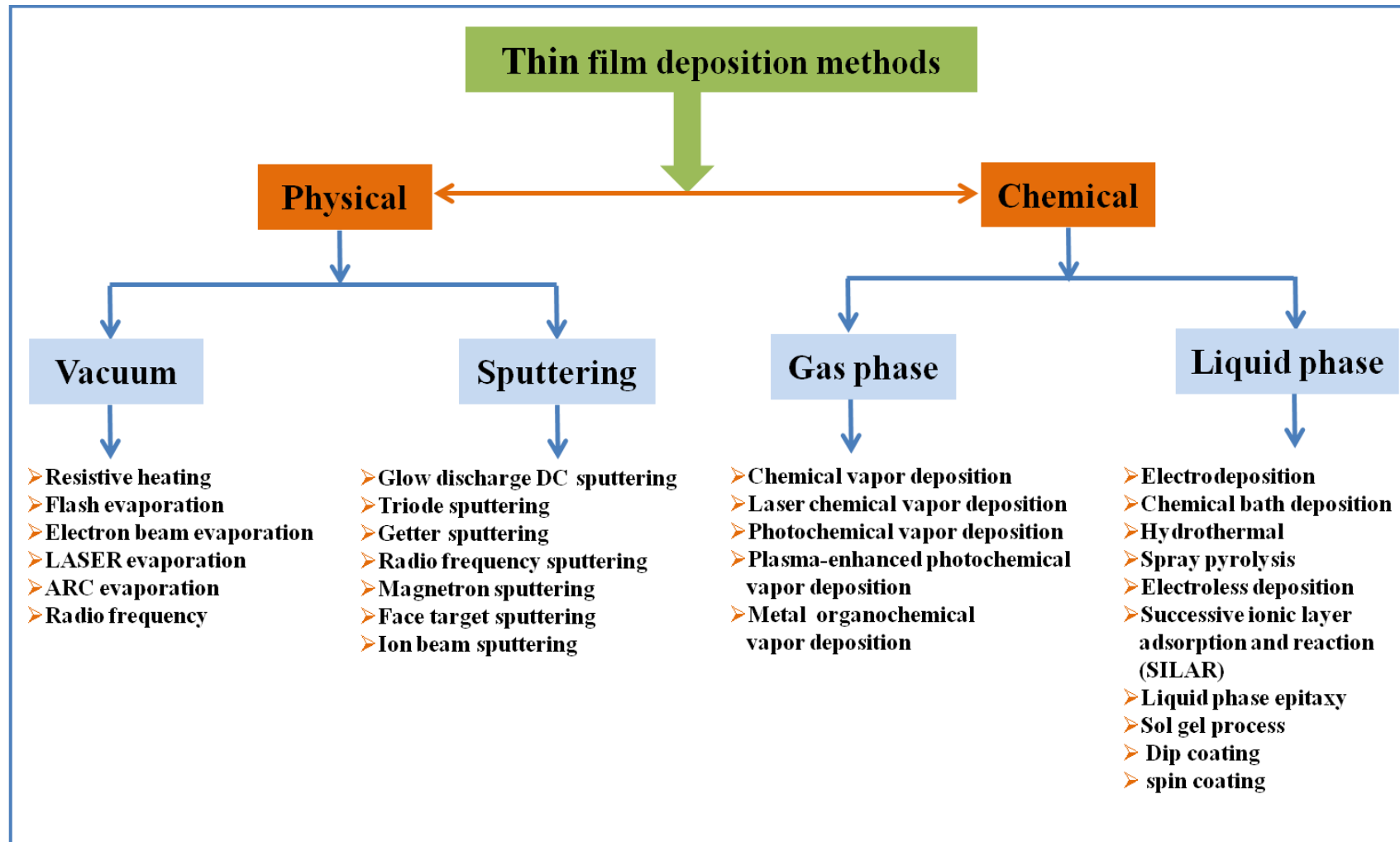


Chart 2.1: Brief taxonomy of thin film deposition methods.

Liquid phase method involves electrodeposition [14], CBD, SILAR [15, 16], liquid phase epitaxy [17], spray pyrolysis [18], dip coating [19], spin coating [20], hydrothermal, etc. [21]. As compared to physical deposition methods, chemical deposition methods are well suitable for producing large scale surface area thin films. Also, the chemical methods are inexpensive, simple, environment friendly, minimum wastage of material, easily available, and carried out at low or room temperature for the deposition of rare earth chalcogenide thin films.

2.3 Theoretical background of chemical methods:

2.3.1 Layer-by-Layer method:

The Layer-by-Layer (L-b-L) method is simple, inexpensive, binder-free and reliable for deposition of thin films at low or room temperature and also thickness controllable method. The schematic of L-b-L method is shown in **Fig 2.2**.

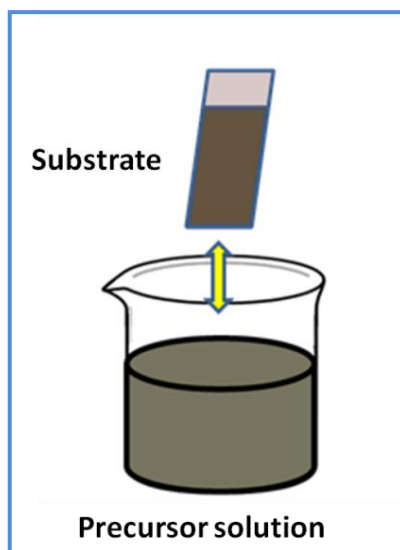


Fig. 2.2: The schematic of L-b-L method.

In the L-b-L method, well polished substrate is immersed into a suspension of well dispersed solution consisting of the desired material and then substrate is dried in air. The size and thickness of thin films could be controlled by changing the number of dip and drying cycles in the suspension solution. Using this method method, films can be deposited on any type of shape and size of a substrate like cylindrical, spherical shapes. Also, the large area can be deposited on both sides of the substrate. High quality semiconducting or superconducting, insulator and conducting thin films on nanoparticles can be deposited by this method with good thickness and uniformity. The hydrophilic and hydrophobic nature of substrate plays a vital role while depositing the

material. In order to deposit or coat, surface activation, passivation and formation of nucleation centre are required in some of the cases.

2.3.2 Chemical bath deposition (CBD) method:

The CBD method is binder-free, simple and inexpensive method used for the preparation of thin film. It does not need vacuum system and other costly equipment and it depends upon the two main reaction mechanisms; one is homogeneous and the other is heterogeneous. This method gives easy control over the preparative parameters to attain the better thickness of thin film. Mane and Lokhande [22] have explained CBD method reaction mechanism for film formation with the effect of preparative parameters in detail. Many review articles have discussed on the chemical methods for thin film deposition [22-26]. The experimental setup for the synthesis of metal sulfide thin films using CBD method is demonstrated in Fig. 2.3.

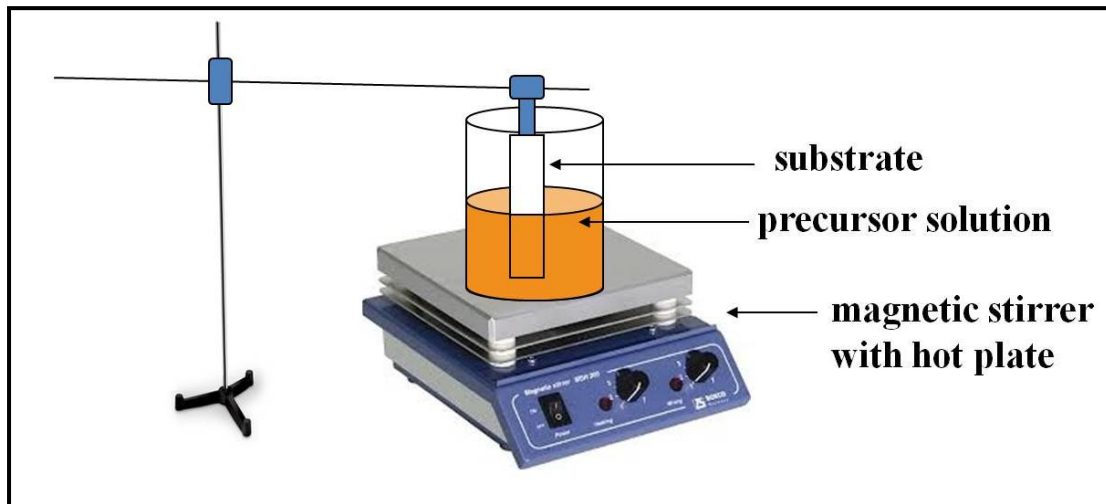


Fig. 2.3: The schematic of CBD method.

2.3.2.1 Concept of ionic and solubility product:

When, sparingly soluble salt XY, placed in water, a saturated solution containing X^+ and Y^- ions in contact with un-dissolved solid XY are obtained and equilibrium is established between the solid phase and ions in the solution as,



$$M = C_x^+ \cdot C_y^- / C_{xy} (S) \quad (2.2)$$

Where, C_x^+ : concentrations of X^+ , C_y^- : concentrations of Y^- and C_{xy} : concentrations of XY ions in the solution. The concentration of a pure solid phase is a constant number,

$$\text{i. e. } C_{xy} (S) = \text{constant} = M' \\ M = C_x^+ \cdot C_y^- / M' \quad (2.3)$$

$$M M' = C_x^+ \cdot C_y^- \quad (2.4)$$

Since, M and M' are constant, the product MM' is also constant, say Ms, therefore above equation becomes,

$$M_s = C_x^+ \cdot C_y^- \quad (2.5)$$

Ms is known as solubility product (SP) and ($C_x^+ \cdot C_y^-$) is known as the ionic product (IP). In case of saturated solution, the IP of ions is equal to the SP. But when IP exceeds the SP i.e. $IP/SP = S > 1$, the solution is supersaturated, precipitation occurs and ions combine on the substrate and in the solution to form nuclei [22, 27].

2.3.2.2 Theoretical background of nucleation and growth:

2.3.2.2.1 Basics of nucleation and growth:

Chemical methods consist of nucleation and growth; we will treat the ion-by-ion and hydroxide cluster mechanisms independently.

a) Ion-by-ion growth mechanism:

For homogenous nucleation requires a high degree of saturation in the ion-by-ion growth mechanism. The presence of free particle, the surface introduces a degree of heterogeneity that facilitates nucleation. For this reason deposition proceed by the ion-by-ion mechanism. The surface can be admitted as a catalyst for the nucleation.

b) Hydroxide cluster mechanism:

In hydroxide cluster mechanism, nucleation of chalcogenide is easy, since a solid phase, the previously present metal hydroxide and the process are proceeding by substitution reaction over that the solid phase. In this case, initially the deposition is the adhesion of hydroxide to substrate.

Advantages of CBD method:

- i) It is a binder-free, simple, inexpensive method for deposition of the large scale area films.
- ii) Low/room temperature the preparation of thin film can be carried out.
- iii) Different types of substrates can be used.
- iv) It does not necessarily require vacuum or costly instrument at any stage.
- v) Stoichiometric synthesis is achieved since the fundamental building blocks are ions rather than the atom.
- vi) It results in uniform and pinhole-free preparations as the solution always remains in touch with the substrates.

vii) The preparative parameters such as concentration, deposition time etc. affecting thickness of film can be easily controlled.

viii) The toxic gases are not evolved.

2.3.2.3 Role of preparative parameters:

The experimental set up used for synthesis of metal chalcogenide thin films is illustrated in **Fig. 2.3**. The rate of deposition and thickness of thin film depend upon various factors like solution supersaturation state, stirring rate, number of nucleation sites, etc. The growth kinetics of the thin film deposition based on the solute concentration i.e. number of ions presence in the bath and their velocities. The synthesis parameters are explained as following:

A) pH of the bath:

The pH is nothing but the negative logarithm of H^+ ions concentration, which is restricted by using complexing agent. The rate of reaction and rate of film deposition depends upon the supersaturation state. If solution is less supersaturated, then the rate of MX formation is slower (where M and X is the number of metal and chalcogenide ions, respectively). The formation of many X ions from a particular anionic source basically depends upon the solution pH. When the bath pH is raised, the formation rate of X ions will decrease and hence, the rate of formation will be slowed down. If pH is decreased, the concentration of X ions raises to make the formation of possible thin film.

B) Complexing agent:

To embrace the metal cation and avoid the precipitation of material to be formed is the function of complexing agent. During the film formation process, it slowly releases the cations to react with anions in the bath. However, if the concentration of complexing agent is increased, then metal ion concentration decreases. As a result, the reaction rate and precipitation are reduced, this leads to the slow rate of deposition film.

C) Temperature:

The film formation rate depends on the temperature. With increase in the temperature, dissociation rate of complexed anions and cations increases. This results into higher concentrations of M^+ and X^- ions and hence the deposition rate. But in several cases, the thickness of film may be reduced at the higher temperature. For e.g., when solution is supersaturated at the less pH with increase in temperature, this leads to

formation of precipitate and the thickness of film is low. On the other hand, at higher pH values, precipitation is greatly reduced due to less supersaturation and material is formed over the surface of substrate. Moreover, by keeping higher pH, when temperature is raised, more M^+ and X^- ions are available to form MX and therefore, the higher thickness film is obtained.

D) Concentration:

In this case, MX with greater film thickness is obtained. But, when X^- ion concentration is boosted beyond some limit, then rate of precipitation raises leading to low quantity of MX over the surface of substrate which results into less film thickness.

E) Substrate:

The substrate to be used for the formation of thin films, also plays a significant role in deciding thickness of film and deposition rate. When the deposited material lattice matches with substrate, the less change in free energy, this is facilitating the nucleation and further growth of film.

2.3.3 Theoretical background of successive ionic layer adsorption and reaction (SILAR) method:

2.3.3.1 Basics of SILAR method:

The best characteristics of thin film formation such as adherent, uniform and thin are possible using SILAR method. In CBD method, the thin film formation takes place when IP exceeds the SP. But, the formed precipitate in the bulk of solution cannot be avoided. In order to evade such loss of material or unnecessary precipitation, SILAR is a modified version of CBD method. In the mid-1980, the SILAR method was used for the synthesis of metal chalcogenide thin films [24]. Ristov et al [25] originally reported a SILAR method as a versatile chemical immersing method. Nicolau and Menard [26] preferred the name as SILAR. SILAR is a successive ionic layer adsorption and reaction method. Generally, the SILAR method includes adsorption, reaction and rinsing. This method mainly depends upon adsorption and reaction mechanism. **Fig. 2.4** shows the schematic of SILAR deposition method.

(A) Adsorption:

The first step of deposition of thin film is adsorption process, where the cations are adsorbed over the substrate surface and Helmholtz electric double layer is formed, which is formed owing to the chemical or Van der Waals force and it is composed

couple layers. The positively charged cations form inner electric layers. The second layer is negatively charged anions having the counter layer of cations.

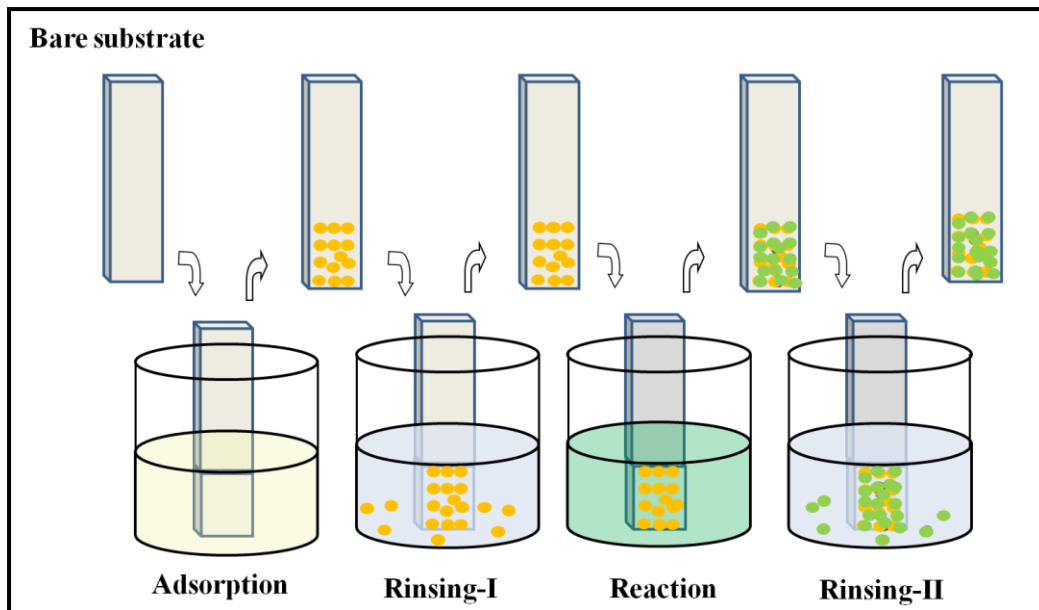


Fig. 2.4: The schematic of SILAR deposition method.

(B) Rinsing-I:

The use of rinsing-I is to eliminate the loosely/unbounded adsorbed cations over the surface of a substrate. Generally, for the rinsing of film material, double distilled water (DDW) is used.

(C) Reaction:

From the anionic precursor solution, anions react with pre-adsorbed cations and form a molecule/compound.

(D) Rinsing- II:

In this step, eliminate the unreacted and excess species, and a byproduct of reaction from a diffusion layer. Generally, DDW is used as a rinsing purpose.

The deposition of thin film mainly based on the thicknesses of film, which is controlled by varying various preparative parameters such as bath temperature, cations and anions concentrations, complexing agent, adsorption, rinsing and reaction time.

SILAR method advantages:

The SILAR method advantages are as follows

- a) It is a binder-free, eco-friendly, simple and convenient method for deposition of a large area thin films.
- b) This method is carried out at low/room temperature.

- c) The rate of deposition can be easily controlled.
- d) Any type of substrate can be used.
- e) This method does not need a vacuum/high quality targets at any stage.
- f) The film thickness can be simply controlled by changing the deposition parameters [28].

2.3.3.2 Effect of preparative parameters:

In SILAR method, the growth kinetics is based on ion concentration, adsorption and reaction time, rinsing time, temperature and complexing agent. The various preparation parameters are discussed as follows,

(I) Concentration:

The growth of film is affected by varying the precursor solution concentration, in the chemical deposition methods. If the concentrations of metal ions are more than the certain ion concentration, the rate of reaction becomes greater and less film thickness is obtained. More concentration of metal ion results in formation of higher film thickness.

(II) pH:

For higher value of pH, the reaction rate rapidly increases or decreases and at a certain value of pH, the metal ion concentration decreases to a level that the IP of metal and chalcogenide becomes less than the metal chalcogenide SP and the film will not be formed.

(III) Temperature:

Film thickness variation can be possible by changing the bath temperature. The compound anion and dissociation of complex depend upon the temperature. The dissociation is greater at high temperature and resulted in higher deposition rate. At lower/room temperature the rate of film formation is slow. The thickness of film is boosted with boost the temperature linearly.

(IV) Complexing agent:

The concentration of metal ions can be restricted by drop wise adding complexing agents. Increase in the complexing agent concentration decreases the metal ions concentration. Therefore, the reaction rate and formation of a precipitate are reduced leading to higher terminal film thickness. The thin film deposition over surface of substrate is due to only adsorption phenomenon. The thin film development occurs via a combination of rescued metal ions from the metal ions complex and chalcogenide

sources. Ethylenediaminetetraacetic (EDTA), tartaric acid (TA), citric acid (CA), oxalic acid (OA), triethanolamine (TEA) are some common complexing agents.

(V) Adsorption and reaction time:

The adsorption and reaction time play vital role in the deposition of thin film. When adsorption time is more than reaction time, the film formation takes place by assorted reaction and results into large terminal thickness. The equal adsorption and reaction time results into consistent reaction which provides uniform and adherence film formation.

(VI) Rinsing time:

It is the most essential step in the thin film formation. If the rinsing time is lower than required, loosely/unabsorbed cations may not be eliminated completely from the surface of substrate. Sufficient rinsing time provides uniform and good quality film.

2.4 Thin film characterization techniques:

2.4.1 X-ray diffraction (XRD) technique:

The XRD technique is used to determining the atomic spacing and crystal structure. Max von Laue in 1912 discovered that the crystalline substances act as three-dimensional (3D) diffraction gratings for XRD wavelengths similar to the spacing of planes in crystal lattice. The XRD investigation primarily depends on the crystalline samples and constructive interference of monochromatic X-ray. If once the X-rays are generated from a cathode ray tube (CRT) and filtered to construct monochromatic radiation. Then, the monochromatic radiation collimates and highly concentrated towards the applied sample. While, the X-rays are partially distributed by atoms of a crystal, also they are strike on the crystal surface. The remaining X-rays are again scattered by atoms in the next layer of atoms. In that way, the diffraction pattern form. The diffraction pattern illustrates the peak, when the X-rays are diffracted by two different layers are in phase then the constructive interference occurs. If the X-ray beams are diffracted by two different layers and when it is out of phase, then there is no peak due to the destructive interference. The Bragg's conditions satisfy then XRD diffraction peaks are occurring [29],

$$2d \sin \theta = n \lambda \quad (2.6)$$

Where, d , θ , n , and λ are the interplanar distance, angle of incidence or Bragg's angle, an integer and wavelength of X-ray, respectively.

For determination of sample crystal structure three methods are used.

i) Laue method, ii) Rotating crystal method and iii) Powder method.

Laue method is an oldest method and it is used to find out of crystal structure, where X-ray wavelength is variable, and incidence angle is not variable. In rotating crystal method, the incidence angle is fixed and wavelength of X-ray is variable.

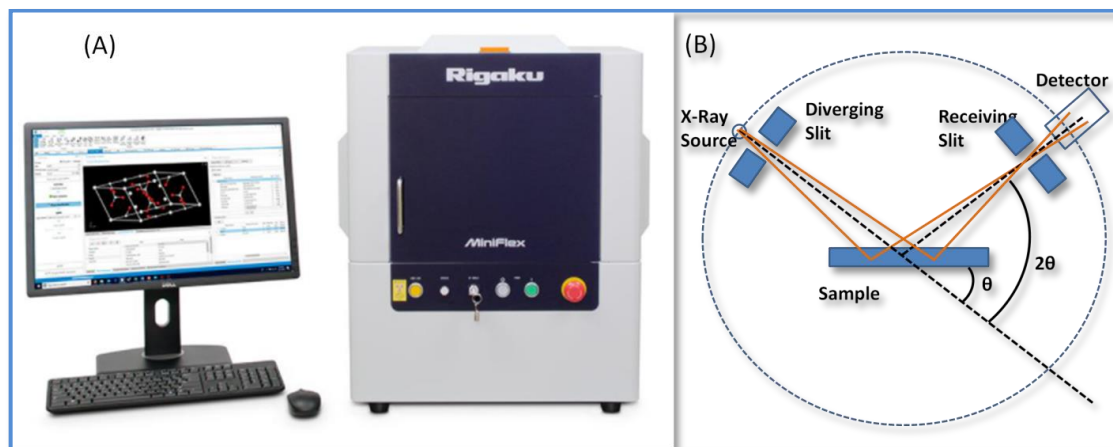


Fig. 2.5: (A) Photograph of Rigaku Miniflex-600 XRD unit and (B) the schematic of X-ray diffractometer [30].

For the simply examination of sample crystal structure, powder method is generally used. In case of powder method, the X-ray wavelength is fixed, and incidence angle is variable. **Fig. 2.5(A)** demonstrates the photograph of Rigaku Miniflex-600 XRD unit and **Fig. 2.5(B)** shows the schematic of X-ray diffractometer. The average crystalline size, (D) of prepared material is calculated from Scherer's equation [31].

$$D = K \cdot \lambda / \beta \cdot \cos\theta \quad (2.7)$$

Where, K, λ , β and θ are the constant, X-ray wavelength (1.54 Å), full width and half maxima (FWHM) and Bragg's angle, respectively.

2.4.2 X-ray photoelectron spectroscopy (XPS):

To identify the chemical state, elemental composition and quantity of elements exist on the surface of the material, XPS is a strong surface sensitive and quantitative spectroscopic technique. The XPS spectrometer works on the principle of photoelectric effect, which can be interpreted from the following relation [33].

$$E_k = h\nu - BE - \phi \quad (2.8)$$

where, E_k , $h\nu$, BE and ϕ are the ejected photoelectron kinetic energy owing to bombarded of X-ray photon from the shell, the incident X-ray photon energy, the binding energy of the electron in the shell and work function, respectively.

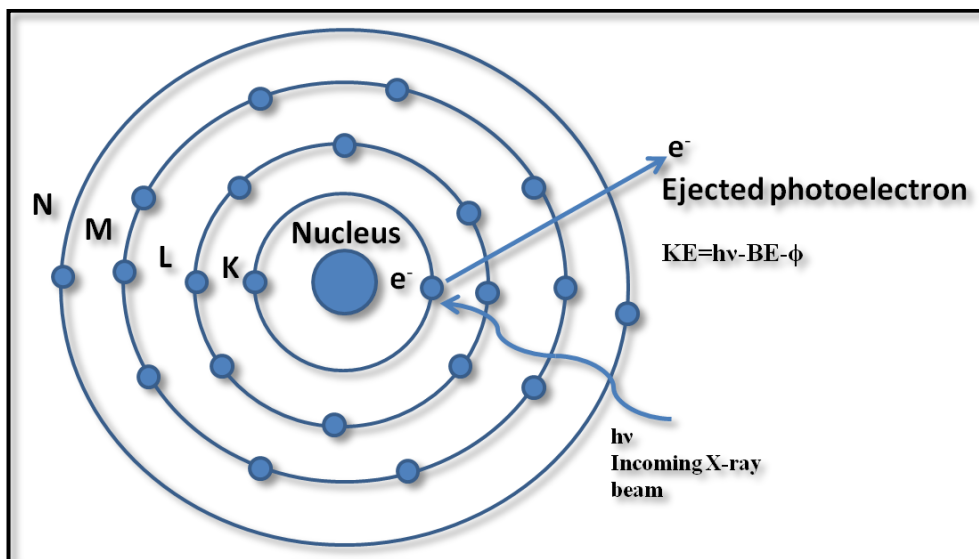


Fig. 2.6: Ejection of photoelectron after bombardment of Al K α ($h\nu = 1486.6$ eV)/Mg K α ($h\nu = 1253.6$ eV) radiations in the XPS measurements [32].

Typically, in the performing procedure of XPS spectroscopy, the sample surface is bombarded regularly with X-ray source Al K α radiations ($h\nu = 1486.6$ eV)/Mg K α ($h\nu = 1253.6$ eV), which generates the emission of photoelectrons from the surface of the sample as illustrated in the **Fig. 2.6**. An analyzer of electron energy is characteristic of the element to measure the energy of emitted photoelectrons. These emitted electrons kinetic energy is a characteristic of the element, from which the photoelectrons are originated. The intensity and positions of peaks in an energy spectrum provide the desired chemical state with quantitative information. From intensity of photoelectron peak and binding energy, the chemical state, elemental identity, and quantity of detected elements can be determined. The average depth is found to be approximately 5 nm as per analysis by XPS measurement. The basic requirements of photoemission experiment are,

- (a) An X-ray radiation source with fixed energy.
- (b) An electron energy analyzer (which scatter the emitted electrons with kinetic energy, and thereby estimate an emitted electron energy flux).
- (c) A vacuum condition (to enable the emitted photoelectrons study without interference from the collisions of gas ions/molecule).

2.4.3 Fourier transform Raman spectroscopy (FT-Raman):.

It is a significant practical tool used for speedily finding out molecules with specific molecular structures. When a radiation beam having a specific frequency is

traveled throughout a transparent sample, then the frequency of final state has fixed that of initial, this process is known as Rayleigh or elastic scattering. In case of inelastic scattering, the initial and final states have dissimilar frequencies. Generally, in the final state of scattering, the radiation beam has some other frequencies than the incident radiation. The anti-stokes line is because of the higher frequencies and the stokes line is because of lower frequencies than that of the incident radiation [37]. The molecule composed of vibrational spectrum is known as Raman band which represents the normal vibrations. The Raman band occurs owing to the Raman scattering with a change in rotational, electronic or vibrational energies of a molecule. Also, the atomic arrangement, chemical masses and bands of the atoms are more significant in the molecule for identification of molecule spectrum [38]. **Fig 2.7** illustrates the block ray diagram of FT-Raman spectrophotometer

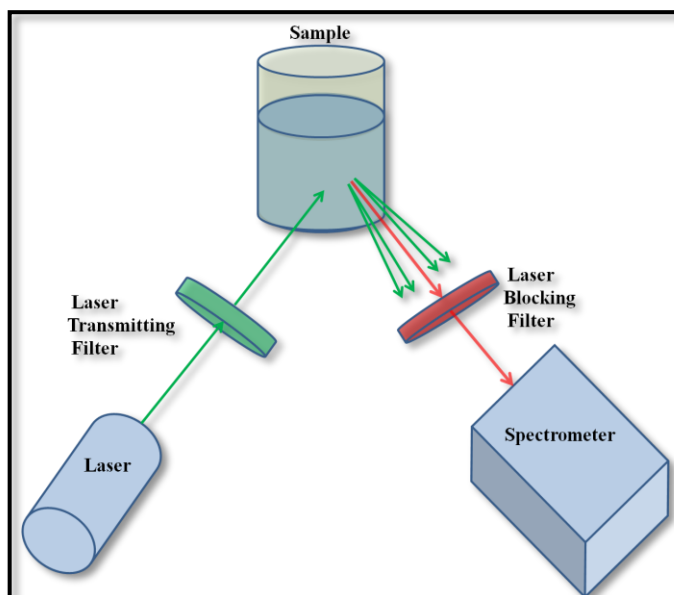


Fig 2.7: The block ray diagram of FT-Raman spectrophotometer [36].

Theory:

When a sample is exposed to monochromatic light in the visible region, the sample absorbs light and a major portion of it gets transmitted through the sample. However, a small part of the light gets scattered by the sample in every direction. The scattered and incident light has a particular frequency. When the scattering is observed at the right angle to the incident beam, 99 % of the scattered light has similar to incident light, this type of scattering is known as Rayleigh scattering. Only 1 % light scattered with various frequencies other than the incident frequency, which is known to Raman scattering..

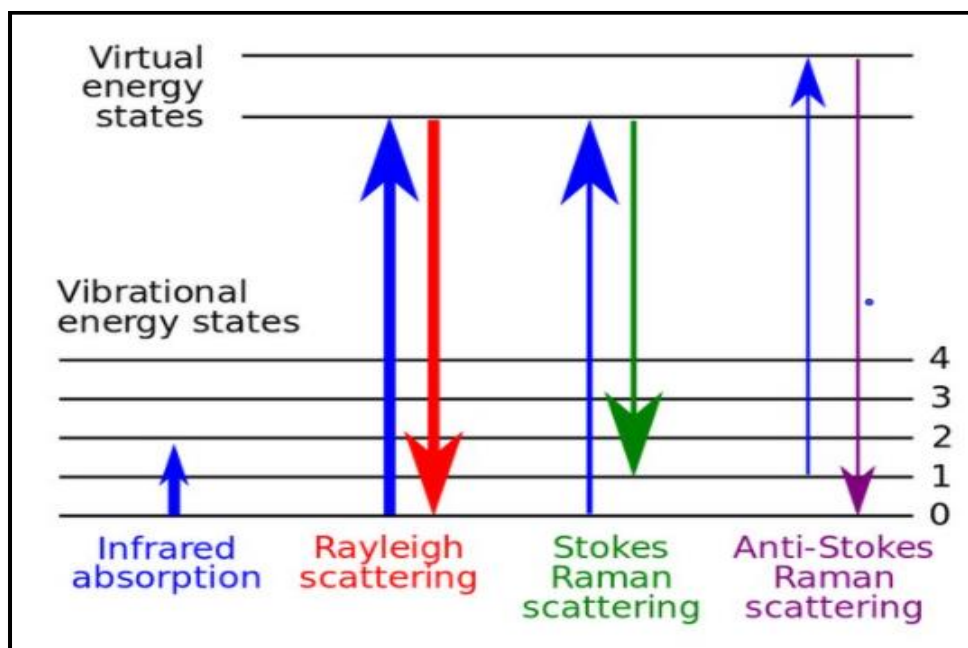


Fig 2.8: Energy level diagram showing different states involved in Raman spectroscopy [39].

Raman scattering is a two-photon process. Electrons have various vibration levels which are defined by specific energy differences. When an incident monochromatic light interacts with an electron in the sample, the electron absorbs energy from an incident photon and goes to a virtual state of energy. Electron falls back to an energy level by losing energy. When the energy lost equal to the energy of an incident photon, the electron falls back to its initial level and loses the one photon. Therefore, the molecule doesn't have any Raman active modes. The secondary photon has same frequency as the incident photon and Rayleigh scattering occurs, sometimes electrons while losing energy from the virtual state can fall back to vibration levels.

Fig. 2.8 illustrates an energy level diagram indicating states involved in Raman spectroscopy

The Raman shift ($\Delta\nu$) is negative for anti-stokes and positive for stokes lines. The Raman spectrum gives the molecular finger print, which is different for different molecules. By investigating the Raman spectrum one can identify the rotational levels and thus a particular molecule. Similarly, the intensity of a particular Raman line helps to determine the concentration of a molecule in the sample.

2.4.4 Field-emission scanning electron microscopy (FE-SEM):

FE-SEM is a powerful technique used to the find out surface texture of deposited materials at high resolution [40]. As compared to other microscopies such as

optical and scanning electron microscopes, it uses electrons to illuminate sample surface. It is capable of imaging at more magnification than the light microscopes, owing to a smaller wavelength of electrons as a comparison of visible light [41]. The lanthanum hexaboride and tungsten are used for filaments as common materials. It uses a field emission gun that has small electrostatic distortions and made a clear image with spatial resolution < 2 nm which is better as compared to SEM [42].

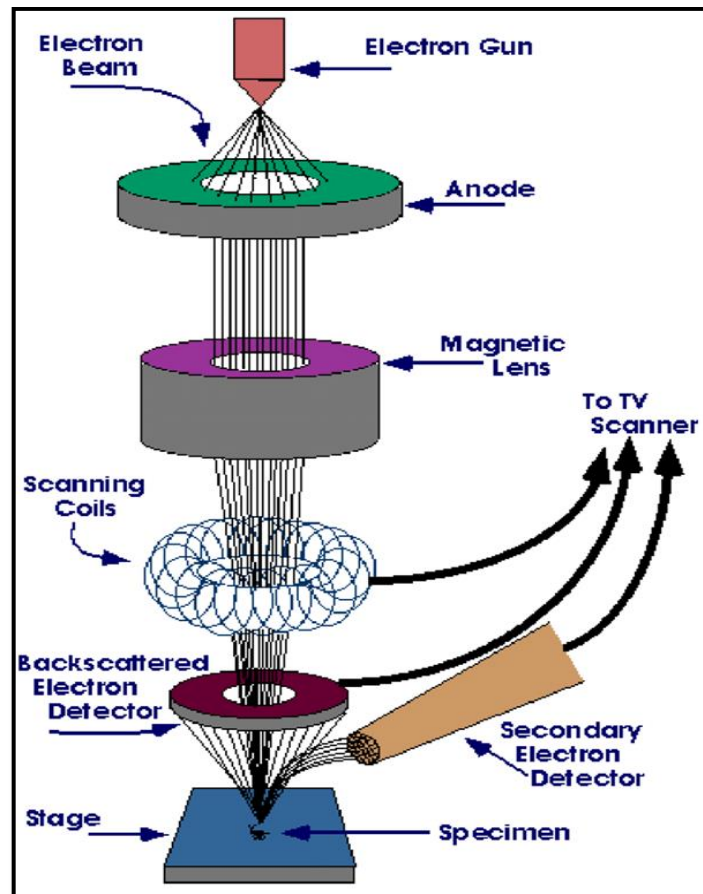


Fig. 2.9: The block diagram of FE-SEM [43].

The emission sources are classified into two main categories such as field emitter and thermionic emitter. Electrons are generated from field emission sources and accelerated at an extremely high gradient of an electric field. In the big vacuum column (less than 7-10 Pa) released primary electrons are allowed to focus and deflect through electronic lenses which produce a narrow beam that bombards the object. The secondary electron lands on the lens detector and collected to produce an electronic signal. The recorded electrical signals are amplified and translated into a scanned image. The scanned images are seen on the display. **Fig. 2.9** shows the block diagram of FE-SEM.

2.4.5 Transmission electron microscopy (TEM):

In the recent period for all types of materials, morphological characterizations are very significant. To carry out the applied and fundamental research of material, surface morphological information is needed for its structural correlation. Transmission electron microscopy (TEM) is an important tool that can provide information up to nano-level [44]. The construction wise fundamental TEM comprises a vacuum system, an electron gun, high voltage generator, electromagnetic lenses, associated with electronic and recording devices. To illuminate the specimen, the TEM required an electrons source. The column of a microscope is maintained vacuum at the high level of scattering to prevent electrons via inside the microsphere atmosphere.

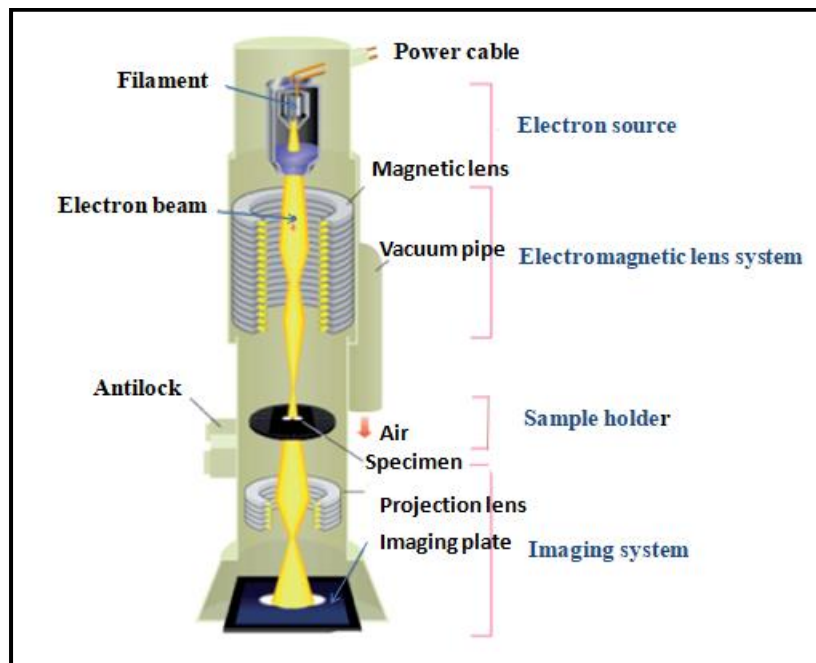


Fig. 2.10: General layout of electron beam path in TEM [45].

Electrons are concentrated through a bunch of electromagnetic lenses over the specimen, which has been produced by electron transport by specific specimen preparation method. The specific specimen preparation method involves thinning the specimen either by electrochemical dissolution/by the bombardment with ions, the thickness range of the specimen is between 50-100 nm for it to be electron transparent. The bunch of lenses applied for concentrating the beams over the specific specimen is not forming an image of lenses. These lenses are illuminated a specific specimen from only one side. A bunch of lenses is utilized instead of a single lens to provide different illuminating conditions such as nano-beam illumination convergent beam illumination

and parallel beam illumination. This also allows superior control over the beam size. The first ray forming lens is an objective lens. The image made by the objective lens act as an object to the succeeding lens and so on. In modern day, the TEM technique has 5 to 6 image forming lenses. **Fig. 2.10** illustrates the general layout of electron beam path in TEM.

TEM reveals the details of interior structure-in some cases as tiny as individual atoms. It includes four parts given as follows,

(I) Electron source:

Electron source consists of anode and cathode. A cathode is a tungsten filament heated electromagnetically at a greater negative potential, emits electrons. The anode (At positive potential) accelerates electron beam towards sample specimen positioned below to anode as demonstrated in **Fig. 2.10**.

(II) Electromagnetic lens:

An electromagnetic lens is a combination of aperture and magnetic lens. Magnetic lens produce a precise magnetic field, this acts as an optical lens for electrons to focus them. Aperture is a thin disc having a diameter of 2 to 100 μm used to remove unwanted electrons from hitting the specimen of a sample. Hence, the electromagnetic system allows well defined narrow energy electron to pass through to hit the target specimen under study.

(III) Sample holder:

For position and movement of sample specimen, the sample holder is equipped with mechanical arm

(IV) Imaging system:

An imaging system includes an electromagnetic lens system and screen. Electromagnetic lens has two lenses; first is used for refocusing electron beam after transmitting through ultrathin sample specimen and second lens is used for enlarging of image on the project screen.

The high resolution transmission electron microscopy (HR-TEM) images quality depends on the scattering effect; hence the sample preparation for HR-TEM must be done very well. A metal grid is used to support the sample, which is a flat disc with a mesh used to support a very thin section of sample. **Fig. 2.11(A)** shows the sample holder and **Fig. 2.11(B)** shows the copper grid used to support the sample in this study.

To prepare a powder sample ready for HR-TEM measurement, a tiny quantity of powder is dispersed in a low boiling point solvent and ultrasonicated the solution. The tiny drop of solution is carefully put on the grid. In the present investigation, the HR-TEM images and selected area electron diffraction (SAED) patterns are collected through TEM unit.

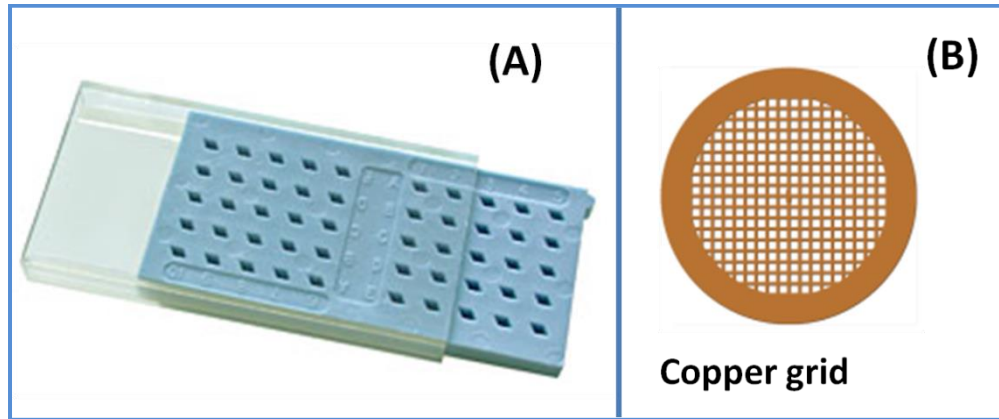


Fig. 2.11: Photographs of (A) TEM grid holder and (B) copper grid [46, 47].

2.4.6 Contact angle measurement system:

The contact angle is a significant technique for the measurement of contact angle and thin film surface wettability. Also, using this technique, it is possible to determine the surface free energy. The capacity of thin film material to interact with liquid is wettability. **Fig. 2.12(A)** demonstrates the photograph of Rame-Hart contact angle meter. The contact angle image of a liquid sample on a solid thin film surface is illustrated in **Fig. 2.12(B)**. The contact angle is the angle between surface of a solid and tangent drawn to the liquid surface, measures inside the liquid. If the contact angle is greater than 90° , then it is said to be hydrophobic and film surface is less wettable. The contact angle of material is above 170° , then it is said to be a super-hydrophobic surface. In the case of super hydrophilic nature, the contact angle is equal to or less than 5° and the surface is highly wettable. The contact angle is less than 90° , then it is known as a hydrophilic nature surface and it is more wettable [48, 49]. For the measurement of contact angle, various methods are used. If the three phases are in equilibrium condition, then the net force is zero. The contact angle (θ) is determined by the Young's equation [50],

$$\gamma_{s,v} = \gamma_{s,l} + \gamma_{l,v} \cos\theta \quad (2.9)$$

Where, $\gamma_{s,v}$, $\gamma_{s,l}$ and $\gamma_{l,v}$ are the solid-vapour, solid-liquid and liquid-vapour interfacial energies, respectively.

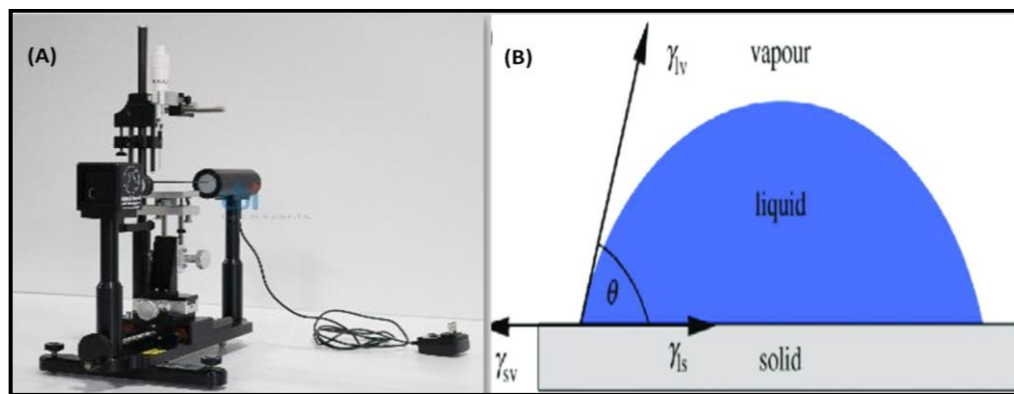


Fig. 2.12: (A) Photograph of Rame-Hart contact angle meter and (B) the contact angle image of a liquid drop on a solid thin film surface [51, 52].

2.5 Theoretical background of supercapacitor:

The supercapacitor is an electrochemical capacitor has energy density more than the conventional capacitor and power density more than a battery, which gains and delivers charges quickly. The supercapacitor possesses more benefits over the battery and conventional capacitor. The supercapacitor has long cyclic stability. It has high Cs, energy density, and power density. It is not harmful like a battery. Therefore, it is used in many applications like hybrid electric vehicles, telecommunication, light weight power supplies for small aircraft and backup for uninterruptable power supply.

2.5.1 Supercapacitor device:

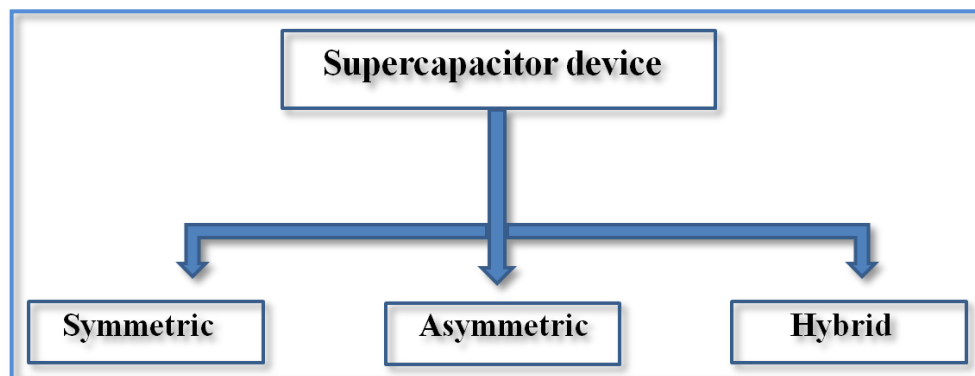


Fig. 2.13: Types of supercapacitor device.

Fig. 2.13 shows the category of supercapacitor device. There are three types of supercapacitors like symmetric, asymmetric and hybrid supercapacitor devices. There are large numbers of research articles on the symmetric and asymmetric configuration of supercapacitive cells, and it is crucial to define average terminologies refer to these devices [53]. Moreover, these terms of symmetric, asymmetric and hybrid are used for devices only not to electrodes. The high-power devices and limited energy storing

capacity of capacitors while the batteries are the high-energy devices but low power density. The combination of both systems is expected to develop a high performance single device.

Symmetric supercapacitor (SSc) system can be fabricated using both similar electrodes of same charge storage mechanism. For example both are EDLC (like as carbon based electrodes such as activated carbon (AC) and carbon nanotubes (CNTs), etc.) or pseudocapacitor (metal oxide/hydroxide, sulfides, etc.) electrodes.

A new device designed by two different electrode materials with different charge storage mechanism or the electroactive materials having various ratios of the redox-active sites is known as asymmetric supercapacitors (ASCs). Most of the time, the electrodes are based on the capacitive or pseudocapacitive mechanism, and the device can provide a wide working window with high energy density at high power rates and long-standing cyclic stability. The term asymmetric should only be used when pseudocapacitive or EDLC electrodes (both EDLC and both pseudocapacitive or one EDLC//one pseudocapacitive) are concerned. For examples AC//MnO₂.

Hybrid system device can be assembled using two dissimilar electrodes of different charge mechanisms, for examples, one battery type pseudocapacitor (nickel hydroxide (Ni(OH)₂)) and one capacitive AC [54-56]. These devices show the electrochemical signature in between battery-type and supercapacitor electrodes and defined as hybrid supercapacitor (HSc). In this device, the working potential window is utilized to reach the faradic potential battery like electrode, which enhances the energy storage ability of supercapacitor. The hybrid device shows more capacitive performance owing to hybridization [57-62].

According to the thermodynamic, the SSc use same potential window electrodes to reach the extreme voltage for supercapacitor. On the other hands, ASCs and HSCs use the dissimilar potential windows of the negative and positive electrodes to reach the greatest working voltage for supercapacitor. As a result, to great extent improved energy storing ability is recorded for ASCs and HSCs supercapacitors. SSc does not require charging balance to reach the huge value of voltage and energy density. But charge balancing ($Q_+ = Q_-$) in the ASCs and HSCs supercapacitor electrodes is necessary to achieve the high voltage and energy storage values. Since, the stored charges are correlated to the specific capacitance (Cs), and mass (m) of the electrode,

the optimized mass ratio from the negative and positive electrodes can be calculated from the following relation [63-65],

$$Q_+ = Q_- \quad (2.10)$$

$$m_+ \times Cs_+ \times \Delta V_+ = m_- \times Cs_- \times \Delta V_- \quad (2.11)$$

$$\frac{m_+}{m_-} = \frac{Cs_- \times \Delta V_-}{Cs_+ \times \Delta V_+} \quad (2.12)$$

Where, Q (+ or -), m (+ or -), Cs (+ or -) and ΔV (+ or -) are the charges in coulomb, mass of electrode material (mg), Cs of positive and negative electrode ($F\ g^{-1}$), working potential window (V), respectively.

2.5.2 Cyclic voltammetry (CV):

This is a powerful technique to understand the electrochemical supercapacitive processes at interface of electrode/electrolyte. It is extensively used to investigate the faradic reaction reversibility and find out the potential window of electrodes/devices. The principle of CV is to estimate the resulting current simultaneously, when applying a linear voltage to an electrode/device between initial and final voltage [66]. In CV, the electrode potential is varied linearly between two fixed potentials and back to returned again original potential to complete one cycle. Such potential cycles are repeated multiple times. During the applied potential rate, the current is deliberated as a function of potential. The graph appearing from such analysis is known as cyclic voltammogram. The CV study enables us to know [67],

- a) pseudo-quantitative and qualitative investigations
- b) kinetic examination by scanning a massive range of scan rates; and
- c) determination of voltage window

The CV measurements are usually carried out in two/three-electrode configuration, if CV measurement in a three-electrode configuration having a counter electrode (CE), working electrode (WE) and a reference electrode (RE). In CV measurement, the electrode working potential is measured against the RE. The typical CV curve is shown in **Fig. 2.14**. The specific capacitance (C_s) of thin film electrode calculated from CV curve using equation,

$$C_s = \frac{1}{ms(V_2 - V_1)} \int_{V_1}^{V_2} I(V) dV \quad (2.13)$$

Where, $\int_{V_1}^{V_2} I(V) dV$ indicates the integrated current response of prepared electrode in A

g^{-1} , s is the scan rate in mV s^{-1} , m is the mass of active material in mg cm^{-2} , V_1 and V_2 represent initial and final potential of potentials window in volt, respectively.

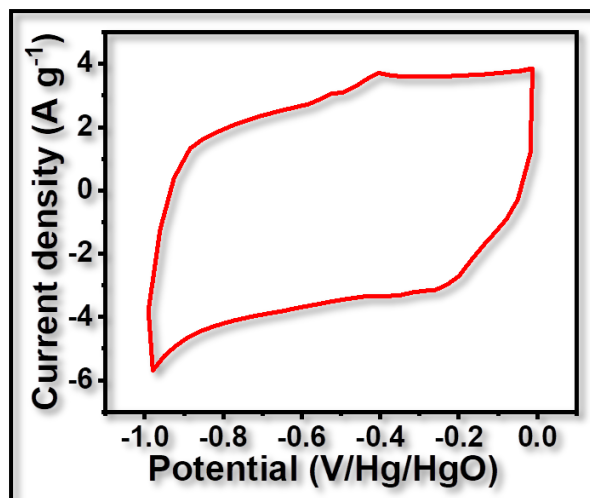


Fig. 2.14: The typical CV curve.

2.5.3 Galvanostatic charge discharge (GCD):

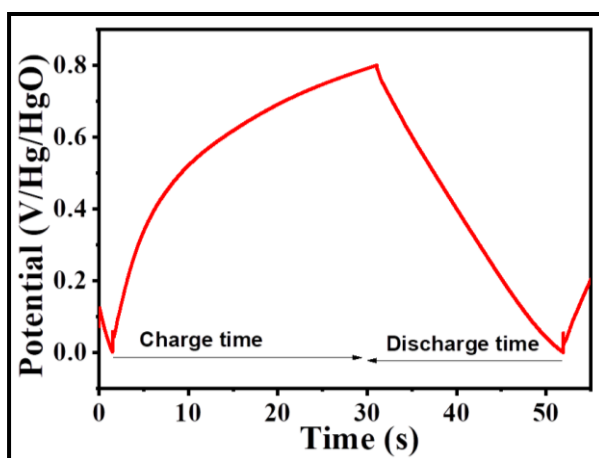


Fig. 2.15: The typical GCD curve.

This technique is extensively used to determine the electrochemical cycling stability and capacitance of electrodes/devices. The GCD principle is to compute the resulting voltage at the same time when applying a fixed current to an electrode/device between initial and final voltage [66]. This is different technique from CV, in which current is controlled and only voltage is measured. It is also known as chronopotentiometry which gives access to various parameters such as resistance, capacitance and cyclic stability [68]. Basically, GCD curve behavior is four types such as EDLC, surface redox pseudocapacitor, intercalation pseudocapacitor and battery type faradic reaction. The typical GCD curve is shown in Fig. 2.15. The C_s is determined from discharge curves using the following relation.

$$C_s = \frac{I \times dt}{m \times \Delta V} \quad (2.14)$$

Where, I is constant current density (A g⁻¹), dt is discharge time (s), m is a mass of deposited electrode (mg) and ΔV is discharge voltage (V).

The energy density (E.D.) and power density (P.D.) are calculated from the following equations,

$$E.D. = 0.5 CV^2 \quad (2.15)$$

$$P.D. = E.D. / dt \quad (2.16)$$

Where, the C, V and dt are the specific capacitance, potential window and discharge time, respectively.

2.5.4 Electrochemical impedance spectroscopy (EIS):

This is one of the powerful techniques and it is also known as the AC impedance spectroscopy technique to understand the impedance behavior of supercapacitor at the interface of electrode/electrolyte. In EIS, a tiny AC signal is utilized to the supercapacitor cell over a range of frequencies from a few mHz to KHz. The current response to the utilized AC signal is counted as an output. The response of electrochemical supercapacitive impedance is normally indicated by a Nyquist plot [69]. It is the plot of real part versus imaginary part of impedance. This technique is very crucial due to it decides the frequency dependent and independent parts of Nyquist plot separately.

Let a sinusoidal voltage signal $I(\omega) = I_o \sin(\omega t + \phi)$ be its output and $V(\omega) = V_o \sin\omega t$ will be an input signal response. Then the impedance can be written as,

$$Z(\omega) = V(\omega) / I(\omega) = V_o \sin\omega t / I_o \sin(\omega t + \phi), \text{ and} \quad (2.17)$$

$$Z(\omega) = Z_o \sin\omega t / \sin(\omega t + \phi) \quad (2.18)$$

Therefore, the impedance is expressed in terms of magnitude, phase shift φ and Z_o. Using the Eulers equation $e^{i\phi} = \cos\phi + i\sin\phi$, impedance can be expressed as a complex quantity. The sinusoidal voltage and current response signals are expressed as [70],

$$V(\omega) = V_o \exp(i\omega t) \quad (2.19)$$

$$I(\omega) = I_o \exp(i\omega t - \phi) \quad (2.20)$$

Therefore, a complex quantity is represented as,

$$Z(\omega) = Z_o \exp(i\phi) = Z_o (\cos\phi + i\sin \phi) \quad (2.21)$$

Real and imaginary parts of impedance are separated, and Nyquist plot is drawn as demonstrated in **Fig. 2.16**. The equivalent series resistance (ESR), charge transfer resistance (R_{ct}) and diffusion impedance of electrochemical devices can be investigated by Nyquist plot. The comparison between EIS and CV is an EIS a sinusoidal voltage signal, which is imposed at ranges of frequency and the resulting current is counted, while a linear voltage is utilized in a CV. Several electrochemical terms raised in impedance spectroscopy as below,

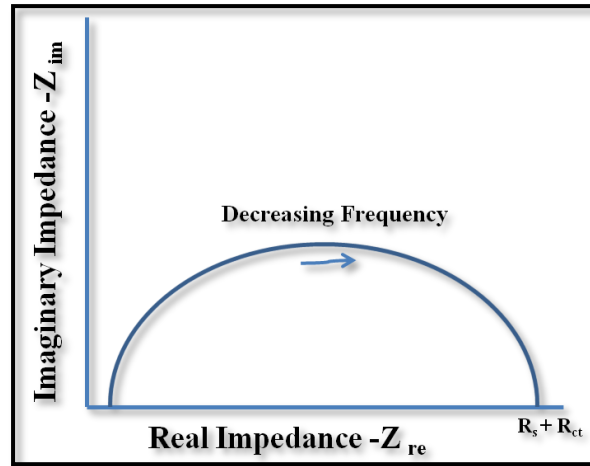


Fig. 2.16: A typical Nyquist curve [71].

(I) Electrolyte resistance:

It is often a significant part of the impedance of an electrochemical supercapacitor device. A three-electrode potentiostat device compensates for the solution resistance between the reference and counter electrodes. But, solution resistance between the working electrode and the reference electrode must be considered while modelling electrochemical supercapacitor cell. An ionic solution resistance depends on the ionic concentration, temperature type of ions, and the areal geometry in which the current is passed. Within the bounded area as (A), and length (l), carrying a consistent current, the corresponding resistance is defined as,

$$R = \rho \frac{l}{A} \quad (2.22)$$

Where, ρ is the solution resistivity and its reciprocal ρ (κ) is more commonly used. κ is called as solution conductivity and its relations with solution resistance are:

$$R = \frac{1}{\kappa} \cdot \frac{l}{A} \Rightarrow \kappa = \frac{l}{RA} \quad (2.23)$$

The electrochemical supercapacitor devices do not have the consistent current distribution throughout the definite electrolyte area. Therefore, the measurement of

solution resistance using its solution conductivity will be not accurate. It can be determined from the EIS curve [70].

(II) Double layer capacitance:

It exists between the electrode interface and its surrounded electrolyte solution. It is formed at the interface as ions from the solution adsorb at the surface of electrode. A charged electrode is alienated from the charged ions using an insulating space, which is an order of angstroms (Å). Since the charges are separated via an insulator forms a capacitor, a bare metal deep in an electrolyte solution and behavior like a capacitor [70]. One can estimate simply that there will be 20 to 60 μF of capacitance for every 1 cm^2 of electrode area though the value of the double layer capacitance based on a number of variables like electrode potential, ionic concentration, oxide layers, electrode roughness, ions type, temperature, impurity adsorption, etc.

$$X_C = 1/\omega C \quad (2.24)$$

$$X_C = 1/2\pi fC \quad (2.25)$$

Where, X_C is the capacitor impedance

(III) Charge transfer resistance:

The resistance in this example is formed through a single, kinetically controlled electrochemical reaction. In this case, we have a single reaction at equilibrium. Consider the following reversible reaction



This charge transfer reaction has a certain speed which is based on the reaction temperature, kind of reaction, reaction potential and concentration of reaction products.

(IV) Diffusion resistance:

It depends on the frequency of the potential perturbation. The creating impedance is known to be Warburg impedance. At superior frequencies, the Warburg impedance is tiny in magnitude since diffusing electrolyte ions in solution don't have to move so far. At minor frequencies, the ions diffuse further, which raises the Warburg impedance [71].

2.6 References:

- 1 A. Burke, *J. Power Sources*, 91, (2000), 37-50.
- 2 H. J. Choi, J. H. Kim, H. K. Kim, S. H. Lee, Y. H. Lee, *Electrochim. Acta.*, 208, (2016), 202-210.
- 3 X. Du, L. Wang, W. Zhao, Y. Wang, T. Qi, C.M. Li, *J. Power Sources*, 323, (2016), 166-173.
- 4 M. Winter and R. J. Brodd, *Chem Rev.*, 104, (2004), 4245-4270.
- 5 R. A. Rightmire, *Electrical energy storage apparatus*. U. S., Patent 3288641, (1966).
- 6 H. I. Becker, *Low voltage electrolytic capacitors*. U. S., Patent 2800616, (1957).
- 7 K. L. Chopra, I. J. Kaur, 'Thin film Device Application', Plenum Press, New York (1983).
- 8 J. George, 'Preparation of Thin Films', Marcel Dekker, Inc. New York, (1992).
- 9 M. C. Vasudev, K. D. Anderson, T. J. Bunning, V. V. Tsukruk, R. R. Naik, *ACS Appl. Mater. Interfaces*, 5, (2020), 3983-3993.
- 10 P. M. Martin, 'Handbook of deposition technologies for films and coatings: science, applications and technology', William Andrew, (2009).
- 11 S. D. Allen, *J. Appl. Phys.*, 52, (1981), 6501-6507.
- 12 <https://www.sciencedirect.com/topics/chemistry/metal-organic-chemical-vapor-deposition>.
- 13 S. Müller, W. DeBoer, M. Schneider, A. Sabellek, M. Schmanau, Christoph Rühle, T. Schneider, R. Hall-Wilton, *Phys. Status Solidi A*, 206, (2009), 2091-2097.
- 14 S. S. D. Mishra, K. K. Saini, C. Kant, M. Pal, *Mater. Chem. Phys.*, 146, (2014), 324-329.
- 15 R. N. Bulakhe, N. M. Shinde, R. D. Thorat, S. S. Nikam, C. D. Lokhande, *Curr. Appl. Phys.*, 13, (2013), 1661-1667.
- 16 E. G. uneri, F. G. ode, S. C. evi, *Thin Solid Film*, 589, (2015), 578-583.
- 17 Z-G. Gu, W-Q. Fu, X. Wu, J. Zhang, *Chem. Commun.*, 52, (2016,) 772-775.
- 18 T. D. Dongale, S. V. Mohite, A. A. Bagade, P. K. Gaikwad, P. S. Patil, R. K. Kamat, K. Y. Rajpure, *Electron. Mater. Lett.*, 11, (2015), 944-948.
- 19 M. Abdel Rafea, A. Farag, N. Roushdy, *J. Alloys Compd.*, 485, (2009), 660-666.
- 20 M. Thirumoorthi and J. Thomas Joseph Prakash, *J. Asian Ceram. Soc.*, 4, (2016), 39-45.
- 21 H. Jeong and Y. Yoo, *Surf. Coat. Techno.*, 284, (2015), 26-30.
- 22 R. S. Mane and C. D. Lokhande, *Mater. Chem. Phys.*, 65, (2000) 1-31.
- 23 S. M. Pawar, B. S. Pawar, J. H. Kim, O. S. Joo, C. D. Lokhande, *Curr. Appl. Phys.*, 11, (2011), 117-161.
- 24 A. B. Lundin and G. A. Kitaev, *Inorg. Mater.*, 1, (1965), 2107-2111.
- 25 M. Ristov, G. J. Sinadinovski, I. Grozdanov M. Mitreski, *Thin Solid Films*, 149, (1987), 65-71.
- 26 Y. F. Nicolau and J. C. Menard, *J. Cryst. Growth*, 92, (1988), 128-142.

- 27 G. Hodes, 'Chemical Solution Deposition of Semiconductor Films', Marcel Dekker Inc., New York. (2001).
- 28 H. M. Pathan and C. D. Lokhande, Bull. Mater. Sci., 27, (2004), 85-111.
- 29 V. Petkov, Mater. Today, 11, (2008), 28-38.
- 30 http://chemwiki.ucdavis.edu/Analytical_Chemistry/Instrumental_Analysis/Diffraction/Powder_X-ray_Diffraction.
- 31 B. D. Cullity, 'Elements of X-rays Diffraction', Second ed., Addison-Wesley, London (1978).
- 32 <https://wiki.utep.edu/pages/viewpage.action?pageId=51217144>.
- 33 <https://www.rigaku.com/products/xrd/miniflex>.
- 34 <https://opentextbc.ca/universityphysicsv3openstax/chapter/the-michelson-interferometer/>
- 35 https://www.researchgate.net/publication/237268629-A-reliable-compact-and-low-cost-Michelson-wavemeter-for-laser-wavelength_measurement/figures?lo=1.
- 36 <https://www.semrock.com/filter-types-for-raman-spectroscopy-applications.aspx>.
- 37 <https://www.intechopen.com/chapters/10504>.
- 38 https://en.wikipedia.org/wiki/Raman_spectroscopy.
- 39 https://en.wikipedia.org/wiki/Raman_spectroscopy#/media/File:Raman_energy_levels.svg.
- 40 https://www.vcbio.science.ru.nl/public/pdf/feSEM_info_eng.pdf.
- 41 <http://mceff.mtu.edu/acmal/electronmicroscopy/FE-Form-Function.htm>.
- 42 <http://areeweb.polito.it/ricerca/carbongroup/fac-feSEM.html>.
- 43 <http://www.njit.edu/njcep/facilities/fieldemission.php>.
- 44 D. B. Williams and C. B Carter, 'Transmission electron microscopy' plenum press, New York, (1996).
- 45 <https://warwick.ac.uk/fac/sci/physics/current/postgraduate/regs/mpagswarwick/ex5/techniques/structural/tem/>.
- 46 <https://www.indiamart.com/proddetail/copper-tem-grid-21151312230.html>.
- 47 https://www.tedpella.com/grids_html/gridbox.htm.
- 48 M. Abdul Qadeer, S. Saif Ali, H. Fei, Hamid, Roshan, Earth Sci Rev., 181, (2018), 1-11.
- 49 J. Rao, S. S. Anjum, M. Craig J. R. Nicholls, J. Coat. Technol. Res., 15, (2018), 87-94.
- 50 T. T. Chau, W. J. Bruckard, P. T. L. Koh, A. V. Nguyen, Adv. Colloid Interface Sci., 150, (2009), 106-115.
- 51 <http://www.ramehart.com/200.htm>.
- 52 <https://en.wikipedia.org/wiki/Dewetting>.
- 53 T. Brousse, D. Bélanger, J. W. Long, J. Electrochem. Soc., 162, (2015), 5185-5189.
- 54 K. Naoi, S. Ishimoto, J. I. Miyamoto, W. Naoi, Energy Environ. Sci., 5, (2012), 9363-9073.
- 55 W. N. Katsuhiko Naoi, S. Aoyagi, J.-I. Miyamoto, T. Kamino, Acc. Chem. Res., 46, (2013), 1075-1083.

- 56 M. R. Lukatskaya, B. Dunn, Y. Gogotsi, *Nat. Commun.*, 7, (2016), 12647-12660.
- 57 L. Shi, C. Pang, S. Chen, M. Wang, K. Wang, Z. Tan, P. Gao, J. Ren, Y. Huang, H. Peng, Z. Liu, *Nano Lett.*, 17, (2017), 3681-3687.
- 58 Y. Jin, S. Li, A. Kushima, X. Zheng, Y. Sun, J. Xie, J. Sun, W. Xue, G. Zhou, J. Wu, F. Shi, R. Zhang, Z. Zhu, K. So, Y. Cui, J. Li, *Energy Environ. Sci.*, 10, (2017), 580-592
- 59 J. Wang, Y. Cui, D. Wang, *Adv. Mater.*, 31, (2019), 1801993-1802017.
- 60 Y. Liu, N. Zhang, C. Yu, L. Jiao, J. Chen, *Nano Lett.*, 16, (2016), 3321-3328.
- 61 Q. Xu, J. K. Sun, G. Li, J. Y. Li, Y. X. Yin, Y. G. Guo, *Chem. Commun.*, 53, (2017), 12080-12083.
- 62 X. Wang, Y. Liu, Y. Wang, L. Jiao, *Small*, 12, (2016), 4865-4873.
- 63 D. P. Dubal, N. R. Chodankar, A. Vinu, D. H. Kim, P. Gomez-Romero, *ChemSusChem* 10, (2017), 2742-2750.
- 64 D. P. Dubal, N. R. Chodankar, G. S. Gund, R. Holze, C. D. Lokhande, P. Gomez-Romero, *Energy Technol.*, 3, (2015), 168-176.
- 65 D. P. Dubal, R. Holze, P. Gomez-Romero, *Sci. Rep.*, 4, (2015), 7349-7358.
- 66 B. E. Conway, 'Electrochemical Supercapacitors: scientific fundamentals and technological applications', Springer, (1999).
- 67 P. L. Taberna and P. Simon, Weinheim, (2013), 111-130.
- 68 A. Yu, V. Chabot, J. Zhang, CRC Press Taylor & Francis Group Inc., Boca Raton, (2013), 287-288.
- 69 M. E. Orazem and B. Tribollet, New Jersey, (2008), 333-362.
- 70 <http://www.gamry.com/application-notes/EIS/basics-of-electrochemicalimpedance-spectroscopy>.
- 71 <http://www.ecochemie.nl/download/Applicationnotes/Autolab-Application-Note-EIS06.pdf>.

Chapter-III

*Chemically synthesized ytterbium sulfide
thin films: characterization and
supercapacitive performance*

Chapter-III

Chemically synthesized ytterbium sulfide thin films: characterization and supercapacitive performance

Sr. no.	Title	Page no.
3.	Introduction	53
3A.	Section -A Chemically synthesized ytterbium sulfide thin films: characterization and supercapacitive behaviour (CBD method)	53
3A.1	Introduction	53
3A.2	Experimental details	54
	<i>3A.2.1 Substrate cleaning</i>	54
	<i>3A.2.2 Precursors</i>	54
	<i>3A.2.3 Synthesis of ytterbium sulfide thin films</i>	54
	<i>3A.2.4 Characterization</i>	54
3A.3	Results and discussion	55
	3A.3.1 Thin film formation and reaction mechanism	55
	3A.3.2 Structural studies	56
	<i>3A.3.2.1 X-ray diffraction (XRD)</i>	56
	<i>3A.3.2.2 X-ray photoelectron spectroscopy (XPS)</i>	57
	<i>3A.3.2.3 Fourier transform Raman spectroscopy (FT-Raman)</i>	58
	3A.3.3 Morphological study	58
	<i>3A.3.3.1 Contact angle measurement</i>	58
	<i>3A.3.3.2 Scanning electron microscopy (SEM)</i>	59
	<i>3A.3.3.3 Transmission electron microscopy (TEM)</i>	60
	3A.3.4 Supercapacitive study	61
	<i>3A.3.4.1 Cyclic voltammetry (CV)</i>	61
	<i>3A.3.4.2 Galvanostatic charge discharge (GCD)</i>	62
	<i>3A.3.4.3 Stability</i>	62
	<i>3A.3.4.4 Electrochemical impedance spectroscopy (EIS)</i>	63
3B.	Section- B Chemically synthesized ytterbium sulfide thin films: characterization and supercapacitive performance (SILAR method)	63
3B.1	Introduction	63
3B.2	Experimental details	64
	<i>3B.2.1 Substrate cleaning</i>	64
	<i>3B.2.2 Precursors</i>	64
	<i>3B.2.3 Deposition of Yb₂S₃ thin films</i>	64
	<i>3B.2.4 Characterization</i>	65
3B.3	Results and discussion	65

	3B.3.1	Thin film formation and reaction mechanism		65
	3B.3.2	Structural studies		65
		<i>3B.3.2.1</i>	<i>XRD</i>	65
		<i>3B.3.2.2</i>	<i>XPS</i>	66
	3B.3.3	Morphological study		67
		<i>3B.3.3.1</i>	<i>Contact angle measurement</i>	67
		<i>3B.3.3.2</i>	<i>Field emission scanning electron microscopy (FE-SEM)</i>	67
	3B.3.4	Supercapacitive study		68
		<i>3B.3.4.1</i>	<i>CV</i>	68
		<i>3B.3.4.2</i>	<i>GCD</i>	69
		<i>3B.3.4.3</i>	<i>Stability</i>	70
		<i>3B.3.4.4</i>	<i>EIS</i>	70
3C	Conclusions			71
3D	References			73

3. Introduction:

The section-A deals about the synthesis of ytterbium sulfide (Yb_2S_3) thin films by chemical bath deposition (CBD) method. In addition, the structural and morphological characterizations with electrochemical measurement of Yb_2S_3 thin films are studied. This section includes the introduction, preparation of Yb_2S_3 thin films via CBD method, film formation and reaction mechanism. The structural, morphological and wttability characterizations like as XRD, FT-Raman, SEM and contact angle of Yb_2S_3 thin films are investigated. The electrochemical properties of Yb_2S_3 thin film are investigated using CV, GCD and EIS measurements in 1M KOH electrolyte solution.

Section -A

3A. Chemically synthesized ytterbium sulfide thin films: characterization and supercapacitive behaviour (CBD method)

3A.1 Introduction:

In the improvement of supercapacitor performance nanostructured surface morphologies play an important role and such morphologies can be easily synthesized by low cost and scalable CBD method [1]. As compared to other deposition routes, CBD method is an attractive route to synthesize thin film due to it's advantages like, cost-effective equipment, low temperature process, easy to handling of preparative parameters etc. The CBD method does not require binder for deposition of nanomaterials on different kinds of substrates (conducting and non-conducting), which is useful for industrial application as it avoids corrosion and oxidation of substrate [2-4].

In recent past, rare earth metal (REM) sulfides have been studied as novel supercapacitive materials as their electrical conductivity is more than metal oxides, and large operating potential window is comparable with other oxide and hydroxide materials. Scanty reports are available in the literature for REM sulfide thin films in supercapacitive application. Amongst the REM sulfides, samarium sulfide (Sm_2S_3) and lanthanum sulfide (La_2S_3) thin films were as synthesized by SILAR and CBD methods [5-8]. The La_2S_3 films were deposited by hydrothermal method [9] and yttrium sulfide thin films were prepared using electrodeposition method [10]. All these films were tested for their supercapacitive performance.

In this section, Yb_2S_3 thin films on stainless steel (SS) substrates are synthesized by CBD method. The Yb_2S_3 thin films are characterized using physico-chemical

techniques. The electrochemical supercapacitive behavior of Yb_2S_3 thin films is studied using CV, EIS and GCD techniques in 1 M KOH aqueous electrolyte.

3A.2 Experimental details:

3A.2.1 Substrate cleaning:

For the thin film preparation, the well polished and cleaned substrate is the main requirement. The substrate with a surface added impurity gives unbridled growth of thin film, results in to the development of non-uniform thin film. Also, the electrical conductivity of substrate is a basic need in supercapacitor application; hence the simply available, high conducting and inexpensive SS substrate is used to supercapacitor application. The cleaning process for SS substrate was adopted as below;

- i) The SS substrate was mirror polished using the 1200 grade polish paper,
- ii) using detergent and double distilled water (DDW), SS substrates were washed,
- iii) the SS substrate was cleaned ultrasonically for 20 min, and
- iv) finally, SS substrate was air dried in AR grade acetone and then utilized for synthesis of thin film.

3A.2.2 Precursors:

The ytterbium (III) chloride ($\text{YbCl}_3 \cdot 7\text{H}_2\text{O}$), citric acid ($\text{C}_6\text{H}_8\text{O}_7$) and sodium thiosulphate ($\text{Na}_2\text{S}_2\text{O}_3$) were used without further purification. DDW was used as a solvent in the experiment. All solutions were freshly prepared and used for the synthesis of Yb_2S_3 thin film. Potassium hydroxide (KOH) solution was used as an electrolyte for testing of electrochemical supercapacitive properties.

3A.2.3 Synthesis of ytterbium sulfide thin films:

The Yb_2S_3 thin film was deposited on the SS substrate by CBD method. The 0.1 M ytterbium trichloride and 0.15 M sodium thiosulphate solutions prepared in separate beakers and mixed together in equal volume in 100 ml beaker and vigorously stirred for 10 min and then few drops of citric acid (0.5 M) were added slowly to maintain the pH of bath 2 ± 0.1 . Then, polished SS substrate was vertically dipped in beaker and the bath was kept at 80°C for 180 min.. After 180 min., yellow-whitish colored Yb_2S_3 film was obtained on SS substrate. The film was air dried at room temperature (27°C) and used for further characterization studies.

3A.2.4 Characterization:

The structural characterization of Yb_2S_3 thin film was carried out using X-ray diffractometer (Rikagu 600 mini flex benchtop machine). The contact angle measured

was using Rame-Hart instrument (USA). The Raman study of Yb_2S_3 thin film was recorded with Raman spectrometer (Bruker Multi RAM) in the spectral wavelength range of $100\text{--}600\text{ cm}^{-1}$. The chemical states of elements in Yb_2S_3 were confirmed using X-ray photoelectron spectrometer (ThermoVG Scientific, United Kingdom). The morphological characterization of Yb_2S_3 thin films were recorded using scanning electron microscope (SEM, JEOL-6360, Japan) and transmission electron microscope (TEM, Philips CM-30 unit, Point Resolution = 2.4 \AA) with an acceleration voltage of 300 kV.

The electrochemical supercapacitive properties of Yb_2S_3 thin film were tested in three electrode system using Yb_2S_3 thin film as a working electrode, platinum wire as a counter electrode and mercury/mercury oxide (Hg/HgO) as a reference electrode in 1 M KOH electrolyte. The CV, GCD and EIS studies were carried out with battery cyclers (Zive MP1 workstation, S. Korea).

3A.3 Results and discussion:

3A.3.1 Thin film formation and reaction mechanism:

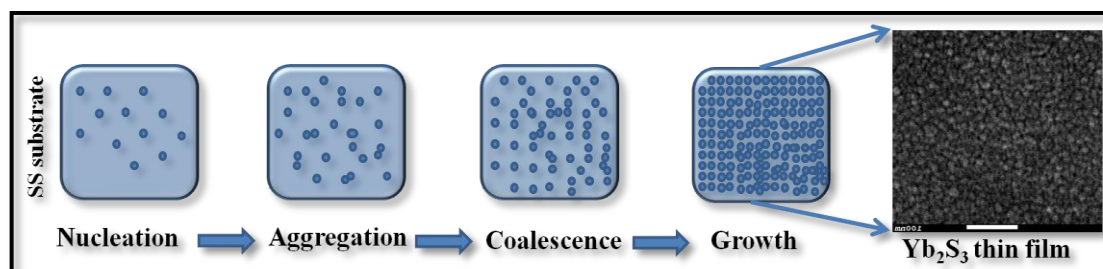


Fig. 3.1: The schematic representation of steps involved the preparation of Yb_2S_3 thin film by CBD method.

The Yb_2S_3 nanomaterials can be prepared by chemical reactions in which nucleation, aggregation, coalescence and growth process of constituent materials takes place [4, 11]. In CBD method, there are two taxonomy of growth mechanisms during thin film formation process: (i) ion-by-ion growth, where the ions are deposited sequentially at the nucleation sites on the surface of substrate, and (ii) adsorption of colloidal particles to form nuclei and further these particles grow by aggregation and coalescence to form thin film, which is pertained as cluster-by-cluster growth mechanism [12, 13]. The Yb_2S_3 thin films obtained from an aqueous citric acid complexed Yb^{3+} ion from YbCl_3 and sulfide ions, from sodium thiosulfate ($\text{Na}_2\text{S}_2\text{O}_3$). Finally, Yb^{3+} and S^{2-} ions combine by an ion-by-ion process to form thin film on the SS substrate [14]. The schematic representation for preparation of Yb_2S_3 thin film is shown

in **Fig. 3.1**. When the ionic product of Yb^{3+} and S^{2-} exceeds the solubility product of Yb_2S_3 then Yb_2S_3 film is formed on the substrate. The possible reaction in the reaction bath is as follows;

The Yb^{3+} ions are complexed with $\text{C}_6\text{H}_8\text{O}_7$ to form complexed ytterbium ions presented as,



$\text{Na}_2\text{S}_2\text{O}_3$ solution dissociates by virtue half-cell reaction as below [15]



The dissociation of $\text{Na}_2\text{S}_2\text{O}_3$ in acidic bath medium is as follows [16]



Electron generated in reaction (3.2) reacts with sulfur atom formed in the reaction (3.4) to gives S^{2-} ions.



The formed sulfide ions (S^{2-}) react with Yb^{3+} ions in the solution to form Yb_2S_3 molecule as.



At the initial stage of reaction, ytterbium sulfide nuclei are developed on the SS substrate as well as in the solution. Furthermore, these nucleation centers act as basic building blocks to develop nano-grains thin film. As the ionic product (I.P.) exceeds the solubility product (S.P.), large numbers of ions are collected around the nucleation centers to form clusters. Subsequently, the coalescence and growth of these clusters lead to thin film formation [17-19]. The optimized preparative parameters for deposition of Yb_2S_3 film are given in **table 3.1**.

Table 3.1: The optimized preparative parameters for deposition of Yb_2S_3 film.

Precursor solutions	YbCl_3 (0.1 M), $\text{Na}_2\text{S}_2\text{O}_3$ (0.15 M) (1:1)
pH	2 ± 0.1
Complexing agent	Citric acid ($\text{C}_6\text{H}_8\text{O}_7$)
Deposition time (min)	180
Deposition temperature (degree celsius)	80

3A.3.2 Structural studies:

3A.3.2.1 X-ray diffraction (XRD):

The XRD pattern of Yb_2S_3 thin film is shown in **Fig. 3.2**. The peaks at 2θ values matched with (202), (401), and (115) planes for monoclinic crystal structure of Yb_2S_3

(JCPDS Card no. 65-2373). The peak in XRD pattern shown by the hash (#) corresponds to SS substrate. The crystalline size of particles in Yb_2S_3 thin film is found to be 8.15 nm for (401) plane. Pujari et al [16] prepared Yb_2S_3 thin film on glass as well as SS substrates and observed orientations along (401), (310), (103), (-210), (202), (-113), (-313) and (313) planes of monoclinic crystal structure. The crystallite size D' 8.15 nm was calculated using relation 2.7.

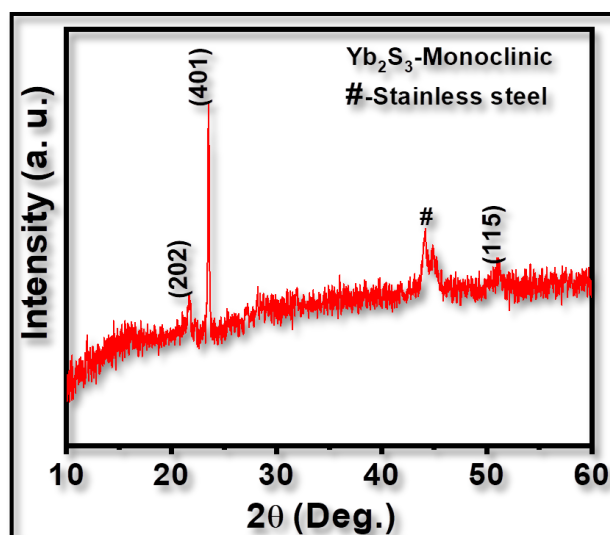


Fig. 3.2: The X-ray diffraction pattern of Yb_2S_3 thin film.

3A.3.2.2 X-ray photoelectron spectroscopy (XPS):

The XPS is a basic type of technique to know about an elemental presence and their chemical states at the surface of thin film material. Therefore, chemical states of the elements present in Yb_2S_3 were studied by XPS analysis. Fig. 3.3(A) illustrates the survey spectrum of Yb_2S_3 film material, which demonstrates no other elemental peaks different from the peaks of Yb, S, C, and O, confirming that the sample is pure. Fig. 3.3(B-C) shows the XPS spectra of Yb_2S_3 thin film which indicate the characteristics peaks of Yb4d and S2p with their binding energies. The deconvoluted peaks at binding energies of 185.6, 189.1, 192.5, 195.73, and 199.36 eV in Fig. 3.3(B) denoted as a, b, c, d, and e, respectively, are attributed to +3 oxidation state of Yb and these binding energies are in good agreements with the previous report [20]. The state of S2p present in Yb_2S_3 film is shown in Fig. 3.3(C). The binding energy peak at 164.12 eV corresponds to sulfur in Yb_2S_3 implying two states of sulfur. The S2p spectrum peaks located at 164.12 and 165.10 eVs correspond to the $\text{S}2p_{3/2}$ and $\text{S}2p_{1/2}$ orbitals of the divalent sulfide ions (S^{2-}), respectively [6, 21]. These results confirm the formation of Yb_2S_3 material.

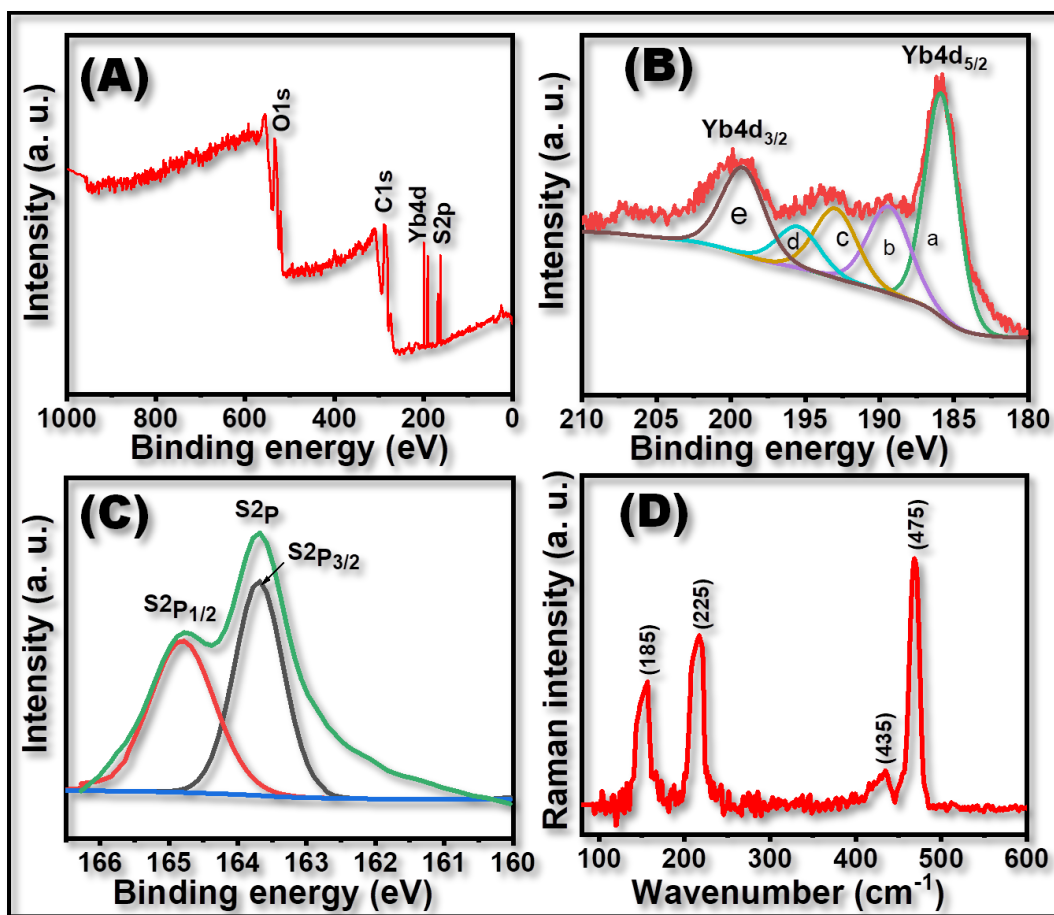


Fig. 3.3: (A) The XPS survey spectrum of Yb₂S₃ thin film, (B) XPS spectrum of Yb4d region and (C) XPS spectrum of S2p region, and (D) FT- Raman spectrum for Yb₂S₃ thin film.

3A.3.2.3 Fourier transform Raman spectroscopy (FT-Raman):

FT-Raman scattering was recorded to investigate the crystal quality and vibration properties of Yb₂S₃ thin film. **Fig. 3.3(D)** displays the FT-Raman spectrum for Yb₂S₃ film examined in the wavenumber range of 50–600 cm⁻¹. The bands at 185, 225, 435 and 475 cm⁻¹ confirm the formation of Yb₂S₃ thin film [8, 22]. Furthermore, weak bands in wavenumber range of between 150-250 cm⁻¹ may be the stretching vibration mode of ytterbium sesquisulfides, as reported by Knight and White [23]. Thus, the FT-Raman spectrum further confirms the formation of Yb₂S₃, consistent with the XRD result.

3A.3.3 Morphological study:

3A.3.3.1 Contact angle measurement:

Wettability is the important surface property for application in supercapacitor. Wetting of thin film surface depends on chemical content and surface morphology.

Contact angle is nothing but the wettability of a solid surface. If the wettability is more, less is the contact angle ($\theta < 90^\circ$) and surface is hydrophilic. If wettability is low, higher is the contact angle ($\theta > 90^\circ$) and surface is hydrophobic. Contact angle study was carried out using a water droplet on the surface of Yb_2S_3 thin film. **Fig. 3.4(A)** shows the contact angle image on Yb_2S_3 thin film. The Yb_2S_3 thin film displays 61.2° angle confirming its hydrophilic nature. Such hydrophilic nature (61.2°) is helpful for making interfacial contact between surface of Yb_2S_3 thin film and electrolyte. Kumbhar et al [6] synthesized of Sm_2S_3 thin films using CBD method and reported contact angle of 21° . Ghogare et al [9] deposited LaS_2 thin film by hydrothermal method with contact angle of 46.9° . Such diverse values of contact angles are obtained due to the different surface nature of thin films.

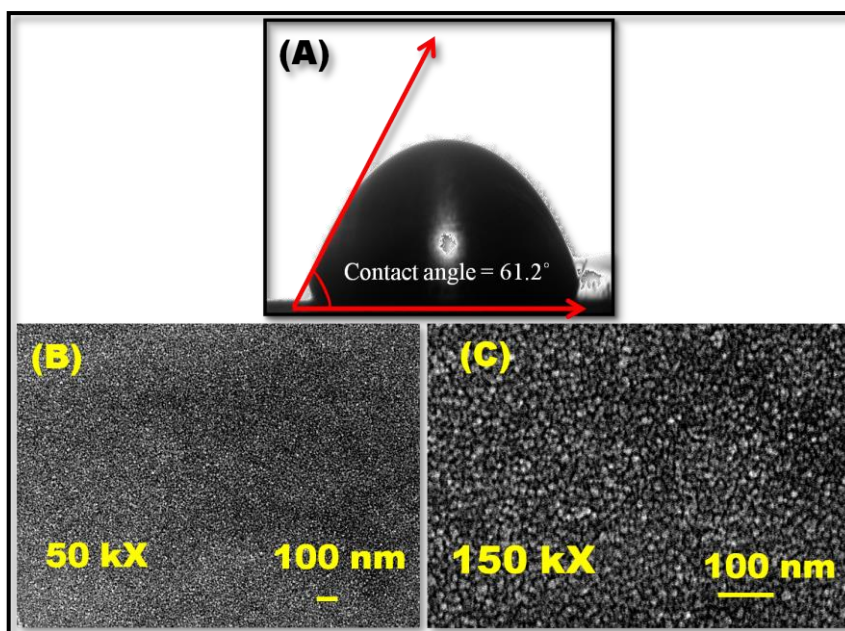


Fig. 3.4: (A) Contact angle and SEM images of Yb_2S_3 thin films at (B) 50 kX and (C) 150 kX magnifications.

3A.3.3.2 Scanning electron microscopy (SEM):

The SEM is an important technique to find surface morphology of thin film electrode material. In thin film, surface morphology plays a crucial role to lead to high specific capacitance (C_s) value. **Fig. 3.4(B-C)** shows surface morphologies of Yb_2S_3 thin film at magnifications of 50 kX and 150 kX. The nano-grains like crystallites of Yb_2S_3 material are uniformly spread over the substrate (50 kX). These crystallites are interconnected with each other, as seen at high magnification (150 kX) (**Fig. 3.4C**). These nano-grains are connected to each other to form clusters. Interconnected nano-

grains effectively increase the surface area and large accessibility of the material. The high surface area facilitates large number of active sites for charge storage in supercapacitor [24]. Pujari et al [16] observed nanoparticles and non-uniformly distributed nanorods-like morphology for Yb_2S_3 thin film prepared by hydrothermal method. Kumbhar et al [5] synthesized Sm_2S_3 thin film by SILAR method and displayed honeycomb-like morphology. Patil and Lokhande [8] deposited La_2S_3 thin film by CBD method and obtained porous ridges type surface morphology. Such different types of morphologies were obtained due to different preparative parameters and methods.

3A.3.3.3 Transmission electron microscopy (TEM):

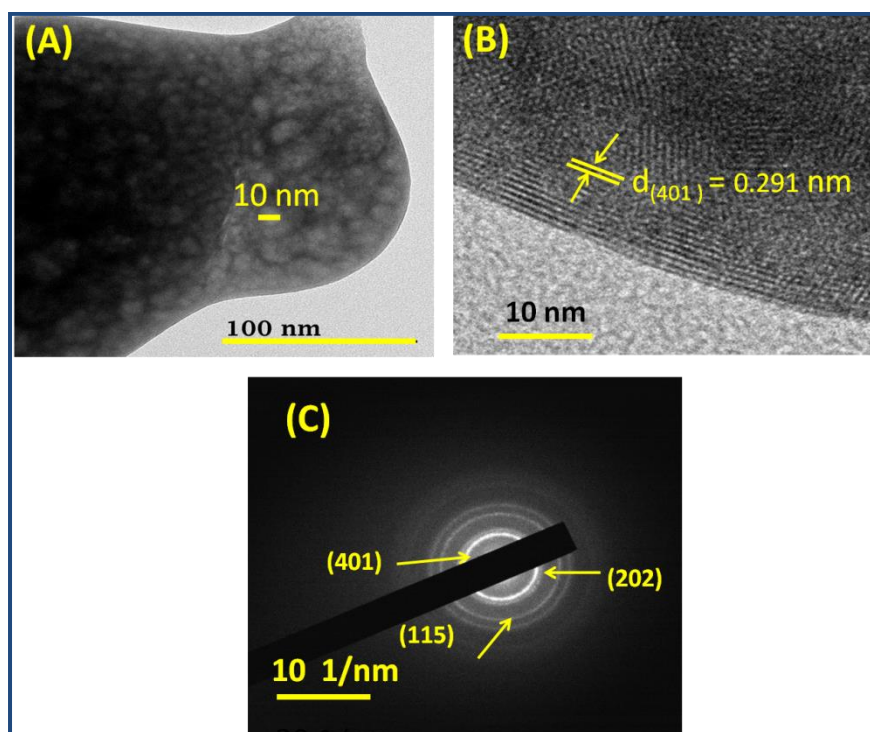


Fig. 3.5: (A-B) HR-TEM images and (C) selected area electron diffraction (SAED) pattern of Yb_2S_3 sample.

The crystal structure and crystallite size of Yb_2S_3 electrode were determined using TEM images. The high-resolution transmission electron microscopy (HR-TEM) images of Yb_2S_3 sample are illustrated in **Fig. 3.5(A-B)**. The HR-TEM images clearly show the formation of interconnected crystallites in the range of 10 nm which is in good agreement with the results from the SEM images shown in **Fig. 3.4(B-C)**. Such nanocrystallites provide easy access to the electrolyte ions for improved supercapacitor performance. The HR-TEM image analysis shows interplanar spacing (d) of 0.291 nm corresponding to (401) plane of Yb_2S_3 as shown in **Fig. 3.5(B)**. The interplanar spacing

0.291 nm is in well agreement with crystallographic interatomic distance of Yb_2S_3 electrode material calculated from the XRD analysis. The corresponding selected area electron diffraction (SAED) pattern of Yb_2S_3 electrode in **Fig. 3.5(C)** shows diffuse rings indicating the formation of nanocrystallites. Other interplanar distances (d) of 3.15, 2.91, and 2.53 nm measured from HR-TEM image of lattice fringes in the **Fig. 3.5(C)**, correspond to (202), (401), and (115) planes of Yb_2S_3 , confirming XRD results.

3A.3.4 Supercapacitive study:

3A.3.4.1 Cyclic voltammetry (CV):

Fig. 3.6(A) shows the CV curves of Yb_2S_3 electrode at various scan rates. The CV curves are plotted between 5 to 200 mV s^{-1} scan rates in 1 M KOH electrolyte within -1.2 to -0.2 V/ Hg/HgO. The values of C_s are calculated from CV curves using relation 2.13.

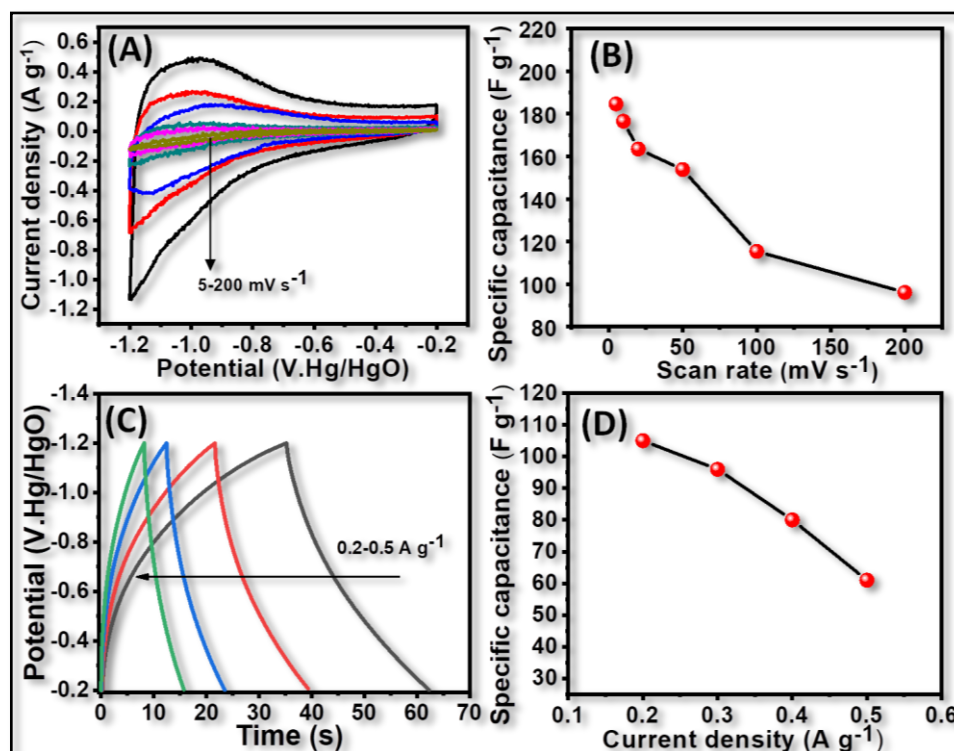


Fig.3.6: (A) The CV curves at scan rates from 5-200 mV s^{-1} , (B) plot of specific capacitance versus scan rates, (C) galvanostatic charge-discharge curves of Yb_2S_3 film at 0.2-0.5 A g^{-1} current densities, and (D) plot of specific capacitance versus current density.

From **Fig. 3.6(A)**, it is found that the increase in scan rate results in to high area under the curve. The value of C_s decreases with increasing scan rate due to a smaller amount of utilization of electrode material in to the faradic reaction in the electrolyte. The electrode operated at high scan rate results in to collision and fast movement of

ions towards surface of the electrode. The charge storage capacity is decreased due to the less participation of ions in the reaction [6]. **Fig. 3.6(B)** shows the variation of specific capacitance with scan rate. The Yb_2S_3 electrode exhibits highest specific capacitance of 184.6 F g^{-1} at 5 mV s^{-1} scan rate.

3A.3.4.2 Galvanostatic charge discharge (GCD):

The GCD curves of Yb_2S_3 electrode at different current densities (0.2 to 0.5 A g^{-1}) in 1 M KOH electrolyte are shown in **Fig. 3.6(C)**. The non-linear nature of GCD curves exhibits pseudocapacitive behavior of Yb_2S_3 electrode. The charge-discharge mechanism for Yb_2S_3 thin film is proposed as [6].



The C_s is determined from discharge curves from the relation 2.14. The plot of specific capacitance versus current density is shown in **Fig. 3.6(D)**. The Yb_2S_3 electrode exhibits C_s of 105 F g^{-1} at current density 0.2 A g^{-1} and 61 F g^{-1} at 0.5 A g^{-1} .

3A.3.4.3 Stability:

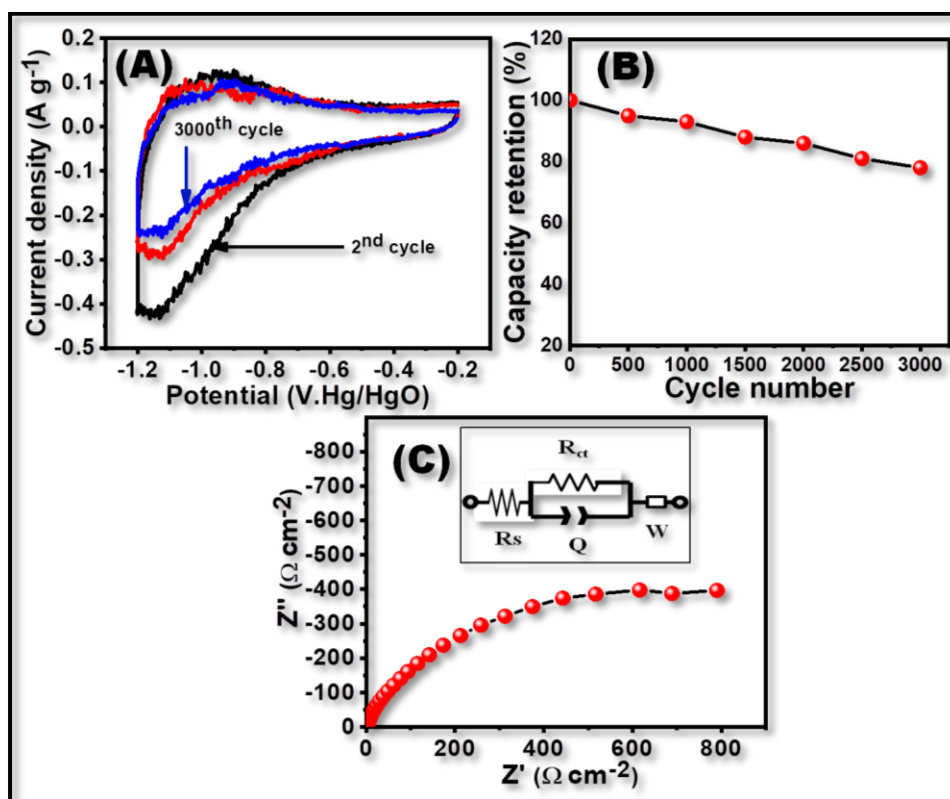


Fig. 3.7: (A) The cyclic stability of Yb_2S_3 film electrode at scan rate of 50 mV s^{-1} in 1 M KOH electrolyte, (B) the plot of capacity retention with cyclic number and (C) Nyquist plot of Yb_2S_3 film [Inset shows the equivalent circuit].

In supercapacitor application, an electrochemical stability of electrode is important aspect for practical applicability. **Fig. 3.7(A)** shows the CV curves recorded

upto 3000 cycles within the potential window of -1.2 to - 0.2 V.Hg/HgO at 50 mV s⁻¹ scan rate. It is seen that the area under the curves of CV cycles decreases with increase in the number of cycles. Similarly, corresponding specific capacitance decreases from 154.3 to 125 F g⁻¹ after 3000 cycles. The decrease in the specific capacitance is due to the degradation of active material as well as irreversibility of electrode material during charging and discharging process of CV cycles [25-27]. The plot of capacity retention with cycle number is shown in **Fig. 3.7(B)**. The Yb₂S₃ electrode displays good electrochemical capacity retention of 81 % after 3000 CV cycles. Similar types of electrochemical retentions between 78 to 85 % are reported for other REM chalcogenide electrodes in aqueous electrolyte [6, 7, 16, 27].

3A.3.4.4 Electrochemical impedance spectroscopy (EIS):

Using EIS, charge transfer at the interface between Yb₂S₃ electrode and KOH electrolyte is investigated [28]. Nyquist plot (Z real versus Z imaginary) of Yb₂S₃ thin film in the frequency range of 0.1 to 1000 Hz at 10 mV AC amplitude is shown in **Fig. 3.7(C)** and inset shows corresponding equivalent circuit. The solution resistance (R_s) of 3.42 Ω cm⁻² is observed from initial part of impedance plot in high frequency and charge transfer resistance (R_{ct}) of 8.96 Ω cm⁻² and Warburg resistance (W) of 0.03 Ω cm⁻² are obtained in the low frequency region from impedance plot. The electrochemical impedance parameters of Yb₂S₃ thin film are given in **table 3.2**.

Table 3.2: The electrochemical impedance parameters of Yb₂S₃ thin film.

Parameter	Value of parameter
R _s (Ω cm ⁻²)	0.37
Q (mF)	0.85
R _{ct} (Ω cm ⁻²)	8.96
W (Ω cm ⁻²)	0.03

Section: B

3B: Chemically synthesized ytterbium sulfide thin films: characterization and supercapacitive performance (SILAR method)

3B.1 Introduction:

The present section deals with the synthesis of Yb₂S₃ thin films via SILAR route and their structural, wettability and surface textural characterization using X-ray photoelectron spectroscopy (XPS), X-ray diffraction (XRD), contact angle and field emission scanning electron microscope (FE-SEM) techniques. The supercapacitive properties of Yb₂S₃ thin film are investigated in 1M Na₂SO₄ electrolyte.

3B.2 Experimental details:

3B.2.1 Substrate cleaning:

The substrate cleaning procedure is described in section 3A.2.1.

3B.2.2 Precursors:

The AR grade ytterbium (III) chloride ($\text{YbCl}_3 \cdot 6\text{H}_2\text{O}$) $\geq 99\%$ and sodium sulfide (Na_2S) were purchased from Thomas Baker and Sigma Aldrich, and used without purification. Sodium sulfate (Na_2SO_4) electrolyte was used to the testing of supercapacitive performance of Yb_2S_3 thin film electrode.

3B.2.3 Deposition of Yb_2S_3 thin film:

The Yb_2S_3 film was prepared by SILAR method using aqueous 0.10 M YbCl_3 and 0.15 M Na_2S solutions as the cationic and anionic precursor sources, respectively. Four steps of the SILAR process for Yb_2S_3 thin film deposition were as follows:

I) The well polished SS substrate was immersed in ytterbium ion (Yb^{3+}) containing solution for 20 s, to adsorb Yb^{3+} ions over the SS substrate, II) after that the substrate was immersed 20 s in DDW to eliminate the excess adsorbed and loosely bonded Yb^{3+} ions, III) the substrate was dipped in S^{2-} ions containing solution for 20 s, where S^{2-} ions reacted on the preadsorbed Yb^{3+} ions, and IV) the substrate was again immersed 20 s in the DDW to eliminate the unreacted S^{2-} ions or weakly bound Yb_2S_3 molecules. The uniform and adherent Yb_2S_3 thin film was obtained after repeating such 120 SILAR cycles. **Fig. 3.8** shows SILAR experimental setup for deposition of Yb_2S_3 electrode [Inset shows the photograph of Yb_2S_3 thin film].

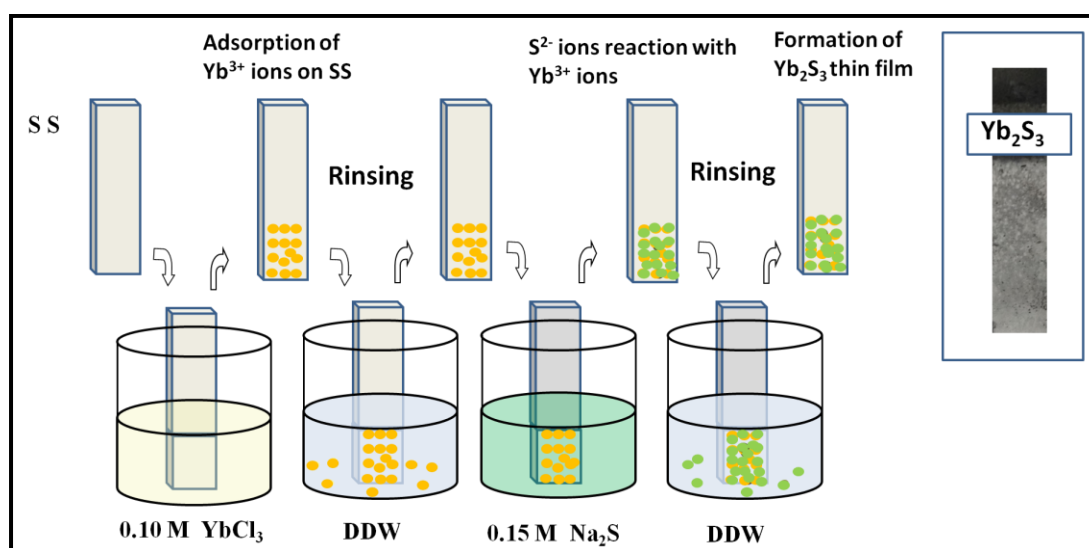


Fig. 3.8: Experimental setup of SILAR method for preparation of Yb_2S_3 thin film [Inset shows the photograph of Yb_2S_3 thin film].

3B.2.4 Characterization:

The characterization tools for the structural, morphological, contact angle and supercapacitive (CV, GCD, EIS and stability) studies are illustrated in section 3A.2.4.

3B.3 Results and discussion:

3B.3.1 Thin film formation and reaction mechanism:

When the ionic product (I.P.) of Yb^{3+} and S^{2-} ions exceeds the solubility product (S.P.), Yb_2S_3 film is formed over the SS substrate. The possible reactions are described by following steps as:

The Yb^{3+} ions (pH~4.5) are obtained by dissolving ytterbium chloride as



When SS substrate is dipped in Yb^{3+} ions containing solution, Yb^{3+} ions are adsorbed over SS substrate due to the force of attraction such as Van-der Waals, chemical or cohesive force between ions and substrate surface.

The substrate is immersed in S^{2-} ions (pH~12) containing solution,



Formation of Yb_2S_3 film on SS substrate takes place as,



The Yb_2S_3 film is dipped in the DDW to separate the sulfide ions or loosely attached Yb_2S_3 particles from the substrate. The mass of Yb_2S_3 film of 0.12 mg cm^{-2} for 120 cycles is determined using weight difference method. Preparative parameters for synthesis Yb_2S_3 thin film by SILAR method are shown in **table 3.3**.

Table 3.3: Preparative parameters for synthesis of Yb_2S_3 thin film by SILAR method.

Parameter	Precursor solutions	
	Cationic YbCl_3	Anionic Na_2S
Concentrations (M)	0.10	0.15
pH	4.5	12
Dipping time (s)	20	20
Drying time (s)	10	10
Rinsing time (s)	20	20
Deposition temperature (degree celsius)	27	27

3B.3.2 Structural studies:

3B.3.2.1 XRD:

Fig. 3.9 reveals the XRD pattern of Yb_2S_3 electrode over the SS substrate. The

diffraction peaks at 23.10° , 28.30° and 30.15° match with the (h k l) planes of (401), (012), and (600) of the monoclinic crystal structure of Yb_2S_3 (JCPDS card no. 65-2373). Such structure was also obtained for previously reported Yb_2S_3 films prepared by CBD and hydrothermal methods [29, 16]. The average crystallite size (D) was evaluated from (equation 2.7) Scherer's relation. The calculated average crystallite size for plane (401) was 45.37 nm. The broader and intense peaks in the XRD spectrum marked by hash (#) are associated with SS substrate.

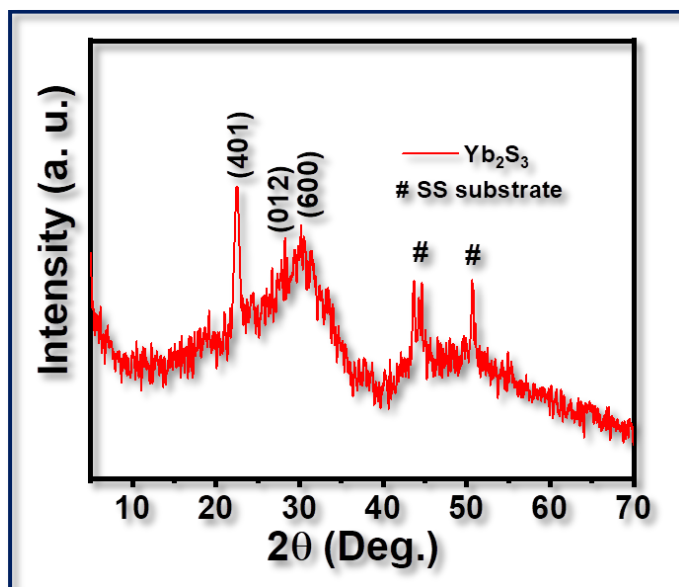


Fig. 3.9: The X-ray diffraction pattern of Yb_2S_3 thin film.

3B.3.2.2 XPS:

The XPS technique was used to study the oxidation states of elements in Yb_2S_3 film material. Fig. 3.10(A) demonstrates the survey spectrum of Yb_2S_3 film material, which shows no other elemental peaks different from the peaks of Yb, S, C, and O, confirming that the sample is pure. Fig. 3.10(B) illustrates the broad scan XPS spectrum of Yb4d. The deconvoluted peaks at binding energies of 185.6, 189.1, 192.5, 195.73, and 199.36 eV in Fig. 3.10(B) denoted as a, b, c, d, and e, respectively, are attributed to +3 oxidation state of Yb [30, 31]. Fig. 3.10(C) displays the broad scan XPS spectrum of S2p region. The deconvolution peaks at binding energies of 163.7 eV and 165.1 are attributed to $\text{S}2\text{p}_{3/2}$ and $\text{S}2\text{p}_{1/2}$ states which suggest -2 oxidation state of S [21, 32]. The XPS and XRD analyses confirm the formation of Yb_2S_3 electrode material via SILAR route.

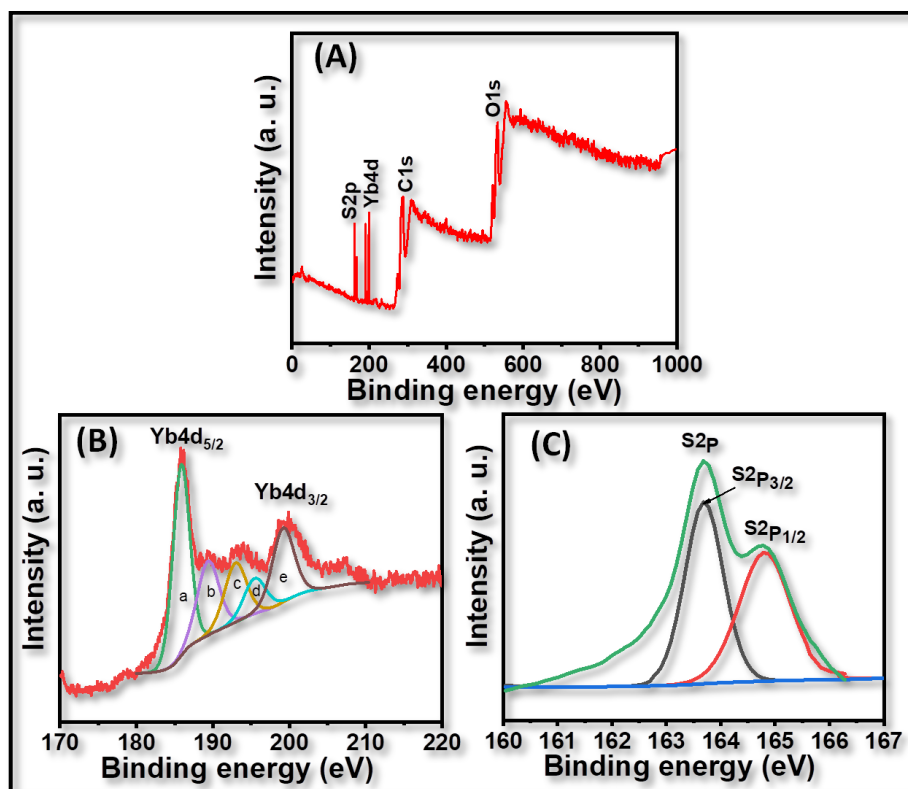


Fig. 3.10: (A) XPS survey spectrum of Yb_2S_3 thin film, (B) XPS spectrum of Yb4d region and (C) XPS spectrum of S2p region.

3B.3.3 Morphological study:

3B.3.3.1 Contact angle measurement:

For electrochemical supercapacitive behavior, the surface wettability is of significant importance. Wetting the surface material of electrode basically depends on the chemical content and surface textural of the thin film surface. If contact angle is greater than 90° , the film surface is hydrophobic and for lower than 90° , it is known to be hydrophilic. The water contact angle image in **Fig. 3.11(A)** shows the hydrophilic nature (57°) of Yb_2S_3 electrode. Pujari et al [16] obtained contact angle of 49.7° for Yb_2S_3 thin film synthesized by hydrothermal method. Also, Ghogare et al [9] reported contact angle of 46.9° for hydrothermally deposited La_2S thin film.

3B.3.3.2 Field emission scanning electron microscopy (FE-SEM):

For supercapacitor behaviour, the surface of electrode plays a vital role [32]. To study the surface texture of Yb_2S_3 film, the FE-SEM technique was employed. **Fig. 3.11(B, C)** shows the FE-SEM images of Yb_2S_3 electrode at magnifications of 5 kX and 10 kX. The Yb_2S_3 nanoparticles are agglomerated over the SS substrate and interconnected to each other, as seen at 5 kX magnification. **Fig. 3.11(C)** demonstrates

the average size of Yb_2S_3 nanoparticles is 250 nm. Generally, the morphology of material depends upon the method and preparation parameters of deposition. For e.g. Ghogare et al [9] observed nanopetal-like surface for La_2S thin film deposited by hydrothermal method. Kumbhar et al [33] observed tree-roots like diffused nanoflakes for chemically deposited Sm_2S_3 film. Ubale et al [29] chemically synthesized Yb_2S_3 film and obtained nanograins-like surface architecture. Pujari et al [16] reported distributed nanorods-like surface for hydrothermally deposited Yb_2S_3 thin film and Kumbhar et al [34] chemically deposited Sm_2Te_3 film and obtained barley like surface nature.

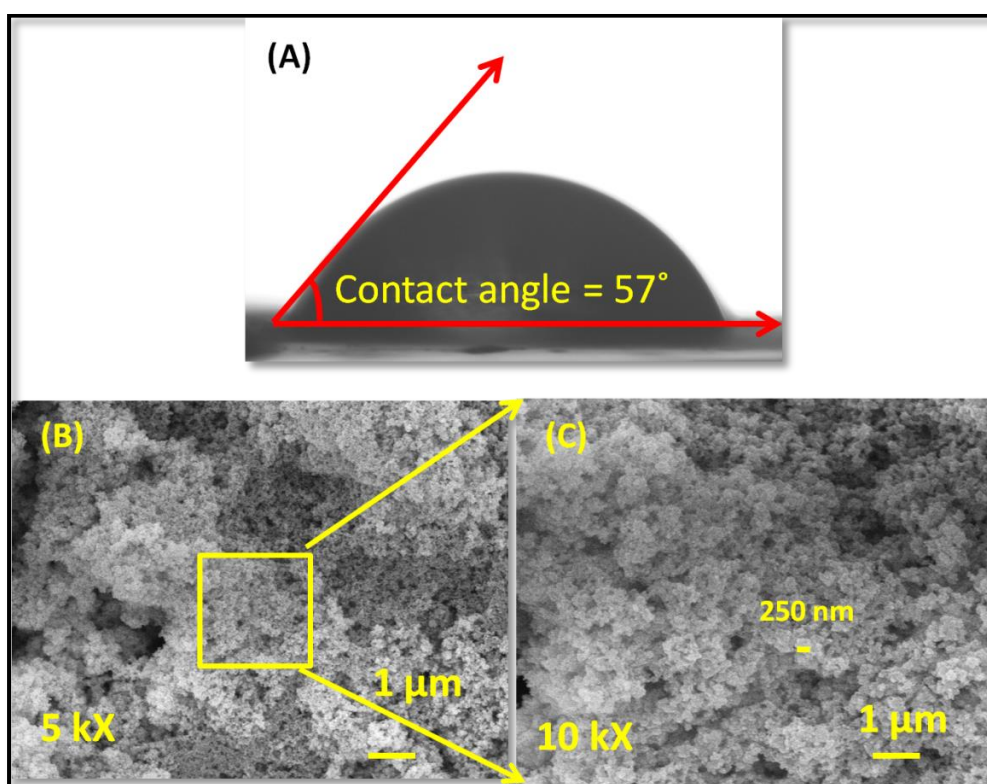


Fig. 3.11: (A) Contact angle and FE-SEM images of Yb_2S_3 thin films at (B) 5 kX and (C) 10 kX magnifications.

3B.3.4: Supercapacitive study:

3B.3.4.1 CV:

To explore the applicability of Yb_2S_3 film, CV curves were studied in 1.0 M Na_2SO_4 solution in potential range of -1 to 0 V.Hg/HgO. The CV plots of Yb_2S_3 thin film at various scan rates of 5 to 200 mV s^{-1} are demonstrated in **Fig. 3.12(A)**. The value of C_s is determined from CV plot using the relation 2.13. The Yb_2S_3 thin film showed C_s of 181 F g^{-1} at the scan rate of 5 mV s^{-1} . The plot of C_s versus scan rate in

Fig. 3.12(B) indicates that C_s value decreases with increase the scan rate. The enhancement in C_s at low scan rate is due to the utilization of external and internal electrode material for electrochemical reactions; whereas at higher scan rate, the C_s is due to contribution from external surface only [35, 36].

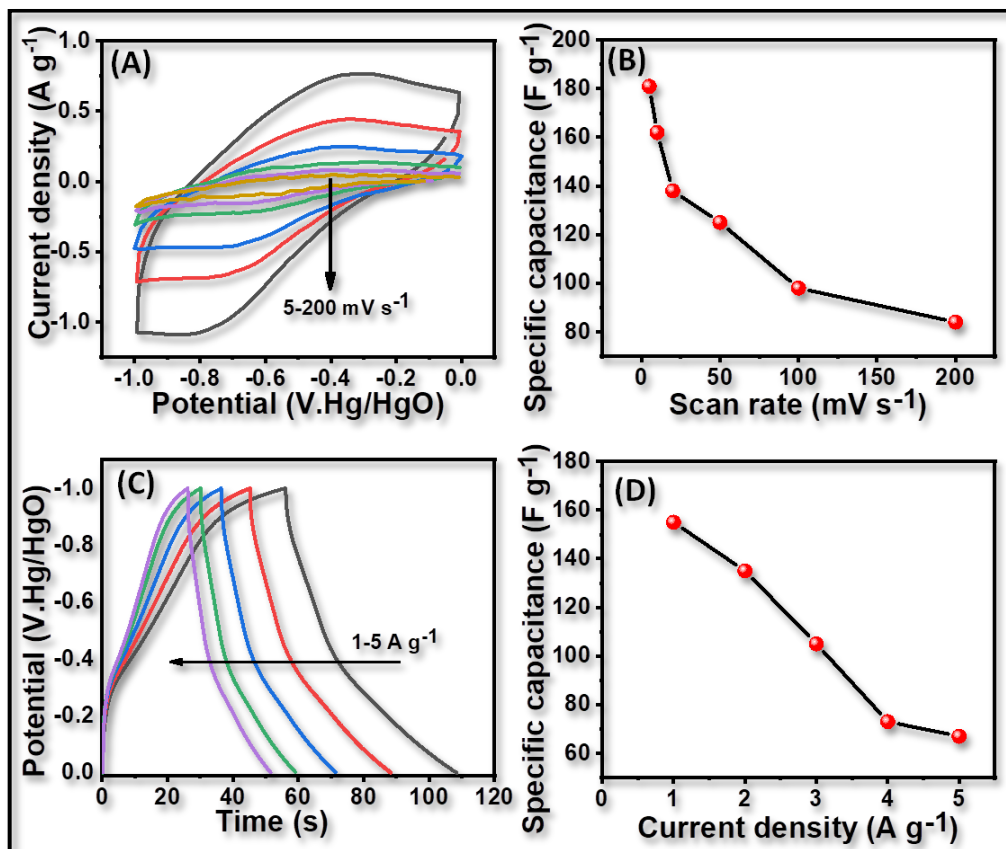


Fig. 3.12: (A) The CV curves of Yb₂S₃ at different scan rates of 5-200 mV s⁻¹, (B) plot of C_s versus scan rate, (C) GCD curves at current densities of 1-5 A g⁻¹, and (D) plot of C_s versus current density.

3B.3.4.2 GCD:

Further, the GCD studies at various current densities of 1-5 A g⁻¹ in the potential range of -1 to 0 V.Hg/HgO are depicted in **Fig. 3.12(C)**. The nonlinear shape of GCD curves may be owing to the faradic reaction or pseudocapacitive nature. The values of C_s are calculated using the equation 2.14.

The C_s of 155 F g⁻¹ is achieved at current density of 1 A g⁻¹. The plot of C_s versus current density in **Fig. 3.12(D)** shows that C_s decreases with increase in the current density owing to the lower utilization of active site electrode material at high current density [37]. The possible electrochemical reversible redox reaction due to the insertions/reinsertion of electrolyte ions between the electrode surface and electrolyte is



3B.3.4.3 Stability:

Electrochemical cyclic stability is a significant factor in application of thin film electrode in devices. **Fig. 3.13(A)** demonstrates the stability of Yb_2S_3 thin film for 3000th CV cycles at scan rate of 100 mV s^{-1} . **Fig. 3.13(B)** shows the plot of C_s versus cycle number, which clearly indicates that, C_s of Yb_2S_3 electrode slowly decreases with increase in number of CV cycles. The Yb_2S_3 thin film exhibits 83 % capacity retention for 3000 CV cycles. Similar electrochemical capacity retentions in the range from 78 to 85 % are reported for other REM chalcogenide thin film materials in the aqueous electrolytes [8, 16, 37, 33].

3B.3.4.4 EIS:

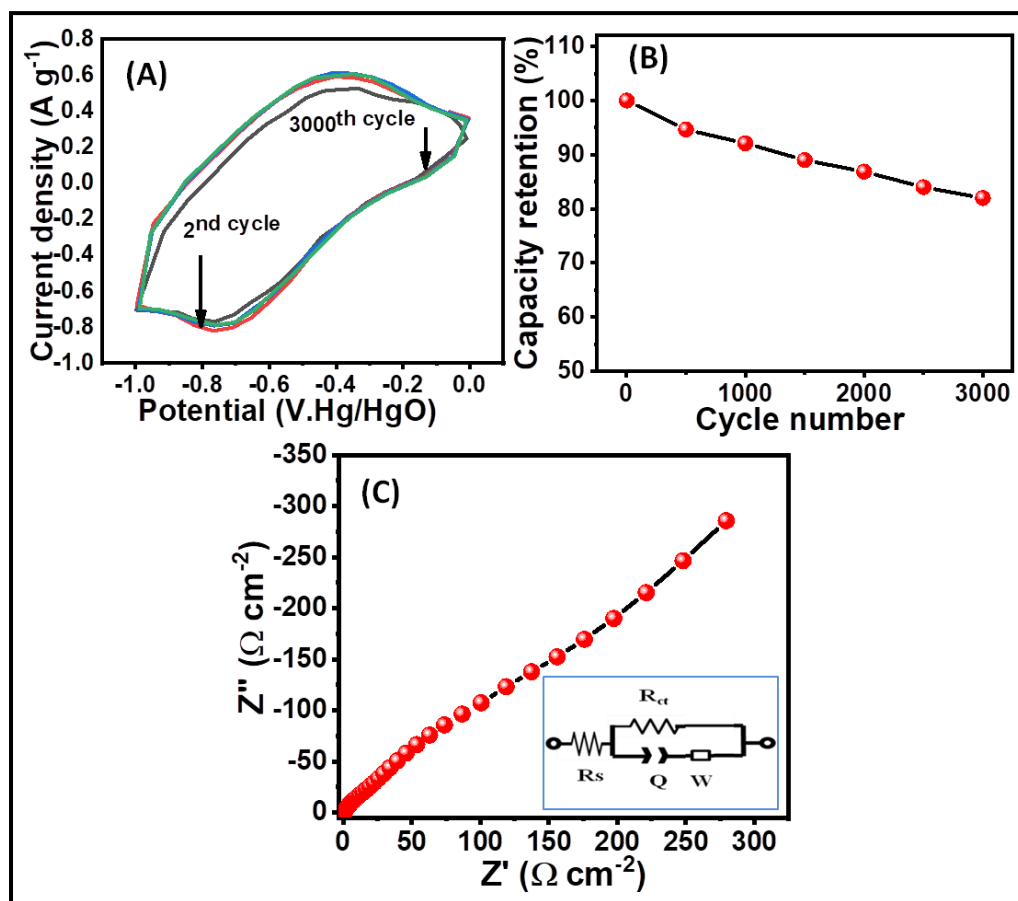


Fig. 3.13: (A) Electrochemical cyclic stability of Yb_2S_3 sample at scan rate of 100 mV s^{-1} , (B) plot of capacity retention with cycle number and (C) Nyquist plot of Yb_2S_3 sample (Inset illustrates the best fitted equivalent circuit).

Fig. 3.13(C) illustrates the Nyquist plot of Yb_2S_3 electrode in 1 M Na_2SO_4 electrolyte. The Nyquist plot demonstrates the tiny semicircle in the high frequency domain corresponding to the charge transfer process. Warburg resistance (W) is a result

of lower frequency region dependence of ion diffusion or transport in the applied electrolyte [3]. The higher frequency region of the Nyquist plot illustrates the R_s , which arises due to the combination of intrinsic resistance of thin film, ionic resistance of the electrolyte, and contact resistance of film electrode and current collector [38]. The well fitted equivalent circuit derived from Nyquist plot data illustrated as an inset of Fig. 3.13(C) gives values of R_s , R_{ct} and W as 4.29, 56 and $60.32 \Omega \text{ cm}^{-2}$, respectively. Table 3.4 shows fitted parameters of equivalent circuit data. Table 3.5 shows electrochemical performance of CBD and SILAR deposited Yb_2S_3 thin films.

Table 3.4: The EIS parameters of Yb_2S_3 thin film in 1 M Na_2SO_4 electrolyte.

Parameter	Values of parameter
$R_s (\Omega \text{ cm}^{-2})$	4.29
$Q (\text{mF})$	1.753
$R_{ct} (\Omega \text{ cm}^{-2})$	56
$W (\Omega \text{ cm}^{-2})$	60.32

3C: Conclusions:

Interconnected nano-grains and nanoparticles, Yb_2S_3 thin films have been successfully prepared over SS substrates by CBD and SILAR methods, respectively. The structural analyses show that the formations of nanostructured Yb_2S_3 films over the substrate surface have hydrophilic nature. The supercapacitive performances are investigated in KOH and Na_2SO_4 electrolytes. Further, the results of cyclic voltammetry show that CBD deposited the Yb_2S_3 thin films exhibited the specific capacitance of 184.6 F g^{-1} with cyclic stability of 81 % at scan rate of 100 mV s^{-1} . SILAR synthesized Yb_2S_3 thin films exhibited the specific capacitance of 181 F g^{-1} with 83 % life cyclic at scan rate of 100 mV s^{-1} . The CBD deposited Yb_2S_3 thin film showed excellent electrochemical performance.

Table 3.5: The supercapacitive performance of CBD and SILAR deposited Yb_2S_3 thin films.

Method	Electrolyte	Spe. Cap. (Cs) (F g^{-1})	Potential range (V.Hg/HgO)	Sol. Resi., (R_s)($\Omega \text{ cm}^{-2}$)	Charge tran. Resi.,(R_{ct})($\Omega \text{ cm}^{-2}$)	Cyclic stability (%)
CBD	KOH	184.6	-1.2 to -0.2	0.370	8.96	81
SILAR	Na_2SO_4	181	-1to 0	4.29	56	83

The specific capacitance of as prepared material is depends on the surface morphology and suitable electrolyte solution. **Table 3.5** shows that the specific capacitance of CBD method prepared Yb_2S_3 thin film is better than SILAR deposited Yb_2S_3 thin film due to the nano-grained surface morphology and suitable electrolyte solution. This type of morphology is more helpful for electrolyte ion penetration in the electrode during redox reaction. Also, the ionic conductivity of electrolyte ions is mostly useful to enhance the electrochemical properties of material. Ionic conductivity of K^+ ions ($73 \text{ cm}^2 \Omega^{-1} \text{ mol}^{-1}$) is higher than Na^+ ions ($50 \text{ cm}^2 \Omega^{-1} \text{ mol}^{-1}$). The tiny hydrated radius of K^+ ions favors faster ionic mobility and interaction with electrode material, thereby resulting in enhanced supercapacitor properties.

3D: References:

1. D. S. Dhawale, A. Vinu, C. D. Lokhande, *Electrochim. Acta.*, 46, (2011), 9482-9487.
2. R. S. Mane and C. D. Lokhande, *Mater. Chem. Phys.*, 65, (2000), 1-31.
3. A. A. Yadav, V. S. Kumbhar, S. J. Patil, N. R. Chodankar, C. D. Lokhande, *Ceram. Int.*, 42, (2016), 2079-2084.
4. C. D. Lokhande, *Mater. Chem. Phys.*, 28, (1991), 145-149.
5. V. S. Kumbhar, A. D. Jagadale, N. S. Gaikwad, C. D. Lokhande, *Mater Res Bull.*, 56, (2014), 39-44.
6. V. S. Kumbhar, A. C. Lokhande, N. S. Gaikwad, C. D. Lokhande, *Ceram. Int.*, 41, (2015), 5758-5764.
7. S. J. Patil, V. S. Kumbhar, B. H. Patil, R. N. Bulakhe, C. D. Lokhande, *J. Alloys Compd.*, 611, (2014), 191-196.
8. S. J. Patil and C. D. Lokhande, *Mater. Des.*, 87, (2015), 939-948.
9. T. T. Ghogare, R. B. Pujari, A. C. Lokhande, C. D. Lokhande, *Appl. Phys. A*, 124, (2018), 248-252.
10. U. K. Mohite, K. M. Gadhave, C. D. Lokhande, *Indian J. Pure Appl. Phys.*, 32, (1994), 772-777.
11. N. M. Soudagar, V. K. Pandit, R. B. Pujari, K. B. Chorghade, C. D. Lokhande, S. S. Joshi, *Int. J. Eng. Res. Technol.*, (IJERT), 10, (2017), 587-594.
12. N. R. Chodankar, G. S. Gund, D. P. Dubal, C. D. Lokhande, *RSC Adv.*, 4, (2014), 61503-61513.
13. G. Hodes and M. D. Inc, 'Chemical solution deposition of semiconductor films', New York, (2002), pp. 1-38.
14. S. S. Karade, K. Banerjee, S. Majumder, B. R. Sankapal, *Int. J. Hydrog. Energy*. 726, (2016), 1-8.
15. R. B. Pujari, A.C. Lokhande, A. A. Yadav, J. H. Kim, C. D. Lokhande, *Mater. Des.*, 108, (2016), 510-517.
16. R. B. Pujari, A. C. Lokhande, T. T. Ghogare, S. B. Kale, C. D. Lokhande, *J. Mater. Sci. Mater. Electron.*, 29, (2018), 14116-14121.
17. G. S. Gund, D. P. Dubal, B. H. Patil, S. S. Shinde, C. D. Lokhande, *Electrochim. Acta.*, 92, (2013), 205-215.
18. D. P. Dubal, G. S. Gund, C. D. Lokhande, R. Holze, *Energy Technol.*, 2, (2014), 401-408.
19. B. Saravanakumar, K. K. Purushothaman, G. Muralidharan, *ACS Appl. Mater. Interfaces.*, 4, (2012), 4484-4490.
20. A. Arivarasan, S. Bharathi, S. Ezhilarasi, S. Arunpandiyam, R. Jayavel, *J. Inorg. Organomet Polym Mater.*, 29, (2019), 859-868.
21. S. S. Karade, D. P. Dubal, B. R. Sankapal, *RSC Adv.*, 6, (2016), 39159-39165.
22. H. D. Dhaygude, S. K. Shinde, D. P. Dubal, G. M. Lohar, V. J. Fulari, *J. Mater. Sci. Mater. Electron.*, 26, (2015), 8563-8567.
23. D. S. Knight and W. B. White, *J Solid State Chem.*, 4, (1989), 1-18.
24. S. S. Karade, D. P. Dubal, B. R. Sankapal, *Energ Environ Sci.*, 2, (2017), 10405-10412.
25. S. B. Kale, A. C. Lokhande, R. B. Pujari, C. D. Lokhande, *J. Colloid Interface Sci.*, 532, (2018), 491-499.
26. R. B. Pujari, A. C. Lokhande, J. H. Kim, C. D. Lokhande, *RSC Adv.*, 6, (2016), 40593-40601.

27. S. J. Patil, V. C. Lokhande, N. R. Chodankar, C. D. Lokhande, *J. Colloid Interface Sci.*, 469, (2016), 318-324.
28. A. M. Patil, V. C. Lokhande, A. C. Lokhande, N. R. Chodankar, T. Ji, J. H. Kim, C. D. Lokhande, *RSC Adv.*, 6, (2016), 68388-68401.
29. S. B. Ubale, R. N. Bulakhe, V. J. Mane, D. B. Malavekar, I In, C. D. Lokhande, *Appl Nanosci.*, 10, (2020), 5085-5097.
30. L. Chen, G. Zheng, G. Yao, P. Zhang, S. Dai, Y. Jiang, H. Li, B. Yu, H. Ni, S. Wei, *ACS Omega*, 5, (2020), 8766-8776.
31. R. B. Pujari, A. C. Lokhande, A. R. Shelke, J. H. Kim, C. D. Lokhande, *J. Colloid Interface Sci.*, 496, (2017), 1-7.
32. J. H. Kim, *New J. Chem.*, 42, (2018), 2733-2742.
33. V. S. Kumbhar, A. D. Jagadale, C. D. Lokhande, *J. Power Sources*, 234, (2013), 107-110.
34. V. S. Kumbhar, A. C. Lokhande, N. S. Gaikwad, C. D. Lokhande, *Chem. Phys. Lett.*, 645, (2016), 112-117.
35. S. S. Raut and B. R. Sankapal, *Electrochim. Acta.*, 198, (2016), 203-211.
36. D. P. Dubal, G. S. Gund, R. Holze, C. D. Lokhande, *J. Power Sources*, 242, (2013), 687-698.
37. A. A. Yadav, A. C. Lokhande, J. H. Kim, C. D. Lokhande, *Int. J. Hydrog. Energy.*, 41, (2016), 18311-18319.
38. B. Frenzel, P. Kurzweil, H. Ronnebeck, *J. Power Sources*, 196, (2011), 5364-5376.

Chapter-IV

SILAR synthesized, ytterbium sulfide, graphene oxide and graphene oxide/ytterbium sulfide composite thin films: characterization and supercapacitive performance

Chapter-IV

SILAR synthesized, ytterbium sulfide, graphene oxide and graphene oxide/ytterbium sulfide composite thin films: characterization and supercapacitive performance

Sr. no.	Title	Page no.
4.1	Introduction	75
4.2	Experimental details	76
	4.2.1 <i>Substrate cleaning</i>	76
	4.2.2 <i>Precursors</i>	76
	4.2.3 Synthesis	76
	4.2.3.1 <i>Synthesis of graphene oxide</i>	76
	4.2.3.2 <i>Synthesis of graphene oxide thin films</i>	77
	4.2.3.3 <i>Synthesis of ytterbium sulfide thin films</i>	77
	4.2.3.4 <i>Synthesis of graphene oxide/ytterbium sulfide composite thin films</i>	78
	4.2.3.5 <i>Characterization</i>	78
4.3	Results and discussion	79
	4.3.1 Thin film formation and reaction mechanism	79
	4.3.2 Structural studies	80
	4.3.2.1 <i>X-ray diffraction (XRD)</i>	80
	4.3.2.2 <i>X-ray photoelectron spectroscopy (XPS)</i>	81
	4.3.3 Morphological study	82
	4.3.3.1 <i>Contact angle measurement</i>	82
	4.3.3.2 <i>Field emission scanning electron microscopy (FE-SEM)</i>	83
	4.3.3.3 <i>Transmission electron microscopy (TEM)</i>	84
	4.3.4 Supercapacitive study	84
	4.3.4.1 <i>Cyclic voltammetry (CV)</i>	84
	4.3.4.2 <i>Galvanostatic charge discharge (GCD)</i>	86
	4.3.4.3 <i>Stability</i>	87
	4.3.4.4 <i>Electrochemical impedance spectroscopy (EIS)</i>	88
4.4	Conclusions	89
4.5	References	91

4.0: SILAR synthesized ytterbium sulfide, graphene oxide and graphene oxide/ytterbium sulfide composite thin films: characterization and supercapacitive performance

4.1 Introduction:

Activated carbon, carbon allotropes, carbon nanotubes and graphene materials are used in EDLC [1, 2]. Among these carbon allotropes, graphene is one of the most promising candidates for use in the potential application due to its large surface area, high electrical conductivity, excellent mechanical properties, chemical stability and low cost [3-6]. It is a two-dimensional (sp^2) form of graphite material which has various applications such as solar cells, supercapacitors and multi-functional materials [7-9]. The tunable oxygenous functional groups of graphene oxide (GO) facilitate the modification on the surface and make it a promising material for composites with other materials [10]. The water dispersion of GO is simple as compared to the graphene and provides an easy path for preparing its composite with metal oxides, conducting polymers, and metal chalcogenides for the enhancement of electrochemical capacitive performance [11-13].

The rare earth metal (REM) chalcogenides with variety in the composition, structure, and presence of 4f electrons have attracted great attention in recent years. [14]. These properties make them widely applied in electronics, petrochemical, metallurgy, machinery, energy, and light industry [15]. In last few years, REM sulfide thin films such as samarium sulfide (Sm_2S_3) [16], lanthanum sulfide (La_2S , La_2S_3) [17, 18], ytterbium sulfide (Yb_2S_3) [19, 20], yttrium sulfide (Y-S) [21] have been synthesized by different chemical methods such as SILAR, CBD, hydrothermal and electrodeposition, respectively. These REM sulfide thin films are investigated as a material for electrochemical capacitor due to high electrical conductivity, good rate capacity and large potential window as compared to other oxide and hydroxide materials.

The present chapter deal with the SILAR method is used for the deposition of Yb_2S_3 , GO, and GO/ Yb_2S_3 composite thin film materials. It is a simple, inexpensive binder-free and low-temperature method, which involves immersion of substrate into separately placed cationic and anionic solutions for material formation [22-25]. The Yb_2S_3 , GO, and GO/ Yb_2S_3 composite thin films are characterized by X-ray diffraction (XRD), X-ray photoelectron spectroscopy (XPS), contact angle, field emission

scanning electron microscopy (FE-SEM) and transmission electron microscopy (TEM). Further, Yb_2S_3 , GO and $\text{GO}/\text{Yb}_2\text{S}_3$ composite thin films are used in the three-electrode system to test electrochemical supercapacitive activities using the CV, GCD and EIS.

4.2 Experimental details:

4.2.1 Substrate cleaning:

The substrate cleaning procedure is described in section 3A.2.1.

4.2.2 Precursors:

All the AR grade reagents such as ytterbium (III) chloride ($\text{YbCl}_3 \cdot 7\text{H}_2\text{O}$), sodium sulfide (Na_2S), natural graphite flexes, hydrogen peroxide (H_2O_2 30 %), potassium permanganate (KMnO_4 , 99.9 %), sulphuric acid (H_2SO_4 98 %), hydrochloric acid (HCl 35.4 %) and polyvinyl alcohol (PVA) were purchased from Sigma Aldrich and used without further purification. The DDW was used as a solvent in the experiment. All solutions were freshly prepared for the synthesis of Yb_2S_3 , GO, and $\text{GO}/\text{Yb}_2\text{S}_3$ thin films. Sodium sulfate (Na_2SO_4) electrolyte was used for the study of electrochemical properties of Yb_2S_3 , GO, and $\text{GO}/\text{Yb}_2\text{S}_3$ thin films.

4.2.3 Synthesis:

4.2.3.1 Synthesis of graphene oxide:

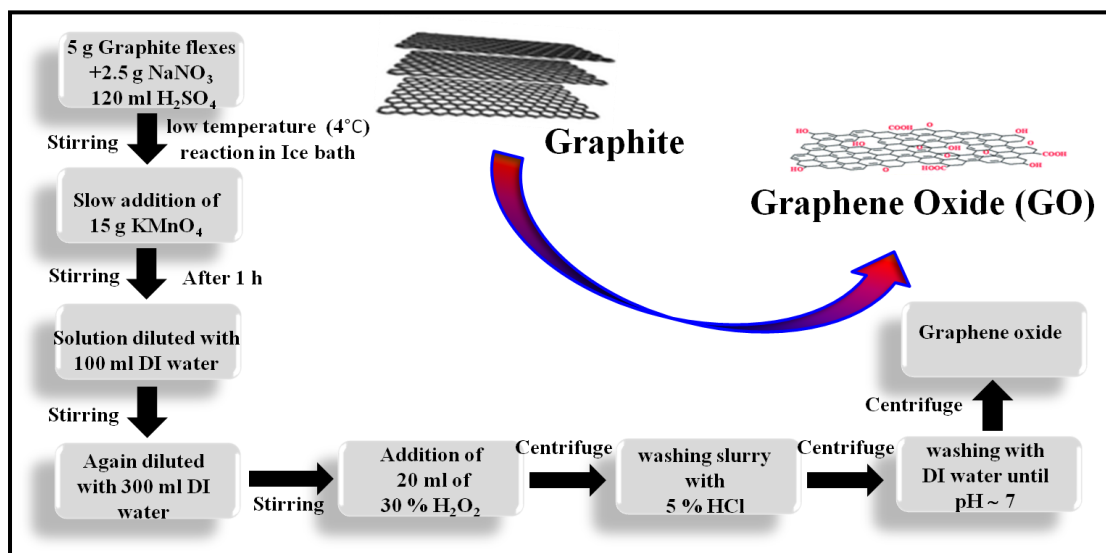


Fig. 4.1: Flow chart for synthesis of GO.

The GO was prepared using commercial graphite flaxes by a Modified Hummers method [26, 27]. Graphite flaxes (5 g) and NaNO_3 (2.5 g) were added into 120 mL of concentrated H_2SO_4 in an ice bath with constant stirring for 60 minutes. Then, KMnO_4 (15 g) was added with constant stirring. The mixture was stirred for 720

minutes at a room temperature (300 K). Successively, 150 mL of diluted 30 % H_2O_2 was added drop wise in to the mixture to reduce the residual KMnO_4 . For purification, the mixture was washed with HCl and DDW for many times. Afterward, the suspension was centrifuged at 10000 rpm and washed several times. The exfoliation of GO was achieved by ultrasonication of the dispersion in ultrasonic bath. Finally, the homogeneous GO aqueous dispersion was obtained and used for the deposition of GO thin films. The synthesis of GO is demonstrated in **Fig. 4.1**.

4.2.3.2 Synthesis of graphene oxide (GO) thin films:

Layer-by-Layer (L-b-L) method was used for the preparation of GO thin films. The synthesized GO was taken and exfoliated (1.0 mg mL^{-1}) in 100 mL DDW for 45 minutes using the ultrasonic bath. In well-dispersed GO sheets solution, mirror-polished SS substrate was immersed vertically and kept for 25 s and withdrawn gradually and dried for 50 s to improve the adherency of GO sheets on the substrate. Such 120 cycles were repeated to get the uniform deposition of GO film. Schematic of the deposition of GO thin film by L-b-L method is shown in **Fig. 4.2** [Inset shows the photograph of GO thin film obtained on SS substrate].

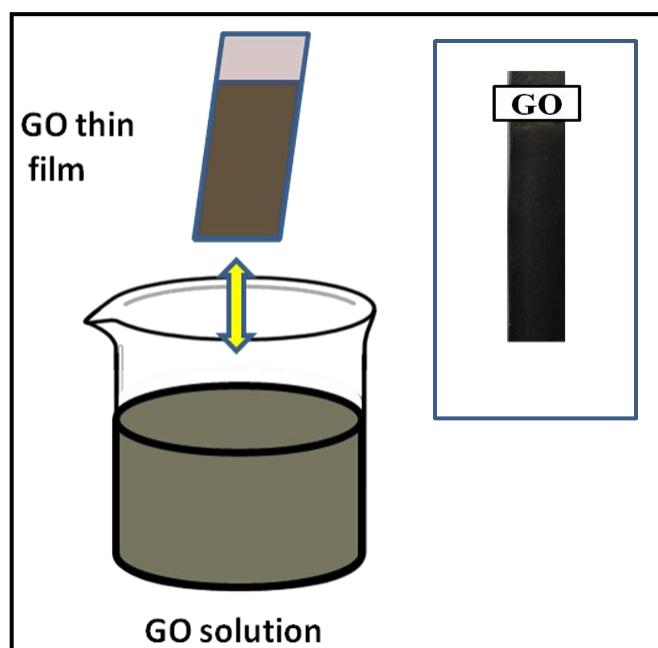


Fig. 4.2: The schematic of L-b-L method for deposition of GO thin film [Inset shows the photograph of GO thin film].

4.2.3.3 Synthesis of ytterbium sulfide (Yb_2S_3) thin film:

The synthesis of Yb_2S_3 thin film by SILAR method procedure is described detail in section **3B.2.3**.

4.2.3.4 Synthesis of graphene oxide/ytterbium sulfide (GO/Yb₂S₃) composite thin film:

GO/Yb₂S₃ composite thin films were prepared by immersion the SS substrate in the dispersed GO solution, which is separately placed before cationic and anionic solutions, followed by rinsing and air drying after every immersion. **Fig. 4.3** shows a schematic of the synthesis of GO/Yb₂S₃ SILAR thin films. Herein, a six-beaker SILAR system was employed to carry out the deposition of GO/Yb₂S₃ thin films. The first, third and fifth beakers contain ~50 mL well dispersed GO (1 mg mL⁻¹), 0.10 (M) YbCl₃ and 0.15 (M) Na₂S solutions, respectively. The second, fourth and sixth beakers contain DDW for rinsing. After repeating 120 cycles, uniform thin film of GO/Yb₂S₃ was achieved. Inset of **Fig. 4.3** shows the photograph of GO/Yb₂S₃ composite thin film.

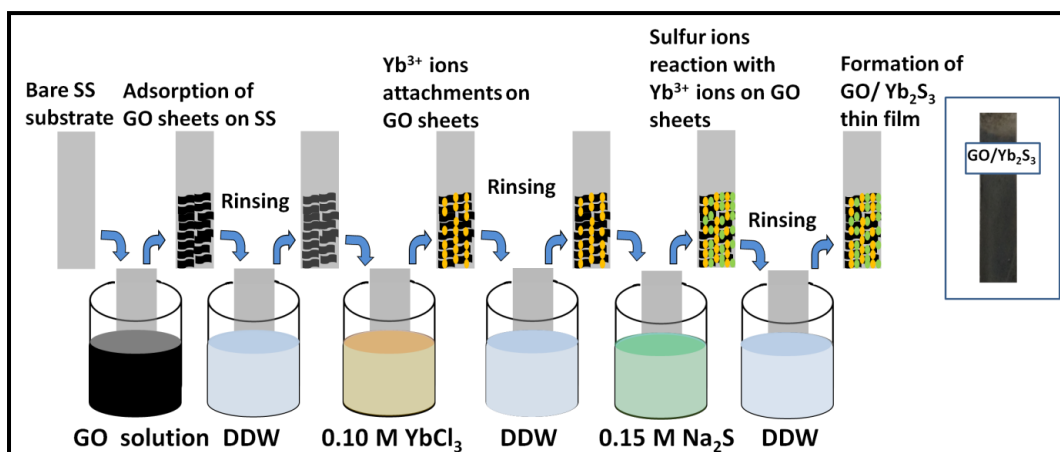


Fig. 4.3: The schematic of SILAR method for the synthesis of GO/Yb₂S₃ composite thin film [Inset shows the photograph of GO/Yb₂S₃ thin film].

4.2.3.5 Characterization:

The crystalline structures of Yb₂S₃, GO and GO/Yb₂S₃ composite thin films were determined using an X-ray diffractometer (Rigaku Miniflex-600) at an accelerating voltage of 30 kV and current 15 mA. The XRD spectra were obtained in the range of 5-75° at a scanning speed of 0.5° per minute. The chemical states and composition of elements in GO/ Yb₂S₃ composite thin film were confirmed through an X-ray photoelectron spectrometer (ThermoVG Scientific, United Kingdom). Contact angles were investigated with water drop by Rame-Hart instrument USA. The morphological characterization of Yb₂S₃, GO and GO/Yb₂S₃ composite thin films was carried out by field emission scanning electron microscope (model Crossbeam 1560 XBFIB workstation) and transmission electron microscope (TEM, Philips CM-30 unit, Point Resolution = 2.4 Å) with an acceleration voltage of 300 kV.

The electrochemical properties of Yb_2S_3 , GO, and GO/ Yb_2S_3 composite thin film were tested in the three-electrode cell system using Yb_2S_3 , GO, and GO/ Yb_2S_3 composite thin films as a working electrode, platinum plate as a counter electrode, and mercury/mercury oxide (Hg/HgO) as a reference electrode. Electrochemical study was carried out in 1.0 M Na_2SO_4 aqueous electrolyte. The electrochemical capacitive performance of thin films was recorded by CV, GCD, and EIS using a battery cycler (ZIVE MP1 workstation, S. Korea).

4.3 Results and discussion:

4.3.1 Thin film formation and reaction mechanism:

4.3.1.1 GO thin film formation:

The well-dispersed GO nanosheets were applied to SS substrate using a layer-by-layer (L-b-L) deposition method. GO sheets are coated on the SS substrate due to the chemical or Vander Waals force of attraction between surface of SS substrate and GO sheets. In L-b-L method, deposition cycles were repeated for 120 times to achieve the uniform GO thin films [23, 24]. The 0.37 g cm^{-2} of GO nanosheets was deposited after 120 cycles on a surface area of 5 cm^2 . The optimized preparative parameters at the room temperature (300K) for deposition of GO thin films (L-b-L method) are illustrated in **table 4.1**.

Table 4.1: Optimized preparative parameters for room temperature (300K) deposition of GO thin films.

Parameters	GO solution
Concentration (M)	1.0 (mg/mL)
pH	4.7
Dipping time (s)	25
Drying time (s)	50
Deposition cycle	120

4.3.1.2 Formation of GO/ Yb_2S_3 composite thin films:

The GO/ Yb_2S_3 composite thin films were deposited by immersing the SS substrate in well dispersed GO solution and air drying. Subsequently, dipping SS substrate in separately placed (YbCl_3) cationic and (Na_2S) anionic precursors with rinsing between every immersion. The ion-by-ion deposition process of Yb_2S_3 on GO nanosheets takes place and the layer of GO/ Yb_2S_3 composite was formed on the SS substrate. The above process was repeated for 120 times to obtain uniform GO/ Yb_2S_3

composite films. Schematic of GO/Yb₂S₃ composite thin film formation by SILAR method is shown in **Fig. 4.3** (Inset shows the photograph of GO/Yb₂S₃ composite thin film). Optimized preparative parameters of GO/Yb₂S₃ composite thin film deposition are shown in **table 4.2**. The 0.65 g cm⁻² of GO/Yb₂S₃ composite material was deposited after 120 cycles on SS substrate.

Table 4.2 The optimized preparative parameters at the room temperature (300K) for deposition of GO/Yb₂S₃ composite thin films.

Parameters	Precursor solutions		
	GO	(Cationic) YbCl ₃	(Anionic) Na ₂ S
Concentrations (M)	1.0 (mg/mL)	0.10	0.15
pH	4.7	4.5	12
Dipping time (s)	25	20	20
Drying time (s)	50	10	10
Rinsing time (s)	20	20	20
Deposition cycle	120		

4.3.2 Structural studies:

4.3.2.1 X-ray diffraction (XRD):

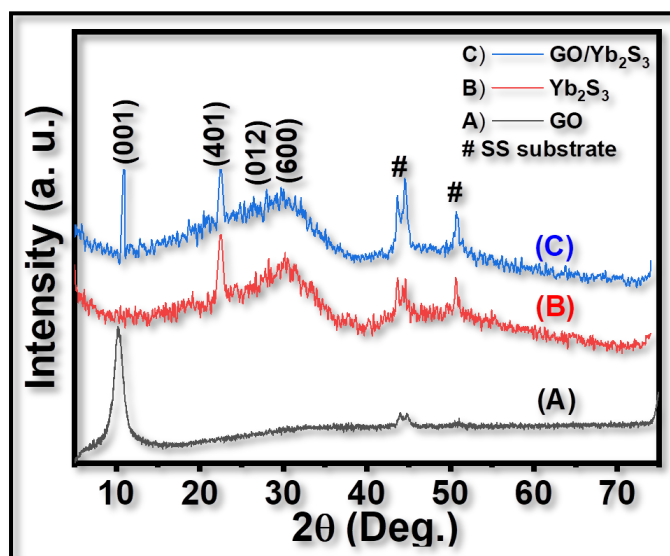


Fig. 4.4: The X-ray diffraction patterns of (A) GO, (B), Yb₂S₃ and (C) GO/Yb₂S₃ composite thin films.

The XRD patterns were used to analyze the crystal structure formation of Yb₂S₃, GO and GO/Yb₂S₃ composite thin films. **Fig. 4.4** shows the XRD spectra of GO, Yb₂S₃, and GO/Yb₂S₃ composite thin films on SS substrate. The XRD pattern of GO (A) revealed an intense and sharp peak at 10.45° indicating (001) plane of GO corresponding to the interplanar spacing of 0.83 nm GO sheets [23, 24]. The diffraction

patterns of Yb_2S_3 (B) and $\text{GO}/\text{Yb}_2\text{S}_3$ (C) show intense peaks corresponding to (401), (012), and (600) planes of monoclinic crystal structure of Yb_2S_3 material (JCPDS card no. 65-2373) [36, 37]. The XRD pattern revealed that $\text{GO}/\text{Yb}_2\text{S}_3$ composite is nanocrystalline. The crystallite size, D was determined using Scherrer's equation 2.7. The crystallite sizes of Yb_2S_3 and $\text{GO}/\text{Yb}_2\text{S}_3$ composites are 65.45 and 67.14 nm, respectively using (401) plane. The peaks in XRD patterns shown by the hash (#) correspond to SS substrate.

4.3.2.2 X-ray photoelectron spectroscopy (XPS):

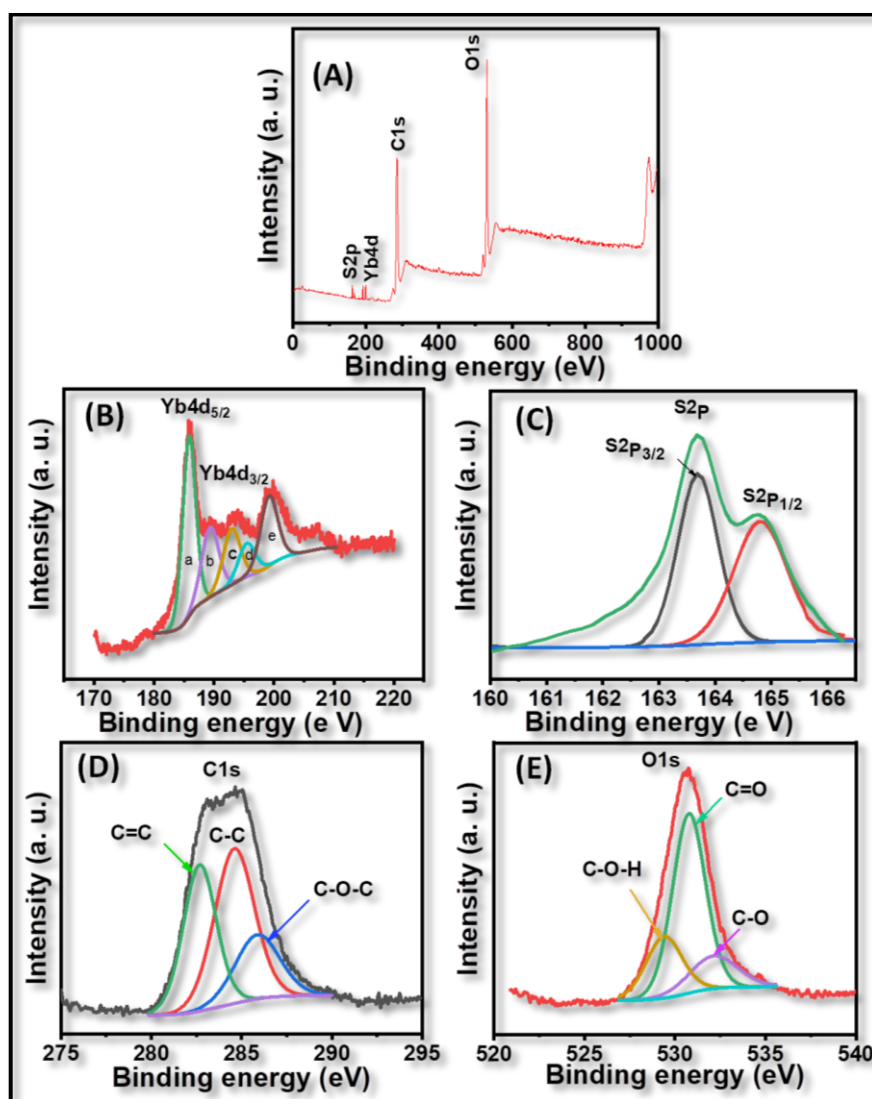


Fig. 4.5: (A) The XPS survey spectrum of $\text{GO}/\text{Yb}_2\text{S}_3$ composite thin film and XPS spectra of (B) Yb4d region, (C) S2p region, (D) C1s region and (E) O1s region of $\text{GO}/\text{Yb}_2\text{S}_3$ thin film.

Chemical composition and oxidation states of elements in $\text{GO}/\text{Yb}_2\text{S}_3$ nanocomposite compound material were investigated using XPS spectra. The XPS

survey spectrum of GO/Yb₂S₃ sample illustrated in **Fig. 4.5(A)** reveals the existence of S2p, Yb4d, O1s and C1s elemental states. **Fig. 4.5(B-E)** shows the high resolution XPS spectra of Yb4d, S2p, C1s, and O1s. The chemical states of Yb4d illustrated in **Fig. 4.5(B)**. The deconvoluted peaks at binding energies of 185.6, 189.1, 192.5, 195.73, and 199.36 eV in **Fig. 4.5(B)** denoted as a, b, c, d, and e, respectively, are attributed to +3 oxidation state of Yb [19, 28].

Fig. 4.5(C) indicates S2p spectrum with peaks S2p_{3/2} and S2p_{1/2} cited at the binding energies of 163.6 and 164.9 eV, which is attributed to the sulfur orbital of divalent sulfide ions (S²⁻) [29, 30]. The observed C1s spectrum peaks of C=C, C-C and C-O-C with located the binding energies of 283.5, 284.5 and 286.2 eV, respectively are depicted in **Fig. 4.5(D)**. The O1s spectrum peaks of C-O-H, C=C and C-O at cited binding energies of 530, 531.5 and 532.5 eV, respectively shown in **Fig. 4.5(E)** are consistent with the literature values [31, 32].

4.3.3 Morphological study

4.3.3.1 Contact angle measurement:

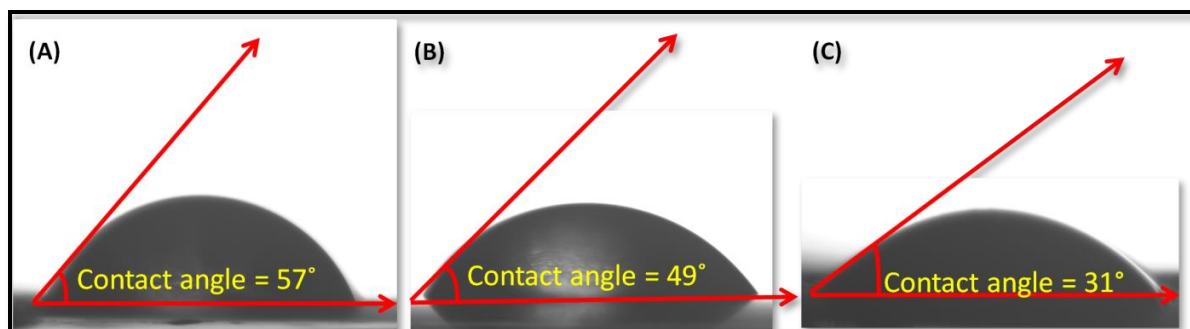


Fig. 4.6: Contact angle images of (A) Yb₂S₃, (B) GO and (C) GO/Yb₂S₃ composite thin films.

Wettability of the electrode surface is an important property for supercapacitor applications [1]. The water contact angle images of Yb₂S₃, GO, and GO/Yb₂S₃ composite thin films are shown in **Fig. 4.6(A-C)**. If the wettability is more, less the contact angle value ($\theta < 90^\circ$), then the surface is hydrophilic. If wettability is high the contact angle value ($\theta > 90^\circ$), then surface is hydrophobic. The water contact angle values of GO, Yb₂S₃ and GO/Yb₂S₃ composite films are 57°, 49° and 31°, respectively, of which GO/Yb₂S₃ composite film is more hydrophilic as compared with other two films [16]. Ubale et al [19] deposited Yb₂S₃ thin film on SS substrate by CBD method and observed contact angle 61.2°. Ghogare et al [23, 24] synthesized GO, GO/La₂S₃

and GO/Sm₂S₃ thin films by SILAR method and obtained contact angle values of 80°, 37° and 5°, respectively.

4.3.3.2 Field emission scanning electron microscopy (FE-SEM):

The FE-SEM images of Yb₂S₃, GO and GO/Yb₂S₃ composite thin films are demonstrated in **Fig. 4.7(A-C)** at 10 kX magnification. In case of Yb₂S₃ thin film, the nanoparticles are spread over the substrate as shown in **Fig. 4.7(A)**. Inset of **Fig. 4.7(A)** displays that the nanoparticles with size of nanoparticles in between the 200-250 nm are interconnected. **Fig. 4.7(B)** shows the homogeneous layer structure formed with wrinkles-like morphology of GO thin film. The wrinkles present in GO thin film may be due to the formation of thin layer and wide length of GO nanosheets [7, 8].

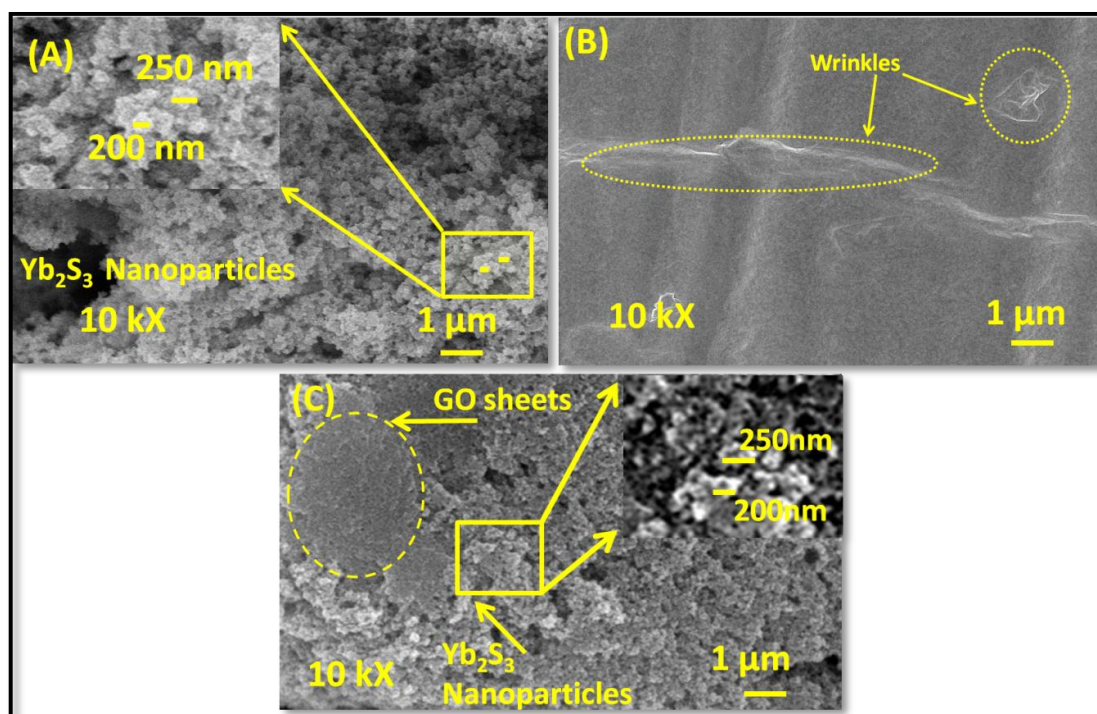


Fig. 4.7: FE-SEM images of (A) Yb₂S₃, (B) GO and (C) GO/Yb₂S₃ composite thin films at magnification of 10 kX.

Fig. 4.7(C) displays that Yb₂S₃ nanoparticles are aggregated on the surface of GO sheets, forming GO/Yb₂S₃ nanocomposite. The porous structure of composite is controlled due to the wrinkles of GO. The size of Yb₂S₃ nanoparticles is in between 200-250 nm as seen as inset of **Fig. 4.7(C)**. It might be noted that Yb₂S₃ nanoparticles are tightly adhered with GO sheets during SILAR process, which facilitates the aggregation of nanoparticles and restacking of GO sheets. The porous nanoparticles structure is helpful for the enhancement of supercapacitive activities. Pujari et al [20] deposited Yb₂S₃ thin film using the hydrothermal method and observed non-uniform

distributed nanorods. Ubale et al [19] synthesized Yb_2S_3 thin film by CBD method and displayed nano-grains like morphology. Ghogare et al [23, 24] deposited GO, $\text{GO}/\text{La}_2\text{S}_3$ and $\text{GO}/\text{Sm}_2\text{S}_3$ composite thin films by SILAR method and observed homogeneous layer structure, grass-like and flower-like surface morphologies, respectively.

4.3.3.3 Transmission electron microscopy (TEM):

TEM technique was used to find out the surface morphology, particle size and crystal structure of $\text{GO}/\text{Yb}_2\text{S}_3$ composite thin film material. The TEM images of $\text{GO}/\text{Yb}_2\text{S}_3$ composite thin film are shown in Fig. 4.8(A-C). Fig. 4.8(A) displays that Yb_2S_3 nanoparticles are agglomerated over the GO sheets. Fig. 4.8(B) illustrates the interplanar spacing (d) of $\text{GO}/\text{Yb}_2\text{S}_3$ thin film material as 0.237 nm, which is in agreement of interplanar spacing (d) determined from XRD studies. The interplanar spacing of 0.241 nm corresponds to the (401) plane of Yb_2S_3 and GO sheets spacing in the high-resolution transmission electron microscope (HR-TEM) image (Fig. 4.8(B)). The selected area electron diffraction (SAED) pattern image of $\text{GO}/\text{Yb}_2\text{S}_3$ reveals the nanocrystalline nature of material as shown in Fig. 4.8(C). It shows diffuse rings indicating the formation of nanoparticles. These results confirm of the formation of $\text{GO}/\text{Yb}_2\text{S}_3$ composite thin film material.

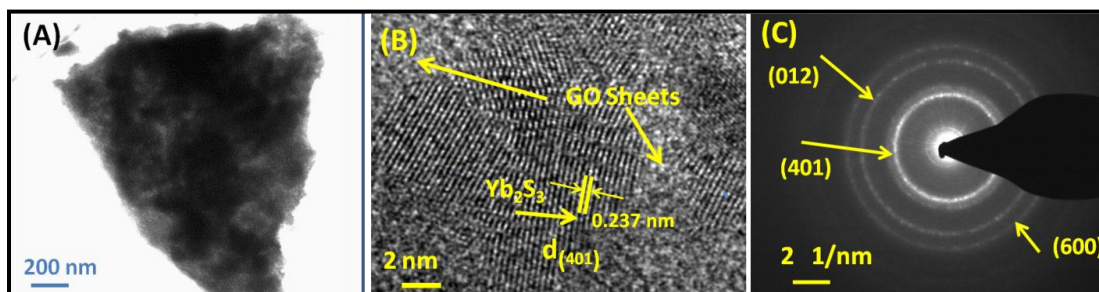


Fig. 4.8: (A, B) HR-TEM images, and (C) selected area electron diffraction (SAED) pattern of $\text{GO}/\text{Yb}_2\text{S}_3$ composite material.

4.3.4 Supercapacitive study:

4.3.4.1 Cyclic voltammetry (CV):

The CV measurement was performed to analyze the supercapacitive performance of Yb_2S_3 , GO and $\text{GO}/\text{Yb}_2\text{S}_3$ composite electrodes using a three-electrode cell configuration system within a potential window of -1.0 to 0 V.Hg/HgO in 1.0 M Na_2SO_4 electrolyte. Fig. 4.9(A-C) shows the CV curves of Yb_2S_3 , GO and $\text{GO}/\text{Yb}_2\text{S}_3$ composite electrodes in the scan range of 5- 200 mV s^{-1} . The quasi-rectangular curves

of Yb_2S_3 , GO and GO/ Yb_2S_3 thin films show the pseudocapacitor behavior. The area under of CV curve of GO/ Yb_2S_3 composite electrode is larger than the bare GO and Yb_2S_3 electrodes as seen in **Fig. 4.9(C)**. The specific capacitance (C_s) of Yb_2S_3 , GO and GO/ Yb_2S_3 composite electrodes was calculated from equation 2.13.

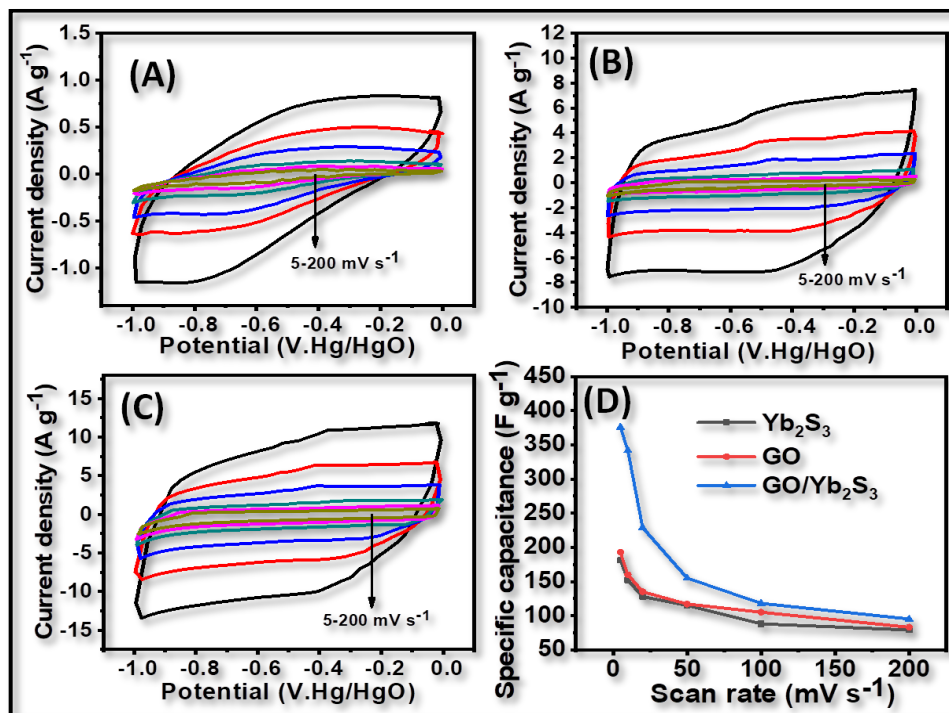


Fig. 4.9: The CV curves (A) Yb_2S_3 , (B) GO and (C) GO/ Yb_2S_3 composite thin films at varied scan rates of 5-200 mV s⁻¹, and (D) plots of specific capacitance versus scan rates for Yb_2S_3 , GO and GO/ Yb_2S_3 composite thin films.

The GO/ Yb_2S_3 composite electrode exhibits maximum specific capacitance of 376 F g⁻¹ compared to Yb_2S_3 (181 F g⁻¹) and GO electrodes (193 F g⁻¹) within potential window of -1.0 to 0.0 V.Hg/HgO at 5 mV s⁻¹ scan rate. The synergistic effect of GO/ Yb_2S_3 composite thin film results in enhancing electrochemical supercapacitive activities [16]. The improvement of C_s in GO/ Yb_2S_3 composite thin film could be due to the porous and interconnected morphology which leads to efficient charge storage and also facilitates the electrolyte diffusion and aggregation of electroactive material during the insertion/deinsertion time [12].

Fig. 4.9(D) indicates the plots of specific capacitance versus scan rate for Yb_2S_3 , GO and GO/ Yb_2S_3 composite electrodes. The C_s decreases with increase in the scan rate. The capacitance of Yb_2S_3 , GO and GO/ Yb_2S_3 composite electrodes decreased from 181 to 80 F g⁻¹, 193 to 85 F g⁻¹ and 376 to 115 F g⁻¹, respectively with scan rates from 5 to 200 mV s⁻¹. The decrease in C_s at higher scan rate is assigned to the presence of

inner active sites that cannot maintain the faradic transitions due to the diffusion effect of ions within the electrode [11].

4.3.4.2 Galvanostatic charge discharge (GCD):

The GCD curves of Yb_2S_3 , GO and $\text{GO}/\text{Yb}_2\text{S}_3$ composite electrodes recorded ($1-5 \text{ A g}^{-1}$) in the potential range from -1 to 0 V.Hg/HgO are shown in **Fig. 4.10(A-C)**. As seen in **Fig. 4.10 (A-C)**, GCD curves of Yb_2S_3 thin film are non-linear due to the pseudocapacitive nature where electrochemical adsorption-desorption reactions between the interface of electrode and electrolyte take place [33]. The GCD curves of GO thin film are linear due to the surface and near surface controlled capacitive behavior from GO thin film. For $\text{GO}/\text{Yb}_2\text{S}_3$ composite electrode, charging and discharging curves are almost symmetric due to its corresponding discharge counterpart with a small internal resistance (IR) drop, indicating the pseudocapacitive contribution along with the double layer contribution. The C_s of Yb_2S_3 , GO and $\text{GO}/\text{Yb}_2\text{S}_3$ composite electrodes are evaluated from relation 2.14.

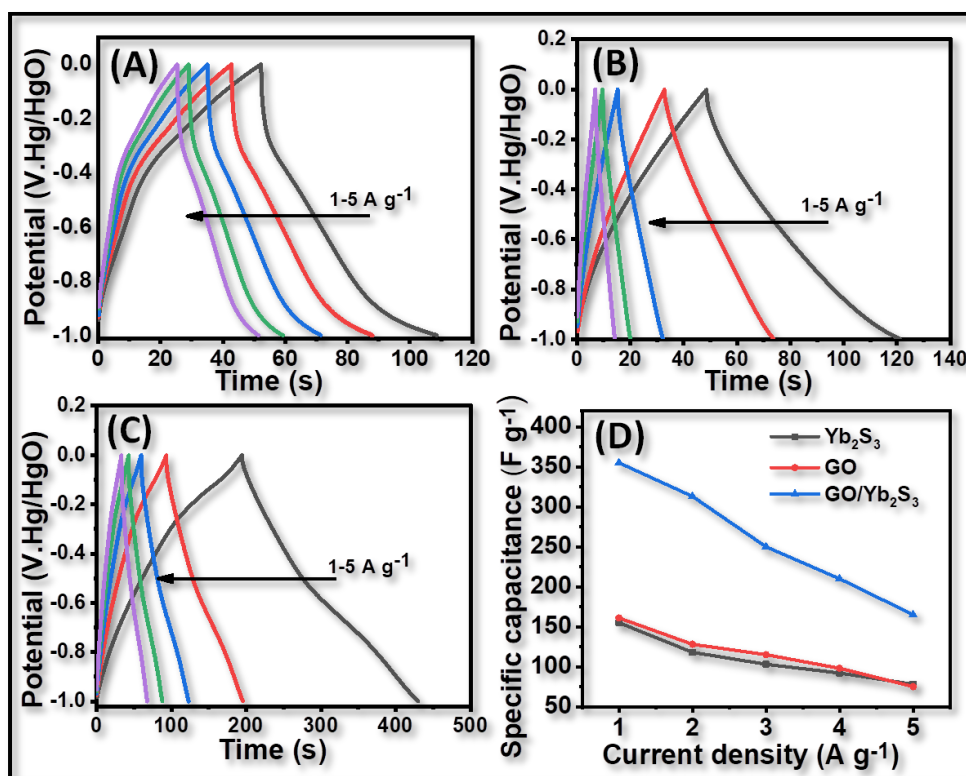
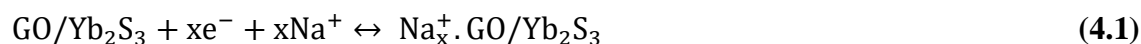


Fig. 4.10: The GCD curves of (A) Yb_2S_3 , (B) GO and (C) $\text{GO}/\text{Yb}_2\text{S}_3$ composite thin films at various current densities $1-5 \text{ A g}^{-1}$, and (D) plots of specific capacitance versus current density for Yb_2S_3 , GO and $\text{GO}/\text{Yb}_2\text{S}_3$ composite thin films at current densities of $1-5 \text{ A g}^{-1}$.

The maximum C_s achieved for Yb_2S_3 , GO and $\text{GO}/\text{Yb}_2\text{S}_3$ composite electrodes are 155, 161 and 350 F g^{-1} , respectively. The plots of C_s versus charging current

densities for Yb_2S_3 , GO and $\text{GO}/\text{Yb}_2\text{S}_3$ composite electrodes are illustrated in **Fig. 4.10(D)**. During the GCD cycling test of Yb_2S_3 , GO and $\text{GO}/\text{Yb}_2\text{S}_3$ composite electrodes, the charge/discharge time period enhanced at the lower current density, as the ions may totally occupy the active sites between the interface of electrode and electrolyte. Similarly, the charge/discharge time period decreased at higher current density, as the ions occupy the partial number of active sites between the interface of electrode and electrolyte, indicating that C_s is inversely proportional to the current density [34, 35].

The charge-discharge mechanism of $\text{GO}/\text{Yb}_2\text{S}_3$ composite thin film is proposed by the following relation as,



4.3.4.3 Stability:

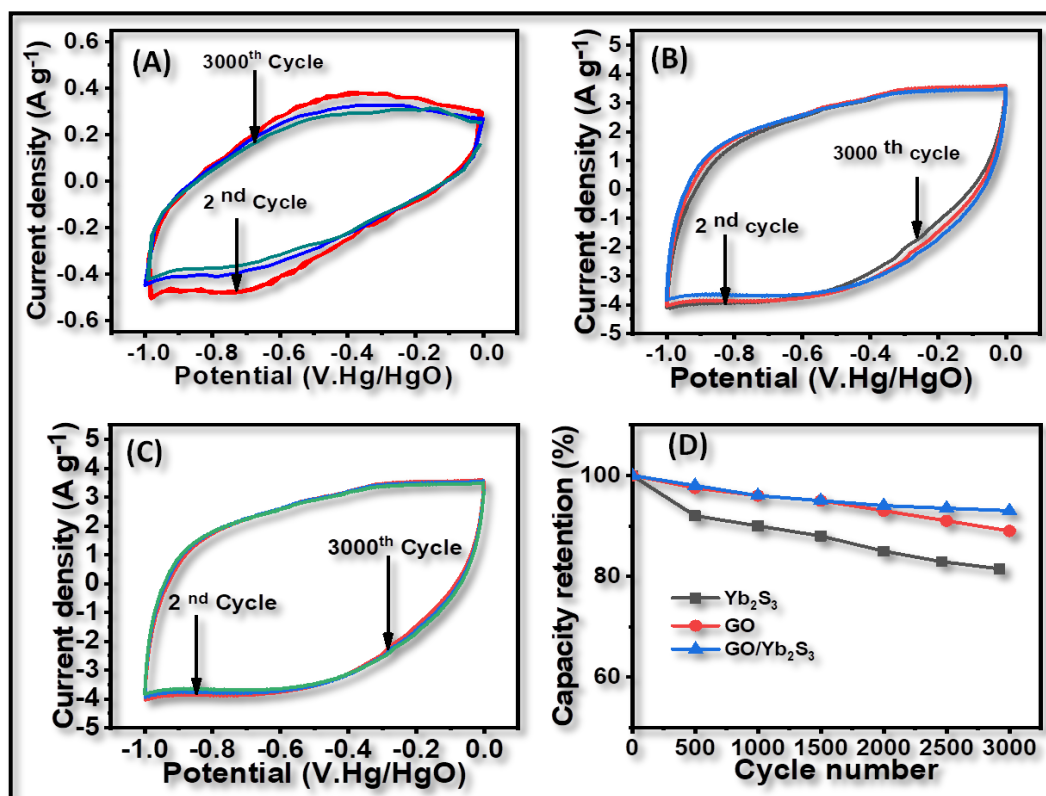


Fig. 4.11: Cyclic stability curves of (A) Yb_2S_3 , (B) GO, and (C) $\text{GO}/\text{Yb}_2\text{S}_3$ composite thin films at scan rate 100 mV s^{-1} , and (D) capacity retentions of Yb_2S_3 , GO and $\text{GO}/\text{Yb}_2\text{S}_3$ composite thin films.

The long term electrochemical cyclic stability is an important factor for the use of supercapacitors in practical applications. **Fig. 4.11(A-C)** shows the cyclic behavior over 3000 CV cycles of Yb_2S_3 , GO and $\text{GO}/\text{Yb}_2\text{S}_3$ composite electrodes. It is seen from

Fig. 4.11(D) that, Yb_2S_3 , GO and GO/ Yb_2S_3 composite electrodes have 83, 89 and 93 % capacitive retention over 3000 CV cycles, respectively. The GO/ Yb_2S_3 electrode shows the higher capacitive retention over Yb_2S_3 and GO thin films indicating less loss of active material in the electrolyte during CV cycling (**Fig. 4.11(C)**). Pujari et al [20] reported 78 % cyclic retention over 1000 cycles for hydrothermally deposited Yb_2S_3 thin film. Ghogare et al [23] reported 88.14 % cyclic retention over 2000 cycles for SILAR synthesized GO/ Sm_2S_3 composite thin films.

4.3.4.4 Electrochemical impedance spectroscopy (EIS) study:

The Nyquist plots of Yb_2S_3 , GO and GO/ Yb_2S_3 composite electrodes in the three electrode system obtained using the EIS in the frequency range from 100 kHz to 0.01 Hz are shown as **Fig. 4.12(A-C)**. The R_s suggesting the ionic resistance of applied electrolyte was calculated by non-zero intercept in the real axis (Z') from the Nyquist curve [36]. The R_{ct} at an electrolyte-electrode boundary region is particular by semi-circular arc at higher frequency region [37]. The W is liable for travel between the lower and higher frequency regions.

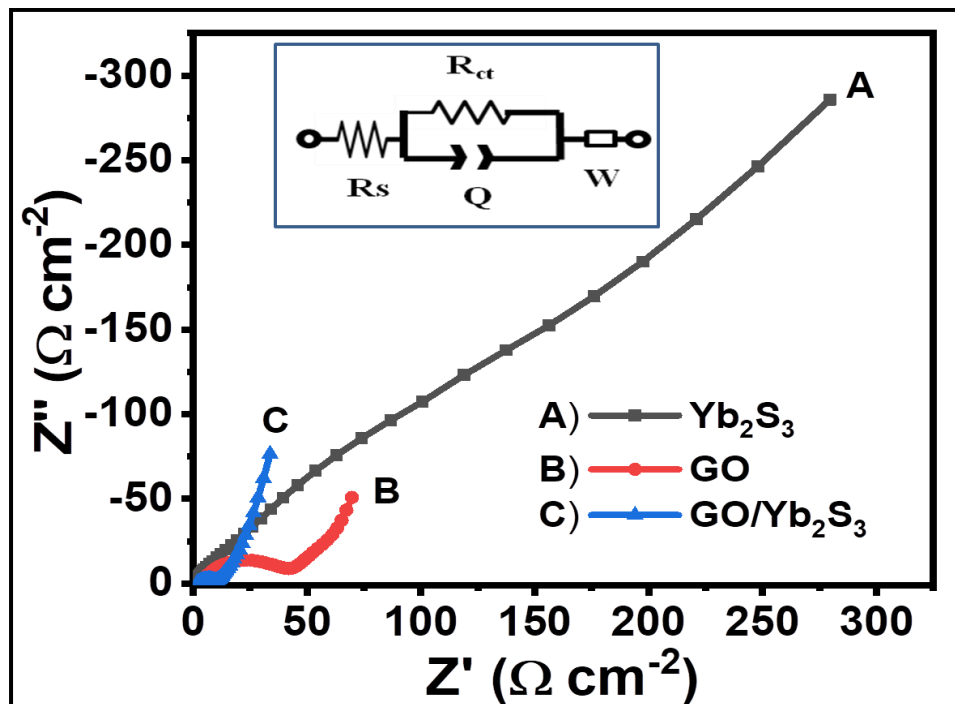


Fig. 4.12: Nyquist plots of (A) Yb_2S_3 , (B) GO and (C) GO/ Yb_2S_3 composite thin films [Inset shows the equivalent fitted circuit].

The Nyquist plots of Yb_2S_3 , GO and GO/ Yb_2S_3 composite electrodes have an almost vertical line in the low-frequency region, indicating a capacitive behavior. The R_s , R_{ct} and W values are calculated from best fitted data curves. The equivalent circuit

diagram is demonstrated as inset of **Fig. 4.12**. The Nyquist plots (**Fig. 4.12**) of Yb_2S_3 , GO and $\text{GO}/\text{Yb}_2\text{S}_3$ composite electrodes consist of a semicircle loops at initial (high-frequency region) and later sloped line (at a low-frequency region). The first point of the semicircle loops are ascribed to R_s and end points to R_{ct} , and the slope of the line at low frequency is attributed to the W resistance. In the high-frequency region, Yb_2S_3 , GO and $\text{GO}/\text{Yb}_2\text{S}_3$ composite electrodes show the solution resistance (R_s) of 4.29, 3.07 and 1.70 $\Omega \text{ cm}^{-2}$, respectively. The R_{ct} of $\text{GO}/\text{Yb}_2\text{S}_3$ (8 $\Omega \text{ cm}^{-2}$) composite electrode is less as compared to Yb_2S_3 (56 $\Omega \text{ cm}^{-2}$) and GO (38 $\Omega \text{ cm}^{-2}$) thin film electrodes. Less R_s and R_{ct} suggest a small electrochemical resistance and high charge-transfer rate between the electrolyte and the active material. Warburg resistances (W) of Yb_2S_3 , GO and $\text{GO}/\text{Yb}_2\text{S}_3$ composite electrodes are 60.32, 43.74 and 10.51 $\Omega \text{ cm}^{-2}$, respectively. EIS parameters of Yb_2S_3 , GO and $\text{GO}/\text{Yb}_2\text{S}_3$ thin films are shown in **table 4.3**. The improvement of electronic transportation in $\text{GO}/\text{Yb}_2\text{S}_3$ composite electrode is evidenced from EIS analysis.

Table 4.3: EIS parameters of Yb_2S_3 , GO and $\text{GO}/\text{Yb}_2\text{S}_3$ thin films.

Parameter	Thin films		
	Yb_2S_3	GO	$\text{GO}/\text{Yb}_2\text{S}_3$
R_s ($\Omega \text{ cm}^{-2}$)	4.29	3.07	1.70
Q (mF)	117.3	24.12	9.16
R_{ct} ($\Omega \text{ cm}^{-2}$)	56.00	38.00	8.00
W ($\Omega \text{ cm}^{-2}$)	60.32	43.74	10.51

4.4: Conclusions:

In summary, Yb_2S_3 , GO, and $\text{GO}/\text{Yb}_2\text{S}_3$ composite thin films are successfully prepared by SILAR method over SS substrates at room temperature. The $\text{GO}/\text{Yb}_2\text{S}_3$ composite thin film showed monoclinic crystal structure with hydrophilic nature. Morphology of $\text{GO}/\text{Yb}_2\text{S}_3$ composite thin film showed porous nanoparticles. Supercapacitive performance of $\text{GO}/\text{Yb}_2\text{S}_3$ composite thin film achieved a high C_s of 376 F g^{-1} , which is more than that of Yb_2S_3 (181 F g^{-1}) and GO (193 F g^{-1}) at scan rate 5 mV s^{-1} within potential range of -1 to 0 V in 1.0 M Na_2SO_4 electrolyte. The $\text{GO}/\text{Yb}_2\text{S}_3$ composite thin film showed better electrochemical supercapacitive performance than GO and Yb_2S_3 thin films. **Table 4.4** shows the supercapacitive performance of Yb_2S_3 , GO and $\text{GO}/\text{Yb}_2\text{S}_3$ thin films.

Table 4.4: Supercapacitive performance of Yb₂S₃, GO and GO/Yb₂S₃ thin films.

Method	Thin film	Spe. Cap. (Cs) (F g ⁻¹)	Potential range (V.Hg/HgO)	Sol. Resi., (Rs.(Ω cm ⁻²))	Charge tran. Resi.,(Rct.(Ω cm ⁻²))	Cyclic stability (%)
L-b-L	GO	193	-1 to 0	3.07	38	89
SILAR	Yb ₂ S ₃	181	-1 to 0	4.29	56	83
SILAR	GO/Yb ₂ S ₃	376	-1 to 0	1.70	8.0	93

The GO/Yb₂S₃ composite thin film showed the porous nanoparticles surface morphology. The porous nanoparticles morphology obtained due to Yb₂S₃ composite with GO. The role of GO is to control pore structure. The porous surface texture can be applicable for electrochemical reaction. The porous morphology of GO/Yb₂S₃ composite thin film electrode material is useful for more intercalation/deintercalation of electrolyte ion during a redox reaction. Therefore, specific capacitance of GO/Yb₂S₃ composite thin film electrode is enhanced.

4.5 References:

1. P. Asen and S. Shahrokhian, *J. Electroanal. Chem.*, 823, (2018), 505-516.
2. J. Zhang, L. Su, L. Ma, D. Zhao, C. Qin, Z. Jin, K. Zhao, *J. Electroanal. Chem.*, 790, (2017), 40-49.
3. Y. Li, Q. Yan, Y. Wang, Y. Li, M. Zhu, K. Cheng, X. Zhang, *Appl. Surf. Sci.*, 493, (2019), 506-513.
4. A. K. Geim and K. S. Novoselov, *Nat. Mater.*, 6, (2007), 183-191.
5. D. Tian, X. Lu, G. Nie, M. Gao, N. Song, C. Wang, *Appl. Surf. Sci.*, 458, (2018), 389-396.
6. G. Yang, *Nano Res. Lett.*, 12, (2017), 387-403.
7. O. C. Compton and S. T. Nguyen, *Small*, 6, (2010), 711-723.
8. S. Mao, H. Pu, J. Chen, *RSC Adv.*, 2, (2012), 2643-2662.
9. K. S. Novoselov , A. K. Geim , S. V. Morozov , D. Jiang , Y. Zhang , S. V. Dubonos , I. V. Grigorieva, *science oct.*, 306, (2004), 666-669.
10. X. Zhou, J. Zhang, H. Wu, H. Yang, J. Zhang, S. Guo, *J. Phys. Chem. C*, 115, (2011), 11957-11961.
11. G. S. Gund, D. P. Dubal, B. H. Patil, S. S. Shinde, C. D. Lokhande, *Electrochim. Acta.*, 92, (2013), 205-215.
12. K-J. Huang, L. Wang, Y-J. Liu, Y-M. Liu, H-B. Wang, T. Gan, L-L. Wang, *Int. J. Hydrog. Energy*, 38, (2013), 14027-14034.
13. Q. Zhang, Y. Li, Y. Feng, W. Feng, *Electrochim. Acta.*, 90, (2013), 95-100.
14. C. Z. Yao, B. H. Wei, H. X. Ma, Q. J. Gong, K.W. Jing, H. Sun, L. X. Meng, *Mater. Lett.*, 65, (2011), 490-492.
15. Y. Li, B. Guan, A. Maclellan, Y. Hu, D. Li, J. Zhao, Y. Wang, H. Zhang, *Electrochim. Acta.*, 241, (2017), 1-47.
16. V. S. Kumbhar, A. C. Lokhande, N. S. Gaikwad, C. D. Lokhande, *Ceram. Int.*, 41, (2015), 5758-5764.
17. T. T. Ghogare, R. B. Pujari, A. C. Lokhande, C. D. Lokhande, *Appl. Phys., A*, 124, (2018), 248-252.
18. S. J. Patil and C. D. Lokhande, *Mater. Des.*, 87, (2015), 939-948.
19. S. B. Ubale, R. N. Bulakhe, V. J. Mane, D. B. Malavekar, I. In, C. D. Lokhande, *Appl. Nanosci.*, 10, (2020), 5085-5097.
20. R. B. Pujari, A. C. Lokhande, T. T. Ghogare, S. B. Kale, C. D. Lokhande, *J. Mater. Sci.: Mater. Electron.*, 29, (2018), 14116-14121.
21. U. K. Mohite, K. M. Gadhave, C. D. Lokhande, *Indian J. Pure Appl. Phys.*, 32, (1994), 772-777.
22. C. D. Jadhav, S. S. Karade, B. R. Sankapal, G. P. Patil, P. G. Chavan, *Chem. Phys. Lett.*, 723, (2019), 146-150.
23. T. T. Ghogare, A. C. Lokhande, R. B. Pujari, C. D. Lokhande, *SN Applied Sciences*, 1, (2019), 110-117.
24. T. T. Ghogare, V. C. Lokhande , T. Ji , U. M. Patil , C. D. Lokhande, *Surf. Interfaces*, 19, (2020), 100507-100513.
25. H. M. Pathan and C. D. Lokhande, *Bull. Mater. Sci.*, 27, (2004), 85-111.
26. J. Kim, L. J. Cote, F. Kim, W. Yuan, K. R. Shull, J. X. Huang, *J. Am. Chem. Soc.*, 132, (2010), 8180-8186.
27. W. S. Hummers and R. E. Offeman, *J. Am. Chem. Soc.*, 80, (1958), 1339-1339.
28. F. Rivera-López, and M. Pérez, *Surf. Interface Anal.*, 44, (2012), 927-930.

29. S. S. Karade, D. P. Dubal, B. R. Sankapal, RSC Adv., 6, (2016), 39159-39165.
30. R. B. Pujari, A. C. Lokhande, A. A. Yadav, J. H Kim, C. D. Lokhande, Mater. Des., 108, (2016), 510-517.
31. S. J. Patil, J. H. Kim, D.W. Lee, J. Power Sources, 342, (2020), 652-665.
32. B. G. Sundara Raj, R. N. Radhika Ramprasad, A. M. Asiri, J. J. Wu, S. Anandan, Electrochim. Acta., 156, (2015), 127-137.
33. V. J. Mane, D. B. Malavekar, S. B. Ubale, R. N. Bulakhe, Insik In, C. D. Lokhande, Electrochem. Acta., 335, (2020), 135613-135664.
34. P. A. Shinde, V. C. Lokhande, A. M. Patil, A. A. Yadav, C. D. Lokhande, Int. J. Eng. Res. Technol., 10, (2017), 532-537.
35. B. Pandit, D. P. Dubal, P. Gómez-Romero, B. B. Kale, B. R. Sankapal, Sci. Rep., 7, (2017), 43430-43442.
36. S. A. Pande, B. Pandit, B. R. Sankapal, Mater. Lett., 209, (2017), 97-101.
37. B. Pandit, G. K. Sharma, B. R. Sankapal, J. Colloid Interface Sci., 505, (2017), 1011-1017.

Chapter-V

***Synthesis, Characterization and
Supercapacitive Performance of
Manganese Oxide Thin Films***

Chapter-V

Synthesis, characterization and supercapacitive performance of manganese oxide thin films

Sr. no.	Title	Page no.
	Section -A	93
5A.	Synthesis and characterization of manganese oxide thin films (SILAR method)	
5A.1	Introduction	93
5A.2	Experimental details	94
	<i>5A.2.1 Substrate cleaning</i>	94
	<i>5A.2.2 Precursors</i>	94
	<i>5A.2.3 Synthesis of manganese oxide thin films</i>	94
	<i>5A.2.4 Characterization</i>	94
5A.3	Results and discussion	95
	<i>5A.3.1 Film formation and reaction mechanism</i>	95
	<i>5A.3.2 Structural studies</i>	96
	<i>5A.3.2.1 X-ray diffraction (XRD)</i>	96
	<i>5A.3.2.2 X-ray photoelectron spectroscopy (XPS)</i>	97
	<i>5A.3.2.3 Fourier transform infrared spectroscopy (FT-IR)</i>	98
	<i>5A.3.2.4 Morphological study</i>	98
	<i>5A.3.2.4.1 Contact angle measurement</i>	98
	<i>5A.3.2.4.2 Field emission scanning electron microscopy (FE-SEM)</i>	99
	Section- B	100
5B.	Supercapacitive performance of manganese oxide thin films (SILAR method)	
5B.1	Supercapacitive study	100
	<i>5B.1.1 Cyclic voltammetry (CV)</i>	100
	<i>5B.1.2 Galvanostatic charge discharge (GCD)</i>	100
	<i>5B.1.3 Stability</i>	101
	<i>5B.1.4 Electrochemical impedance spectroscopy (EIS)</i>	101
5C.	Conclusions	102
5D.	References	103

Section -A

5A: Synthesis and characterization of manganese oxide thin films (SILAR method):

5A.1: Introduction:

The sample range of metal oxides (ruthenium, nickel, and manganese oxides, etc.) is used as supercapacitor thin film electrode materials [1]. Among the various transition metal oxides, manganese oxide (MnO_2) is an extensively used in oxidation catalyst materials, supercapacitors, aqueous batteries, and other fields due to their low toxicity, abundant reserves, and simple synthesis process [2-5]. Especially in the field of supercapacitors, MnO_2 is considered one of the most promising positive window electrode materials. The reasons of the admirable supercapacitive properties of MnO_2 can be summed up in two aspects. From the point of view, an electrochemical properties, MnO_2 shows excellent supercapacitive properties: (i) a high theoretical capacitance ($1,370 \text{ F g}^{-1}$) referring to the single-electron faradic reaction of each manganese atom; (ii) a large potential window (0.0-1.0 V), and (iii) superb electrochemical supercapacitive behavior in the neutral electrolyte, leading to lower chemical corrosion of current collector [6]. In the point of view of economy and environmental protection, MnO_2 is environmentally friendly, abundant in earth and it has low price [7]. These unique physical and chemical properties make MnO_2 an ideal choice for pseudocapacitor thin film electrode materials. It is worth noting that, MnO_2 contains a number of crystal structures, including α -, β -, γ -, δ -, and λ - MnO_2 ; and its electrochemical energy storage properties are determined by various crystal forms. Research has shown that, the chain or tunnel structure of α -, β -, and γ - MnO_2 with large two dimensional tunneling structures facilitate electron transfer to provide a relatively large specific capacitance value [8, 9]. The surface area of δ - MnO_2 with a sheet or layered-like structure is more favorable for cation intercalation/deintercalation than the amorphous structure. The three-dimensional hinge structure of λ - MnO_2 can provide more active sites for superior supercapacitor properties [10].

There are more studies on the bulk MnO_2 and less on film MnO_2 . The MnO_2 films have been prepared by various methods viz., co-precipitation [11], liquid-phase exfoliation (LPE) [12], potentiostatic electrodeposition [13], hydrolyzing [14], synergistic [15], etc. As compared to the other deposition methods, SILAR is an attractive one due to its own advantages such as cost effectiveness, simplicity and

reproducibility. It is greatly suitable for producing large-scale area thin films at room temperature and avoids corrosion or oxidation of metallic substrate [16].

In the present chapter, MnO₂ thin films were prepared on SS substrate via SILAR method. The MnO₂ thin films were characterized by X-ray diffraction (XRD), X-ray photoelectron spectroscopy (XPS), Fourier transform infra red spectroscopy (FT-IR), contact angle and field emission scanning electron microscopy (FE-SEM) techniques. Supercapacitive properties of MnO₂ thin films were studied using the CV, GCD, and EIS tests in 1 M Na₂SO₄ electrolyte.

5A.2 Experimental details:

5A.2.1 Substrate cleaning:

The cleaning of substrate procedure part is described in section 3A.2.1 (Chapter-III).

5A.2.2 Precursors:

All the AR grade reagents such as manganese sulfate (MnSO₄), potassium permanganate (KMnO₄, 99.9%) and sodium sulfate (Na₂SO₄) were purchased from Thomas baker and used without further purification. DDW was used as a solvent in the experiment. All solutions were freshly prepared.

5A.2.3 Synthesis of manganese oxide thin films:

The MnO₂ thin film was prepared by immersing the substrate in individually placed cationic (0.1 M MnSO₄) and anionic (0.1 M KMnO₄) precursor solutions and rinsing with every immersion time. Formation of MnO₂ thin film material by SILAR method on SS substrate is described in following four steps (a-d):

a) The SS substrate is dipped in 50 ml DDW containing 0.1 M MnSO₄ solution for 10 s, the Mn²⁺ ions are adsorbed on SS substrate. b) Then substrate is dipped in DDW for 20 s to the eliminating the loosely bounded Mn²⁺ ions. c) After the substrate is dipped in 50 ml DDW containing 0.1 M KMnO₄ solution for 10 s, the O²⁻ ions reacts with Mn²⁺ ions on the substrate and forms as MnO₂ molecule. d) Repeated step 'b' to eliminate the unreacted or unbounded O²⁻ ions or molecules. This completes one SILAR cycle for the formation of MnO₂ film. Such 90 SILAR cycles were repeated to get an uniform MnO₂ film.

5A.2.4 Characterization:

The crystallographic study of MnO₂ film was carried out using X-ray diffractometer (Rikagu 600 mini flex). The surface morphology of MnO₂ film was

examined by field emission scanning electron microscope (model Crossbeam 1560 XBFIB workstation). The chemical states of elements in MnO_2 film were confirmed using X-ray photoelectron spectrometer (ThermoVG Scientific, United Kingdom). The chemical bands and vibration modes were identified using an alpha (II) Bruker instrument. The water contact angle was measured by Rame-Hart USA. Electrochemical behavior was tested in three electrode cell system using MnO_2 thin film as a working electrode, platinum as a counter electrode and mercury/mercury oxide (Hg/HgO) as a reference electrode using battery cycler (ZIVE MP1 workstation, S. Korea). The electrochemical characterisations such as CV, GCD and EIS were studied in 1 M Na_2SO_4 electrolyte.

5A.3 Results and discussion:

5A.3.1 Film formation and reaction mechanism:

In order to prepared MnO_2 film over SS substrate via SILAR method, 0.1 M MnSO_4 solution was used as a cation (Mn^{2+}) source and 0.1 M KMnO_4 solution as an anion (O^{2-}) source. When SS substrate was immersed in cationic Mn^{2+} solution, the cations Mn^{2+} were adsorbed over the SS substrate.

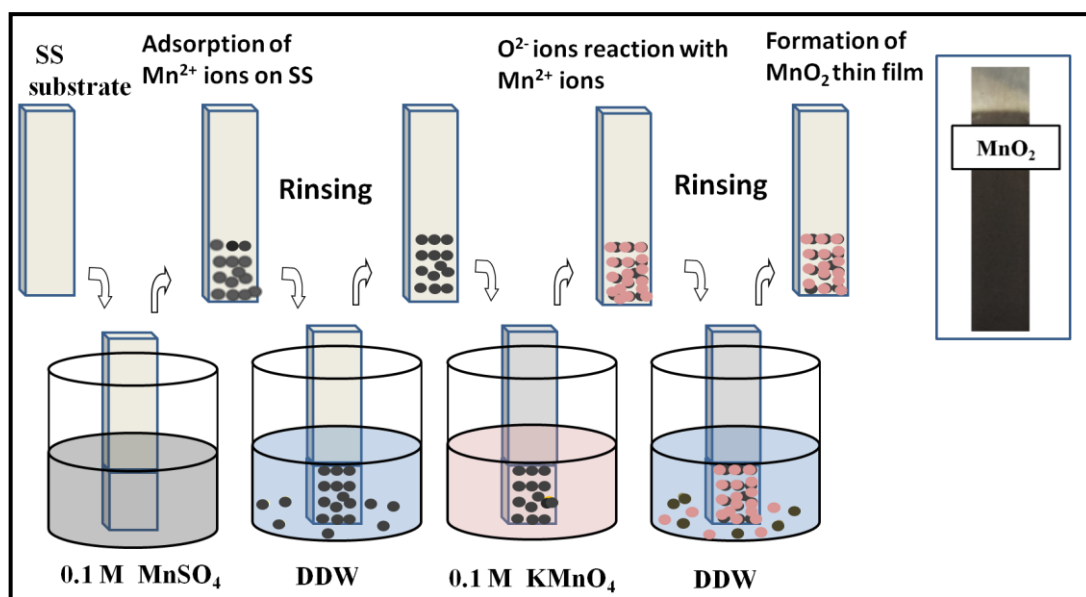


Fig. 5.1: The schematic preparation for deposition of MnO_2 thin film electrode by SILAR method [Inset shows the photograph of MnO_2 thin film electrode].

Then the SS substrate was dipped in DDW to remove the loosely bounded Mn^{2+} ions. The substrate was immersed in anionic solution, the O^{2-} ions were reacted with Mn^{2+} ions for the formation of MnO_2 thin film. Lastly, the substrate was again dipped

in DDW to remove the unreacted O²⁻ ions or molecules. This completes one deposition cycle of MnO₂ film formation. The possible MnO₂ formation reaction can be written as,

$$3\text{MnSO}_4 + 2\text{KMnO}_4 + 2\text{H}_2\text{O} \rightarrow 5\text{MnO}_2 + \text{K}_2\text{SO}_4 + 2\text{H}_2\text{SO}_4 \quad (5.1)$$

In this case, KMnO₄ precursor solution acts as a strong oxidizing agent. These films are used as positive electrode in asymmetric devices. The schematic preparation for deposition of MnO₂ thin film electrode by SILAR method is shown in **Fig. 5.1** [Inset shows the photograph of MnO₂ thin film electrode by SILAR method]. The optimized preparative parameters for deposition of MnO₂ film by SILAR method are given in **table 5.1**.

Table 5.1: Preparative parameters for deposition of MnO₂ thin film by SILAR method.

Parameter	Precursor solutions	
	Cationic MnSO ₄	Anionic KMnO ₄
Concentrations (M)	0.1	0.1
pH	6.5	5.5
Dipping time (s)	10	10
Drying time (s)	10	10
Rinsing time (s)	20	20
Deposition temperature (degree celsius)	27	27

5A.3.2 Structural studies:

5A.3.2.1 X-ray diffraction (XRD) study:

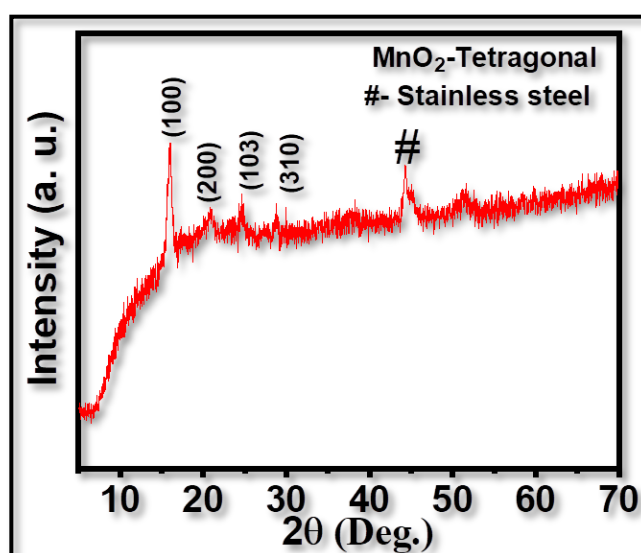


Fig. 5.2: The XRD pattern of MnO₂ thin film.

The XRD pattern of MnO₂ thin film material is demonstrated in **Fig. 5.2**. The diffraction peaks correspond to the (100), (200), (103) and (310) planes of tetragonal

phase of α -MnO₂ thin film material [JCPDS card no. 44-0141] [16]. The XRD pattern revealed that α -MnO₂ thin film material is nanocrystalline. The crystallite size ‘D’ was determined from Scherer’s equation was 43 nm using (100) plane. The diffraction peaks denoted by hash (#) correspond to SS substrate. The lower intensity of diffraction peaks for MnO₂ film indicates the nanocrystalline nature.

5A.3.2.2 X-ray photoelectron spectroscopy (XPS):

To investigate the chemical composition and oxidation state in MnO₂ thin film material, XPS was examined. The survey scan spectrum of MnO₂ thin film demonstrated in Fig. 5.3(A) reveals the existence of Mn2p and O1s elemental states. Fig. 5.3(B, C) displays high resolution XPS spectra of MnO₂ material. The binding energy peaks at 642.2 and 653.3 eV correspond to Mn2p_{3/2} and Mn2p_{1/2} states, respectively [17]. The O1s spectrum peaks of C-O-H, C=C and C-O at cited binding energies of 530, 531.5 and 532.5 eV, respectively shown in Fig. 4.5(E) are good agreement with literature [18]. These results confirm the formation of MnO₂ thin film material.

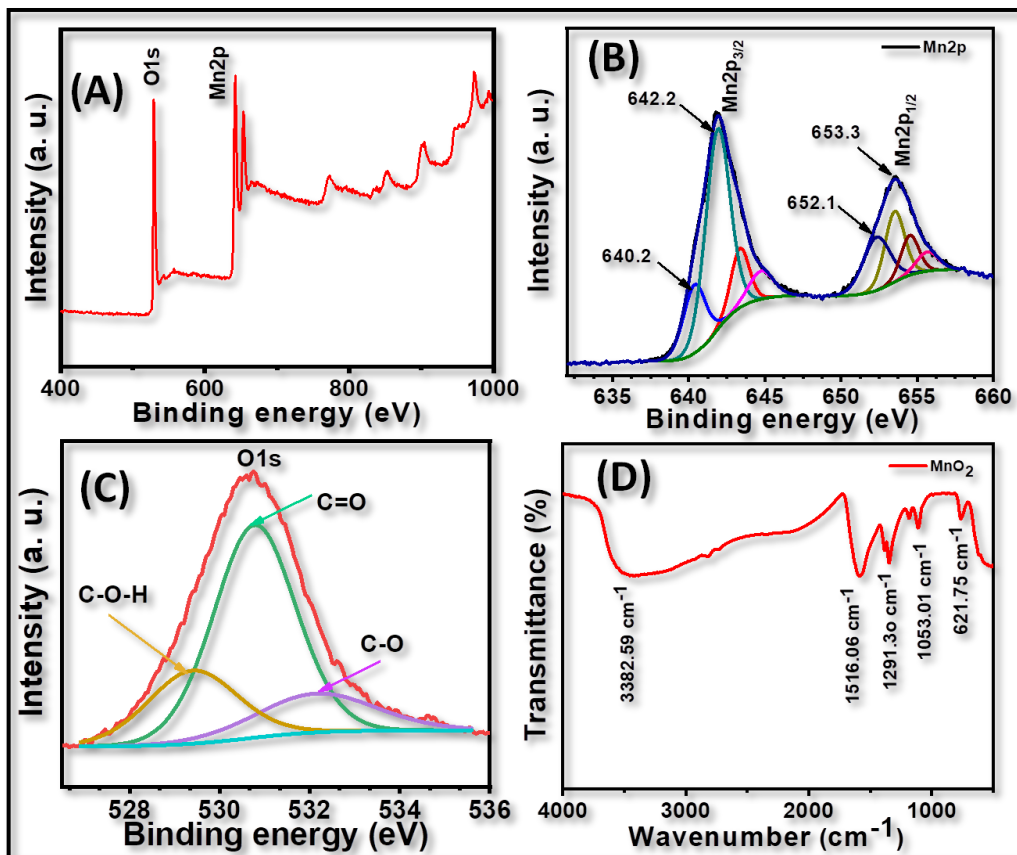


Fig. 5.3: (A) The XPS survey spectrum of MnO₂ thin film. The XPS spectra of MnO₂ thin film for (B) Mn2p region and (C) O1s region and (D) FT-IR spectrum of MnO₂ thin film.

5A.3.2.3 Fourier transform infrared spectroscopy (FT-IR):

FT-IR is a sensitive tool for find out vibration mode and different bands from thin film material. The MnO_2 sample was characterized via FT-IR spectroscopic technique in the wavenumber range between from $4000\text{-}400\text{ cm}^{-1}$. **Fig. 5.3(D)** demonstrates the FT-IR spectrum of MnO_2 thin film. The broad band or peak at wavenumber of 3382 cm^{-1} is assigned due to -OH stretching vibration mode [19]. The absorption peak at a wavelength of 1516 cm^{-1} certify the -C-O bending vibrations joining with Mn-atoms [20]. A number of small incorporated peaks around of 1291 and 1053 cm^{-1} are twisting vibration of O-H bonds connected to Mn-atoms [21]. The incorporated peak at 621 cm^{-1} is related to the linking mode of Mn-O stretching mode [22].

5A.3.2.4 Morphological study:

5A.3.2.4.1 Contact angle measurement:

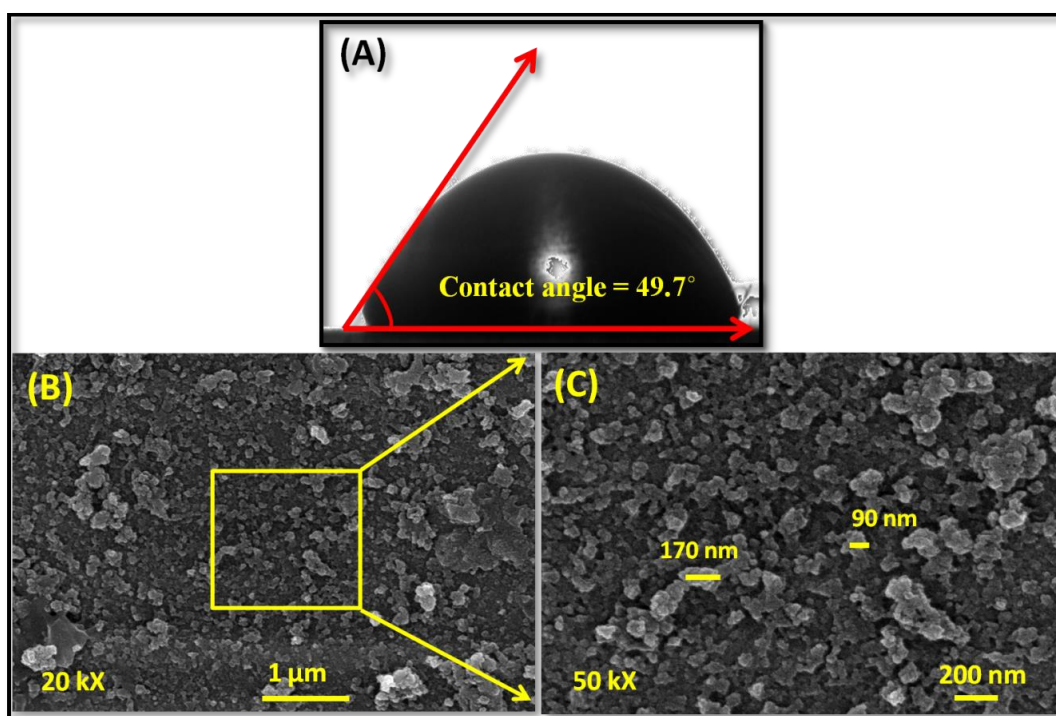


Fig. 5.4: (A) Contact angle image of MnO_2 thin film. The FE-SEM images of MnO_2 thin film at magnifications of (B) 20 kX and (C) 50 kX.

Wettability of the electrode surface is an important property for supercapacitor applications [23]. The contact angle measurement was made to find out the nature or hydrophilic/hydrophobic property of MnO_2 thin film on SS substrate. The contact angle image of MnO_2 thin film is shown in **Fig. 5.4(A)**. Contact angle value of 49.7°

indicates the hydrophilic nature of MnO₂ thin film, which is useful to improve the electrochemical performance [24, 25].

5A.3.2.4.2 Field emission scanning electron microscopy (FE-SEM):

The FE-SEM is an important and convenient technique to analyze the surface textural properties of thin film material. In thin film, surface morphology plays important role lead to enhance the specific capacitance (Cs). The FE-SEM images of MnO₂ thin film material are shown in **Fig. 5.4(B-C)** at magnification of 20 kX and 50 kX. The MnO₂ nanoparticles are interconnected with each other and spread over the substrate as depicted in **Fig. 5.4(B)**. The size of nanoparticles varies between 90-170 nm as seen in **Fig. 5.4(C)** at magnification of 50 kX. Such nanoparticles are useful to enhance the electrochemical supercapacitive activities [26]. Singu and Yoon [27] obtained nanosphere surface texture of MnO₂ films by SILAR method. Jana et al [28] synthesized hierarchical MnO₂ thin film via facile hydrothermal method and observed nanorods surface morphology. Patil et al [29] converted surface architecture of SILAR synthesized MnO₂ film from interlocked cubes to porous nanowalls.

Section- B

5B: Supercapacitive performance of manganese oxide thin films:

5B.1 Supercapacitive study:

5B.1.1 Cyclic voltammetry (CV):

The CV curves of MnO₂ thin film in 1.0 M Na₂SO₄ electrolyte within a potential window of 0.0 to +1.0 V.Hg/HgO at a various scan rates are shown in **Fig. 5.5(A)**. **Fig. 5.5(B)** shows the plot of C_s at different scan rates of MnO₂ thin film material. MnO₂ thin film exhibits the C_s of 421 F g⁻¹ at scan rate 5 mV s⁻¹.

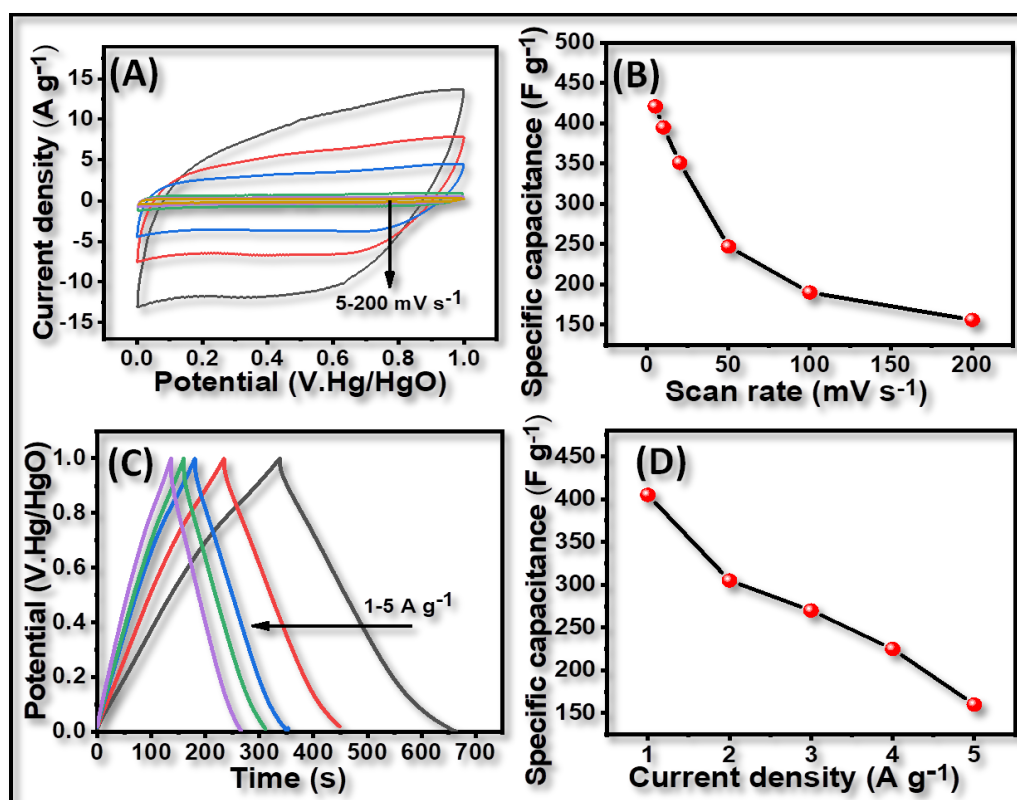


Fig. 5.5: (A) The CV curves of MnO₂ thin film at varied scan rates from 5 to 200 mV s⁻¹, (B) plot of C_s versus different scan rates at 5-200 mV s⁻¹, (C) the GCD curves of MnO₂ thin film at various current densities of 1-5 A g⁻¹ and (D) plot of C_s versus current density of 1-5 A g⁻¹.

5B.1.2 Galvanostatic charge discharge (GCD):

To investigate the rate capability and to determine the C_s of MnO₂ thin film, the GCD test was performed at different current densities [29]. The GCD curves of MnO₂ thin film at different current densities at 1-5 A g⁻¹ in the potential window of 0.0-1.0 V.Hg/HgO in the 1.0 M Na₂SO₄ is shown in **Fig. 5.5(C)**. The C_s of 405 F g⁻¹ is

obtained at 1.0 A g^{-1} current density. **Fig. 5.5(D)** illustrates the plot of C_s versus different current density of $1\text{-}5 \text{ A g}^{-1}$.

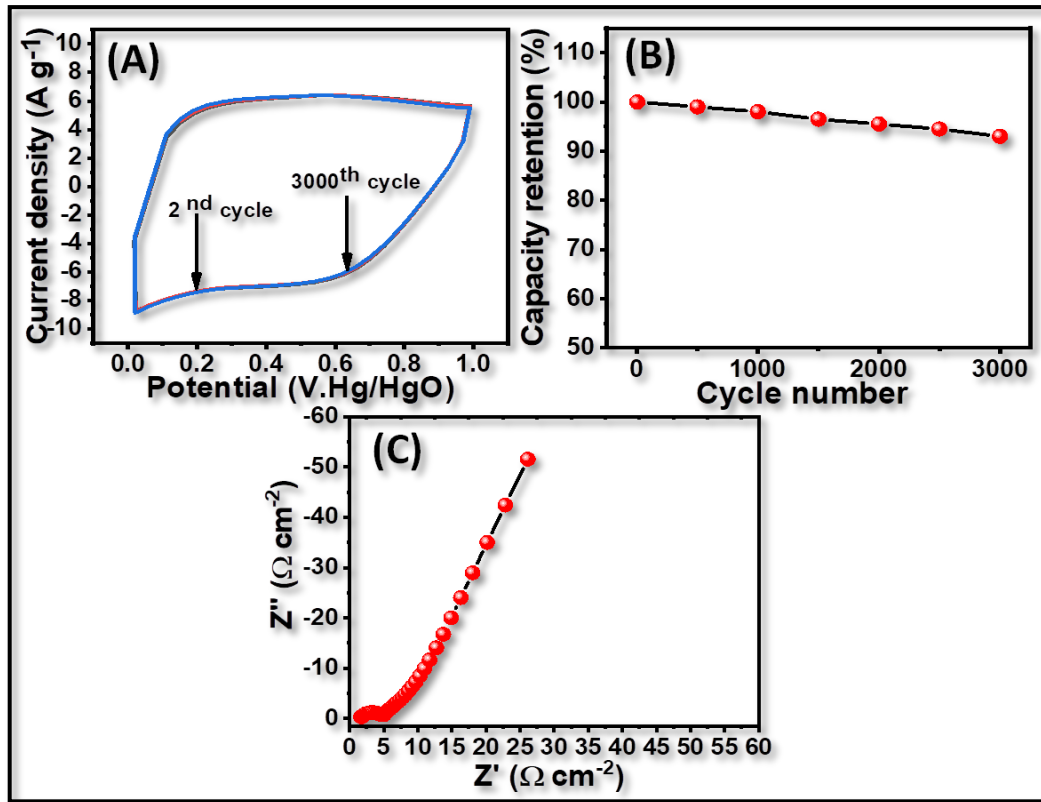


Fig. 5.6: (A) The stability CV curves of MnO_2 thin film, (B) plot of capacity retention versus cycle number and (C) Nyquist plot of MnO_2 thin film.

The bulk faradic reaction is may be due to the insertion/reinsertion of electrolyte ions in the bulk of MnO_2 as [30].



5B.1.3 Stability:

Fig. 5.6(A) illustrates the electrochemical long life cyclic performance of MnO_2 thin film recorded up to 3000 cycles at a scan rate of 100 mV s^{-1} . The plot of capacity retention versus cyclic number for MnO_2 thin film material is shown in **Fig. 5.6(B)**. The MnO_2 thin film exhibits 94 % capacititive retention over 3000 CV cycles. The small decay seen in the long life cycling stability is attributed to the degradation of the thin film active material in an electrolyte during cycling CV process [31].

5B.1.4 Electrochemical impedance spectroscopy (EIS):

The Nyquist plot of MnO_2 thin film in the range of frequency between 0.001 Hz to 1 MHz is depicted in **Fig. 5.6(C)** and inset shows fitted equivalent circuit. The Nyquist plot indicates a tiny semicircle at high frequency domain, which is credited to

the charge transfer process. The R_s determined from the X-axis intercept of the Nyquist plot is $0.81 \text{ } (\Omega \text{ cm}^{-2})$. In the lower frequency range, the straight line nature is attributed to the ion diffusion in the electrolyte as the Warburg resistance. The R_{ct} and W values of MnO_2 electrode are 4.46 and $5.71 \text{ } \Omega \text{ cm}^{-2}$, respectively. The EIS parameters of MnO_2 thin film are shown in **table 5.2**.

Table 5.2: The EIS parameters of MnO_2 thin film in $1\text{M Na}_2\text{SO}_4$ electrolyte.

Parameter	Values of parameter
$R_s \text{ } (\Omega \text{ cm}^{-2})$	0.81
$Q \text{ (mF)}$	1.853
$R_{ct} \text{ } (\Omega \text{ cm}^{-2})$	4.46
$W \text{ } (\Omega \text{ cm}^{-2})$	5.71

5C. Conclusions:

The MnO_2 thin film was synthesized on SS substrate using simple, binder-free and inexpensive SILAR method. The FE-SEM study showed the nanoparticles-like surface texture. The MnO_2 thin film showed hydrophilic nature with contact angle of 49.7° . It showed C_s of 421 F g^{-1} at a scan rate of 5 mV s^{-1} in $1 \text{ M Na}_2\text{SO}_4$ electrolyte with 94 % capacitive retention for 3000 CV cycles. This study indicates that MnO_2 thin film electrode is a promising candidate as a cathode material for asymmetric supercapacitor device.

5D. References:

1. S. Corujeira Gallo, X. Li, K. Futterer, C. A. Charitidis, H. Dong, *Acs Appl. Mater. Inter.*, 9, (2017), 23195-23201.
2. M. Zhu, Z. Wang, H. Li, X. Yuan, C. Zhi, *Energy Environ. Sci.*, 11, (2018), 2414-2422.
3. F. Li, J. Wang, L. Liu, J. Qu, Y. Li, V. K. Bandari, *Adv. Sci.*, 6, (2019), 1901051-1901060.
4. H. Wei, X. Wang, Y. Zhang, W. Du, X. Sun, F. Jiang, *J. Electroanal. Chem.*, 853, (2019), 113561-113570.
5. S. Luo, L. Xie, F. Han, W. Wei, Y. Huang, H. Zhang, *Adv. Funct. Mater.*, 29, (2019), 1901336-1901345.
6. Y. Xie, C. Yang, P. Chen, D. Yuan, K. Guo, *J. Power Sources*, 425, (2019), 1-9.
7. W. Wei, X. Cui, W. Chen, D. G. Ivey, *Chem. Soc. Rev.*, 40, (2011), 1697-1721.
8. F. Gao, X. Tang, H. Yi, C. Chao, L. Na, J. Li, *Chem. Eng., J.* 322, (2017), 525-537.
9. J. Huang, Y. Dai, K. Singewald, C. C. Liu, S. Saxena, H. Zhang, *Chem. Eng., J.*, 370, (2019), 906-915.
10. A. Malak-Polaczyk, C. Matei-Ghimbeu, C. Vix-Guterl, E. Frackowiak, *J. Solid State Chem.*, 183, (2010), 969-974.
11. P. Ahuja, R. K. Sharma, G. Singh, *J. Mater. Chem. A*, 3, (2015), 4931-4937.
12. N. Sinan and E. Unur, *J. Electrochem. Sci. Technol.*, 11, (2020), 50-59.
13. B. P. Relekar, S. A. Mahadik, S. T. Jadhav, A. S. Patil, R. R. Koli, G. M. Lohar, V. J. Fulari, *J. Electron. Mater.*, 47, (2018), 2731-2738.
14. C. Wan, *Int. J. Electrochem. Sci.*, 13, (2018), 12320-12330.
15. D. Gueon and J. H. Moon, *ACS Sustainable Chem. Eng.*, 5, (2017), 2445-2453.
16. V. J. Mane, D. B. Malavekar, S. B. Ubale, V. C. Lokhande, C. D. Lokhande, *Inorg. Chem. Commun.*, 110, (2020), 107853-107872.
17. X. Li, J. Shen, N. Li, M. Ye, *J. Power Sources*, 282, (2015), 194-201.
18. Z. Y. Leong and H. Y. Yang, *ACS Appl. Mater. Interfaces*, 11, (2019), 13176-13184.
19. S. Maiti, A. Pramanik, S. Mahanty, *ACS Appl. Mater. Interfaces*, 6, (2014), 10754-10762.
20. S. R. Ede, A. Ramadoss, S. Anantharaj, U. Nithiyantham, S. Kundu, *Chem. Phys.*, 16, (2014), 21846-21859.
21. P. Asen and S. Shahrokhian, *J. Electroanal. Chem.*, 823, (2018), 505-516.
22. D. Dubal, D. Dhawale, R. Salunkhe, S. Pawar, C. D. Lokhande, *Appl. Surf. Sci.*, 256, (2010), 4411-4416.
23. S. J. Patil, B. H. Patil, R. N. Bulakhe, C. D. Lokhande, *RSC Adv.*, 4, (2014), 56332-56342.
24. N. R. Chodankar, G. S. Gund, D. P. Dubal, C. D. Lokhande, *RSC Adv.*, 4, (2014), 61503-61513.
25. R. B. Pujari, A. C. Lokhande, T. T. Ghogare, S. B. Kale, C. D. Lokhande, *J. Mater. Sci. Mater. Electron.*, 29, (2018), 14116-14121.
26. Y. Hu, H. Zhu, J. Wang, Z. Chen, *J. Alloys Compd.*, 42, (2011), 10234-10240.
27. B. Singu and K. Yoon, *J. Alloys and Compd.*, 695, (2017), 771-778.
28. M. Jana, S. Saha, P. Samanta, N. Murmu, N. Kim, T. Kuila, J. Lee, *J. Power Sources*, 340, (2017), 380-392.
29. A. M. Patil, V. C. Lokhande, U. M. Patil, P. A. Shinde, C. D. Lokhande, *ACS*

- Appl. Mater. Interfaces, 6, (2018), 787-802.
30. V. J. Mane, D. B. Malavekar, S. B. Ubale, R. N. Bulakhe, Insik In, C. D. Lokhande, Electrochem. Acta., 335, (2020), 135613-135664.
 31. P. A. Shinde, V. C. Lokhande, A. M. Patil, A. A. Yadav, C. D. Lokhande, Int. J. Eng. Res. Technol., 10, (2017), 532-537.

Chapter-VI

***Fabrication and performance evaluation
of flexible solid state symmetric and
asymmetric supercapacitor devices based
on ytterbium sulfide, graphene
oxide/ytterbium Sulfide composite and
manganese oxide electrodes***

Chapter-VI

Fabrication and performance evaluation of flexible solid state symmetric and asymmetric supercapacitor devices based on ytterbium sulfide, graphene oxide/ytterbium sulfide composite and manganese oxide electrodes

Sr. no.	Title	Page no.
6.0	Introduction	105
6.1	Section -A	106
6.1A	Fabrication and performance evaluation of (Yb ₂ S ₃ /Yb ₂ S ₃) flexible solid state symmetric supercapacitor device (CBD method)	106
6.1A.1	Introduction	106
6.1A.2	Experimental details	106
	6.1A.2.1 <i>Electrode preparation</i>	106
	6.1A.2.2 <i>Polymer gel electrolyte (PVA-KOH) preparation</i>	106
	6.1A.2.3 <i>Fabrication of flexible solid state symmetric supercapacitor (FSS-SSc) device (CBD method)</i>	106
6.1A.3	Supercapacitive performance of FSS-SSc device	107
	6.1A.3.1 <i>Cyclic voltammetry (CV)</i>	107
	6.1A.3.2 <i>Galvanostatic charge discharge (GCD)</i>	108
	6.1A.3.3 <i>Ragone plot</i>	109
	6.1A.3.4 <i>Flexibility</i>	109
	6.1A.3.5 <i>Stability</i>	110
	6.1A.3.6 <i>Electrochemical impedance spectroscopy (EIS)</i>	111
6.2	Section -B	112
6.2B	Fabrication and performance evaluation of (Yb ₂ S ₃ /Yb ₂ S ₃) flexible solid state symmetric supercapacitor device (SILAR method)	112
6.2B.1	Introduction	112
6.2B.2	Experimental details	112
	6.2B.2.1 <i>Electrode preparation</i>	112
	6.2B.2.2 <i>Polymer gel electrolyte (PVA-Na₂SO₄) preparation</i>	112
	6.2B.2.3 <i>Fabrication of flexible solid state symmetric supercapacitor (FSS-SSc) device (SILAR method)</i>	112
6.2B.3	Supercapacitive study of FSS-SSc device	113
	6.2B.3.1 <i>Cyclic voltammetry (CV)</i>	113
	6.2B.3.2 <i>Galvanostatic charge discharge (GCD)</i>	115
	6.2B.3.3 <i>Ragone plot</i>	115
	6.2B.3.4 <i>Flexibility</i>	115
	6.2B.3.5 <i>Stability</i>	116
	6.2B.3.6 <i>Electrochemical impedance spectroscopy (EIS)</i>	117
6.3	Section- C	118
6.3C	Fabrication and performance evaluation of (GO/Yb ₂ S ₃ //GO/Yb ₂ S ₃) flexible solid state symmetric	118

		supercapacitor device (SILAR method)	
	6.3C.1	Introduction	118
	6.3C.2	Experimental details	118
		<i>6.3C.2.1 Electrode preparation</i>	118
		<i>6.3C.2.2 Polymer gel electrolyte (PVA-Na₂SO₄) preparation</i>	119
		<i>6.3C.2.3 Fabrication of flexible solid state symmetric supercapacitor (FSS-SSc) device (SILAR method)</i>	119
	6.3C.3	Supercapacitive performance evaluation	119
		<i>6.3C.3.1 Cyclic voltammetry (CV)</i>	120
		<i>6.3C.3.2 Galvanostatic charge discharge (GCD)</i>	121
		<i>6.3C.3.3 Ragone plot</i>	121
		<i>6.3C.3.4 Flexibility</i>	121
		<i>6.3C.3.5 Stability</i>	123
		<i>6.3C.3.6 Electrochemical impedance spectroscopy (EIS)</i>	123
6.4	Section- D		125
	6.4D	Fabrication and performance evaluation of (GO/Yb₂S₃//MnO₂) flexible solid state asymmetric supercapacitor device (SILAR method)	125
	6.4D.1	Introduction	125
	6.4D.2	Experimental detail	125
		<i>6.4D.2.1 Electrode preparation</i>	125
		<i>6.4D.2.2 Polymer gel electrolyte (PVA-Na₂SO₄) preparation</i>	125
		<i>6.4D.2.3 Fabrication of flexible solid state asymmetric supercapacitor (FSS-ASSc) device (SILAR method)</i>	125
	6.4D.3	Supercapacitive performance evaluation of FSS-ASc device	126
		<i>6.4D.3.1 Cyclic voltammetry (CV)</i>	126
		<i>6.4D.3.2 Galvanostatic charge discharge (GCD)</i>	127
		<i>6.4D.3.3 Ragone plot</i>	128
		<i>6.4D.3.4 Flexibility</i>	128
		<i>6.4D.3.5 Stability</i>	130
		<i>6.4D.3.6 Electrochemical impedance spectroscopy (EIS)</i>	130
6.5	Conclusions		132
6.6	References		134

6.0 Introduction:

The rare earth metal (REM) chalcogenides have much attention in different fields due to their unique physico-chemical characteristics [1]. In the rare earth metal chalcogenides, the REM sulfides have more conductivity and large potential window than the other oxide and hydroxide materials. In rare earth metal, ytterbium exhibits the multiple oxidation states (Yb^+ , Yb^{2+} and Yb^{3+}), which leads to enhance the specific capacitance (C_s). Therefore, ytterbium sulfide (Yb_2S_3) is a one of the potential material for supercapacitor. The REM chalcogenides are used in different fields such as sensor [2], microelectronics [3], photoelectrochemical cell [4], protective coating layer [5], biomedicine [6] and supercapacitor [7].

Moreover, a boost in value of C_s and wide working voltage are the effective approaches to enhance the energy density of symmetric and asymmetric devices [8]. As a cathode electrode, manganese oxide (MnO_2) (pseudocapacitive) has been widely investigated due to its low cost, ecofriendly nature, high theoretical C_s , and positive wide potential window (0 to +1 V). Formation of nanostructured MnO_2 thin film over a stainless steel substrate is binder-free, uniform, and adherent, which is useful for improving cycling performance of the electrode [9]. On the other hand, as a negative electrode material, the carbon based composite electrodes (graphene/ MoS_2 , MWCNTs/ MoS_2 , GO/ Sm_2S_3 and GO/ La_2S_3 electrodes) with wide potential operating window (0 to -1 V) and high stability are used [10-13]. An energy density (E.D.), indicated as $\text{E.D.} = 0.5 \text{ CV}^2$ (E.D. is directly proportional to the capacitance and square of working potential window), may be improved by raising the capacitance of active electrode materials and working potential window (V) [14, 15]. GO/ Yb_2S_3 nanocomposite, a new material, can be used as a negative electrode material in electrochemical supercapacitors owing to its wide negative potential window, high capacitance and cycling stability. The combination of MnO_2 as a positive and GO/ Yb_2S_3 as a negative thin film electrode in solid-state supercapacitor is not studied, so far.

This chapter deals with preparation of Yb_2S_3 , GO/ Yb_2S_3 composite and MnO_2 electrodes by chemical methods such as CBD and SILAR. The fabrication of symmetric and asymmetric devices was carried out using the Yb_2S_3 , GO/ Yb_2S_3 composite and MnO_2 electrodes in PVA-KOH, and PVA- Na_2SO_4 polymer gel

electrolytes. The supercapacitive performance of symmetric and asymmetric devices was evaluated using the various techniques such as CV, GCD and EIS. Also, practical demonstration symmetric and asymmetric supercapacitor devices is made.

6.1 Section-A

6.1A: Fabrication and performance evaluation of (Yb₂S₃/Yb₂S₃) flexible solid state symmetric supercapacitor device (CBD method)

6.1A.1 Introduction:

This section deals with the electrode preparations, fabrication and supercapacitive performance evaluation of flexible solid state symmetric supercapacitor (FSS-SSc) device (CBD method).

6.1A.2 Experimental details:

6.1A.2.1 Electrode preparation:

The CBD method was used for synthesis of Yb₂S₃ electrodes on stainless steel (SS) substrate. The preparative parameters for Yb₂S₃ electrodes are given detailed in **chapter-III 3A.1.3**.

6.1A.2.2 Polymer gel electrolyte (PVA-KOH) preparation:

A 3 g of polyvinyl alcohol (PVA) was dissolved in 30 mL DDW at the temperature of 354 K to get transparent and viscous gel solution [16]. In to this 1.0 M 20 mL freshly prepared KOH solution was added drop wise to form PVA-KOH gel electrolyte.

6.1A.2.3 Fabrication of flexible solid state symmetric supercapacitor (FSS-SSc) device:

Fig. 6.1(A-C) shows the device fabrication process of Yb₂S₃/PVA-KOH/Yb₂S₃ configuration. The Yb₂S₃ films deposited on SS substrate were used as electrodes in the device fabrication. The edges of Yb₂S₃ electrodes were sealed with insulating tape to avoid the electrical short circuit as shown in **Fig 6.1(A)**. The gel electrolyte was prepared by dissolving a polyvinyl alcohol (PVA) and potassium hydroxide (KOH) in DDW. The thin layer of gel electrolyte was pasted over Yb₂S₃ electrodes (**Fig 6.1(B)**). The pressure ~ 1.0 ton was applied on the assembled device using hydraulic press to remove air and voids with the intention of good contact and to improve its mechanical properties (**Fig 6.1(C)**).

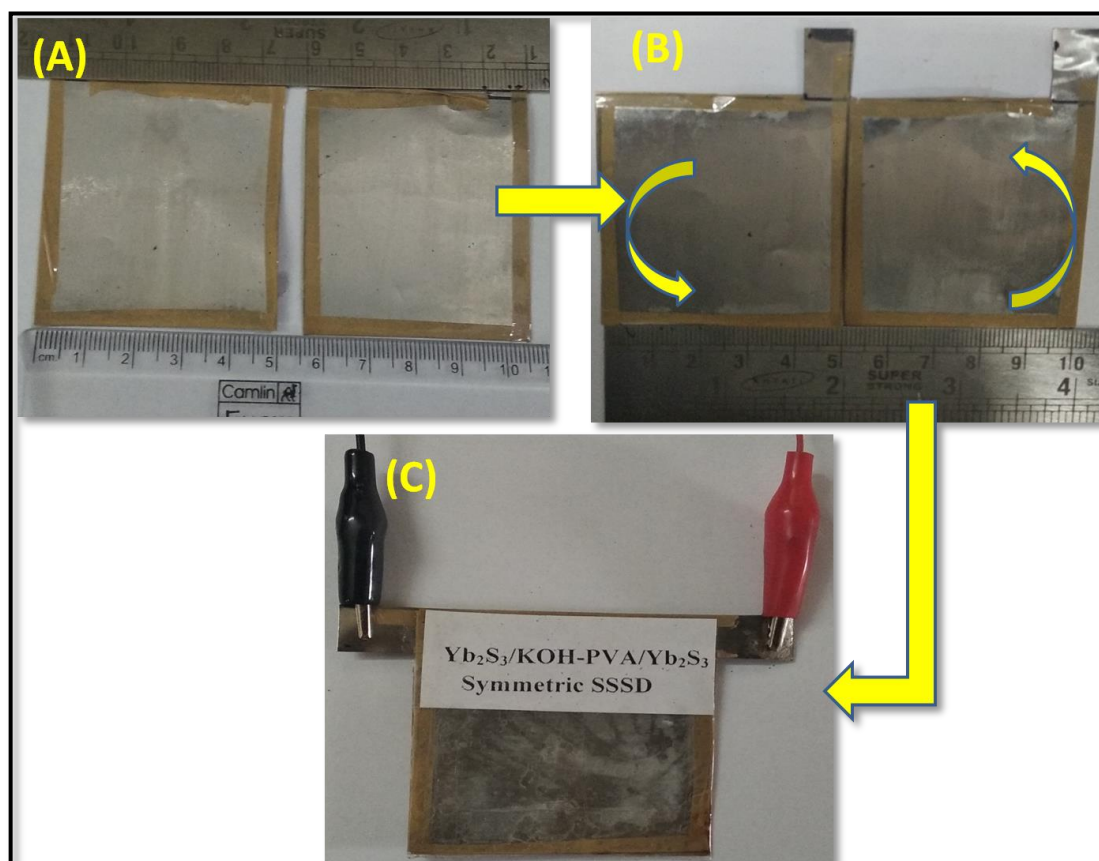


Fig. 6.1: Photographs of (A) Yb_2S_3 electrode with sealed edges by tape, (B) application of thin layer of gel electrolyte on both Yb_2S_3 electrodes and (C) assembly of device ($5 \times 5 \text{ cm}^2$).

6.1A.3 Supercapacitive performance of FSS-SSc device:

6.1A.3.1 Cyclic voltammetry (CV):

Fig. 6.2(A) illustrates the performance of FSS-SSc device studied in various potential windows from 1.0 to 1.8 V at 100 mV s^{-1} scan rate. The FSS-SSc device displays symmetric area under curve at potential window up to 1.6 V [17].

The CV curves of device displayed in **Fig. 6.2(B)** are recorded with scan rates ranging from 5 to 200 mV s^{-1} in the potential window 0 to 1.6 V. **Fig. 6.2(C)** shows the C_s values of device at different scan rates. The device C_s decreases from 15 to 8 F g^{-1} as scan rate changes from 5 to 200 mV s^{-1} . The maximum C_s at low scan rate is due to more utilization in the active material and time for electrochemical reaction process [18].

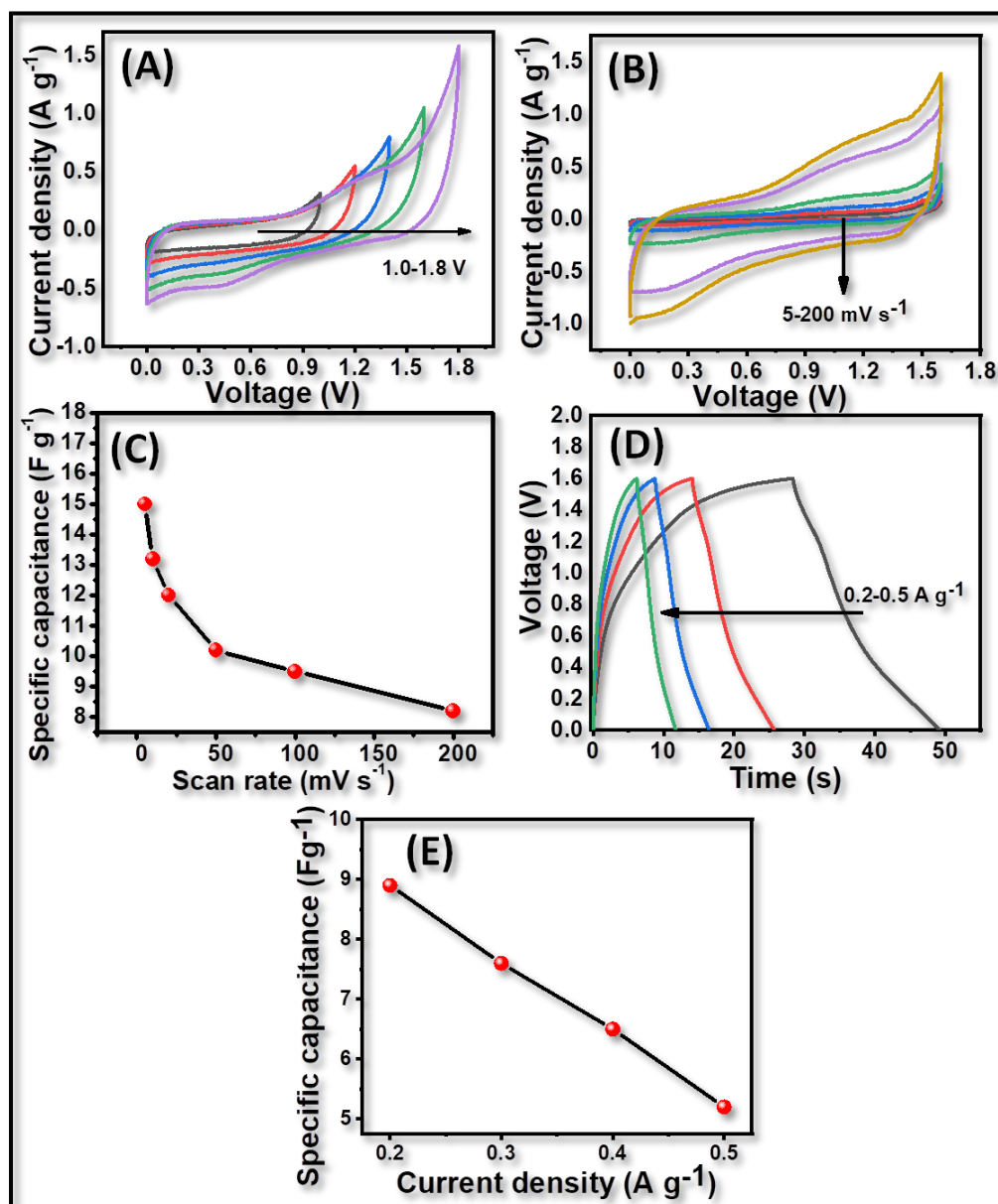


Fig. 6.2: (A) The CV curves for selection of potential window at different voltages, (B) the CV curves for Yb₂S₃/PVA-KOH/Yb₂S₃ FSS-SSc device at scan rates of 5-200 mV s⁻¹, (C) plot of specific capacitance versus scan rate, (D) the GCD curves for Yb₂S₃/PVA-KOH/Yb₂S₃ FSS-SSc device at 0.2 - 0.5 A g⁻¹ current densities, and (E) plot of specific capacitance versus current density.

6.1A.3.2 Galvanostatic charge discharge (GCD):

The GCD curves for the device recorded at current densities of 0.2 to 0.5 A g⁻¹ are shown in Fig. 6.2(D). The GCD curves show the quasi-triangular shape, therefore GCD curves exhibit surface redox pseudocapacitor behaviour [19]. As current density increases from 0.2 to 0.5 A g⁻¹, discharge time decreases which may be due to the enhancement of insufficient active material involved in oxidation and reduction

reactions under higher current densities. **Fig. 6.2(E)** indicates the plot of specific capacitance versus charging current density. The maximum C_s of 9.0 F g^{-1} is obtained at a current density of 0.2 A g^{-1} . The large number of electrolyte ions passes inside the electrode owing to nano-grains like morphology as more charging time availability at low current density which results into high C_s value [16].

6.1A.3.3 Ragone plot:

The energy density (E.D.) and power density (P.D.) of device are calculated from the relations 2.15 and 2.16. **Fig. 6.3(A)** shows the Ragone plot of the device. The maximum value of energy density 6.40 Wh kg^{-1} at power density 0.30 kW kg^{-1} is obtained at a current density of 0.2 A g^{-1} . Patil and Lokhande [20] fabricated symmetric solid-state supercapacitor device using lanthanum sulfide electrode with LiClO_4 -PVA gel electrolyte and reported specific energy of 0.14 Wh kg^{-1} at specific power of 22.7 W kg^{-1} .

6.1A.3.4 Flexibility:

To use FSS-SSc device in the portable electronic application as a practical energy storage device, it should have mechanical flexibility along with high power density and high energy density. Therefore, a series of CV measurements within 0-1.6 V potential window were examined for various bending angles of 0° , 45° , 90° , 135° , and 165° at scan rate of 100 mV s^{-1} (**Fig. 6.3(B)**). The mechanical twisting of the device could result in structural degeneration of the electrode, affecting on charge storage capability [21, 22]. The plot of capacitive retention versus bending angle is demonstrated in **Fig. 6.3C** and insets of **Fig. 6.3C** demonstrate photographs of device at different bending angles. The excellent capacity retention (95 %) of the device even over the 165° twisting angle powerfully supports the admirable flexibility and stability of the device. Capacitive retention versus different bending angles of FSS-SSc device is shown in **table 6.1**.

Table.6.1: Capacitive retention values at different bending angles of FSS-SSc device.

Bending angle	Capacitive retention of FSS-SSc device (%)
0°	100
45°	99.5
90°	98
135°	97
165°	95

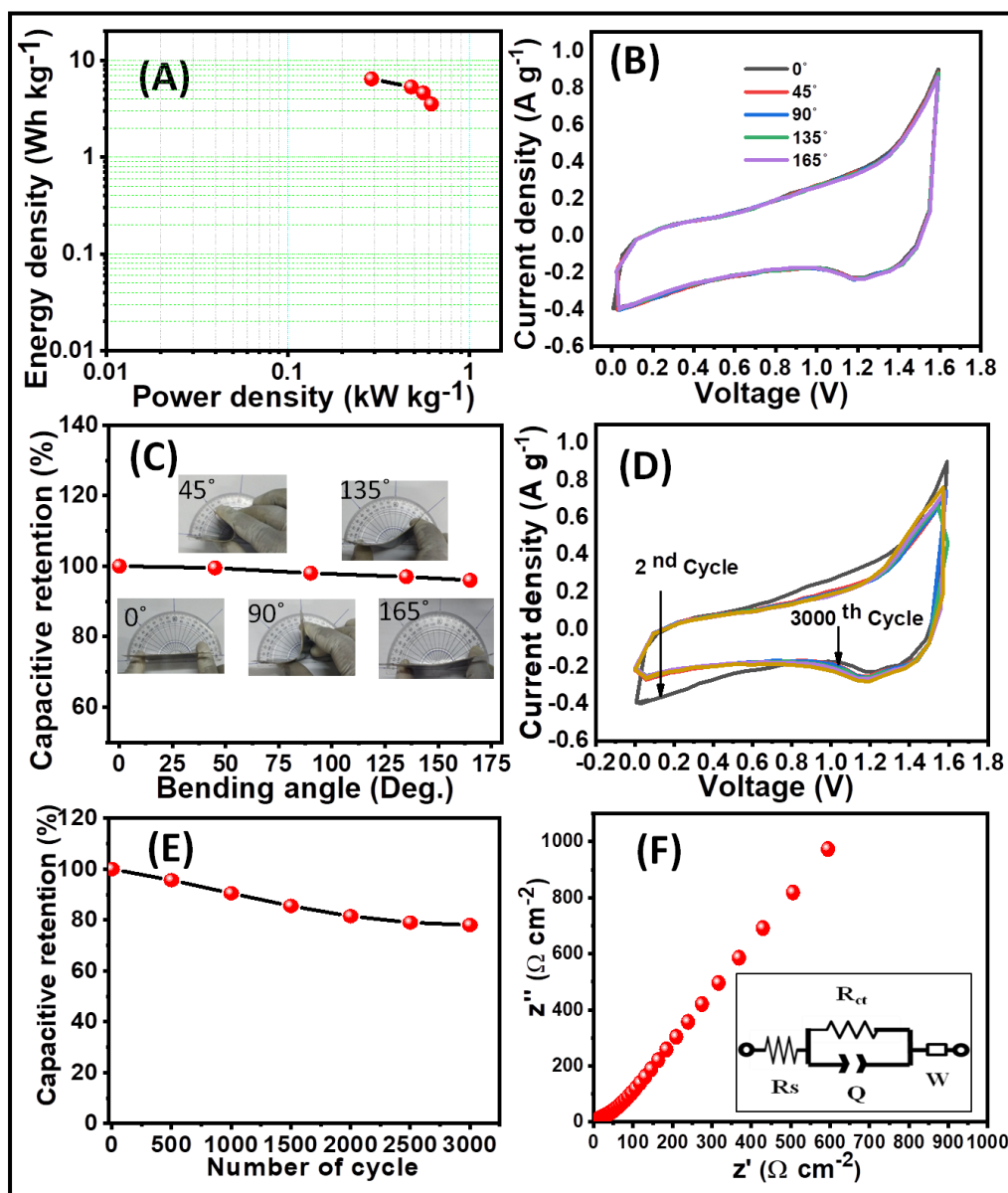


Fig. 6.3: (A) The Ragone plot for $\text{Yb}_2\text{S}_3/\text{PVA-KOH}/\text{Yb}_2\text{S}_3$ FSS-SSc device, (B) the CV curves of FSS-SSc device at various bending angles, (C) plot of capacitive retention versus bending angle [Insets show photograph of device at different bending angles], (D) stability of $\text{Yb}_2\text{S}_3/\text{PVA-KOH}/\text{Yb}_2\text{S}_3$ FSS-SSc device at scan rate of 100 mV s^{-1} with PVA-KOH gel electrolyte, (E) capacitive retentions up to 3000 cycles at a scan rate of 100 mV s^{-1} , and (F) Nyquist plot for $\text{Yb}_2\text{S}_3/\text{PVA-KOH}/\text{Yb}_2\text{S}_3$ FSS-SSc device [Inset shows the equivalent circuit].

6.1A.3.5 Stability:

The cyclic stability of device is a significant parameter in electrochemical process, which was analyzed through CV curve. The CV curves of device were recorded at constant scan rate of 100 mV s^{-1} over 3000 cycles as shown in **Fig. 6.3(D)**. The specific capacitive retention of device is shown in **Fig. 6.3(E)**. The area under

curves of device decreases with increase in the cycle numbers at constant current density, which is due to degradation of electroactive material during charging-discharging process [18]. The device shows 78 % capacitive retention for 3000 CV cycles.

6.1A.3.6 Electrochemical impedance spectroscopy (EIS):

Nyquist plot of device in the frequency region 1 Hz to 0.1 MHz with AC amplitude 10 mV was recorded. **Fig. 6.3(F)** shows the Nyquist plot of device and the inset shows the best fitted equivalent circuit to the Nyquist plot. The Nyquist plot of device gives the R_s of $2.22 \Omega \text{ cm}^{-2}$. In the mid-term frequency part, R_{ct} of $32.5 \Omega \text{ cm}^{-2}$ is observed. In the low frequency region, W of $33.01 \Omega \text{ cm}^{-2}$ is associated with the diffusion of K^+ ions in to Yb_2S_3 electrode. The electrochemical impedance parameters of device are given in **table 6.2**.

Table 6.2: The electrochemical impedance parameters for FSS-SSc device.

Parameter	Value of parameters
$R_s (\Omega \text{ cm}^{-2})$	2.22
$Q (\text{mF})$	29.23
$R_{ct} (\Omega \text{ cm}^{-2})$	32.5
$W (\Omega \text{ cm}^{-2})$	33.01

The demonstration of device was recorded by glowing two red LED. **Fig. 6.4(A, B)** indicates the images of red light emitting diodes (LEDs) glowing for 1 and after 55 s, respectively. The device shows good charge storage ability.

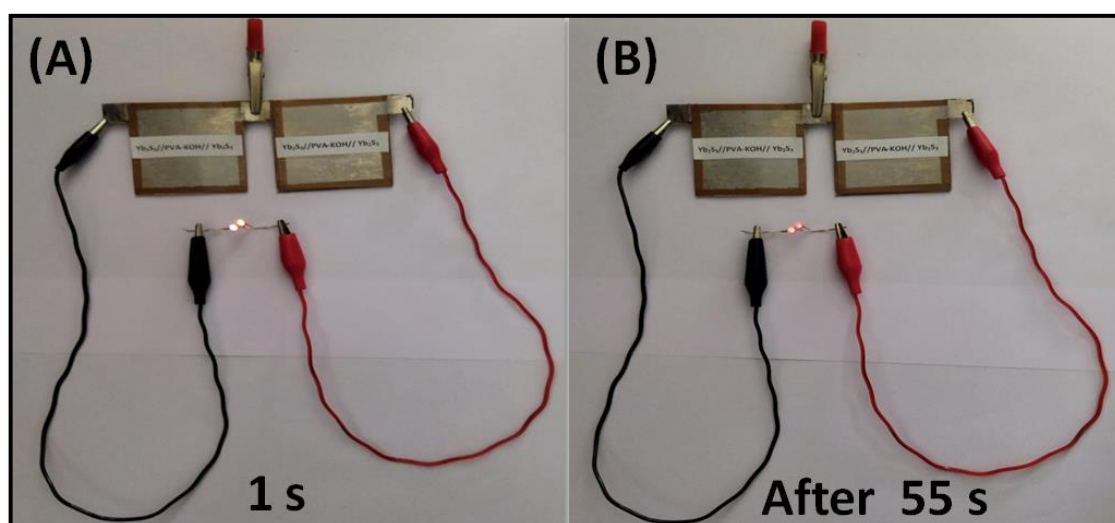


Fig. 6.4: Images of two red LED glowing at (A) 1 and (B) 55 s.

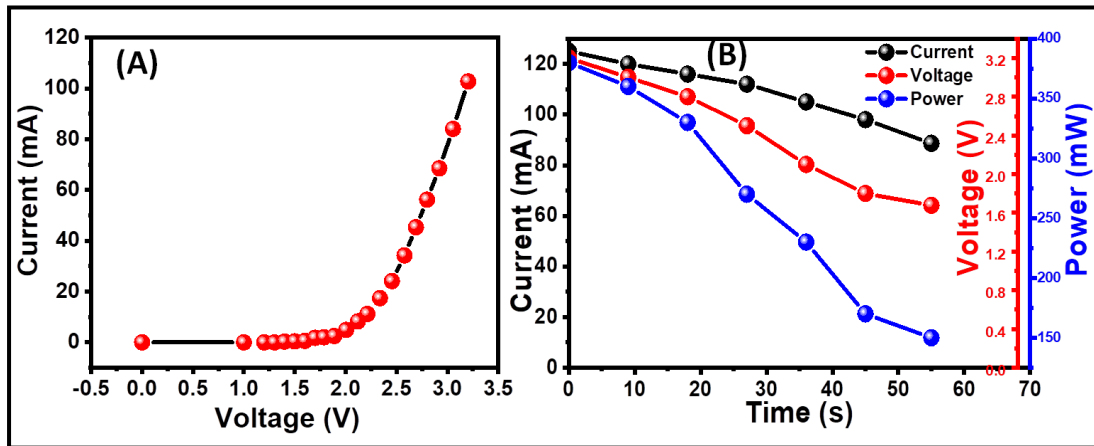


Fig. 6.5: (A) The I-V characteristic of two red LEDs and (B) the current, voltage and power versus time graphs of FSS-SSc device during discharging.

Fig. 6.5(A) illustrates the I-V characteristic of two red LEDs. **Fig. 6.5(B)** demonstrates the plots of current, voltage and power with discharging time of device using two LEDs. It is seen that, the discharge current decreases from 120 to 85 mA and voltage decreases from 3.2 to 1.7 V and the also power decreases from 380 to 150 mW.

6.2 Section -B

6.2B: Fabrication and performance evaluation of (Yb₂S₃/Yb₂S₃) flexible solid state symmetric supercapacitor device (SILAR method)

6.2B.1 Introduction:

Section-B deals with the preparations of Yb₂S₃ electrodes, fabrication and supercapacitive performance evaluation of flexible solid state symmetric supercapacitor (FSS-SSc) device (SILAR method).

6.2B.2 Experimental details:

6.2B.2.1 Electrode preparation:

The synthesis and preparative parameters of Yb₂S₃ electrodes by SILAR method are given in (3B.2.3 and 3B.3.1) chapter-III.

6.2B.2.2 Polymer gel electrolyte (PVA-Na₂SO₄) preparation:

A 6 gm of poly-vinyl alcohol (PVA) was dissolved in 60 mL DDW at the temperature of 354 K to get transparent and viscous gel solution [16]. In to this, 1.0 M 40 mL freshly prepared Na₂SO₄ solution was added drop wise to the formation of PVA-Na₂SO₄ gel electrolyte.

6.2B.2.3 Fabrication of flexible solid state symmetric supercapacitor device:

The FSS-SSc device with the configuration of $\text{Yb}_2\text{S}_3/\text{PVA-Na}_2\text{SO}_4/\text{Yb}_2\text{S}_3$ is depicted in **Fig. 6.6(A-D)**. Two Yb_2S_3 electrodes ($5 \times 5 \text{ cm}^2$) deposited on SS substrate were used in the fabrication of FSS-SSc device as depicted in **Fig. 6.6(A)**. The PVA- Na_2SO_4 polymer gel electrolyte is painted over the electrode surfaces (**Fig. 6.6(B)**). The sides or edges of both electrodes were sealed using insulating plastic tape to avoid an electrical short circuit as illustrated in **Fig. 6.6(C)**. The FSS-SSc device fabricated with a thin layer of electrolyte gel painted on both electrodes was assembled into a sandwiched structure. The FSS-SSc device assembly was sealed with the adhesive tape (**Fig. 6.6(C, D)**) and pressure of ~ 0.7 ton was applied on the assembled FSS-SSc device using hydraulic press with the intention of better mechanical properties. The supercapacitive performance of FSS-SSc device was tested out via CV, GCD, stability and EIS studies.

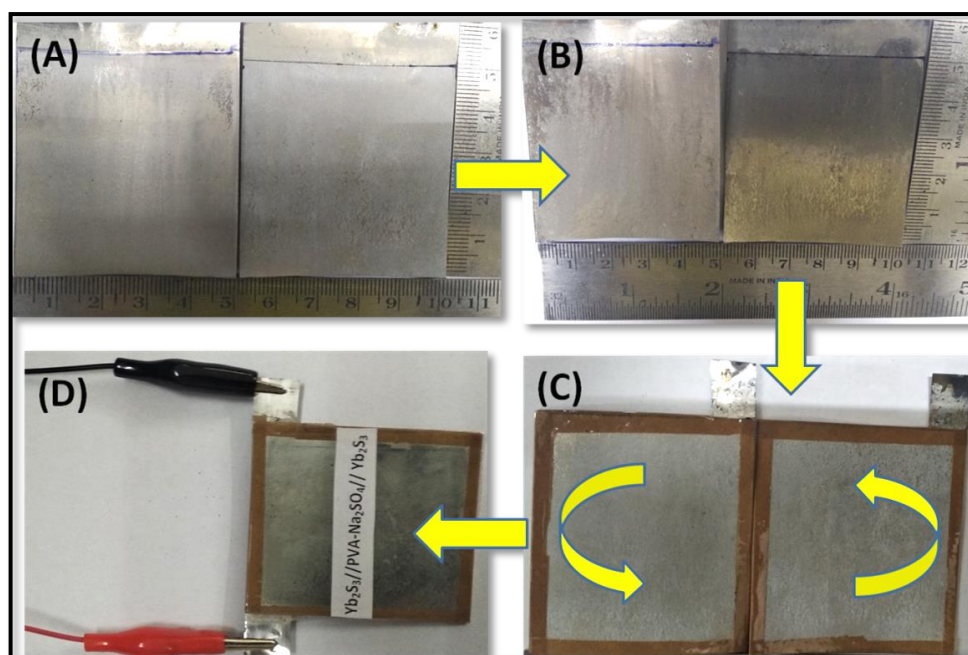


Fig. 6.6: Photographs of (A) Yb_2S_3 deposited on the SS substrate electrodes with ($5 \times 5 \text{ cm}^2$) area, (B) PVA- Na_2SO_4 gel electrolyte painted on Yb_2S_3 electrodes, (C) both the electrode edges sealed with insulator tape and (D) assembled FSS-SSc device.

6.2B.3 Supercapacitive study of FSS-SSc device:

6.2B.3.1 Cyclic voltammetry (CV):

Fig. 6.7(A) illustrates CV plots of FSS-SSc device with various voltage windows (1.0 to 1.8 V) which reveal symmetric area under CV curve up to the potential

window of 1.6 V. Therefore, 1.6 V potential window is chosen for the testing of supercapacitive activity of the device. Fig. 6.7(B) demonstrates the CV plots at various

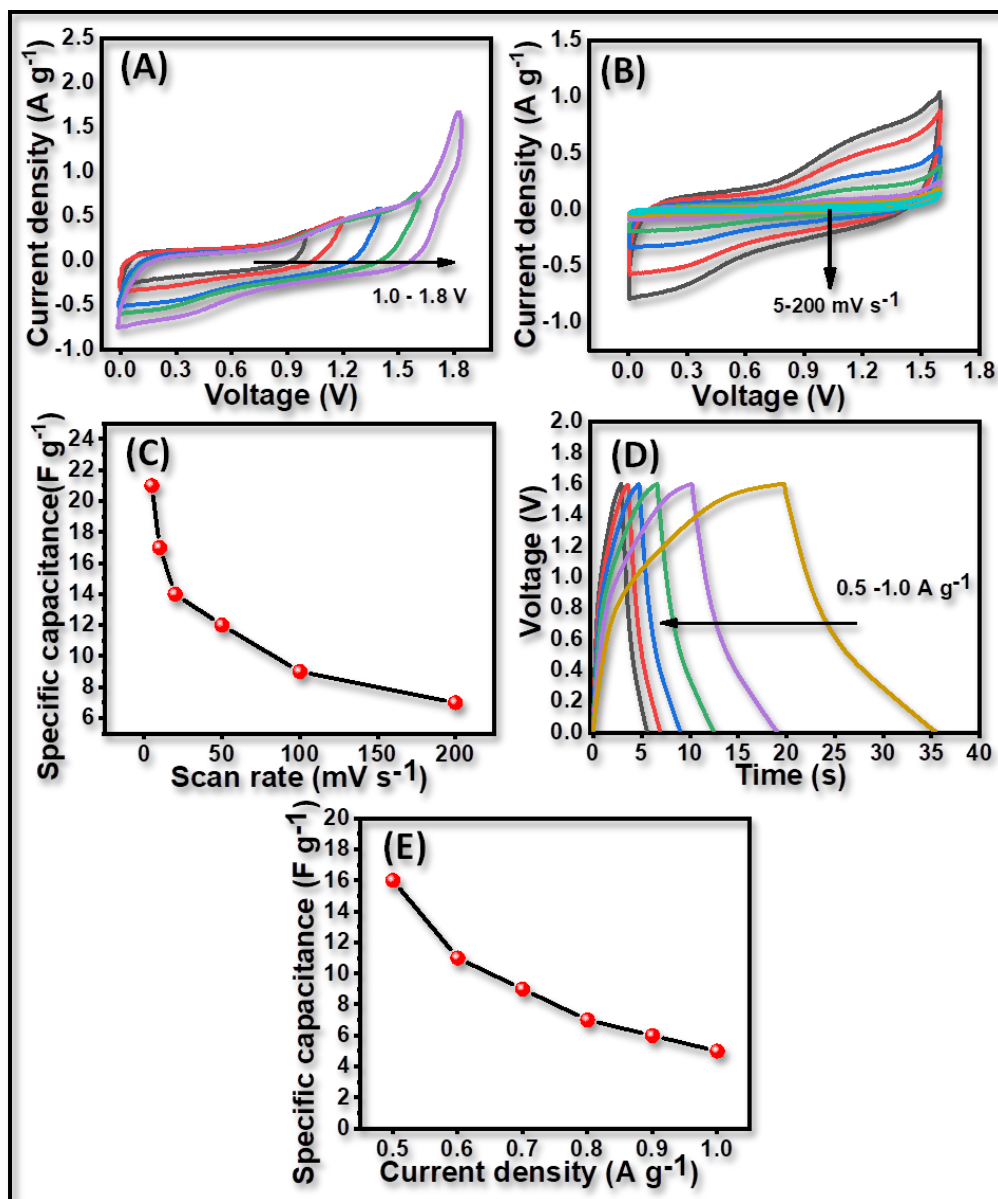


Fig. 6.7: (A) Potential window selection in the voltage ranging from 1.0 to 1.8 V at 100 mV s⁻¹ scan rate, (B) the CV curves of FSS-SSc device at different scan rates of 5-200 mV s⁻¹, (C) plot of Cs versus scan rate, (D) the GCD curves at current densities from 0.5-1.0 A g⁻¹ and (E) plot of Cs versus current density.

scan rates from 5 to 200 mV s⁻¹, which show quasi-rectangular shape of the CV curve. The FSS-SSc device exhibits Cs of 21 F g⁻¹ at the scan rate of 5 mV s⁻¹. Fig. 6.7(C) displays the plot of Cs versus scan rate, which indicates decrease in Cs with increasing scan rate. Yadav et al [23] fabricated FSS-SSc with the configuration as La₂O₃/PVA-

LiClO₄/La₂O₃ and reported Cs of 10 F g⁻¹ at 5 mV s⁻¹ scan rate. Patil and Lokhande [20] reported Cs of 3.3 F g⁻¹ at the scan rate of 5 mV s⁻¹ for FSS-SSc device with the configuration of La₂S₃/PVA-LiClO₄/La₂S₃.

6.2B.3.2 Galvanostatic charge discharge (GCD):

Fig. 6.7(D) reveals the GCD curves of FSS-SSc device at various current densities from 0.5 to 1.0 A g⁻¹. The shape of the GCD curves is quasi-triangular, which is owing to the surface redox pseudocapacitive nature of the device. **Fig. 6.7(E)** shows the plot of Cs versus current density and it indicates that Cs decreases with an increase in current density.

6.2B.3.3 Ragone plot:

The most significant factors, which demonstrate the energy storage ability of device, are the E.D. and P.D. **Fig. 6.8(A)** shows the Ragone plot of device. The FSS-SSc device achieved E.D. of 7.68 Wh k g⁻¹ at the P.D. of 0.38 kW kg⁻¹.

6.2B.3.4 Flexibility:

The flexibility of the device without reducing its supercapacitive performance is of extensively important for the pertinence of device in various portable electronic devices [24, 25]. Therefore, to study the mechanical flexibility of the device, we performed the CV measurement of symmetric device at various bending angles at 100 mV s⁻¹ scan rate **Fig. 6.8(B)**. It is fascinating to note that, bending of device even at an angle of 165°, the shapes of CV curves remains same, signifying the excellent adhesion of active electrode material with current collector and superior feature of the active electrode material/gel electrolyte at interface. **Fig. 6.8(C)** shows the capacitive retention versus bending angle and it is observed that, the device retained 96 % of starting capacitance even at bending of device at an angle of 165°. The insets of **Fig. 6.8C** demonstrates photograph of device at different bending angles. Capacitive retention values at different bending angles of FSS-SSc device are shown in **table 6.3**.

Table 6.3: Capacitive retention values at different bending angles of FSS-SSc device.

Bending angle	Capacitive retention of FSS-SSc device (%)
0°	100
45°	99
90°	98.5
135°	97
165°	96

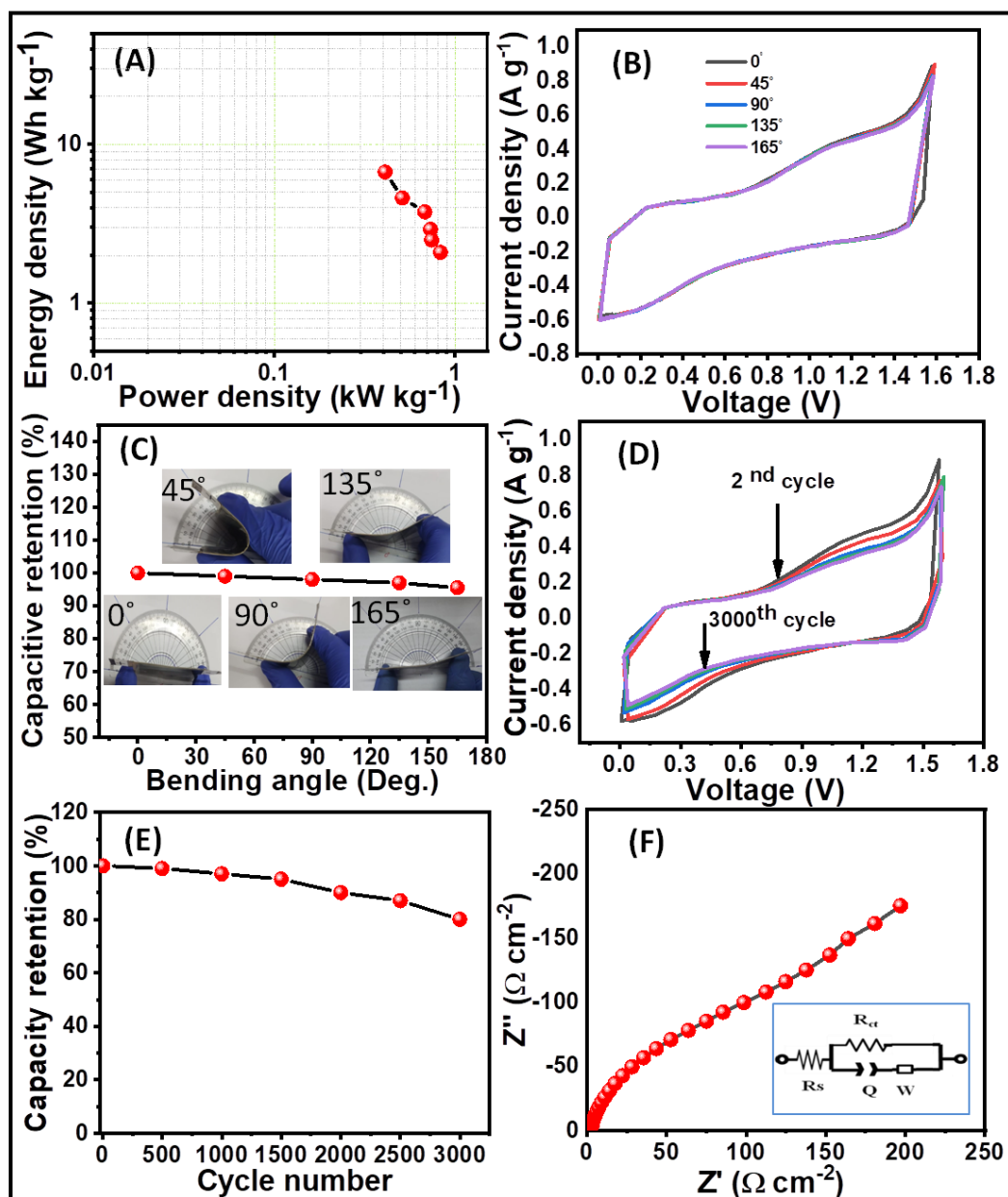


Fig. 6.8: (A) The Ragone plot of FSS-SSc device, (B) the CV curves of FSS-SSC device at different bending angles, (C) plot of capacitive retention versus bending angles [Insets show photograph of device at different bending angles], (D) cyclic stability curves of FSS-SSc device at scan rate of 100 mV s^{-1} for 3000 CV cycles, (E) plot of capacity retention versus cycle number and (F) Nyquist plot of FSS-SSc device (Inset demonstrates the equivalent circuit).

6.2B.3.5 Stability:

Fig. 6.8(D) shows the cyclic stability of the FSS-SSc device at a constant scan rate of 100 mV s^{-1} for 3000 CV cycles, which indicates the area under CV curve decreases with increasing the number of CV cycles. **Fig. 6.8(E)** illustrates the capacity retention versus number of cycle. The FSS-SSc device showed 80 % capacitive

retention after the 3000 CV cycles. Yadav et al [23] fabricated FSS-SSc using La_2O_3 electrode and reported 79 % stability retention over 1000 CV cycles. Patil and Lokhande [20] reported 73 % cyclic retention up to 1000 CV cycles for fabricated FSS-SSc device using La_2S_3 electrodes.

6.2B.3.6 EIS study:

EIS technique was used to investigate the capacitive and resistive components of FSS-SSc device. The Nyquist plot of FSS-SSc device is presented in **Fig. 6.8(F)**. The inset of **Fig. 6.8(F)** demonstrates equivalent circuit and shows values of R_s , R_{ct} and W of the device as 3.5, 46.3 and $48.7 \Omega \text{ cm}^{-2}$, respectively. **Table 6.4** shows fitted parameters for equivalent circuit data.

Table 6.4: Impedance parameters for FSS-SSc device.

Parameter	Values of parameters
$R_s (\Omega \text{ cm}^{-2})$	3.5
Q (mF)	0.85
$R_{ct} (\Omega \text{ cm}^{-2})$	46.3
$W (\Omega \text{ cm}^{-2})$	48.7

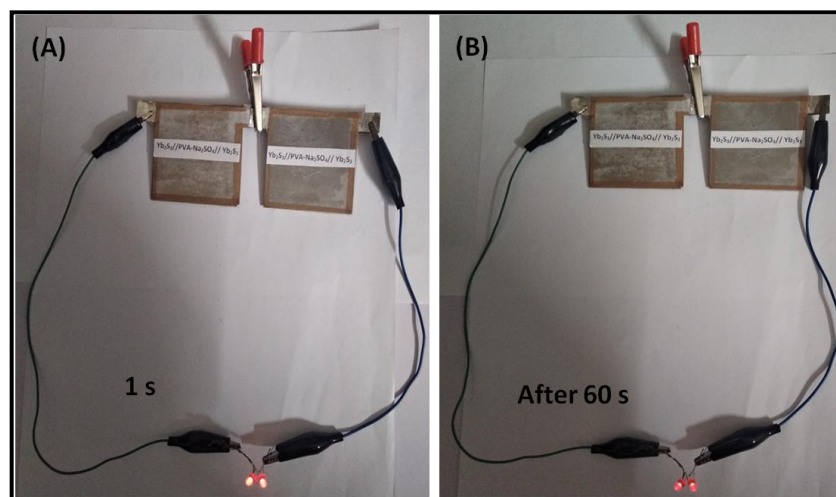


Fig. 6.9: Photographs of two red LEDs glowing at (A) 1 and (B) 60 seconds.

Fig. 6.9 (A, B) show photographs of the device of two series connected devices to glow two red light emitting diodes. Both series connected devices were charged for 30 s and the image of glowing LEDs for time periods of 1 and 60 s is captured. The intensity of LEDs decreases with time (**Fig. 6.9(B)**). Therefore, the significant initial

glowing intensity of LEDs attributed to the high P.D. of the device as well as high E.D. of device is confirmed.

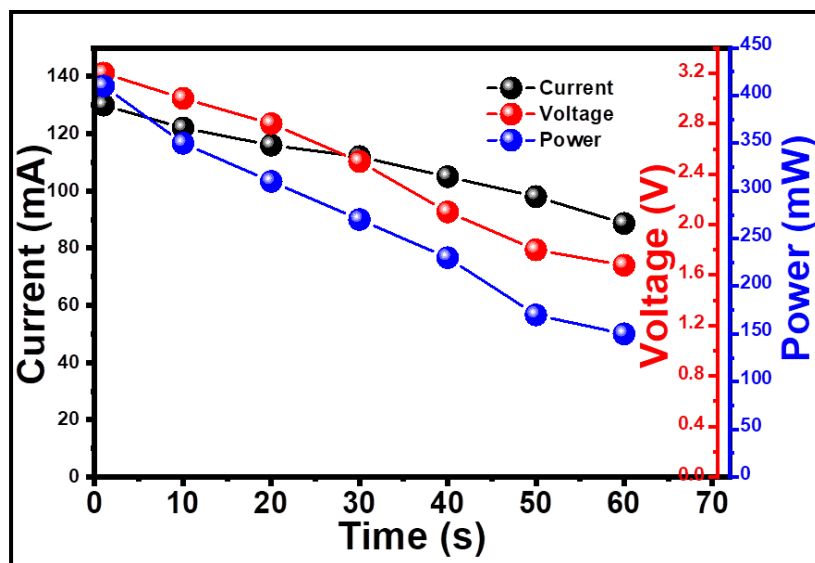


Fig. 6.10: The current, voltage and power versus time graphs of FSS-SSc device during discharging.

The plots of current, voltage and power with discharging time of device are demonstrated in **Fig. 6.10**. It is seen that, the discharge current decreases from 130 to 85 mA and voltage decreases from 3.2 to 1.7 V and also the power decreases from 410 to 150 mW.

The (SILAR) symmetric device exhibited better performance than (CBD) symmetric device. The (SILAR) symmetric device ($\text{Yb}_2\text{S}_3/\text{PVA-Na}_2\text{SO}_4/\text{Yb}_2\text{S}_3$) showed better output in PVA- Na_2SO_4 gel electrolyte owing to the more charge/discharge propagation with good reversibility than (CBD) symmetric device ($\text{Yb}_2\text{S}_3/\text{PVA-Na}_2\text{SO}_4/\text{Yb}_2\text{S}_3$) in PVA-KOH gel electrolyte.

6.3 Section-C

6.3C: Fabrication and performance evaluation of ($\text{GO}/\text{Yb}_2\text{S}_3//\text{GO}/\text{Yb}_2\text{S}_3$) flexible solid state symmetric supercapacitor device (SILAR method)

6.3C.1 Introduction:

The present section deals with synthesis of $\text{GO}/\text{Yb}_2\text{S}_3$ composite electrodes, fabrication and supercapacitive performance of FSS-SSc.

6.3C.2 Experimental details:

6.3C.2.1 Electrode preparation:

The SILAR method is used for synthesis of GO/Yb₂S₃ composite electrodes over SS substrate. The preparative parameters for Yb₂S₃ electrodes are given detailed in (4A.1.3).

6.3C.2.2 Polymer gel electrolyte (PVA-Na₂SO₄) preparation:

The preparation of PVA-Na₂SO₄ polymer gel electrolyte process is described detail in 6.2B.2.2.

6.3C.2.3 Fabrication of (GO/Yb₂S₃//GO/Yb₂S₃) flexible solid state symmetric supercapacitor device:

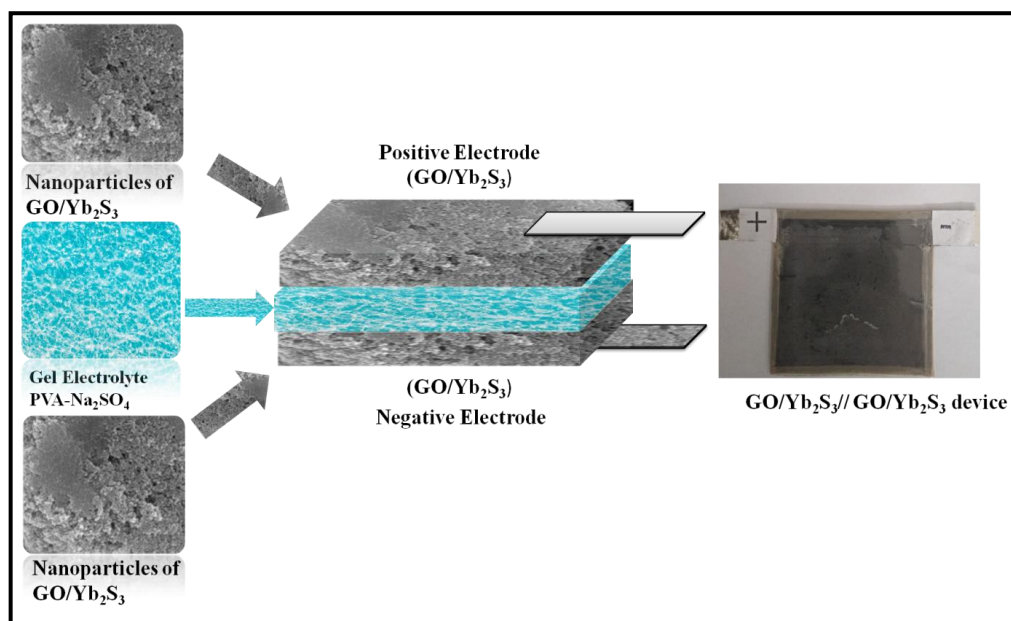


Fig. 6.11: The schematic representation of FSS-SSc device formation of GO/Yb₂S₃//GO/Yb₂S₃ composite electrodes.

A FSS-SSc device of configuration GO/Yb₂S₃//GO/Yb₂S₃ was prepared for testing the practical ability of composite electrodes. The device was made by two identical GO/Yb₂S₃ composite electrodes with sandwiched polymer gel electrolyte. Polymer gel electrolyte offers different features as compared to the liquid electrolyte such as smaller size, leakage-free system, higher range thermal stability as well as excellent electrochemical stability, effective ionic separator and flexible setup for the supercapacitor [26, 27]. The symmetric device fabrication process is explained in detail 6.2B.3. Fig. 6.11 shows the schematic diagram for formation of FSS-SSc (GO/Yb₂S₃//GO/Yb₂S₃) device.

6.3C.3 Supercapacitive performance evaluation of FSS-SSc device:

The electrochemical performance of FSS-SSc (GO/Yb₂S₃//GO/Yb₂S₃) device was carried out with CV, GCD, stability and EIS studies.

6.3C.3.1 Cyclic voltammetry (CV):

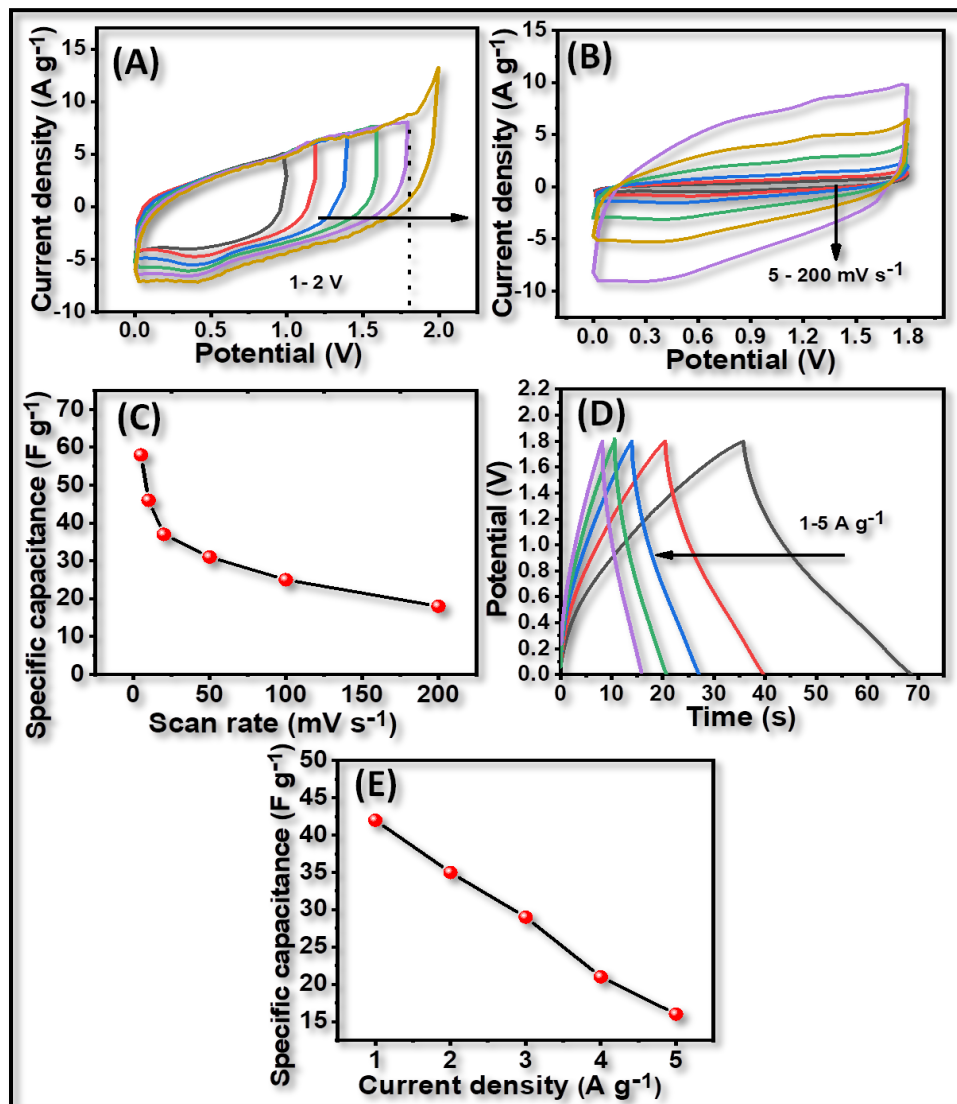


Fig. 6.12: (A) Potential window selection in the voltage range from 1.0 to 1.8 V, (B) the CV curves of FSS-SSc device at varied scan rate of 5-200 mV s⁻¹, (C) plot of specific capacitance versus scan rate, (D) the GCD curves at charging current densities from 1-5 A g⁻¹ and (E) plot of specific capacitance versus current density.

The CV curve measurements of FSS-SSc device was accomplished in different potential windows (1.0 to 1.8 V) at a fixed scan rate of 100 mV s⁻¹ and depicted in **Fig. 6.12(A)**. **Fig. 6.12(A)** reveals that 0.0 to 1.8 V wide potential window is suitable for FSS-SSc device as it exhibits a wider area under the CV curve and excellent current response. **Fig. 6.12(B)** displays the CV curves of the FSS-SSc device examined at scan rate from 5 to 200 mV s⁻¹ in the potential window between 0.0 to 1.8 V. The CV curves

represent the quasi-rectangular like profile with the excellent current response at various scan rates. The device exhibits C_s value of 58 F g^{-1} at scan rate of 5 mV s^{-1} in PVA- Na_2SO_4 gel electrolyte. **Fig. 6.12(C)** illustrates the plot of C_s versus scan rate. The obtained C_s are 18 to 58 F g^{-1} for the scan rates between 200 to 5 mV s^{-1} . As seen from the CV, an electro active material involvement is more at a lower scan rate because of the existence of a wider time scale, which offers the whole utilization of active sites of the electrode material [28].

6.3C.3.2 Galvanostatic charge discharge (GCD):

The GCD curves of FSS-SSc device with varied charging current densities of 1 to 5 A g^{-1} are shown in **Fig. 6.12(D)**. The shape of GCD curves is quasi-triangular, therefore the GCD curves show surface redox pseudocapacitor behaviour [19]. The GCD measurement yields C_s of 42 F g^{-1} at a current density of 1.0 A g^{-1} . The plot of C_s versus current density is shown in **Fig. 6.12(E)**. The C_s of 42 to 16 F g^{-1} are obtained at current densities of 1 to 5 A g^{-1} , respectively. Decrease in the C_s with an increase in the charging current density observed in **Fig. 6.12(E)** may be due to limitations in the charge-transport process at higher current density.

6.3C.3.3 Ragone plot:

Fig. 6.13(A) illustrates Ragone plot of the FSS-SSc device, which exposes the E.D. of 28 Wh kg^{-1} with P.D. of 0.62 kW kg^{-1} at the current density of 1.0 A g^{-1} .

6.3C.3.4 Flexibility:

The mechanical flexibility is crucial for the practical application of the FSS-SSc device [29]. To study of mechanical flexibility of FSS-SSc device, CV curves recorded at various bending angles (0 - 165°) at the scan rate of 100 mV s^{-1} are illustrated in **Fig. 6.13(B)**. The shape of CV curves remains approximately identical even at a bending angle of 165° . This indicates the superior adhesion of active electrode material with the support of SS substrate and a good interface between the active material and PVA- Na_2SO_4 gel electrolyte. The plot of capacity retention with various bending angle is shown in **Fig. 6.13(C)** and its insets demonstrate device photographs at different bending angles. The FSS-SSc device shows excellent mechanical flexibility with 95 % capacitive retention at a bending angle of 165° . Capacitive retention values at different bending angles of FSS-SSc device are demonstrated in **table 6.5**.

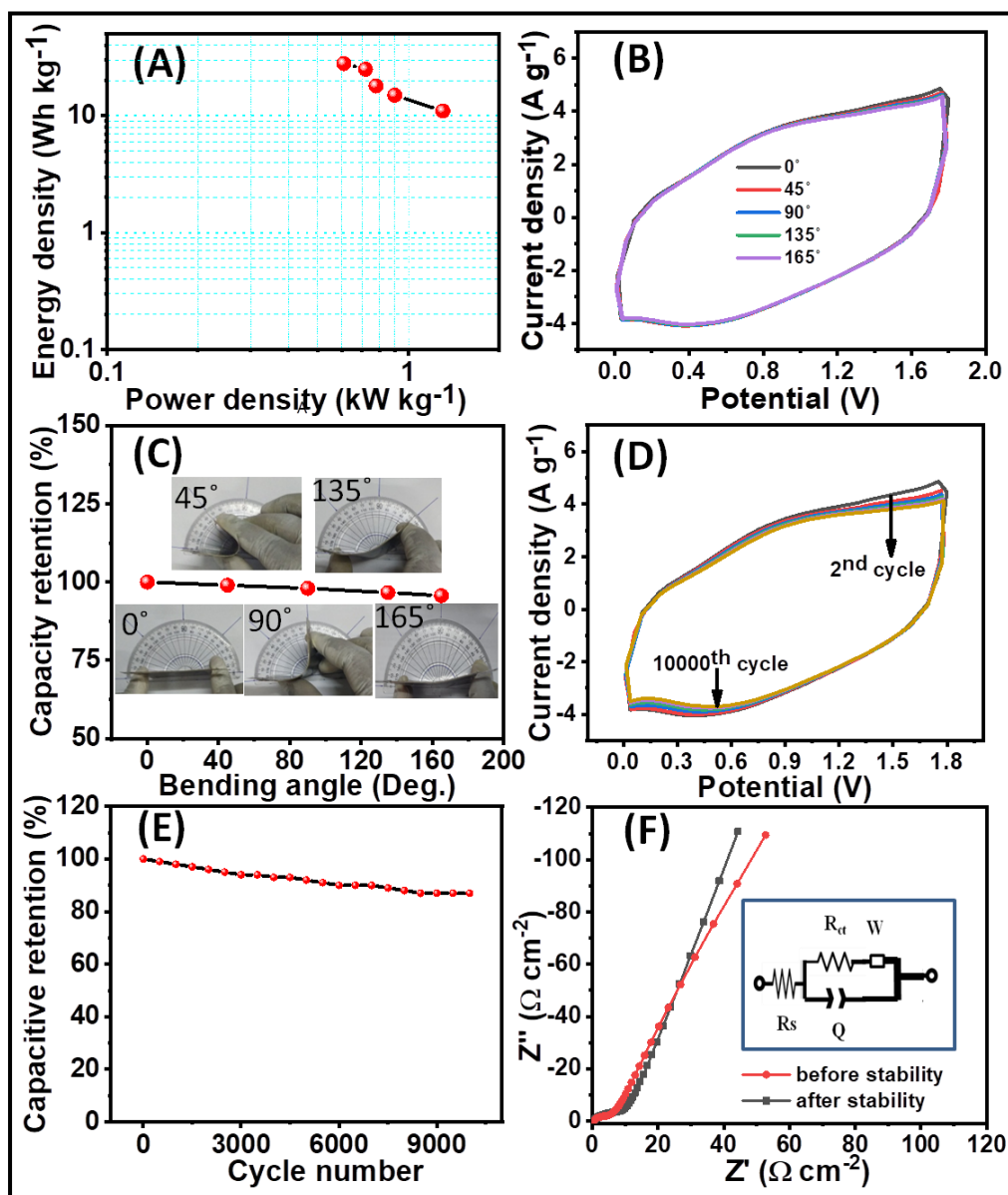


Fig. 6.13: (A) Ragone plot of FSS-SSc device, (B) the CV curves of FSS-SSc device at various bending angles, (C) plot of capacitive retention versus bending angle [Insets show photograph of device at different bending angles], (D) cyclic stability curves of FSS-SSc device at 100 mV s^{-1} over 10000 cycles, (E) plot of capacitance retention versus cycle number and (F) Nyquist plots of FSS-SSc device before and after stability (Inset shows best fitted equivalent circuit).

Table 6.5: Capacitive retention values at different bending angles for FSS-SSc device.

Bending angle	Capacitive retention of FSS-SSc device (%)
0°	100
45°	98.5
90°	97
135°	96.5
165°	95

6.3C.3.5 Stability:

An electrochemical cycling stability of the FSS-SSc device was carried out through CV curves. **Fig. 6.13(D)** shows the CV curves of FSS-SSc device at a scan rate of 100 mV s^{-1} over 10000 CV cycles. With increase in the cycle number, area under the curve slightly decreases. The plot of Cs as a function of cycle number is shown in **Fig. 6.13(E)**. The FSS-SSc device exhibits good capacitive retention of 87 % with sustaining shape of CV profile after 10000 CV cycles.

6.3C.3.6 Electrochemical impedance spectroscopy (EIS):

To investigate resistive parameters of FSS-SSc device, EIS was examined. The Nyquist plots of FSS-SSc device for before and after stability are shown in **Fig. 6.13(F)** and the inset shows the equivalent circuit with the best-fitted impedance data. The R_s , R_{ct} and W values (before stability) calculated from the Nyquist plots are 0.50 , 4.75 and $5.58 \text{ } \Omega \text{ cm}^{-2}$, respectively. After stability R_s , R_{ct} and W values of the FSS-SSc device are 0.74 , 6.8 and $8.46 \text{ } \Omega \text{ cm}^{-2}$, respectively. As there is a tiny change in the R_s value after cycling, it indicates that cycling has no effect on intrinsic resistance of film and contact between film and current collector. The semicircles present before and after cycling are due to the parallel combination of R_{ct} and capacitor (C). The increase in R_{ct} value after cycling is due to the electrochemical loss of electrode material. The raise W value after cycling is owing to the diffusion electrolyte ions [30, 31]. Electrochemical impedance parameters of FSS-SSc device (before and after stability) are illustrated in **table 6.6**.

Table 6.6: Impedance parameters of FSS-SSc device.

Parameter	FSS-SSc device	
	Before stability	After stability
$R_s \text{ (}\Omega \text{ cm}^{-2}\text{)}$	0.50	0.74
$Q \text{ (mF)}$	93	57
$R_{ct} \text{ (}\Omega \text{ cm}^{-2}\text{)}$	4.75	6.8
$W \text{ (}\Omega \text{ cm}^{-2}\text{)}$	5.58	8.46

The practical demonstration of two series-connected FSS-SSC devices is displayed in **Fig. 6.14(A-B)**. Initially, these devices were charged with a potential of $+3.6 \text{ V}$ for 30 s and discharged through a panel of 211 red LEDs for 30 s **Fig. 6.14(A-B)**. The output power of the device was 640 mW cm^{-2} which signifies good charge

storing capability. The similar discharge period compared to the charging period of FSS-SSc device makes suitable candidate for use in practical energy storage devices.

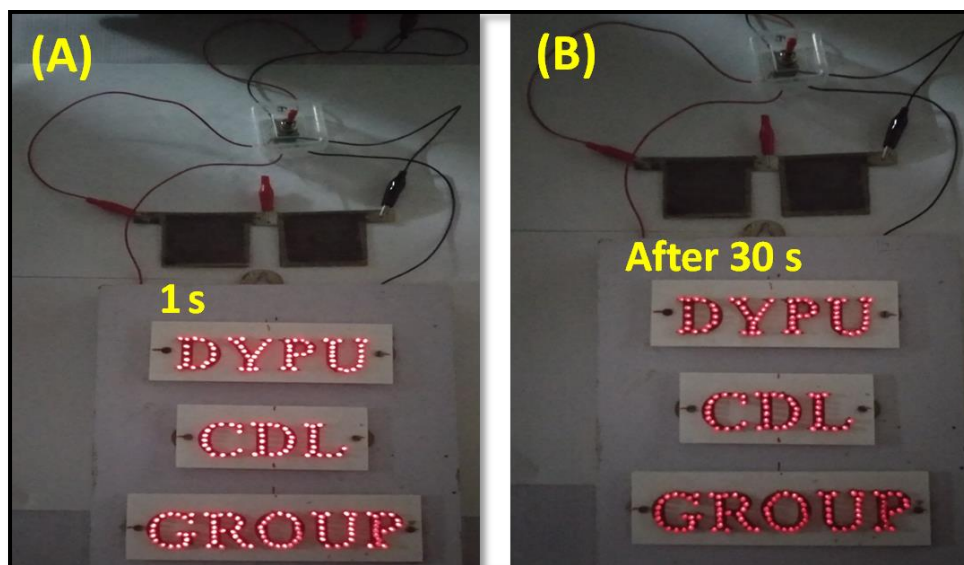


Fig. 6.14: (A, B) Practical demonstration of FSS-SSc device glowing (211) red LEDs panel images at 1 (A) and (B) 30 s.

The I-V characteristic of 211 red LEDs panel is shown in **Fig. 6.15(A)**. At 1.7 V with current 6.0 mA, LEDs panel starts to glow. **Fig. 6.15(B)** shows the plots of current, voltage and power with discharging time of device using 211 LEDs panel. It is seen that the discharge current decreases from 180 to 85 mA and voltage decreases from 3.6 to 1.7 V and the power decreases from 640 to 150 mW.

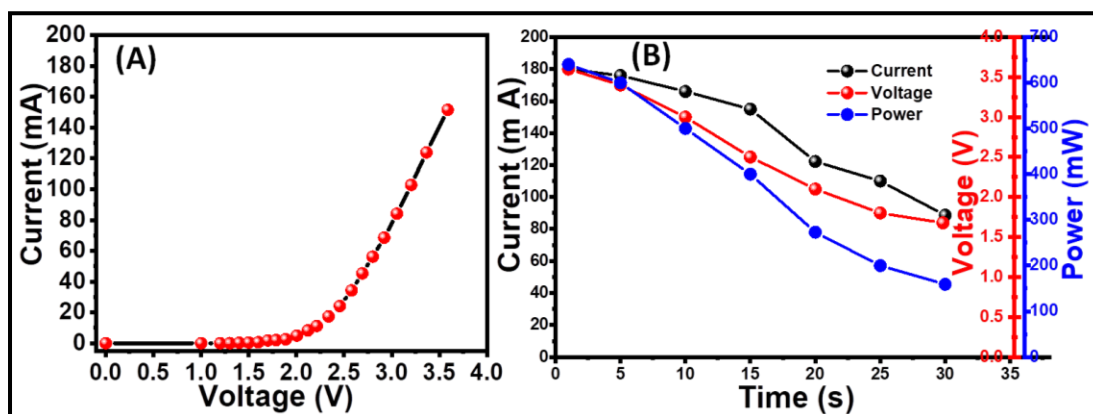


Fig. 6.15: (A) The I-V characteristic of 211 red LEDs panel and (B) the current, voltage and power versus time plots of FSS-SSc device during discharging.

6.4 Section- D

6.4D: Fabrication and performance evaluation of (GO/Yb₂S₃//MnO₂) flexible solid state asymmetric supercapacitor device (SILAR method)

6.4D.1 Introduction:

The MnO₂ thin film material was selected as a positive electrode for the fabrication of FSS-ASSc device. The advantages and some features of MnO₂ thin film material are explained in 5A.1. Also, the preparation of MnO₂ thin film, the structural morphological characterisation of MnO₂ thin film and its supercapacitor properties are briefly described in chapter V.

Section-D deals with the synthesis of GO/Yb₂S₃ and MnO₂ electrodes, fabrication and supercapacitive FSS-ASSc device (SILAR method) performance.

6.4D.2 Experimental details:

6.4D.2.1 Electrode preparation:

The SILAR method was used for synthesis of GO/Yb₂S₃ composite and MnO₂ electrodes. The GO/Yb₂S₃ composite electrode preparation process is detailed in 4.2.3.4 and 4.3.1.3. Also, the synthesis process and preparative parameters of MnO₂ electrode are detailed in 5A.2.3 and 5A.3.1.

6.4D.2.2 Polymer gel electrolyte (PVA-Na₂SO₄) preparation:

The preparation of PVA-Na₂SO₄ polymer gel electrolyte process is described detail in 6.2B.2.2.

6.4D.2.3 Fabrication of (GO/Yb₂S₃//MnO₂) flexible solid state asymmetric supercapacitor (FSS-ASSc) device:

To check the feasibility of the electrode for practical applications, we further fabricated a FSS-ASSc device and evaluated its performance. FSS-ASSc (GO/Yb₂S₃//MnO₂) device was fabricated using GO/Yb₂S₃ composite material as a negative electrode, MnO₂ as a positive electrode and PVA-Na₂SO₄ as a polymer gel electrolyte.

The gel electrolyte was coated on (5 x 5 cm²) area of GO/Yb₂S₃ composite and MnO₂ electrodes. Then assembled device was kept 1 h to press under applied pressure 0.5 ton using a hydraulic press. Fig. 6.16 displays the schematic formation of FSS-ASSc (GO/Yb₂S₃//MnO₂) device. For charge balance, the mass ratio of an anode and

cathode material electrodes was determined from the 2.12 relation [32]. The calculated mass ratio of GO/Yb₂S₃ composite and MnO₂ was 2.0:1.80.

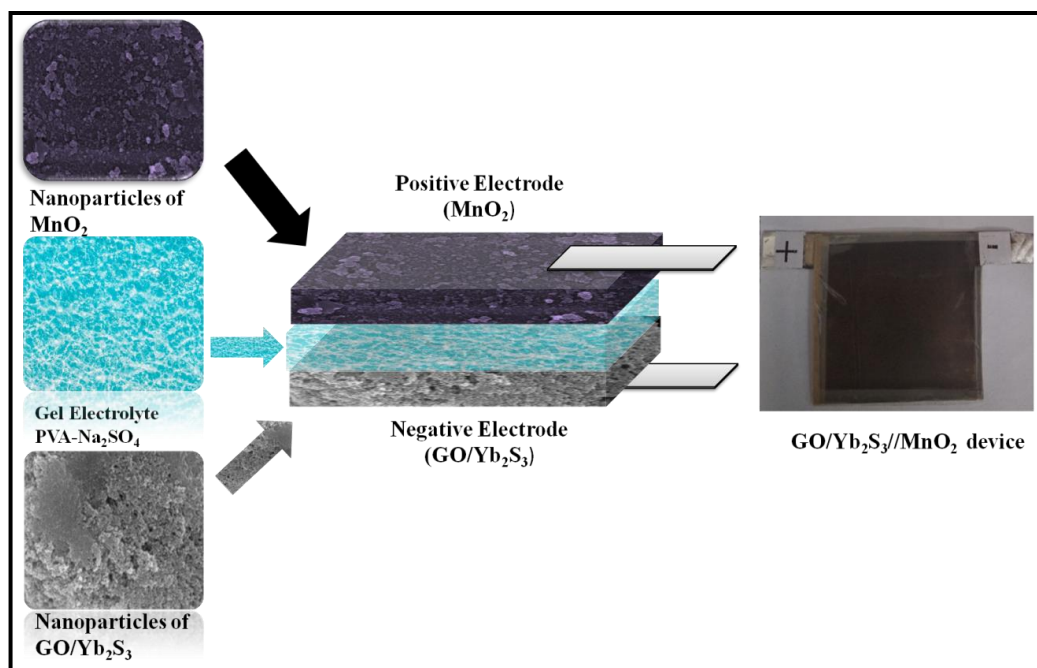


Fig. 6.16: The schematic representation of FSS-ASSc device formation using GO/Yb₂S₃/MnO₂.

6.4D.3 Supercapacitive performance evaluation of FSS-ASC device:

The electrochemical performance of FSS-ASSc (GO/Yb₂S₃/MnO₂) device was carried out by CV, GCD, stability and EIS studies.

6.4D.3.1 cyclic voltammetry (CV):

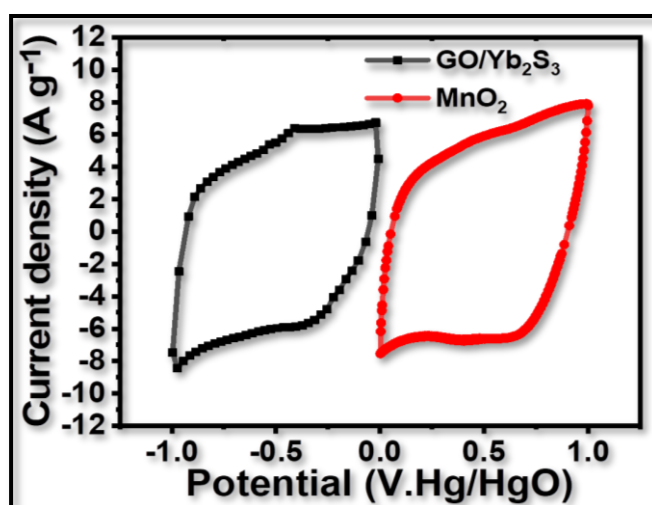


Fig. 6.17: The CV curves of GO/Yb₂S₃ composite and MnO₂ electrodes at scan rate of 100 mV s⁻¹.

The CV test was performed to evaluate the electrochemical behaviour of FSS-ASSc (GO/Yb₂S₃//MnO₂) device. The wide operating potential window and corresponding E.D. are the main advantages of fabricating FSS-ASSc devices. The CV curves of GO/Yb₂S₃ composite and MnO₂ electrodes at 100 mV s⁻¹ scan rate within negative and positive potential windows are shown in **Fig. 6.17**. The working potential windows of MnO₂ and GO/Yb₂S₃ electrode are from 0 to +1.0 V/Hg/HgO and -1.0 to 0 V/Hg/HgO, respectively. Therefore, the GO/Yb₂S₃//MnO₂ asymmetric device can attain the maximum working potential window up to +2.0 V.

Fig. 6.18(A) illustrates CV curves of FSS-ASSc device using varied potential windows at scan rate of 100 mV s⁻¹. The quasi-rectangular CV curve shape observed irrespective potential windows displaying the capacitive behaviour of FSS-ASSc device. The close examination of the CV curve at the wider potential window does not display any signature of the decomposition of electrolyte, indicating that FSS-ASSc device can bear a wide working voltage up to 2.0 V. Thus, the CV shape profile of FSS-ASSc device was further examined as a function of scan rate in potential window of 0 to 2.0 V. **Fig. 6.18(B)** shows CV curves FSS-ASSc (GO/Yb₂S₃//MnO₂) device at different scan rates from 5-200 mV s⁻¹. The shape of CV curves is quasi-rectangular. The plot of variation in Cs versus scan rate is depicted in **Fig. 6.18(C)**. FSS-ASSc device exhibits Cs of 92 F g⁻¹ at a scan rate of 5 mV s⁻¹. The Cs value decreases with increase in the scan rate from 5 to 200 mV s⁻¹, as seen in **Fig. 6.18(C)**. At a higher scan rate (200 mV s⁻¹), the fact that movement of the electrolyte ions has limited time at the surface of the electrode [33, 34].

6.4D.3.2 Galvanostatic charge discharge (GCD):

The GCD curves were recorded at varied current densities of 1-5 A g⁻¹ in potential window of 0 to 2 V as shown in **Fig. 6.18(D)**. The GCD curves show the quasi-triangular shape, therefore GCD curves exhibit surface redox pseudocapacitor behaviour [19]. In this case, a maximum Cs value of 71 F g⁻¹ was obtained at a current density of 1.0 A g⁻¹. The plot Cs versus current density is shown in **Fig. 6.18(E)**. As seen from **Fig. 6.18(E)** discharge time decreases with raising current density which may be due to the inefficient interaction between the electrolyte and thin film electrode at high current density.

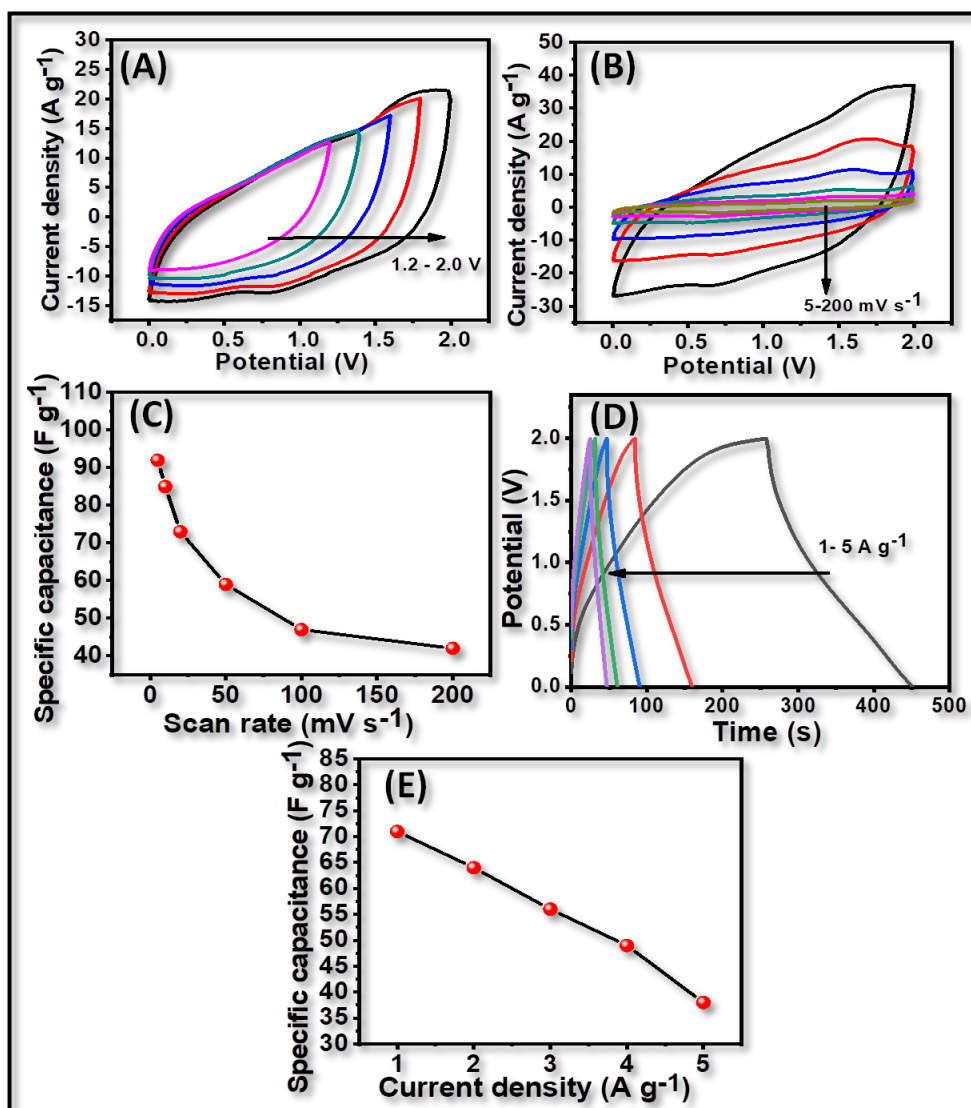


Fig. 6.18: (A) Potential window selection in the voltage ranging from 1.2 to 2.0 V at scan rate of 100 mV s⁻¹, (B) the CV curves of asymmetric device at different scan rate of 5-200 mV s⁻¹, (C) plot of specific capacitance versus scan rate, (D) GCD curves at current densities from 1-5 A g⁻¹ and (E) plot of specific capacitance versus current density.

6.4D.3.3 Ragone plot:

Fig. 6.19(A) shows the Ragone plot of FSS-ASSc device. FSS-ASSc device delivers the high E.D. of 43 Wh kg⁻¹ and P.D. of 0.84 kW kg⁻¹.

6.4D.3.4 Flexibility:

The CV curves of FSS-ASSc device at various bending angles (0°, 45°, 90°, 135° and 165°) at fixed scan rate of 100 mV s⁻¹ are shown in **Fig. 6.19(B)**. The overlapping of CV curves over each other reflects consistent supercapacitive performance with bending of FSS-ASSc device. It recommends that, FSS-ASSc device

is useful as a flexible supercapacitor for the purpose of portable electrical energy storage devices [35]. Moreover, capacitive retention at various bending angles is illustrated in Fig. 6.19(C) and its insets show photograph of device at different bending angles. The FSS-ASSc device retained 97 % of its initial capacitance at a bending angle of 165°. Table 6.7 illustrates the capacitive retention at different bending angles of FSS-ASSc device.

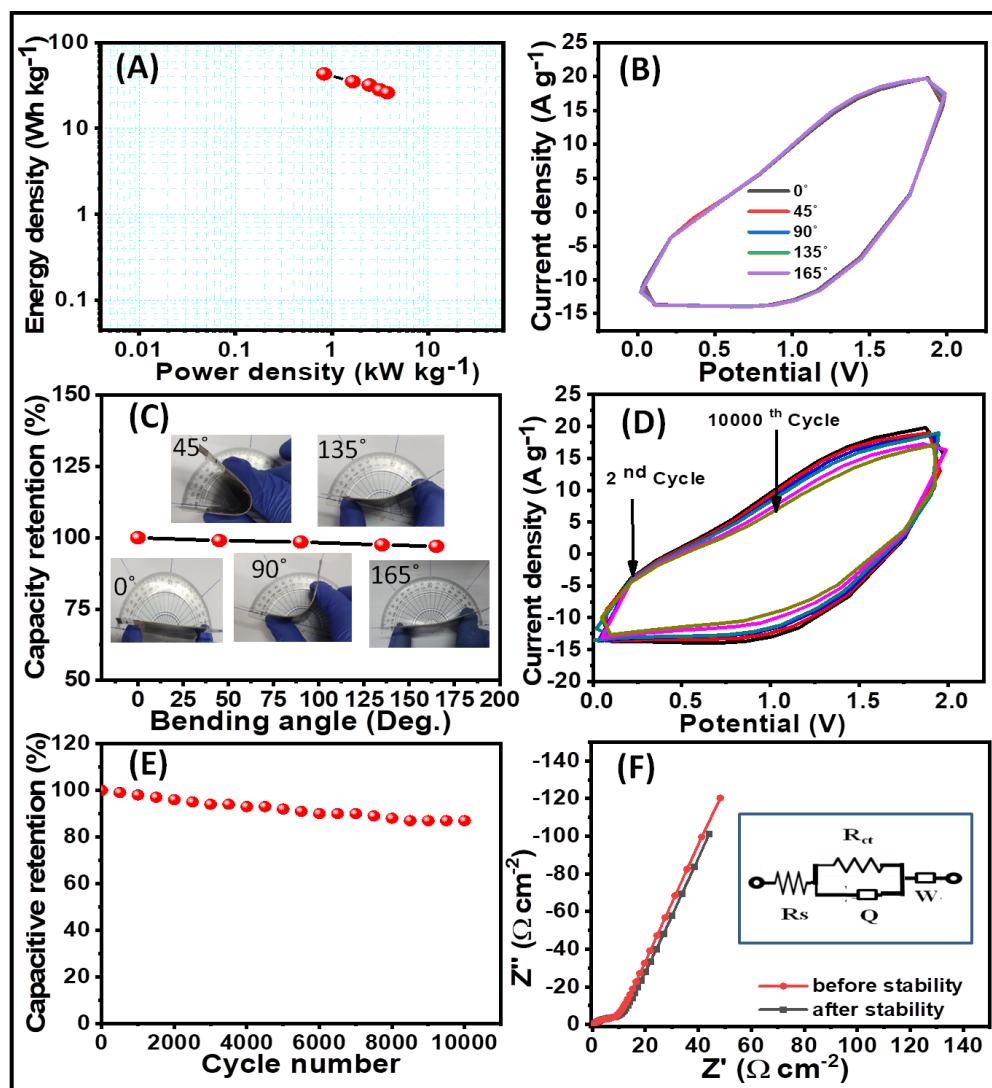


Fig. 6.19: (A) Ragone plot of FSS-ASSc device, (B) the CV curves of FSS-ASSc device at various bending angles, (C) plot of capacity retention versus bending angle [Insets show photograph of device at different bending angles], (D) cyclic stability curves of asymmetric device at 100 mV s⁻¹ over 10000 CV cycles, (E) plot of capacitance retention versus cycle number and (F) Nyquist plots of before and after stability and (inset shows best fitted equivalent circuit).

Table 6.7: Capacitive retention values at different bending angles for FSS-ASSc device.

Bending angle	Capacitive retention of FSS-ASSc device (%)
0°	100
45°	99
90°	98.5
135°	98
165°	97

6.4D.3.5 Cyclic stability:

The cyclic stability of FSS-ASSc device is a significant factor in electrochemical processes. Accordingly, the cyclic performance of the FSS-ASSc device recorded up to 10000 cycles with at a scan rate of 100 mV s⁻¹ are shown in **Fig. 6.19(D)**. **Fig. 6.19(E)** shows the capacitive retention of FSS-ASSc device. The FSS-ASSc device shows 85 % cyclic retention after the 10000 CV cycles. The reduction in Cs value after cycling may be due to the degradation or detachment of active material during CV cycling and loss of electric contact between constituent composite materials.

6.4D.3.6 EIS:

The EIS measurement was recorded in the frequency range of 0.1 Hz to 1 MHz through amplitude of 10 mV and 0 V bias voltage. Nyquist plots before and after stability of FSS-ASSc device are presented in **Fig. 6.19(F)** and the inset shows the equivalent circuit with the best-fitted impedance data. The Rs values of the FSS-ASSc device before and after stability are 0.6 and 0.83 Ω. Rct values of FSS-ASSc device before and after stability are 5.50 and 7.45 Ω cm⁻² obtained from Nyquist plots. The W values of FSS-ASSc device before and after stability are 6.10 and 9.03 Ω cm⁻², respectively. After stability, parameters value are slightly increased due to the loss of material and/or increased contact resistance of current collector with electrode as a result of electrochemical cycling [36]. Electrochemical impedance parameters of FSS-ASSc device before and after stability are illustrated in **table 6.8**.

Table 6.8: Impedance parameters for FSS-ASSc device before and after stability.

Parameter	FSS-ASSc device	
	Before stability	After stability
Rs (Ω cm ⁻²)	0.60	0.83
Q (mF)	85	63
Rct (Ω cm ⁻²)	5.50	7.45
W (Ω cm ⁻²)	6.10	9.03

The good electrochemical performance of FSS-ASSc device demonstrates that nanoparticles and nanocomposite effectively increase the electronic and ionic transportation and decrease the charge-transfer resistance. Also, the strong interfacial bonding between constituent phases in the composite electrode enhances the charge storage ability by shortening the diffusion path length.

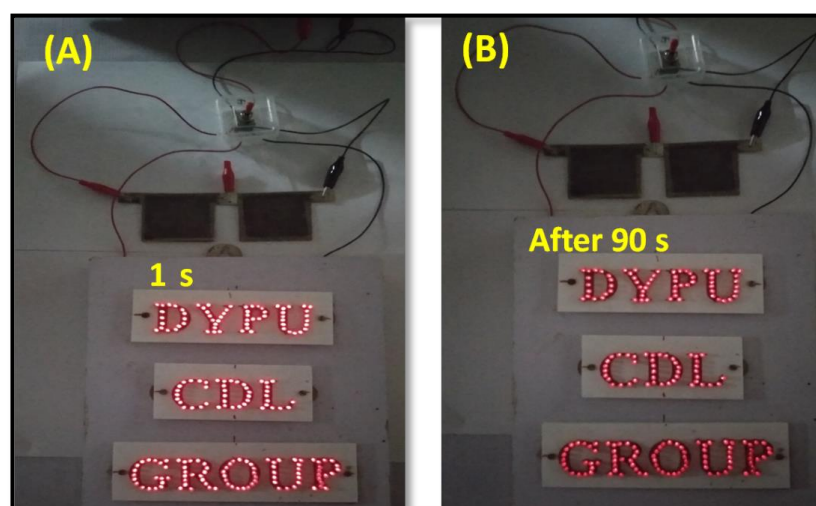


Fig. 6.20: (A, B) Practical demonstration of FSS-ASSc device glowing red (211) LEDs panel images at 1 (A) and (B) 90 s.

The practical demonstration of two series-connected FSS-ASSc devices is displayed in **Fig. 6.20(A, B)**. Initially, these devices are charged with a potential of +4.0 V for 30 s and discharged through a panel of 211 red LEDs for 90 s. The output power of device is 810 mW cm^{-2} which signifies good charge storing capability. The larger discharge period compared to charging period of FSS-ASSc device confirms its suitability for use in practical energy storage devices.

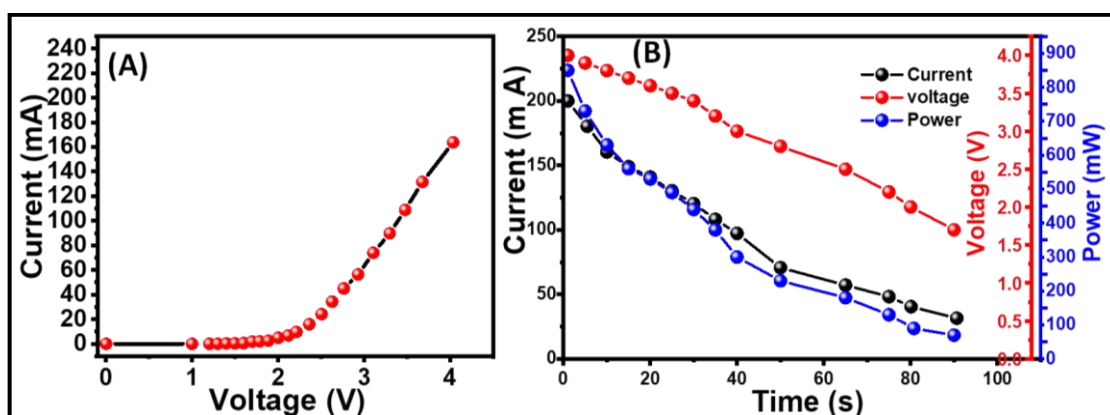


Fig. 6.21: (A) The I-V characteristic of 211 red LEDs panel and (B) the current, voltage and power versus time graphs of FSS-ASSc device during discharging.

Fig. 6.21(A) shows the I-V characteristic of 211 red LEDs panel. **Fig. 6.21(B)** demonstrates the plots of current, voltage and power with discharging time of device using 211 LEDs panel, which indicate that the discharge current reduces from 203 to 38 mA and voltage decreases from 4.0 to 1.7 V and also the power decreases from 840 to 74 mW.

6.5: Conclusions:

The Yb_2S_3 , $\text{GO}/\text{Yb}_2\text{S}_3$ and MnO_2 thin film electrodes were synthesized by simple and low temperature chemical methods (CBD and SILAR) over flexible SS substrates. Flexible symmetric Yb_2S_3 , $\text{GO}/\text{Yb}_2\text{S}_3$ and asymmetric $\text{GO}/\text{Yb}_2\text{S}_3/\text{MnO}_2$ solid state supercapacitor devices were fabricated using the flexible Yb_2S_3 , $\text{GO}/\text{Yb}_2\text{S}_3$ and MnO_2 thin films electrode. For the fabrication of supercapacitor devices, the PVA-KOH and PVA- Na_2SO_4 gel electrolytes were used. Supercapacitive performance of symmetric and asymmetric devices was investigated using CV and GCD and EIS techniques. In symmetric supercapacitor devices, the $\text{GO}/\text{Yb}_2\text{S}_3$ composite electrodes (SILAR) device showed better supercapacitive performance than the bare Yb_2S_3 electrodes (CBD and SILAR) symmetric supercapacitor devices. The $\text{GO}/\text{Yb}_2\text{S}_3$ composite electrodes device exhibited specific capacitance of 58 F g^{-1} . In overall symmetric and asymmetric devices, the asymmetric $\text{GO}/\text{Yb}_2\text{S}_3/\text{MnO}_2$ showed better supercapacitive properties than the other devices. The asymmetric $\text{GO}/\text{Yb}_2\text{S}_3/\text{MnO}_2$ device (SILAR) achieved highest specific capacitance of 92 F g^{-1} . **Table 6.9** shows supercapacitive performance of symmetric and asymmetric devices.

Table 6.9: Supercapacitive performance of symmetric and asymmetric devices.

Sr. no.	Device configuration	Method	Specific cap. (Cs) (F g^{-1})	Energy density (Wh kg^{-1})	Power density (kW kg^{-1})	Stability (%)
1	$\text{Yb}_2\text{S}_3/\text{Yb}_2\text{S}_3$	CBD	15	6.40	0.30	78 (3000 cycle)
2	$\text{Yb}_2\text{S}_3/\text{Yb}_2\text{S}_3$	SILAR	21	7.68	0.38	80 (3000 cycle)
3	$\text{GO}/\text{Yb}_2\text{S}_3//\text{GO}/\text{Yb}_2\text{S}_3$	SILAR	58	28	0.62	87 (10000 cycle)
4	$\text{GO}/\text{Yb}_2\text{S}_3//\text{MnO}_2$	SILAR	92	43	0.84	85 (10000 cycle)

Table 6.9 clearly shows that symmetric device GO/Yb₂S₃ composite electrode based device showed better capacitance (58 F g⁻¹) with E.D. (28 Wh kg⁻¹) and P.D. (0.62 kW kg⁻¹) as compared to bare CBD and SILAR prepared Yb₂S₃ electrode based devices due to GO composite with Yb₂S₃ material. In the symmetric and asymmetric devices based on Yb₂S₃, GO/Yb₂S₃ and MnO₂ electrodes, the asymmetric device (GO/Yb₂S₃//MnO₂) showed excellent supercapacitive performance with Cs (92 F g⁻¹), E.D. (43 Wh kg⁻¹) and P.D. (0.84 kW kg⁻¹).

6.6: References:

1. A. A. Yadav, V. S. Kumbhar, S. J. Patil, N. R. Chodankar, C. D. Lokhande, *Ceram Int.*, 42, (2016), 2079-2084.
2. K. B. Jinesh, V. A. Dam, J. Swerts, C. Nooijer, S. Elshocht, S. H. Brongersma, *Sens Actuators B*, 156, (2011), 276-282.
3. X. B. Liu and R. L. Yu, *Mater. Chem. Phys.*, 101, (2007), 448-454.
4. S. S. Kale, K. R. Jadhav, P. S. Patil, T. P. Gujar, C. D. Lokhande, *Mater Lett.*, 59, (2005), 3007-3009.
5. V. Capodieci, F. Wiest, T. Sulima, J. Schulze, I. Eisele, *Microelectron Reliab*, 45, (2005) 937-940.
6. F. J. Jing, L. Wang, Y. W. Liu, K. Y. Fu, X. B. Zhao, R. Shen, *Thin Solid Films*, 515, (2006), 1219-1222.
7. R. B. Pujari, A. C. Lokhande, T. T. Ghogare, S. B. Kale, C. D. Lokhande, *J. Mater. Sci. Mater. Electron.*, 29, (2018), 14116-14121.
8. P. K. Katkar, S. J. Marje, S. S. Pujari, S. A. Khalate, A. C. Lokhande, U. M. Patil, *ACS Sustain. Chem. Eng.*, 7, (2019), 11205-11218.
9. A. Pendashteh, M. Mousavi, M. Rahmanifar, *Electrochim. Acta.*, 88, (2013), 347-357.
10. K-J. Huang, L. Wang, Y-J. Liu, Y-M. Liu, H-B. Wang, T. Gan, L-L. Wang, *Int. J. Hydrog. Energy*, 38, (2013), 14027-14034.
11. C. D. Jadhav, S. S. Karade, B. R. Sankapal, G. P. Patil, P. G. Chavan, *Chem. Phys. Lett.*, 723, (2019), 146-150.
12. T. T. Ghogare, A. C. Lokhande, R. B. Pujari, C. D. Lokhande, *SN Applied Sciences*, 1, (2019), 110-117.
13. T. T. Ghogare, V. C. Lokhande, T. Ji, U. M. Patil, C. D. Lokhande, *Surf. Interfaces*, 1, (2020), 100507-100513.
14. A. M. Patil, V. C. Lokhande, U. M. Patil, P. A. Shinde, C. D. Lokhande, *ACS Appl. Mater. Interfaces*, 6, (2018), 787-802.
15. N. R. Chodankar, D. P. Dubal, G. S. Gund, C. D. Lokhande, *Energy Technol.*, 3, (2015), 1-8.
16. R. B. Pujari, A. C. Lokhande, A. A. Yadav, J. H. Kim, C. D. Lokhande, *Mater. Des.*, 108, (2016), 510-517.
17. B. Saravanakumar, K. K. Purushothaman, G. Muralidharan, *ACS Appl. Mater. Interfaces*, 4, (2012), 4484-4490.
18. A. M. Patil, V. C. Lokhande, A. C. Lokhande, N. R. Chodankar, T. Jib, J. H. Kim, C. D. Lokhande, *RSC Adv.*, 6, (2016), 68388-68401.
19. N. R. Chodankar, H. D. Pham, A. K. Nanjundan, F. S. Fernando, K. Jayaramulu, D. Golberg, Y-K. Han, D. P. Dubal, *Small*, 16, (2020), 2002806-2002841.
20. S. J. Patil and C. D. Lokhande, *Mater. Des.*, 87, (2015), 939-948.
21. N. R. Chodankar, D. P. Dubal, G. S. Gund, C. D. Lokhande, *Electrochimica. Acta.*, 165, (2015), 338-347.

22. N. R. Chodankar, D. P. Dubal, G. S. Gund, C. D. Lokhande, *J. Energy Chem.*, 25, (2015), 463-471.
23. A. A. Yadav, A. C. Lokhande, J. H. Kim, C. D. Lokhande, *Int. J. Hydrog. Energy*, 41, (2016) 18311-18319.
24. S. Wu, W. Chen, L. Yan, *J. Mater. Chem. A*, 2, (2014), 2765-2772.
25. P. Yang, Y. Ding, Z. Lin, Z. Chen, Y. Li, P. Qiang, M. Ebrahimi, W. Mai, C. P. Wong, Z. L. Wang, *Nano Lett.*, 14, (2014), 731-736.
26. A. A. Yadav, A. C. Lokhande, J. H. Kim, C. D. Lokhande, *J. Ind. Eng. Chem.*, 56, (2017), 90-98.
27. A. C. Lokhande, S. Teotia, A. R. Shelke, T. Hussain, I. A. Qattan, V. C. Lokhande, S. Patole, J. H. Kim, C. D. Lokhande, *Chem. Eng.*, 1, (2020), 125711-255749.
28. D. Wang, L. Xu, J. Nai, T. Sun, *J. Alloys Compd.*, 786, (2019), 109-117.
29. P. A. Shinde, V. C. Lokhande, A. M. Patil, T. Ji, C. D. Lokhande, *Energy Technol.*, 3, (2017), 35-48.
30. M. S. Abouzari, F. Berkemeier, G. Schmitz, D. Wilmer, *Solid State Ion.*, 180, (2009), 922-927.
31. S. Skale, V. Doleček, M. Slemnik, *Corros. Sci.*, 49, (2007), 1045-1055.
32. A. K. Nayak, A. K. Das, *ACS Sustainable Chem. Eng.*, 5, (2017), 10128-10138.
33. K. S. Kumar, N. Choudhary, Y. Jung, J. Thomas, *ACS Energy Lett.*, 3, (2018), 482-495.
34. T-F. Yi, J-J. Pan, T-T. Wei, Y. Li, G. Cao, *Nano. Today*, 33, (2020), 100894-100925.
35. P. K. Katkar, S. J. Marje, S. S. Pujari, S. A. Khalate, P. R. Deshmukh, U. M. Patil, *Synth. Met.*, 267, (2020), 114667-114679.
36. P. A. Shinde, A. C. Lokhande, N. R. Chodankar, A. M. Patil, J. H. Kim, C. D. Lokhande, *Electrochim. Acta.*, 224, (2017), 397- 404.

Chapter-VII

Summary and conclusions

Chapter-VII

Summary and Conclusions

The electric charge storage system includes capacitor, supercapacitors and battery. Unlike batteries, supercapacitor charges and discharges very fast without degrading the material. Supercapacitors are designed to bridge the gap in between battery and conventional capacitor. The recent trends have been attracted to fabricate the solid-state supercapacitor devices in small scale for large area application. Supercapacitors are fabricated in such a way to store and release energy within a second. In terms of potential candidate supercapacitors have to design in wide range of potential. The supercapacitor performance basically depending upon the nature of electrode surface, operating voltage and electrolyte stability. The supercapacitors are classified into three types depends upon the category of charge storage mechanism. The carbon based thin film electrode material shows pure electric double layer capacitors (EDLCs) type behavior, where non-faradic reaction occurs. For pseudocapacitor, the metal chalcogenides, metal oxides and polymers are applied, in which redox reaction occurs. The metal chalcogenides include rare earth chalcogenide materials having better reduction potential helpful in supercapacitive application to increase the potential window range with energy and power densities. The combinations of both materials are used in hybrid supercapacitor.

In this work, preparation of ytterbium sulfide (Yb_2S_3), graphene oxide (GO) and graphene oxide composite with ytterbium sulfide ($\text{GO}/\text{Yb}_2\text{S}_3$) thin films via simple, binder free, and cost effective, SILAR and CBD methods have been carried out. The films are characterized for surface textural, structural, and wettability studies. The electrochemical supercapacitive activities of GO, Yb_2S_3 and $\text{GO}/\text{Yb}_2\text{S}_3$ composite thin film electrodes are studied using the CV, GCD and EIS tests. After checking electrochemical supercapacitive behavior of GO, Yb_2S_3 and $\text{GO}/\text{Yb}_2\text{S}_3$ composite thin film electrodes, fabrication and the electrochemical supercapacitive properties of flexible symmetric and asymmetric supercapacitor devices are evaluated. The work has been distributed into seven chapters.

The **Chapter-I** begins with the introduction of supercapacitor devices, including necessity of supercapacitor, principle of supercapacitor and types of supercapacitor. A detailed account of literature survey on metal chalcogenides thin film and their supercapacitor application are described in chapter-I. Also, the literature

survey on GO based supercapacitors and their properties are included. At the end of this chapter, orientation and purpose of dissertation is discussed. Thin film introduction, brief taxonomy of film deposition methods, theoretical background of SILAR and CBD methods and their preparative parameters are discussed in the beginning part of **Chapter-II**. Also, the structural and surface textural studies of thin films are carried out using different characterization techniques. The structural characterizations of deposited thin films are studied using X-ray diffraction (XRD) and Fourier transform Raman spectroscopy (FT-Raman) techniques. The surface morphological study using field emission scanning electron microscopy (FE-SEM) is explained. The surface wettability investigation is carried out using contact angle measurement. The end part of **Chapter-II** is focused on supercapacitor. It includes supercapacitor device types, symmetric, asymmetric and hybrid capacitors. The supercapacitive parameters like cyclic voltammetry, galvanostatic charge/discharge and impedance analysis are explained in detail.

The **Chapter-III** elaborates the synthesis and characterization of Yb_2S_3 thin films via CBD and SILAR methods and their electrochemical performance in aqueous electrolytes. The chapter-III is divided into two sections. Section 'A' deals with the preparation of Yb_2S_3 thin films via CBD method and their characterizations. In CBD method, Yb^{3+} ions were obtained by dissolving YbCl_3 precursor in DDW. The source of anion, S^{2-} ions was taken from $\text{Na}_2\text{S}_2\text{O}_3$ and deposition was obtained at temperature of 353 K. After 180 min, Yb_2S_3 thin film was formed over stainless steel (SS) substrate. The formation of Yb_2S_3 thin film was identified from XRD and FT-Raman investigations. The scanning electron microscopy (SEM) study showed the nano-grained surface morphology. The surface wettability study examined using drop of water over Yb_2S_3 film showed hydrophilic nature.

The electrochemical behavior of Yb_2S_3 film electrode was tested in aqueous (1 M KOH) electrolyte. The three-electrode system configuration with platinum plate as a counter, Yb_2S_3 film as working and mercury/mercury oxide (Hg/HgO) as a reference electrode were used. The supercapacitive properties of Yb_2S_3 film electrode were studied using the CV, GCD and EIS tests. From the CV investigation, the electrochemical performance was investigated in terms of specific capacitance by varying scan rate. The GCD showed that Yb_2S_3 film electrode has good discharge ability. Further, the electrochemical cyclic stability was tested up to 3000 CV cycle at constant scan rate. The 81 % electrochemical stability of Yb_2S_3 film electrode retained

for 3000 cycles at fixed scan rate of 100 mV s^{-1} . The impedance study of Yb_2S_3 film was carried out in the range of frequency between 0.1 Hz to 1 KHz. The impedance data were further analyzed by plotting the Nyquist plot with best fitted equivalent circuit diagram. Yb_2S_3 film electrode showed specific capacitance (Cs) of 184.6 F g^{-1} at scan rate of 5 mV s^{-1} .

The **Chapter-III**, section 'B' contains preparation and characterization of Yb_2S_3 films via SILAR method. The experimental details for the synthesis of Yb_2S_3 film through SILAR method are described. The process for formation of Yb_2S_3 film was carried out using four steps system. In the 1st step beaker contains cation source as Yb^{3+} ions adsorbed on surface substrate. The loosely adsorbed cations are rinsed in the 2nd beaker which contains double distilled water (DDW). The 3rd beaker is used anion (S^{2-}) source as Na_2S solution. The preadsorbed Yb^{3+} ions reacted with S^{2-} ions and loosely bonded S^{2-} ions rinsed in 4th beaker which contained DDW. This is one SILAR cycle. Such 120 cycles formed well adherent Yb_2S_3 films on surface substrate. The formation of Yb_2S_3 films was confirmed from XRD and X-ray photoelectron spectroscopy (XPS) analyses. The FE-SEM study revealed the nanoparticles surface texture of Yb_2S_3 thin film. The surface wettability study showed that Yb_2S_3 thin film is hydrophilic nature using water droplet. The Yb_2S_3 thin films were utilized as supercapacitor electrode. The results showed that Cs of 181 F g^{-1} is obtained at scan rate of 5 mV s^{-1} . The Yb_2S_3 electrode reflected the cyclic stability of 83 % in aqueous electrolyte after 3000 CV cycle. The impedance results indicated that good capacitive behavior of Yb_2S_3 electrode in the lower frequency region. The CBD prepared thin films showed better results as compared to SILAR synthesized thin film, due to tiny hydrated radius of K^+ ions favors faster ionic mobility and interaction with electrode material, thereby resulting in enhanced supercapacitor properties.

The **Chapter-IV** deals with the preparation, characterization and supercapacitive performance of GO, SILAR Yb_2S_3 and GO/ Yb_2S_3 composite thin films. Beginning part of this chapter describes the preparation and characterization of GO, Yb_2S_3 and GO/ Yb_2S_3 composite thin films via SILAR method. The GO, Yb_2S_3 and GO/ Yb_2S_3 composite thin films were prepared by L-b-L and SILAR methods in aqueous medium using GO, 0.1 M YbCl_3 as cation and 0.15 M Na_2S as anionic sources. The XRD and XPS tests were evident for the structural identification of GO, Yb_2S_3 and GO/ Yb_2S_3 composite thin films materials. The FE-SEM images of these thin films showed the formation of homogeneous layered structure, nanoparticles and porous

nanoparticles like morphologies. The formation of homogeneous layered nanoparticles and porous nanoparticles surface exhibited a contact angle of 49° , 57° and 31° respectively for GO, Yb_2S_3 and GO/ Yb_2S_3 indicating the hydrophilic nature.

At the end of this chapter, from CV investigation, maximum Cs of 181, 193 and 376 F g^{-1} , respectively were obtained at 5 mV s^{-1} scan rate in $1.0 \text{ M Na}_2\text{SO}_4$ electrolyte. The long life cyclic stability of GO, Yb_2S_3 and GO/ Yb_2S_3 composite thin film electrodes was evaluated and these films exhibited stability of 89, 81 and 93 %, respectively. Impedance analysis showed that in aqueous electrolyte GO/ Yb_2S_3 composite thin film electrode exhibited good capacitive behavior.

The **Chapter-V** deals with chemical preparation, characterization of MnO_2 thin film and its supercapacitive performance evaluation in aqueous Na_2SO_4 electrolyte. This chapter is divided in to two sections (A and B). The section 'A' consists of preparation of MnO_2 thin film electrode via SILAR method and its structural, surface morphological and wettability characterization using various characterization tests. The synthesis of MnO_2 thin films by SILAR method are detailed discussed in the section 'A'. The formation of MnO_2 film over SS substrate, the MnSO_4 and KMnO_4 precursors were used as cation and anion solution sources, respectively. After 90 SILAR cycles uniform and well quality MnO_2 film electrode obtained over the substrate. Further, these films were characterized by XRD, XPS and FT-IR studies to identify the formation of MnO_2 . The FE-SEM study revealed the formation of interconnected network of MnO_2 with nanoparticles like surface. The wettability study showed that hydrophilic nature of MnO_2 film surface with 49.7° contact angle using the water drop.

The **Chapter-V** section 'B' supercapacitor performance evaluation of MnO_2 film is described. The MnO_2 film material exhibited 421 F g^{-1} Cs in aqueous $1.0 \text{ M Na}_2\text{SO}_4$ electrolyte. In aqueous electrolyte the SILAR synthesized MnO_2 film electrode showed excellent cyclic stability with the value of 94 %. The EIS analysis revealed that MnO_2 film demonstrated better capacitive behavior. From these results, it is concluded that MnO_2 film has wide potential application.

The **Chapter-VI** deals with the fabrication and performance evaluation of flexible symmetric and asymmetric devices Yb_2S_3 , MnO_2 and GO/ Yb_2S_3 composite based thin film electrodes using solid-state polymer gel electrolytes. This chapter is divided in to four sections. In which section 'A' is focused on fabrication process and supercapacitor performance of flexible solid-state symmetric ($\text{Yb}_2\text{S}_3/\text{PVA-KOH}/\text{Yb}_2\text{S}_3$) supercapacitor (FSS-SSc) device (CBD method). At beginning of section 'A',

preparation of electrode and device fabrication process are described. The Yb_2S_3 film electrodes were synthesized via CBD method over flexible SS. The prepared PVA-KOH electrolyte gel was sandwiched between two electrodes and sealed both electrodes. At the end of section 'A', the supercapacitive behavior of FSS-SSc device was carried out using CV, GCD and EIS tests. The value of C_s of FSS-SSc device was found to 15 F g^{-1} at scan rate of 5 mV s^{-1} . The values of energy density (E.D.) and power density (P.D.) were 6.40 Wh kg^{-1} and 0.30 kW kg^{-1} , respectively observed at 0.2 A g^{-1} current density. The stability of 78 % was retained after 3000 CV cycles for FSS-SSc device.

The section 'B' is focused on fabrication and supercapacitor behavior of FSS-SSc ($\text{Yb}_2\text{S}_3/\text{PVA-Na}_2\text{SO}_4/\text{Yb}_2\text{S}_3$) device (SILAR method). In the initial part of section B, synthesis of electrode and symmetric device fabrication process are described. The flexible Yb_2S_3 film electrodes were deposited via SILAR method. The Yb_2S_3 film was synthesized over flexible SS. The PVA- Na_2SO_4 gel electrolyte was sandwiched between two flexible electrodes. In the final part of section 'B', the supercapacitive performance of FSS-SSc device was studied using CV, GCD and EIS tests. The value of C_s of FSS-SSc device is found to 21 F g^{-1} at scan rate of 5 mV s^{-1} . The values of E.D. and P.D. reached 7.38 Wh kg^{-1} and 0.38 kW kg^{-1} , respectively at 0.5 A g^{-1} current density. The stability of 80 % was retained after the 3000 CV cycles for a symmetric $\text{Yb}_2\text{S}_3/\text{PVA-Na}_2\text{SO}_4/\text{Yb}_2\text{S}_3$ supercapacitor device.

The section 'C' deals with the fabrication and supercapacitive performance of FSS-SSc ($\text{GO}/\text{Yb}_2\text{S}_3//\text{PVA-Na}_2\text{SO}_4//\text{GO}/\text{Yb}_2\text{S}_3$) device (SILAR method). The FSS-SSc device exhibited 58 F g^{-1} C_s at scan rate of 5 mV s^{-1} . The device delivered E.D. of 28 Wh kg^{-1} with P.D. of 0.62 kW kg^{-1} at the current density of 1.0 A g^{-1} .

The section 'D' deals with the fabrication and supercapacitive performance evaluated for flexible solid-state asymmetric ($\text{GO}/\text{Yb}_2\text{S}_3//\text{PVA-Na}_2\text{SO}_4//\text{MnO}_2$) supercapacitor (FSS-ASc) device (SILAR method). The FSS-ASc device showed 92 F g^{-1} C_s at scan rate of 5 mV s^{-1} . The device achieved E.D. of 43 Wh kg^{-1} and P.D. as 0.84 kW kg^{-1} at the current density of 1.0 A g^{-1} . **Chapter-VII** provides the summary of all the chapters.

In conclusions, we have prepared ytterbium sulfide, graphene oxide, graphene oxide composite with ytterbium sulfide and manganese oxide thin films by binder free, simple and cost effective chemical methods and studied their characteristics. The supercapacitive performance was tested in aqueous electrolytes using the CV, GCD and

EIS tests. The results showed maximum values of C_s of 184.6, 181, 193 and 376 $F g^{-1}$ an obtained for Yb_2S_3 (CBD), Yb_2S_3 (SILAR), GO and GO/Yb_2S_3 film electrodes, respectively with 81, 83, 89 and 93 % cyclic stabilities over 3000 cycles. The porous nanoparticles composed surface texture of GO/Yb_2S_3 film electrode showed better supercapacitor performance. **Table 7.1** shows the comparison of supercapacitive performance evaluation of Yb_2S_3 , GO, and GO composite with Yb_2S_3 and MnO_2 thin films in three electrode systems by CBD, L-b-L and SILAR methods. Based on the good electrochemical properties of Yb_2S_3 , GO/Yb_2S_3 and MnO_2 film electrodes, flexible symmetric and asymmetric supercapacitor devices were fabricated and tested their supercapacitor properties using the cyclic voltammetry, galvanostatic charge/discharge and impedance analysis. **Table 7.2** shows the supercapacitive performance evaluation of various symmetric and asymmetric devices. The flexible asymmetric $GO/Yb_2S_3//PVA-Na_2SO_4//GO/Yb_2S_3$ supercapacitor device exhibits maximum C_s of 92 $F g^{-1}$ at a scan rate of 5 $mV s^{-1}$. The cost effective GO/Yb_2S_3 and MnO_2 electrodes based supercapacitors can be useful for various commercial applications in portable and foldable devices.

Table: 7.1: Supercapacitive performance evaluation for various thin film material electrodes.

Sr. No.	Material	Method	Electrolyte (1 M)	Potential window (V.Hg/HgO)	Specific Cap. (Cs) (F g ⁻¹)	Cyclic stability (%)
1	Yb ₂ S ₃	CBD	KOH	-1.2 to - 0.2	184.6	81 (3000)
2	Yb ₂ S ₃	SILAR	Na ₂ SO ₄	-1 to 0	181	83 (3000)
3	GO	L-b-L	Na ₂ SO ₄	-1 to 0	193	89 (3000)
4	GO/Yb ₂ S ₃	SILAR	Na ₂ SO ₄	-1 to 0	376	93 (3000)
5.	MnO ₂	SILAR	Na ₂ SO ₄	0 to 1	421	94 (3000)

Table: 7.2: Supercapacitive performance evaluation for symmetric and asymmetric devices.

Sr. No.	Device configuration	Gel electrolyte	Potential window (V)	Specific Cap. (Cs) (F g ⁻¹)	Energy density (E.D.) (Wh kg ⁻¹)	Power density (P.D.) (kW kg ⁻¹)	Cyclic stability (%)
1	Yb ₂ S ₃ /PVA-KOH/Yb ₂ S ₃	PVA-KOH	0-1.6	15	6.40	0.30	78 (3000)
2	Yb ₂ S ₃ /PVA-Na ₂ SO ₄ /Yb ₂ S ₃	PVA-Na ₂ SO ₄	0-1.6	21	7.68	0.38	80 (3000)
3	GO/Yb ₂ S ₃ //PVA-Na ₂ SO ₄ //GO/Yb ₂ S ₃	PVA-Na ₂ SO ₄	0-1.8	58	28	0.62	85 (10000)
4	GO/Yb ₂ S ₃ //PVA-Na ₂ SO ₄ //MnO ₂	PVA-Na ₂ SO ₄	0-2.0	92	43	0.84	87 (10000)

Future work:

The current motivational work is on the preparation and electrochemical properties of rare earth metal ytterbium sulfide with GO composite thin film electrodes. The future work is proposed as following.

- Higher potential window can be tailored using the organic and redox active electrolytes.
- Enhancement of the supercapacitor device stability by humidity and temperature studies.
- Improvement of cyclic life and efficiency of device using multi walled carbon nanotubes (MWCNT) material.
- Use of hydrophilic salts and other hydrophilic ionic liquids as electrolytes, to improve the performance of device in humid atmosphere.
- Exploration of other gel polymer electrolytes and if necessary nanocomposite of gel polymer electrolytes with different nano-sized filler with high ionic conductivity and good mechanical properties.

8.1 Recommendations:

The presented research work, ytterbium sulfide (Yb_2S_3) thin films were prepared by chemical baths deposition (CBD), successive ionic layer adsorption and reaction (SILAR) methods. The charge storage capacity of these thin films was improved by means of improvement in specific capacitance (C_s), cyclic stability. To achieve this, graphene oxide (GO) was composited with the Yb_2S_3 using SILAR method. The objective of the preparation of composite thin film electrode was to improve specific capacitance and cyclic stability of the material than pristine materials. The solid state symmetric and asymmetric supercapacitor devices fabricated using GO/ Yb_2S_3 composite and manganese oxide (MnO_2) thin film electrodes.

Finally, it is recommended that the use of SILAR is an effective chemical method for enhancing the supercapacitor performance of GO/ Yb_2S_3 thin films. Furthermore, SILAR offer expedient method for resulting nanoparticles with a large surface area under curves and good electrical conductivity, which have been useful for monitoring the porous surface morphology of GO/ Yb_2S_3 thin film.

8.2 Conclusions:

The conclusions from the present research work are listed as follows:

1. The Yb_2S_3 thin films were successfully synthesized on SS substrate via simple and low-cost CBD and SILAR methods and used as working electrodes for supercapacitor applications.
2. The GO/ Yb_2S_3 composite thin films were prepared by the SILAR method on SS substrate.
3. The SILAR synthesized GO/ Yb_2S_3 composite thin films showed maximum C_s of 376 F g^{-1} at scan rate of 5 mV s^{-1} .
4. Because of layer-by-layer deposition of material, porous, nanoparticles like morphology and high surface area under curves.
5. Symmetric supercapacitor device has successfully fabricated using GO/ Yb_2S_3 composite electrodes in PVA- Na_2SO_4 gel electrolyte.

6. The MnO_2 thin film electrodes were prepared on SS substrates by SILAR method and used as cathode electrode for fabrication of asymmetric device.
7. The MnO_2 electrode showed C_s of 421 F g^{-1} with 94 % cyclic retention after 3000 CV cycles.
8. The asymmetric device was fabricated using SILAR deposited $\text{GO/Yb}_2\text{S}_3$ composite and MnO_2 electrodes and it delivered high supercapacitive performance.
9. In addition, the actual demonstration of the asymmetric solid-state device, 211 red LEDs are lightened up to 1.5 min.

8.3 Summary:

The present works deal with the synthesis of Yb_2S_3 , GO and $\text{GO/Yb}_2\text{S}_3$ composite thin films by simple cost effective and binder-free chemical approach. The numbers of preparative parameters were optimized to get porous nanoparticles surface morphology, which successfully increase the electrochemical features of $\text{GO/Yb}_2\text{S}_3$ composite thin film. The composite thin films showed better supercapacitive performance than Yb_2S_3 and GO thin films. Therefore, the composite thin films with excellent electrochemical features were used as one electrode for fabrication of FSS-ASCs device. Furthermore, MnO_2 was selected as positive electrode with a wide potential window.

The general framework of the energy requirements for the generation to come and different energy storage devices has been explained. The principle of supercapacitors, taxonomy of supercapacitor and new trends in research in supercapacitors, the need for supercapacitors, and their work based on the classification have been explained. Also, the literature survey on rare earth metal (REM) chalcogenide thin films and their physical properties, literature survey on REM chalcogenide thin films for supercapacitor performance and literature survey on GO based composite thin films for supercapacitor performance. The REM chalcogenides thin films synthesized by different methods with different morphologies in terms of supercapacitive parameters like C_s , energy density (E. D.), power density (P. D.), and capacity retention is included.

The general introduction to the deposition methods and their classification

were explained. The detailed information about the thin film deposition methods employed in the present study, i.e., the CBD method and the SILAR method, has been given in detail with their advantages and disadvantages. The characterization techniques used for structural, surface morphological, and elemental analysis such as XRD, XPS, FT-IR, FE-SEM, and TEM have been described in detail with their theoretical background. The electrochemical techniques to evaluate the electrochemical features of Yb_2S_3 , GO and GO/ Yb_2S_3 composite thin film electrodes like CV, GCD, and EIS have been discussed in detail.

The Yb_2S_3 thin film has been prepared by simple CBD and SILAR routes, and their electrochemical performance has been investigated in 1M KOH and 1M Na_2SO_4 electrolytes. Yb_2S_3 thin films were characterized by XRD, XPS, SEM and surface wettability study. The XRD analysis confirmed that CBD and SILAR method synthesized Yb_2S_3 thin films exhibited a monoclinic structure. The XPS spectra confirm the chemical purity of the material. FE-SEM images showed the nano-grains and nanoparticles natures of Yb_2S_3 thin films. The Yb_2S_3 thin film electrode showed 184 and 181 $\text{F g}^{-1} \text{Cs}$ at a scan rate of 5 mV s^{-1} for CBD and SILAR prepared thin films, respectively. The Yb_2S_3 thin film electrodes exhibited 81 % (CBD method) and 83 % (SILAR method) cyclic stability after 3000 cycles.

The Yb_2S_3 , GO and GO/ Yb_2S_3 composite thin films have been prepared by a simple SILAR route. Yb_2S_3 , GO and GO/ Yb_2S_3 thin films were characterized by XRD, XPS, FE-SEM, and TEM. The XRD analysis confirmed that SILAR synthesized GO/ Yb_2S_3 composite thin film exhibited a monoclinic structure. The XPS spectra confirm the chemical composition and chemical purity of the material. FE-SEM images showed the porous nanoparticles nature of the GO/ Yb_2S_3 composite thin film. The electrochemical performance of the GO/ Yb_2S_3 composite thin film electrode is tested via a three electrode arrangement in 1M Na_2SO_4 electrolyte. GO/ Yb_2S_3 composite thin film electrode showed maximum Cs of 376 F g^{-1} at scan rate 5 mV s^{-1} . The GO/ Yb_2S_3 composite thin film electrode exhibits 93 % cyclic stability for 3000 cycles.

The MnO₂ thin films were synthesized by SILAR method and their electrochemical performance has been investigated. The MnO₂ thin films were characterized by XRD, XPS, FT-IR and FE-SEM. The XRD analysis confirms that SILAR synthesized thin film showed tetragonal structure. The XPS spectrum confirms the chemical purity of the material. FE-SEM images showed nanoparticles surface morphology. FT-IR analysis confirmed that presence of Mn and O elements. The electrochemical performance of MnO₂ thin film electrode is tested via a three electrode cell arrangement in 1M Na₂SO₄ electrolyte. The maximum Cs 421 F g⁻¹ showed of MnO₂ thin film at scan rate of 5 mV s⁻¹ with 94 % cyclic stability retention for 3000 CV cycles.

The fabrication and supercapacitive performance evaluation of flexible solid state symmetric supercapacitor (Yb₂S₃//Yb₂S₃ and GO/Yb₂S₃//GO/Yb₂S₃) devices (FSS-SSCs) and flexible solid state asymmetric supercapacitor (GO//Yb₂S₃//MnO₂) (FSS-ASCs) device have been studied. The performance of the devices was tested using different techniques such as CV, GCD, EIS and stability. The fabrication of FSS-SSCs (CBD method) device and investigated its supercapacitive performance. The fabrication of FSS-SSCs (SILAR method) device and studied its electrochemical performance. The FSS-SSCs (SILAR method) device (Yb₂S₃/PVA-Na₂SO₄/Yb₂S₃) exhibited 21 F g⁻¹ Cs at a scan rate of 5 mV s⁻¹ with E. D. of 7.68 Wh kg⁻¹ at a P. D. of 0.38 kW kg⁻¹. The fabrication of FSS-SSCs device (GO/Yb₂S₃//PVA-Na₂SO₄//GO/Yb₂S₃) and it showed 58 F g⁻¹ Cs with better capacity retention of 89 % after 10000th cycles. The device exhibited E. D. of 28 Wh kg⁻¹ at a P. D. of 0.62 kW kg⁻¹ and studied supercapacitive performance. The FSS-ASCs device fabricated using GO/Yb₂S₃ and MnO₂ electrodes in the configuration of GO/Yb₂S₃//PVA-Na₂SO₄//GO/Yb₂S₃. The FSS-ASCs device showed 92 F g⁻¹ Cs at scan rate of 5 mV s⁻¹. The FSS-ASCs device delivered E. D. of 43 Wh kg⁻¹ at a P. D. of 0.84 kW kg⁻¹ with cyclic stability retention of 87 % for 10000th cycles. Obtained results suggest that the proposed theme of the (GO/Yb₂S₃//PVA-Na₂SO₄//GO/Yb₂S₃) asymmetric supercapacitor device holds great promise for applications in energy storage devices.

Finally, two FSS–ASCs devices connected in series were able to glow a panel of 211 red LEDs efficiently. The initial power dissipated through FSS-ASCs device was 840 mW cm^{-2} . Finally, the observed results conclude that the MnO_2 and $\text{GO/Yb}_2\text{S}_3$ electrodes based FSS-ASCs can power up small electronic equipment requiring power in the range of 0.01 mW to 0.1 mW.

8.4 Future findings

The current motivational work is on the preparation and electrochemical properties of Yb_2S_3 with GO composite thin film electrodes. The introduction of GO enhances electrical conductivity, surface area under the curve and electrochemical supercapacitive performance of pristine material. The future work is proposed as following.

- 1) Preparation $\text{GO/Yb}_2\text{S}_3$ -MWCNTs nanocomposites electrode using simple and binder free SILAR method.
- 2) Fabrication and supercapacitive performance evaluation of symmetric and asymmetric devices based on $\text{GO/Yb}_2\text{S}_3$ -MWCNTs nanocomposites electrode material in redox active gel electrolyte.
- 3) Understanding the process of energy storage in REM sulfide based compounds and physical characterization using XRD, SEM, TEM, and XPS techniques.
- 4) Further, in situ characterization of symmetric and asymmetric devices through TEM and NMR analyses could give a better understanding of actual processes involved in charge storage.